

DEVELOPMENT OF A SILICON VERTEX TRACKER FOR THE ELECTRON-ION COLLIDER

by

HÅKAN LENNART OLOV WENNLÖF



A thesis submitted to the University of Birmingham for the
degree of DOCTOR OF PHILOSOPHY

School of Physics and Astronomy
College of Engineering and Physical Sciences
University of Birmingham
United Kingdom

May 2021

UNIVERSITY OF
BIRMINGHAM

University of Birmingham Research Archive

e-theses repository

This unpublished thesis/dissertation is copyright of the author and/or third parties. The intellectual property rights of the author or third parties in respect of this work are as defined by The Copyright Designs and Patents Act 1988 or as modified by any successor legislation.

Any use made of information contained in this thesis/dissertation must be in accordance with that legislation and must be properly acknowledged. Further distribution or reproduction in any format is prohibited without the permission of the copyright holder.

Abstract

The electron-ion collider (EIC) will be built at the Brookhaven National Laboratory over the next ten years, with the purpose of giving insight into nucleon structure, origins of nucleon mass and spin, and quark and gluon confinement. This thesis pertains to the silicon vertex tracker for an EIC experiment; the detector closest to the interaction point. The purpose of a silicon vertex tracker is to locate the origin vertex position of charged particles and measure the particle momentum, and the EIC physics goals require detector resolutions beyond current state-of-the-art silicon vertex trackers. The aim of this thesis is to find a suitable silicon sensor technology for further developments by tests performed in a lab and at a testbeam, and to find a silicon vertex tracker geometry with performance matching the EIC physics requirements using simulations.

The baseline sensor for the studies comes from the ALICE inner tracker upgrade, and is called the ALPIDE sensor. A new monolithic silicon sensor development designed to increase depletion is tested and compared to the performance of an ALPIDE-like sensor, and found to improve charge collection performance while keeping the sensor capacitance low. This aids tracking performance, and the new development is thus considered a possible path for development of an EIC-specific sensor. Simulations of different silicon vertex tracker geometries and parameters are performed using GEANT4, and a high-performing layout consisting of inner and outer silicon sensor layers surrounded by a gaseous detector and silicon disks is developed. It is also found that if a more compact tracker is desired, an all-silicon concept outperforms a combination of silicon and gaseous detectors. Further simulations of the best-performing layouts with current projections of possible silicon sensor material thickness and pixel size show that they meet the requirements of the EIC physics goals in terms of momentum resolution if a 3 T solenoidal magnetic field is used, and pointing resolution regardless of magnetic field strength. The silicon vertex tracker developed in this work is one of two baseline tracker concepts used in the ongoing development of an EIC reference detector.

The performance of different detector concepts is also studied using realistic electron-proton collision events generated using PYTHIA and propagated through the detector simulation, with a focus on charmed meson reconstruction. It is found that a compact all-silicon tracker can perform as well as an all-silicon concept with a larger radius in these studies, but a large-radius combination of silicon and gaseous detectors is always better than all-silicon concepts in the studied open charm case.

Acknowledgements

First and foremost I want to thank my supervisors, Laura Gonella and Peter Jones, for giving me the opportunity to be the UK's first EIC Ph.D. student, and for all their help and guidance. I especially appreciate the tireless dedication of Laura throughout the work. Our common high aspirations have produced a lot of nice results. I am also grateful for the guidance of Paul Newman and Phil Ilten concerning the physics studies and event generation. The regular meetings of the Birmingham Instrumentation Laboratory for Particle physics and Applications group have also been a great source of discussions and feedback throughout. I acknowledge that part of the simulations carried out in this work were performed utilising the University of Birmingham's BlueBEAR High Performance Computing facility.

I have been helped a lot through discussions with colleagues in the CERN ATLAS Pixel group and the EIC Yellow Report Tracking Working Group, where I have had the opportunity to discuss my work with many experts. Alexander Kiselev and Jin Huang in particular have been helpful both in furthering my understanding of tracking theory and algorithm limitations, and in providing details of the simulation frameworks used. Throughout the work there have also been plenty of useful interactions with colleagues at the Lawrence Berkeley National Laboratory. I especially want to thank Ernst Sichtermann from LBNL for providing many useful insights and discussions.

All of this adventure would have been much more difficult without the wonderful friends I have made along the way. First of all, I am very grateful to Beckie Trinder, for making me feel welcome in England since my very first week and being a good friend throughout. Our office antics and tea times made the working days much easier even at the roughest times, and our walks kept me sane during lockdown. I am also very grateful to my Nerdvana pals; Jack Bishop, Stuart Pirrie, and Tony Turner. We have had a lot of laughs and shared support through whatever has been going on.

Finally I want to thank my family, and especially my parents, for their unwavering support throughout this and other adventures.

*Till farfar, Olle Wennlöf (juni 1927 - juni 2021).
Tack för all nyfikenhet.*

*“It has long been an axiom of mine that the little things
are infinitely the most important.”*

—Sherlock Holmes

Table of contents

Abstract	ii
Acknowledgements	iii
List of Figures	viii
List of Tables	xv
1 Introduction	1
1.1 History of electron-nucleon scattering	1
1.2 The electron-ion collider	2
1.2.1 Physics goals	4
1.2.2 Collider parameters	5
1.2.3 Detector concepts	6
1.3 Silicon vertex tracker	8
1.4 Thesis outline	9
2 Tracking detector theory	10
2.1 Particle interactions	10
2.1.1 Charged particle interactions	10
2.1.2 Radiation length	11
2.1.3 Multiple scattering	13
2.2 Detector properties	13
2.2.1 Spatial resolution of a segmented detector	13
2.2.2 Pointing resolution	15
2.2.3 Relative momentum resolution	17
2.2.4 Detector coordinate system	19
2.3 Kalman filter track reconstruction	20
2.4 Silicon detectors	22
2.4.1 Silicon properties	22
2.4.2 p-n junction	22
2.4.3 Basic silicon sensor operation	23
2.4.4 Detector noise	24
2.4.5 Monolithic Active Pixel Sensors	25
2.4.5.1 MAPS sensor evolution	26
2.4.5.2 The ALPIDE sensor	27
2.4.5.3 ALICE ITS3 sensor developments	28
3 EIC physics theory	30
3.1 Electron-proton collisions	30

TABLE OF CONTENTS

3.2	EIC physics goals and tracking detector requirements	37
3.2.1	Nucleon structure	37
3.2.2	Nucleon mass	38
3.2.3	Nucleon spin	39
3.2.4	Nuclear effects	39
3.3	Open charm physics	40
3.3.1	Charm production	41
3.3.1.1	The charm structure function	41
3.3.2	Hadronisation	43
3.3.3	Decay	43
4	Sensor studies	45
4.1	Introduction	45
4.2	TowerJazz Investigator studies	45
4.2.1	TowerJazz Investigator test chips	45
4.2.2	Comparing the standard and modified processes	47
4.2.2.1	Experimental setup	47
4.2.2.2	Results	50
4.2.3	Comparing different biasing configurations	55
4.2.3.1	Experimental setup	55
4.2.3.2	Results	56
4.3	MiniMALTA studies	60
4.3.1	MiniMALTA test chip	60
4.3.2	Diamond Light Source testbeam	62
4.3.2.1	Data analysis	63
4.3.2.2	Results	65
4.4	Conclusions and discussion	73
5	General detector layout simulations	75
5.1	Introduction	75
5.2	Experimental setup	76
5.3	Results	80
5.3.1	Radiation length scan	80
5.3.2	Comparison no SVT/SVT+TPC	81
5.3.3	Barrel pixel size	82
5.3.4	Barrel layout studies	83
5.3.5	Time-stamping layer thickness and pixel size	86
5.3.6	Disks, varying pixel sizes	87
5.3.7	Innermost disk position	90
5.3.8	Different inner barrel length, with disks	93
5.3.9	Different parameters on outermost disks	95
5.3.10	Replacing gas TPC with silicon layers and disks	100
5.3.10.1	Different silicon layouts	100
5.3.10.2	Different silicon replacement outer radius	105
5.4	Conclusions	112

6	Focused detector layout simulations	113
6.1	Introduction	113
6.1.1	Central detector region layout	114
6.1.2	Simulation tools	115
6.1.2.1	Fun4All	115
6.1.2.2	PYTHIA	116
6.1.3	Baseline layouts	117
6.1.3.1	Silicon plus TPC baseline	117
6.1.3.2	All-silicon baseline	120
6.1.3.3	All-silicon, 600 mm outer radius	120
6.2	Comparison of silicon sensor technologies	122
6.3	Detector resolution parametrisation	125
6.3.1	Experimental setup	126
6.3.2	Results	127
6.3.3	Discussion	128
6.4	Minimum momentum investigation	131
6.4.1	Experimental setup	131
6.4.2	Results and discussion	132
6.4.3	Resolution study	137
6.5	Event generation	139
6.5.1	Experimental setup	139
6.5.2	Particle distributions	140
6.5.3	Detector acceptance	143
6.6	Open charm event reconstruction	146
6.6.1	D^0 reconstruction	147
6.6.2	D^+ reconstruction	149
6.6.3	D^{*+} reconstruction	150
6.6.4	All photoproduction processes activated	152
6.6.5	Detector kinematic range	153
6.7	Conclusions and discussion	158
7	Conclusions	159
7.1	Sensor studies	159
7.2	Simulations	159
8	Summary	162
9	Future work	165
	Appendices	168
Appendix A	Charged particle interactions	169
Appendix B	Different silicon layouts for comparison with a TPC	172
Appendix C	Detector parametrisation fit results	176
	References	181

List of Figures

1.1	Sketch of the electron-ion collider, based on the existing RHIC beamline.	3
1.2	EIC coverage range in the kinematic variables x and Q^2 , compared to past and current experiments with polarised beams.	4
1.3	The four general detector concepts developed for the EIC, forming the basis for more focused developments started in January 2020.	6
2.1	Energy loss divided by material density (termed “mass stopping power”) for a positive muon traversing copper, as a function of $\beta\gamma$	11
2.2	Sketches of the simplified two-layer detector used in deriving the equation for pointing resolution.	16
2.3	Detector coordinate system, overlaid on a simulated detector. The coordinates of the point \vec{r} are given in three different ways. ρ is the radial distance of the point from the z axis, $r = \vec{r} $, and the angles θ and ϕ are marked.	19
2.4	Kalman filter algorithm illustration using a multi-layer detector.	21
2.5	Illustration of an unbiased p-n junction.	23
2.6	Sketch of a bump-bonded hybrid sensor and a monolithic active pixel sensor. In the hybrid sensor, the sensitive volume is on a separate silicon wafer to the readout electronics. In the monolithic active pixel sensor, the readout electronics are embedded in the same wafer as the sensitive volume.	25
2.7	Schematic view of different ways to reach full depletion of a MAPS sensor, with large or small collection electrode. Cross sections of single pixels are shown.	27
2.8	Artistic view of the ALPIDE chip, showing a cross section of four adjacent pixels.	28
3.1	Electron-proton scattering. X indicates the hadronic final state, the characteristics of which vary with the collision energy (proton for elastic scattering, excited state of proton for inelastic scattering, and shower of hadrons for deep inelastic scattering).	31
3.2	Proton parton distribution functions for two different energy scales (10 GeV ² (a) and 10 000 GeV ² (b)).	35

3.3	The proton structure function F_2 from several experiments, plotted versus Q^2 for different fixed values of x . The values for different x have been scaled by a factor in order to show them all without overlapping.	36
3.4	Feynman diagram showing the leading order process (with a direct photon) of photon-gluon fusion to $c\bar{c}$	41
3.5	The charm structure function $F_2^{c\bar{c}}$ from HERA (combined data from the H1 and ZEUS experiments) and the EMC experiment, plotted versus x for different fixed values of Q^2	42
3.6	Leading order Feynman diagrams for the decay channels for D^0 , D^+ , and D^{*+} mesons investigated in the work presented here.	44
4.1	Schematic view of a pixel, from the side and from above. Definitions of the pixel dimensions that vary between different mini-matrices in the test chips are shown in both views.	46
4.2	Schematic view of a pixel of the TowerJazz Investigator in the standard process (a) and modified process (b). Doping types, depleted regions, and an example particle track are shown.	47
4.3	Schematic view of the TowerJazz Investigator 1 experimental setup.	48
4.4	Comparison of the signal amplitude and rise time for the standard and modified process, using a $20 \times 20 \mu\text{m}^2$ pixel.	51
4.5	Comparison of the signal amplitude and rise time for the standard and modified process, using a $28 \times 28 \mu\text{m}^2$ pixel.	51
4.6	Comparison of the signal amplitude and rise time for the standard and modified process, using a $50 \times 50 \mu\text{m}^2$ pixel.	51
4.7	Plots of signal rise time versus amplitude, for the standard and modified process using a $28 \times 28 \mu\text{m}^2$ pixel.	53
4.8	Schematic view of the TowerJazz Investigator 1B experimental setup.	55
4.9	Comparison of the signal amplitude and rise time for a fixed p-well biasing of -3 V (labelled “PWELL”), and varying substrate biasing (labelled “HV”).	57
4.10	Comparison of the signal amplitude and rise time for a fixed p-well biasing of -6 V (labelled “PWELL”), and varying substrate biasing (labelled “HV”).	57
4.11	Signal rise time versus amplitude, for a p-well biasing of -6 V and a substrate biasing of -15 V.	58
4.12	Comparison of the signal amplitude and rise time for a fixed p-well biasing of -6 V (labelled “PWELL”), and substrate biasing (labelled “HV”) of -6 V and -15 V, for a $20 \times 20 \mu\text{m}^2$ pixel.	59
4.13	Sketch of the electric field lines (marked as black lines with arrows) within a pixel.	59
4.14	MiniMALTA chip sector layout. Sectors under investigation are marked by blue boxes.	61
4.15	Schematic view of a pixel of the MiniMALTA with the extra deep p-well modification (a) and the n-gap modification (b).	62

LIST OF FIGURES

4.16	Example pixel response, with pixel border from fit (a). The colour corresponds to the normalised photon response, between 0% and 100%. The projections and fits for this pixel, using a generalised Gaussian distribution, are shown in (b) and (c).	65
4.17	Total (summed) photon response maps for all available pixels in the three different sectors, for the unirradiated chip. The substrate voltage used is -6 V, and the p-well voltage is -2 V.	66
4.18	Normalised in-pixel photon response per pixel for four different pixels in the three different sectors, for the unirradiated MiniMALTA chip.	67
4.19	Normalised in-pixel photon response per pixel for four different pixels in the MALTA-like sector and the n-gap sector, for the MiniMALTA chip irradiated to 1 MeV neutron equivalents per cm^2	68
4.20	Normalised in-pixel photon response per pixel for four different pixels in the three different sectors, for the MiniMALTA chip irradiated to 1 MeV neutron equivalents per cm^2	69
5.1	Sketch of a cross section along the beam direction of the “standard” simulated silicon vertex tracker barrel, with surrounding TPC and silicon disks. A beampipe runs through the centre of the detector, but is not included in the figure.	80
5.2	Radiation length scans for detector setups. The standard beampipe and TPC are in place in both scans.	81
5.3	Relative momentum resolution and transverse pointing resolution, comparing having a standard barrel with a $20 \times 20 \mu\text{m}^2$ pixel size with a TPC outside, and just having a TPC extending all the way to the same innermost radius as the silicon barrel.	82
5.4	Relative momentum resolution and transverse pointing resolution for different pixel sizes in the silicon vertex tracker barrel.	83
5.5	Relative momentum resolution for different pixel sizes in the silicon vertex tracker barrel, for momenta between 0 and 50 GeV/c.	83
5.6	Relative momentum resolution and transverse pointing resolution for different silicon vertex tracker barrel layouts, for transverse momenta between 0 and 50 GeV/c.	84
5.7	Relative momentum resolution and transverse pointing resolution for different silicon vertex tracker barrel layouts, for transverse momenta between 0 and 5 GeV/c.	85
5.8	Relative momentum resolution and transverse pointing resolution for different time-stamping layer thicknesses.	87
5.9	Relative momentum resolution and transverse pointing resolution for different time-stamping layer pixel sizes.	87
5.10	Relative momentum resolution and pointing resolutions for disk pixel size investigations. The results are from a 7 disk setup equidistant between 250 mm and 1210 mm from the centre point, in a magnetic field of 1.5 T.	89

5.11	Relative momentum resolution and pointing resolutions for disk pixel size investigations. The results are from a 7 disk setup equidistant between 250 mm and 1210 mm from the centre point, at $\eta = 3$, in a magnetic field of 3 T.	90
5.12	Relative momentum resolution and pointing resolutions with a 3 T magnetic field, for 5 disks equally spaced between 250.0 mm and 1210.0 mm from centre point.	91
5.13	Relative momentum resolution and pointing resolutions for a 7 disk layout, with varying innermost disk positions.	92
5.14	Sketch of the layout of the detector, including disks. The inner barrel length is adjusted, and the innermost disk moves accordingly. The green dot indicates the centre point.	94
5.15	Relative momentum resolution and pointing resolutions versus momentum for different lengths of the inner barrel layers.	95
5.16	Relative momentum resolution and pointing resolutions versus pseudorapidity for different lengths of the inner barrel layers.	96
5.17	Detector sketch with pseudorapidity edges for different parts marked.	96
5.18	Relative momentum resolution and pointing resolutions versus momentum, for variations of the pixel size and material thickness of the outermost disk.	98
5.19	Relative momentum resolution and pointing resolutions versus momentum, for variations of the pixel size and material thickness of the penultimate disk.	99
5.20	Sketch of the simulated layout with standard disks, where the gas TPC is replaced by two inner and two outer silicon layers (<i>2+2 layers, long</i>).	101
5.21	Sketch of the simulated layout with optimised disks (<i>5 layers, short; optimised disks</i>), where the gas TPC is replaced by five equidistant silicon layers, as well as disks and rings to give pseudorapidity coverage in the forward and backward regions.	102
5.22	Relative momentum resolution and pointing resolutions versus momentum for different gas TPC replacement configurations.	103
5.23	Relative momentum resolution and pointing resolutions versus pseudorapidity for different gas TPC replacement configurations.	104
5.24	Sketch with pseudorapidity edges marked, and relative momentum resolution versus pseudorapidity for the optimised disks layout.	105
5.25	Relative momentum resolution versus momentum and pseudorapidity for different silicon TPC replacement outer radii, in the momentum range 0 to 5 GeV/c and pseudorapidity range $-1 \leq \eta \leq 1$	107
5.26	Relative momentum resolution versus momentum and pseudorapidity for different silicon TPC replacement outer radii, in the momentum range 0 to 30 GeV/c and pseudorapidity range $0 \leq \eta \leq 1$	107
5.27	Relative momentum resolution and transverse pointing resolution versus momentum for different silicon TPC replacement outer radii, with optimised disk layout. Forward regions ($1 \leq \eta \leq 2.5$).	108

5.28	Relative momentum resolution and transverse pointing resolution versus pseudorapidity for different silicon TPC replacement outer radii, with optimised disk layout. Forward regions ($1 \leq \eta \leq 2.5$). . .	109
5.29	Sketch of the gas TPC (blue) superimposed on the 775.0 mm radius silicon replacement layout (green). The dashed lines indicate $ \eta = 1$.	110
5.30	Relative momentum resolution and transverse pointing resolution versus momentum, comparing 5 layer silicon replacement with gas TPC for different maximum outer radii.	110
5.31	Relative momentum resolution and transverse pointing resolution versus pseudorapidity, comparing 5 layer silicon replacement with gas TPC for different maximum outer radii.	111
6.1	The full beampipe geometry in the central region, as of March 2020. A shadow of a full central tracking detector is also shown.	115
6.2	The silicon plus TPC baseline layout. The top figure shows a schematic sketch of the detector parts, and the bottom figure shows the implementation of it in the Fun4All framework.	118
6.3	The all-silicon baseline layout implementation in the Fun4All framework.	121
6.4	Sketch of the all-silicon layout with a 600 mm outer radius. The black lines represent different silicon layers.	121
6.5	Transverse pointing resolution versus transverse momentum, comparing the old baseline layout (green), the new baseline layout with ITS2-based technology (blue), and the new baseline layout with ITS3-based technology (red).	123
6.6	Relative momentum resolution and pointing resolutions versus momentum, comparing the old baseline layout with the new baseline layout and beampipe radius.	124
6.7	Angular resolutions versus momentum, comparing the old baseline layout with the new baseline layout and beampipe radius.	125
6.8	Relative momentum resolution for the TPC baseline, the all-silicon baseline, and the 600 mm outer radius all-silicon layout, for 1.5 T and 3.0 T magnetic fields. The PWG requirement is also shown, as a dashed red line.	128
6.9	Relative transverse momentum resolution for the TPC baseline, the all-silicon baseline, and the 600 mm outer radius all-silicon layout, for 1.5 T and 3.0 T magnetic fields. The PWG requirement is also shown, as a dashed red line.	129
6.10	Transverse pointing resolution for the TPC baseline, the all-silicon baseline, and the 600 mm outer radius all-silicon layout, for 1.5 T and 3.0 T magnetic fields. The PWG requirement is also shown, as a dashed red line.	130
6.11	Reconstructed fraction of particles, versus transverse momentum (y-axis) and pseudorapidity (x-axis), for kaons and pions, using the baseline silicon plus TPC layout.	132

6.12	Reconstructed fraction of particles, versus transverse momentum (y-axis) and pseudorapidity (x-axis), for kaons in a 1.5 T magnetic field using the silicon plus TPC baseline layout.	133
6.13	Sketch of the forward region of the silicon plus TPC baseline layout, with pseudorapidity edges of different detector parts marked.	134
6.14	Reconstructed fraction of particles, versus transverse momentum (y-axis) and pseudorapidity (x-axis), for kaons and pions, using the all-silicon baseline layout.	135
6.15	Fraction of reconstructed particles versus transverse momentum for kaons in the two investigated magnetic fields using the TPC baseline layout, for different pseudorapidity intervals.	136
6.16	Relative momentum resolution and transverse pointing resolution versus pseudorapidity for pions and kaons and two different magnetic fields; 1.5 T and 3.0 T.	138
6.17	Longitudinal pointing resolution versus pseudorapidity for pions and kaons and two different magnetic fields; 1.5 T and 3.0 T.	138
6.18	Pseudorapidity distributions and transverse momentum distributions of D^0 decay products, for the four investigated collision energies. In the top two plots all decay products are shown, and in the bottom two the pion-kaon pairs are shown.	140
6.19	Example event display, showing vertex positions in the x-z plane. A D^0 meson is generated at the primary vertex, and decays after moving hundreds of micrometres in both the x and z directions.	141
6.20	D^0 decay vertex displacement from collision vertex for collisions of 18 GeV electrons and 275 GeV protons.	142
6.21	Distribution of the proton momentum fraction x carried by the gluon in the photon-gluon fusion process for the four investigated energy combinations.	143
6.22	Pseudorapidity of pion-kaon pairs from D^0 decays, and proton momentum fraction x of the collision generating the D^0 , for the investigated four different energy combinations. The colour indicates the number of counts in a bin.	144
6.23	Pion-kaon pair invariant mass spectrum for two different magnetic field strengths, using the TPC baseline detector.	147
6.24	Mass peak width and signal to background ratio of the D^0 meson (in the decay channel $D^0 \rightarrow K^- + \pi^+$), for four different detector concepts and four different collision energies.	148
6.25	Full invariant mass spectrum of $K\pi\pi$ combinations from 500 000 collisions of 5 GeV electrons and 41 GeV protons, using the TPC baseline layout.	149
6.26	Mass peak width and signal to background ratio of the D^+ meson (in the decay channel $D^+ \rightarrow K^- + \pi^+ + \pi^+$), for four different detector concepts and four different collision energies.	150
6.27	Invariant mass difference spectrum, $M(D^{*+}) - M(D^0) = M(K\pi\pi) - M(K\pi)$, for 500 000 collisions of 5 GeV electrons and 41 GeV protons using the TPC baseline layout in a 1.5 T magnetic field.	151

6.28	Mass peak width and signal to background ratio of the invariant mass difference $M(D^{*+}) - M(D^0) = M(K\pi\pi) - M(K\pi)$, for four different detector concepts and four different collision energies. . . .	152
6.29	Mass peak width and signal to background ratio of the D^0 meson (in the decay channel $D^0 \rightarrow K^- + \pi^+$), for two different detector concepts in a 1.5 T magnetic field, with different physics processes activated.	153
6.30	Mass peak width of a D^0 meson, in bins of the proton momentum fraction x carried by the gluon in the photon-gluon fusion process. .	154
6.31	Signal to background ratio for the D^0 reconstructed invariant mass peak, in bins of x	155
6.32	Mass peak width and signal to background ratio of the D^0 meson (in the decay channel $D^0 \rightarrow K^- + \pi^+$) in bins of the D^0 transverse momentum, for events from collisions of 10 GeV electrons and 100 GeV protons.	156
6.33	Mass peak width and signal to background ratio of the D^0 meson (in the decay channel $D^0 \rightarrow K^- + \pi^+$) in bins of the D^0 pseudorapidity, for events from collisions of 10 GeV electrons and 100 GeV protons.	157

List of Tables

3.1	Fragmentation ratios of c quarks to D mesons.	43
4.1	Pixel properties of the investigated mini-matrices of the TowerJazz Investigator.	49
4.2	The mean rise times, and the width of the rise time distributions (defined as the standard deviation of the Gaussian fit), for the standard and modified process in the TowerJazz Investigator 1.	54
4.3	The mean rise times, and the width of the rise time distributions (defined as the standard deviation of the Gaussian fit), for a p-well bias voltage of -6 V and varying substrate bias voltage.	58
4.4	Analysis results for the unirradiated chip, with a bias of -6 V on the substrate and -2 V on the p-well. Results are shown for each sector.	70
4.5	Analysis results for the irradiated chip, with a bias of -6 V on the substrate and -2 V on the p-well. Results are shown for the two available sectors; MALTA-like and n-gap.	70
4.6	Analysis results for the irradiated chip, with a bias of -20 V on the substrate and -2 V on the p-well. Results are shown for all three investigated sectors.	71
4.7	Summary of results from the MALTA-like sector, for both the unirradiated and irradiated chip and different substrate bias voltages. The p-well bias voltage is -2 V for all studies.	71
4.8	Summary of results from the n-gap sector, for both the unirradiated and irradiated chip and different substrate bias voltages. The p-well bias voltage is -2 V for all studies.	72
4.9	Ratios of the figures of merit for different configurations.	72
4.10	Ratios of the figures of merit for the different sectors in the unirradiated chip, at a substrate bias voltage of -6 V and a p-well bias voltage of -2 V.	73
5.1	Pseudorapidity location of the innermost disk inner radius, for different disk positions.	92
6.1	Positions and lengths of detector parts in the barrel region and the disk region, for the silicon plus TPC baseline.	119
6.2	Radial positions of the MPGD layers, each with a length of 1880 mm. The silicon parts of this layout are the same as presented in Table 6.1.	119

LIST OF TABLES

6.3	Positions and lengths of detector parts in the barrel region and the disk region, for the all-silicon baseline.	120
6.4	Physics Working Group requirements on relative momentum resolution and transverse pointing resolution.	127
6.5	Transverse momentum for spiralling at different detector parts of the TPC baseline, for fields of 1.5 T and 3.0 T. All momenta below the presented values will spiral within the radius of the given detector layer.	133
6.6	Transverse momentum regions where over 90% of particles are reconstructed, for different pseudorapidity intervals. The table shows results for positive kaons in the silicon plus TPC baseline layout. . .	137
6.7	Transverse momentum regions where over 90% of particles are reconstructed, for different pseudorapidity intervals. The table shows results for positive pions in the silicon plus TPC baseline layout. . .	137
6.8	Beam energies used in generating Pythia events.	139
6.9	Fraction of all D^0 decay products outside a detector acceptance of $ \eta \leq 3.25$	145
6.10	Fraction of pion-kaon pairs from D^0 decays outside a detector acceptance of $ \eta \leq 3.25$	145
6.11	Fraction of all D^0 primary decay products outside a detector acceptance in transverse momentum.	145
6.12	Fraction of all D^0 to pion-kaon pair decay products outside a detector acceptance in transverse momentum.	145

Chapter 1

Introduction

The electron-ion collider (EIC) is a new experimental facility currently in the development and design stages, to be built at the Brookhaven National Laboratory. The facility was approved to be built by the United States Department of Energy in January 2020 [1], and the goal is to record the first data in 2030. The EIC will enable study of the properties of nucleons and nuclei with unprecedented accuracy, by colliding electrons with protons and ions in a large range of energies and with high luminosity. Advanced detectors are required to extract data from such collisions, and the work carried out as part of this thesis is focused on development of the innermost subsystem for an EIC detector; the silicon vertex tracker.

1.1 History of electron-nucleon scattering

In 1911, Rutherford, Geiger, and Marsden experimented with scattering of α particles on a gold foil, and through the scattering of the α particles deduced the existence of the atomic nucleus [2]. In 1929, Mott extended the scattering theory to relativistic electrons scattering off the Coulomb field of heavy atoms, taking electron spin into account [3]. Rosenbluth further extended the theory in 1950 by introducing form factors, to also account for the finite size and magnetic moment of the proton [4]. The Rosenbluth formula particularly pertains to elastic scattering of electrons on protons, but can be readily generalised to describe inelastic scattering as well. This is discussed in more detail in Section 3.1.

In the 1950s, Hofstadter and colleagues performed the first scattering experiments using electrons on atomic targets, both in foil and gaseous form [5]. This put constraints on the proton radius, and gave indications of the existence of an internal structure of nucleons. Systematic studies of inelastic scattering were performed in a series of experiments at the Stanford Linear Accelerator Center (SLAC) in the 1960s [6], where electrons were fired at a liquid hydrogen target. These experiments showed that the proton has an internal structure, made the first measurements of the proton structure functions, and found evidence for Bjorken scaling and the Callan-Gross relation (see Section 3.1). After these experiments, more fixed-target experiments were constructed. A notable example is the European Muon

Collaboration experiments at CERN which ran from the late 1970s to the 1980s, investigating the collisions of muons with stationary nucleons and nuclei [7,8].

The natural evolution from fixed-target experiments is collider experiments, where both the electrons and the protons/ions are accelerated. The only electron-proton accelerator ever constructed at the time of writing is the “Hoch Energie Ring Anlage” (HERA) at the Deutsches Elektronen-Synchrotron (DESY) research centre in Hamburg, Germany. HERA collided electrons and positrons with protons, mainly with a centre-of-mass energy of 318 GeV [9]. The collider started operating in 1992, and the final collisions were recorded in 2007. HERA originally contained two general-purpose detectors, named H1 and ZEUS [10, 11]. After a few years of operation, the fixed-target experiments HERMES and HERA B were also added, utilising the same particle beams. Throughout its operation the HERA collider provided a large amount of data elucidating processes in quantum chromodynamics, and made it possible to probe the region of small parton momentum fraction x to a level that has still not been surpassed. Experiments at such low x showed a very high density of gluons, and indicate the existence of gluon saturation. HERA experiments have also constrained the possible size of quark substructure to around $7 \cdot 10^{-19}$ m [9].

Complementary to HERA, more fixed-target experiments were built, and are still in use. Those experiments probe the high parton momentum fraction x . i.e. the valence quark region. An example of such an experiment is the Common Muon and Proton Apparatus for Structure and Spectroscopy (COMPASS) experiment at the Super Proton Synchrotron at CERN [12]. COMPASS uses beams of muons or hadrons, colliding with polarised or unpolarised fixed targets. The experiment has been operating since 2002. Another example of a fixed-target experiment, using the Continuous Electron Beam Accelerator Facility (CEBAF) at the Thomas Jefferson National Accelerator Facility, is the CEBAF Large Acceptance Spectrometer (CLAS) [13]. The CLAS experiment operated between 1997 and 2012 using a fixed polarised or unpolarised target and an electron beam energy of up to 6 GeV, achieving high luminosities of up to 10^{34} cm^{-2} s^{-1} (limited by detector acceptance rather than accelerator capabilities). After the upgrade of the CEBAF accelerator to be able to produce 12 GeV electrons [14], the CLAS experiment was upgraded to the CLAS12 experiment [15]. This experiment is currently running, and can handle luminosities of up to 10^{35} cm^{-2} s^{-1} .

1.2 The electron-ion collider

The electron-ion collider is a natural continuation from HERA; it will collide electrons both with protons and with heavier ions. The EIC will also be the world’s first collider with polarised beams for both electrons and light ions, enabling study of spin effects on the collisions [16]. It will operate in a large range of energies with high luminosity, enabling “tuning” of the experiment’s sensitivity to different physical effects while allowing measurements with high statistical significance. The wide range of ions available will also enable studies of nuclear effects.

The EIC will be built at the Brookhaven National Laboratory, utilising the current Relativistic Heavy Ion Collider (RHIC) beamline, with an added electron injector. After RHIC ceases operation, this injector will be added in the same tunnel, while one existing ion ring is rebuilt and improved and the other is turned into an electron storage ring. Figure 1.1 shows a sketch of the EIC accelerator, based on the RHIC beamline. The sketch shows the different rings and the pre-accelerators

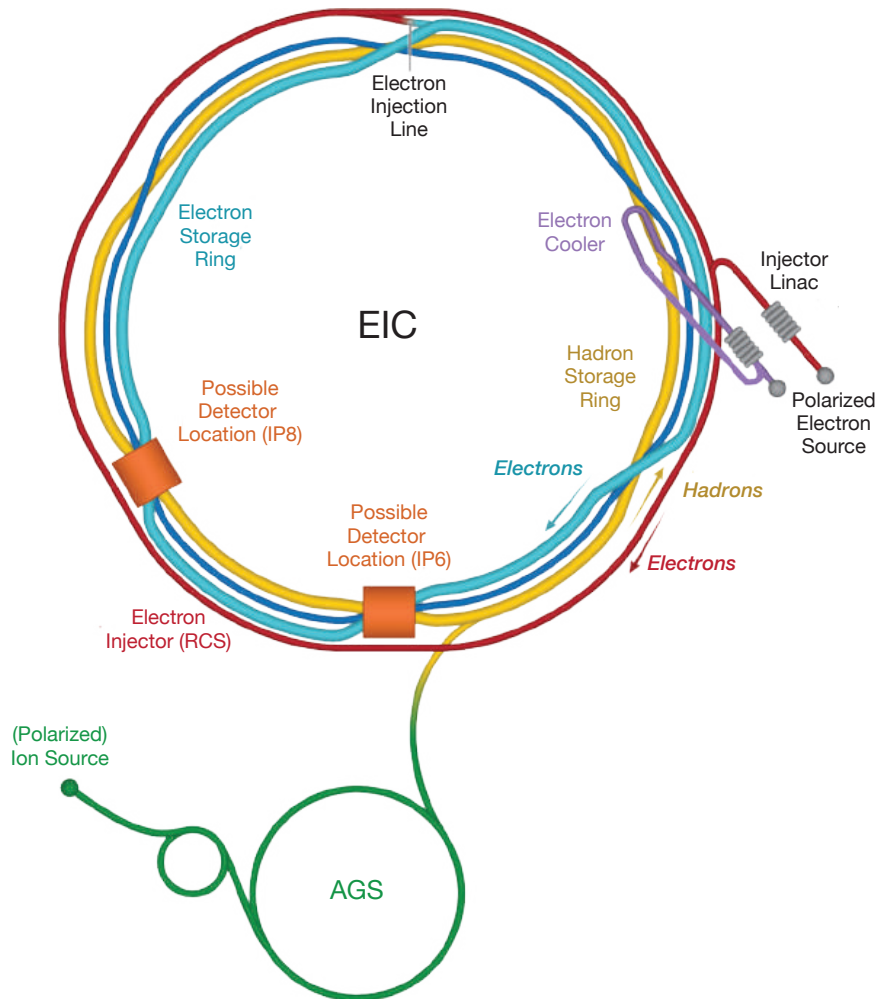


Figure 1.1: Sketch of the electron-ion collider, based on the existing RHIC beamline. “AGS” stands for “alternating gradient synchrotron”, which is used for initial acceleration of the ions. Two collision points are currently envisioned. Figure from [17].

for electrons and ions. The circumference of the main rings is 3.8 km. Two possible detector locations are shown, and it is the ambition of the EIC community to have both populated with detectors. Construction of the EIC is currently envisioned to start at the end of 2023 [18], and research and development and design of detectors has been ongoing since 2011 as part of a generic EIC detector R&D programme [19]. From now through approximately 2025, more targeted research and development work will be carried out to develop EIC detectors [18], and the goal is for data collection to start in 2030.

1.2.1 Physics goals

The main physics goals of the EIC are to increase the understanding of nucleonic properties, such as mass and spin. An overview is given here, while more detail is presented in Section 3.2.

The key science questions are [16]

- How do quarks and gluons generate the emergent nucleon mass and spin?
- What are the spatial and momentum distributions of quarks and gluons inside a nucleon?
- Where does gluon saturation set in, and what happens at the boundary of saturation?
- How do the quark and gluon properties differ in an atomic nucleus compared to a single nucleon?

The EIC will be able to examine physics channels relating to those questions in an unprecedented kinematic range. Figure 1.2 shows how the coverage of the EIC compares to existing polarised collision experiments, in terms of the kinematic variables (parton momentum fraction) x and (four-momentum transfer) Q^2 (see Section 3.1 for definitions) [17]. The yellow region indicates the coverage of the EIC, and the blue and brown areas indicate the region covered by past and cur-

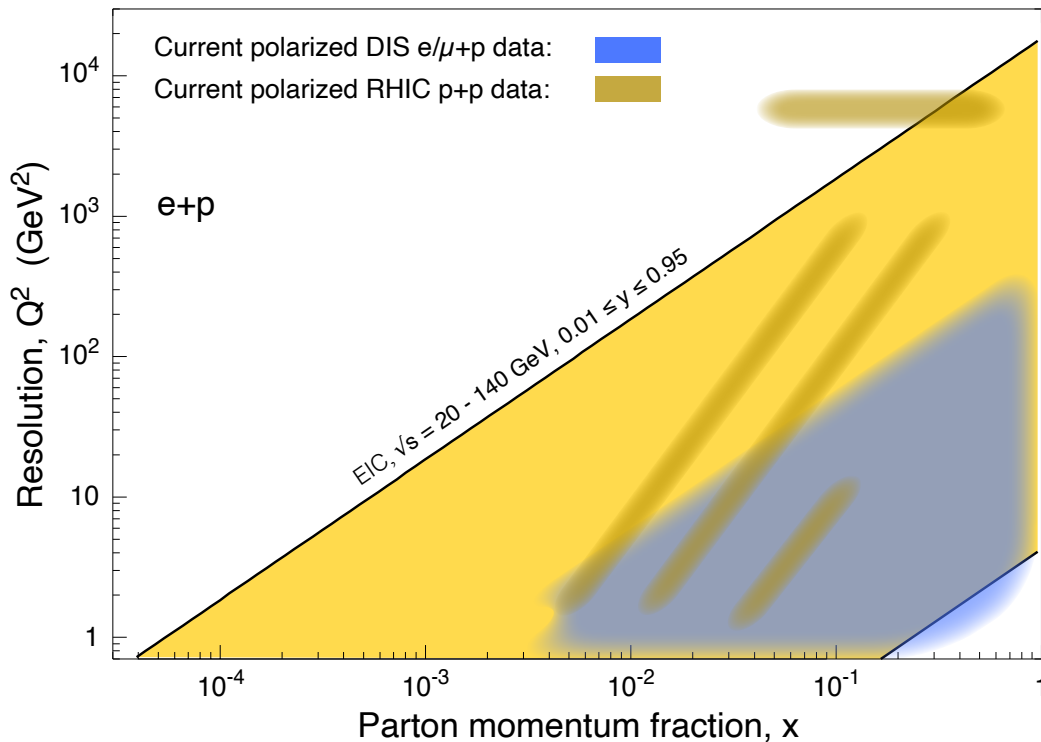


Figure 1.2: EIC coverage range in the kinematic variables x and Q^2 (yellow), compared to past and current experiments with polarised beams (blue and brown). Figure from [17].

rent experiments. The EIC will thus both be able to verify and reduce errors on current results in a large part of the present kinematic range, and add results in a hitherto unobserved part of the phase space. It is important to note that this figure indicates the projected performance of the EIC collider however, and that the actual coverage may be reduced due to an imperfect detector acceptance.

The key physics goals of the EIC are listed above, but the physics programme is currently still evolving. There is for example interest in using the collider to study the partonic structure of photons and mesons [20], and details of the hadronisation and jet formation process.

1.2.2 Collider parameters

In order to elucidate the physics goals of the EIC, the collider needs to have a high luminosity and a large parameter space. The following is an outline of the design requirements of the EIC [17];

- High luminosity; $\mathcal{L} = 10^{33} - 10^{34} \text{ cm}^{-2} \text{ s}^{-1}$.
- Wide range of centre-of-mass energies; 20 to 140 GeV.
- Highly polarised beams; both electrons and protons/light ions up to 70% polarisation.
- Large range of ions; protons to uranium possible.

The high luminosity will enable measurements with high statistics, and investigations of rare events. It is a luminosity 100-1000 times higher than that of the HERA collider. High luminosity also implies a high bunch crossing frequency; in the initial EIC design the bunches will be able to cross every 10 ns, and an interaction will occur on average every 2 μs [17]. The wide range of centre-of-mass energies is needed to give the large kinematic range shown in Figure 1.2, and highly polarised beams enable study of the spin structure of nucleons. The large ion range is desirable to be able to study nuclear effects. The EIC may also include fixed-target experiment possibilities, enabling highly polarised beam collisions using both electrons and ions. This is already done at other collider experiments such as STAR at RHIC [21], and ALICE and LHCb at the Large Hadron Collider [22].

The goal is for the EIC to have two interaction regions and detectors. The interaction regions will most likely be optimised for different centre-of-mass energies, tuning the luminosity to be highest at a certain energy. Having two detectors allows double-checking of results independently. The detector designs will also be complementary, which will reduce the total error on measurements when combining data from the experiments. This has been done successfully with data from the H1 and ZEUS experiments at the HERA collider [23]. Both initial detectors are currently intended to be general purpose detectors using slightly different detector technologies, with each one covering the full fundamental EIC physics programme.

1.2.3 Detector concepts

Research and development towards an EIC detector has been ongoing for the past ten years, with different detector concepts being investigated. Before the official approval and construction site selection of the EIC in January 2020 there were four main different suggested designs for a detector; the BeAST (Brookhaven eA Solenoidal Tracker) [24], the JLEIC [25], ePHENIX [26], and TOPSiDE (Time-of-flight Optimized PID Silicon Detector for the EIC) [27]. The different concepts are shown schematically in Figure 1.3. These concepts have since been developed

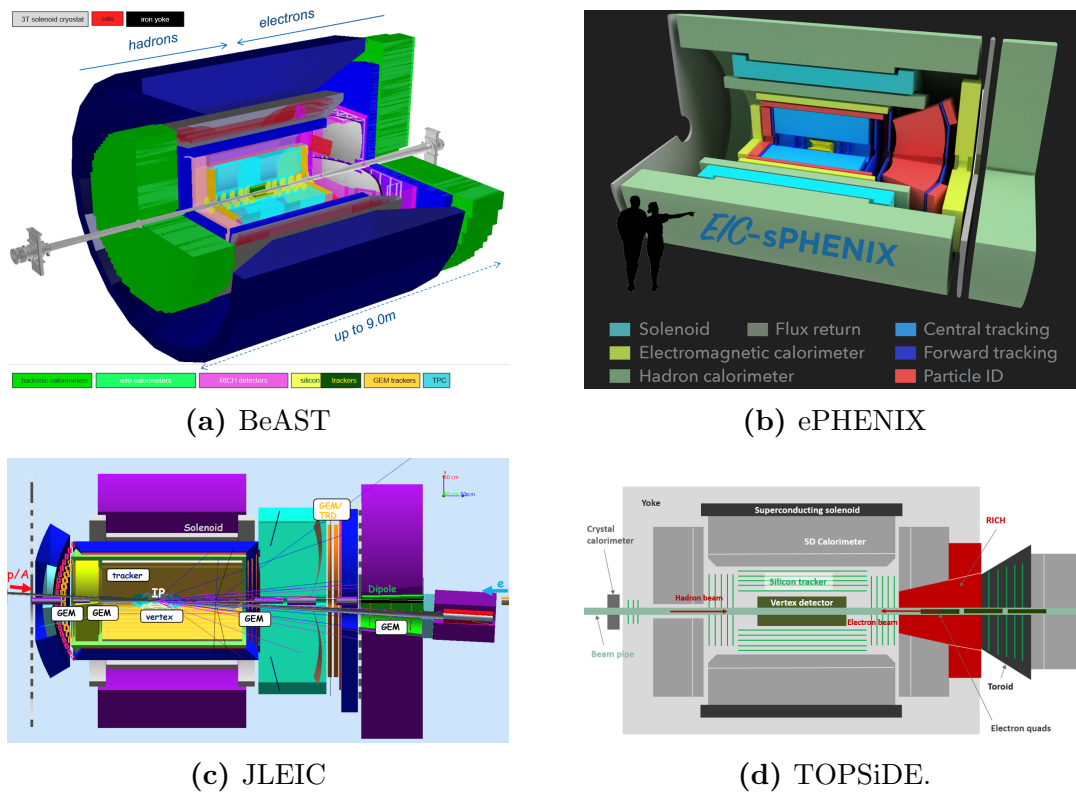


Figure 1.3: The four general detector concepts developed for the EIC, forming the basis for more focused developments started in January 2020 [24].

further into more specific designs, and detector collaborations are currently being formed. The goal is for the EIC to have two complementary general-purpose detectors, where each one can cover the fundamental EIC physics programme. Selection of detector concepts for construction is expected in December 2021.

Broadly, the detector concepts are similar. They all have a cylindrical geometry, with a silicon vertex tracker (SVT) closest to the interaction point. This consists of several cylindrical barrel layers of different radii, and silicon disks in the forward and backward regions (i.e. further along the beam pipe). The SVT is complemented by either a gaseous outer tracker or more silicon detector layers. Outside of the tracking detectors there are dedicated particle identification detectors, followed by calorimeters for measuring the particle energy (by total absorption). All of the concepts also have a solenoidal magnetic field along the beam axis in the

central region, but the field strength is not yet decided on. A high magnetic field simplifies measurements of particle momentum, but it also makes low-momentum particles spiral within the detector, making them more difficult to track.

The purpose of the particle identification detectors is to determine the flavour of particle traversing them. This is used to separate particles from each other (e.g. pions from kaons), which is needed for accurate event reconstruction. Particle identification can be performed by for example using a precise time-of-flight detector measuring the velocity (and hence indirectly the mass when combined with an energy measurement) of the particle, by measuring the energy loss of the particle as it traverses a detector (see Section 2.1.1), or by measuring the Cherenkov light emitted by the particle. For the EIC, Cherenkov detectors are envisioned to be the main means of particle identification, in both the barrel and the forward and backward regions [28]. In the barrel, a “detection of internally reflected Cherenkov light” (DIRC) detector is considered, and in the forward and backward regions ring-imaging Cherenkov (RICH) detectors are considered. These detectors are to be placed immediately adjacent to the inner tracking detectors. If a gaseous time projection chamber (TPC) is present outside of the SVT, it can also aid in particle identification in the barrel region by providing measurements of the energy loss of particles traversing the TPC volume. The performance of particle identification detectors can improve with size. In the initial proton direction the particle identification detector is expected to be larger, as most of the hadrons of an event will go in this direction, making hadron separation more important.

Outside of the particle identification detectors, calorimeters will be placed. Both electromagnetic and hadronic calorimeters are envisioned all around the detector. An electromagnetic calorimeter measures the energy of electrons and photons, and typically consists of homogeneous crystal blocks, with a light-based readout. The hadronic calorimeter measures the energy of hadrons, and also typically consists of energy absorbing materials and crystal blocks or scintillating fibres for readout. An EIC detector will thus have a “shell” structure around the interaction point, with each type of detector subsystem encompassing the ones closer to the interaction point. There will also be further subdetectors in and around the beampipe far from the interaction point, with the purpose of tracking particles scattering with small angles and thus not entering the central detector volume.

The BeAST and ePHENIX concepts have been developed at the Brookhaven National Laboratory (BNL), while JLEIC has been developed at the Thomas Jefferson National Accelerator Facility (TJNAF/JLab). TOPSiDE is an all-silicon detector concept, developed at the Argonne National Laboratory. The silicon vertex tracker, closest to the interaction point, is the focus of the project presented here, making the results presented in this thesis largely independent of the detector concept or concepts finally selected for construction.

During 2020, a “Yellow Report” was produced by the EIC community, outlining the EIC physics programme and the current state of EIC detector studies [17]. Currently the Yellow Report is being used to define a well-integrated EIC reference detector, and the work presented in this thesis is used in forming one of two possible

baseline silicon vertex trackers for such a detector. This silicon vertex tracker was developed using the BeAST SVT as a starting point, which is discussed in more detail in Chapter 5. The BeAST SVT is based on the ALICE ITS upgrade [29] (also known as ITS2), which is a state-of-the-art tracker. The EIC requirements on SVT performance exceed the current state-of-the-art level however, so further developments such as the ones presented in this thesis are necessary.

1.3 Silicon vertex tracker

The work carried out as part of this thesis is focused on development of a silicon vertex tracker that can fit into one or more full EIC detector concepts. The main purpose of the silicon vertex tracker is to find the origin vertex position of tracked particles, while also providing measurements of the particle momentum. The SVT thus needs to have a very high spatial resolution in order to separate primary collision vertices from the secondary decay vertices of short-lived particles formed in the collision. An example of such a particle is the D^0 meson (containing a charm quark), which decays within approximately $120 \mu\text{m}$ from its creation at the collision. Charmed mesons are described in more detail in Section 3.3, and are the main particles of interest in the physics studies carried out in this work.

To achieve the required high spatial resolution, the silicon vertex tracker needs to be placed as close as possible to the interaction point, and be finely segmented. A high power consumption of the silicon sensors increases both the cable thickness and the cooling structures needed for operation, increasing the detector material. A low power consumption is thus needed in order to reduce deviations of the tracked particle trajectory due to multiple scattering in the detector material. These effects are discussed further in Chapter 2. To match the requirements imposed by the EIC physics programme (see Section 3.2) a segmentation of the order of ten micrometres is needed, and the material budget for a detector layer has to be well below one percent of a radiation length (see Section 2.1.2). This is typical for silicon vertex trackers for relatively low energy high-precision experiments such as the EIC. A large detector acceptance is also desired, to enable particle tracking in a large region of the phase space. The detector also needs to be well integrated with surrounding detectors such as particle identification detectors and calorimeters.

As the EIC interaction rate will be up to 500 kHz, the detector readout time must not exceed $2 \mu\text{s}$. A fast readout for the silicon vertex tracker is thus required. Additionally, it can be desirable to time-stamp the bunch crossings, in order to keep track of the polarisation of the registered collision events (as it can change between beam bunches). Knowledge of the current polarisation is important for several of the proposed physics studies, and an accurate separation of bunches with different polarisations will aid in improving the significance of polarisation-dependent measurements. To time-stamp bunch crossings a time resolution below 10 ns is necessary, and one way to achieve such a high resolution can be to use a separate detector layer specifically designed for it. Such a time-stamping layer will need to have fast charge collection and fast readout, which implies that the

readout electronics have to grow larger or use more power. This detector layer may thus need to have a larger segmentation or a higher material budget than the other layers. The effect of adding a time-stamping layer with different parameters than the rest of the silicon vertex tracker is discussed in the simulations presented in Chapter 5. The very high timing resolution is not a necessary feature of a silicon vertex tracker, but can be beneficial to have as long as it does not degrade the momentum and spatial resolutions.

In general, silicon sensors are used to meet the requirements of tracking and vertexing in state-of-the-art collider experiments, and the work presented here shows how it can be done at the EIC. A full silicon vertex tracker concept is developed, consisting of several cylindrical “barrel” layers placed radially around the beampipe and silicon disks in the forward and backward regions, using commercial CMOS imaging technologies to meet the material restrictions and the precision requirements.

1.4 Thesis outline

The work carried out as part of this thesis can be broadly divided up into three parts; silicon sensor studies, general detector simulations, and focused detector simulations including physics event studies, all with the goal of developing a possible silicon vertex tracker for the EIC in terms of both geometry and sensor technology. The silicon sensor studies and the general detector simulations were made at a time when the detailed requirements of the detector were not known. They are thus made with a focus on comparative studies, to find the sensors and detector layouts with the best possible performance with constraints from a draft of the collider design. After site selection in January 2020 more focused simulations could be made, taking the detailed design constraints and detector requirements brought on by the construction site into account. At this time the requirements from the EIC physics programme were also better defined, and the detector performance was compared to these requirements.

In Chapter 2 the theory of segmented tracking detectors and their resolutions is outlined, along with a discussion of silicon sensors. In Chapter 3 electron-proton collision theory is outlined, and the EIC physics channels most relevant to this work are discussed in more detail. Special focus is given to open charm physics. The sensor studies performed as part of this thesis are presented in Chapter 4, describing lab tests and testbeam analysis of different silicon test chips. The general detector simulations made to investigate the performance impact of different detector layouts and silicon sensor parameters using single particle events are presented in Chapter 5. These simulations were carried out before site selection, and the layouts were based on the BeAST tracker layout and the ALICE ITS upgrade. The more focused detector simulations, carried out after site selection, are shown in Chapter 6. These simulations build on from the results of the general simulations. This chapter also presents the work carried out using realistic physics events. Finally, the overall conclusions and possible future work are outlined.

Chapter 2

Tracking detector theory

In this chapter the theory of tracking detectors using segmented sensors is outlined, starting with particle interactions with matter, followed by the theory behind tracking resolutions for a layered detector. A coordinate system used for radially symmetric detectors is also introduced. After this, the most common method of track reconstruction is described. Finally silicon detector operation is described in more detail, with a focus on monolithic active pixel sensors. Following this, Chapter 3 gives an introduction to physics at the EIC.

2.1 Particle interactions

2.1.1 Charged particle interactions

An overview of charged particle interactions with matter is given here, with more details presented in Appendix A.

Charged particles moving through matter lose energy due to electromagnetic interactions with the atoms in the traversed material. The mean energy loss per traversed length is approximated by the Bethe-Bloch formula [30, 31]. As an example the mean energy loss for a positive muon traversing copper is shown in Figure 2.1, as a function of the particle velocity-dependent product $\beta\gamma$. The figure shows the mean energy loss divided by material density, termed “mass stopping power”. The Bethe-Bloch formula is valid in the region marked “Bethe”, between $\beta\gamma \approx 0.05$ and $\beta\gamma \approx 1000$. Below $\beta\gamma \approx 0.05$, the formula breaks down. Radiative effects become more important at high energies for light charged particles such as the muon shown in the figure. The dashed lines in the figure show the energy loss for heavier particles that are not as affected by radiative effects.

For the energy range described by the Bethe-Bloch formula, there is a minimum at around $\beta\gamma = 3$ (but the exact value varies with the atomic number Z of the traversed material). As energy loss increases slowly with increasing particle energy, most particles have mean energy loss rates close to the minimum. Particles with $\beta\gamma \geq 3$ are thus called Minimum Ionising Particles (MIPs), and are often used as an approximation for particle energy loss calculations.

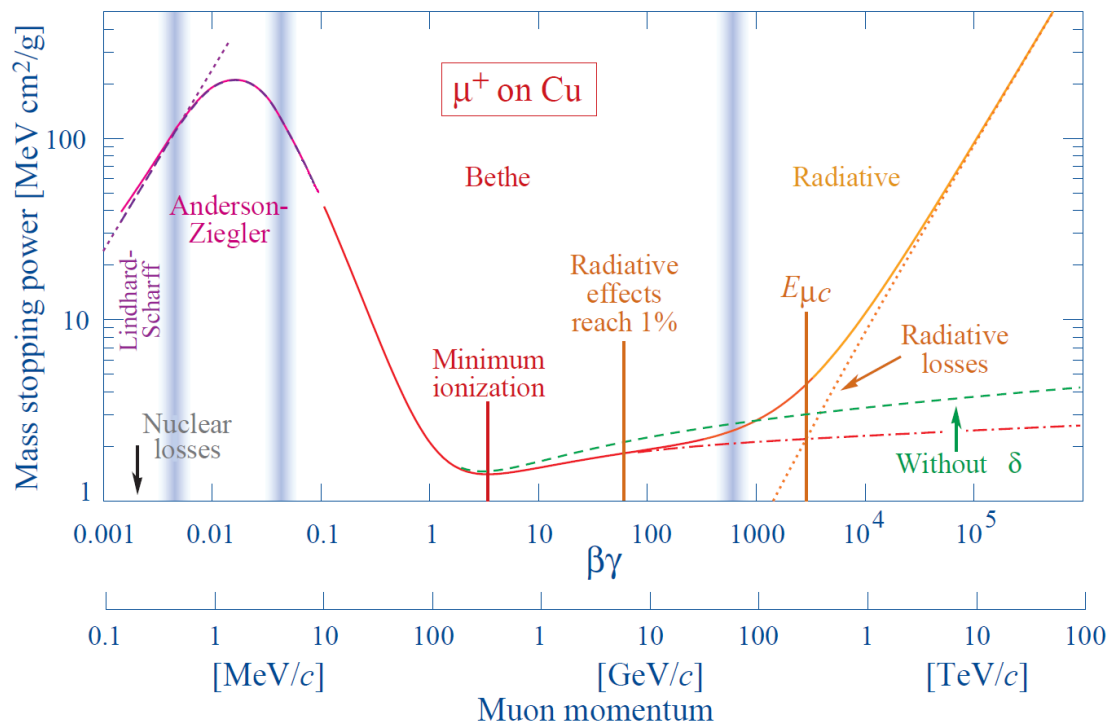


Figure 2.1: Energy loss divided by material density (termed “mass stopping power”) for a positive muon traversing copper, as a function of $\beta\gamma$ [31]. The dashed lines at $\beta\gamma > 3$ represent heavier charged particles, while the filled line for the muon also contains the bremsstrahlung losses that dominate the light charged particle energy loss at high energies. Figure from [32].

The energy loss curve is particle dependent for values of $\beta\gamma$ below the minimum ionising energy. If the energy loss is plotted against the particle momentum, the curve will generally have the same shape, but be shifted slightly for different particle masses. This makes it possible to identify different particles in this energy range by measuring the energy loss.

The fluctuation of energy loss around the mean value for a MIP traversing a thin material is described by a Landau distribution [30,33]. At thicknesses of the order of tens of micrometres, such as for the silicon sensors this work pertains to, the distributions change however [34]. The result is a reduction of the average energy loss as the material grows thinner.

2.1.2 Radiation length

Radiation length is a material property, used to describe how far radiation penetrates into it. It is defined by the energy lost due to bremsstrahlung of an electron (or positron) travelling through the material.

Bremsstrahlung occurs when the incoming charged particle interacts with the Coulomb fields of the atomic nuclei in the traversed material, and loses energy by radiating off a photon. For relativistic electrons, the energy loss per length is

given by [35]

$$\frac{dE}{dx} = -\frac{E(x)}{X_0}, \quad (2.1)$$

where X_0 is a distance known as the radiation length. Integrating this equation, the energy as a function of distance x travelled by the electron is given by

$$E(x) = E_0 \cdot e^{-x/X_0}. \quad (2.2)$$

The initial total energy of the electron is here denoted E_0 . The radiation length X_0 is thus defined as the distance over which the energy of an electron is reduced to a factor of $1/e$ ($\approx 27\%$) of the initial energy due to energy loss from bremsstrahlung.

The radiation length of a material can be calculated from material constants. An approximation is given by [30]

$$X_0 = \frac{1}{\rho} \frac{716.4 \text{ g/cm}^2 \cdot A}{Z(Z+1) \cdot \ln(287/\sqrt{Z})}, \quad (2.3)$$

where ρ is the material density (in g/cm^3), A is the mass number of the material, and Z its atomic number. Using these units, Equation 2.3 gives the radiation length in centimetres.

From Equation 2.3 it can be seen that the radiation length depends on both Z and Z^2 . The Z^2 dependence comes from elastic scattering between the incoming electron and the nucleus, and the Z dependence comes from elastic scattering between the incoming electron and the atomic electrons [30].

Radiation length is a useful tool for characterising the thickness of a detector, and detector material thickness (also called material budget) is commonly expressed in percentages of radiation length. Expressing material thicknesses in terms of the radiation length gives an immediate indication of how much energy is lost for a particle traversing the material, and also an indication of the magnitude of multiple scattering the particle undergoes (see Section 2.1.3).

For mixtures and compounds, the total radiation length can be approximated by summing up the radiation lengths for the individual components of the mixture, weighted by the mass fraction they contribute with [36];

$$\frac{1}{X_0} = \sum_i \frac{w_i}{X_{0,i}}. \quad (2.4)$$

Here w_i is the mass fraction of the compound contributed by element i , $X_{0,i}$ is its radiation length, and X_0 is the total radiation length of the compound.

Radiation length is sometimes given as $\rho \cdot X_0$, where ρ is the material density. The unit used is in those cases commonly g/cm^2 . Silicon at room temperature has a density of approximately 2.33 g/cm^3 , and a radiation length of 21.82 g/cm^2 [36]. Expressed in centimetres, the silicon radiation length is thus 9.36 cm . In terms of radiation length, a $50 \mu\text{m}$ thick silicon wafer thus has a material thickness of approximately 0.05% of X_0 . This is also commonly expressed as $0.05\% X/X_0$ or $0.05\% X_0$.

2.1.3 Multiple scattering

When charged particles traverse a material, they scatter multiple times due mainly to interactions with the Coulomb fields of atomic nuclei in the material. This is known as multiple scattering, or multiple Coulomb scattering. For a finite number of scatters Molière’s theory of multiple scattering describes the full distribution of scattering angles well [37]; for small angles of deflection the distribution is approximately Gaussian, but for larger angles it more resembles Rutherford scattering, with larger tails than a Gaussian distribution. In most cases the Gaussian distribution approximation can be used, since most of the angular deflections of the incident particle caused by the scattering are small. Using this approximation, the distribution of the total scattering angle θ relative to the incidence direction is given by [30]

$$f(\theta) = \frac{1}{\sqrt{2\pi} \cdot \sigma_\theta} \cdot e^{-\theta^2/2\sigma_\theta^2}. \quad (2.5)$$

It is thus a Gaussian distribution centred around 0° (no deflection), with standard deviation σ_θ . The standard deviation of the Gaussian distribution for multiple scattering is given by the “Highland formula” as [38, 39]

$$\sigma_\theta = \frac{13.6 \text{ MeV}/c}{p \cdot \beta} \sqrt{\frac{x}{X_0}} \left(1 + 0.038 \cdot \ln \left(\frac{x}{X_0} \right) \right). \quad (2.6)$$

Here p denotes the momentum of the incident particle, $\beta = v/c$ its velocity (expressed as a fraction of the speed of light), x denotes the distance traversed by the particle through the scattering material, and X_0 denotes the radiation length of the material. Tracking detectors are generally designed to have low material budgets (i.e. small values of x/X_0). For such cases, Equation 2.6 can be approximated as

$$\sigma_\theta \simeq \frac{13.6 \text{ MeV}/c}{p \cdot \beta} \sqrt{\frac{x}{X_0}}. \quad (2.7)$$

From this it can be seen that the distribution of angles gets wider for lower particle momenta and velocities. Hence the particle trajectory is more likely to be more deflected for lower energy particles traversing a detector, reducing the possible accuracy of position measurements. This also shows the importance of keeping the material budget of detectors low, as a thicker detector or a shorter radiation length in it will increase x/X_0 , increasing the probability for a larger multiple scattering angle and thus the uncertainty in measuring track position, degrading tracker resolution.

2.2 Detector properties

2.2.1 Spatial resolution of a segmented detector

The spatial resolution in one direction of a detector segment is mainly determined by the size of the segment in that direction, and the charge sharing between segments. By making the simplifying approximations that charge sharing between

segments is not present, that the readout is binary (i.e. that a particle is either detected or not; there is no signal amplitude information), and that the detector is uniform and fully efficient across the entire segments, the spatial resolution as a function of segment size can be determined analytically.

With these approximations, assuming that the segment reaches between points a and b , an incoming particle will be detected with uniform probability if it hits between the two points, and not at all otherwise. The probability of a detected hit at position x is thus described by a uniform probability function $f(x)$ on the form

$$f(x) = \begin{cases} \frac{1}{b-a} & \text{for } a \leq x \leq b \\ 0 & \text{otherwise.} \end{cases} \quad (2.8)$$

The standard deviation of this will be equal to the error in position of a particle hit in the detector segment. The standard deviation is defined by

$$\sigma = \sqrt{E(X^2) - \mu^2}, \quad (2.9)$$

where $E(X)$ is the expectation value of the stochastic variable X for the probability function, and μ the mean value of the distribution. $E(X)$ is given by

$$E(X) = \int_a^b x f(x) dx = \int_a^b \frac{x}{b-a} dx = \frac{a+b}{2}. \quad (2.10)$$

This is also equal to the mean value μ . For $E(X^2)$ this becomes

$$E(X^2) = \int_a^b \frac{x^2}{b-a} dx = \frac{a^2 + ab + b^2}{3}. \quad (2.11)$$

The standard deviation is thus in total

$$\sigma = \sqrt{\frac{a^2 + ab + b^2}{3} - \left(\frac{a+b}{2}\right)^2} = \sqrt{\frac{(b-a)^2}{12}}. \quad (2.12)$$

The distance between a and b is the segment length. Calling the segment length d , the segment spatial resolution thus becomes

$$\sigma_{\text{seg}} = \frac{d}{\sqrt{12}}. \quad (2.13)$$

Thus, as an estimation, a detector with a segmentation length d in one direction will have a spatial resolution of $d/\sqrt{12}$ in that direction. If charge sharing is present, and readout is not binary, the detector resolution can be improved beyond this level by combining the signals of different segments, weighted by the signal size.

2.2.2 Pointing resolution

The pointing resolution is the accuracy with which the origin vertex position of a particle can be determined by using the hits registered in the detector.

A good approximation of how different parameters affect the pointing resolution can be gathered from studying a two-layer detector. The layers are finely segmented, with errors in spatial measurements of σ_1 and σ_2 . The two layers are located at distances r_1 and r_2 from the point of origin of the particle, where $r_2 > r_1$. A beampipe is considered to be located at a distance r_0 . This is shown schematically in Figure 2.2(a).

Assuming first that the position of the track on the second layer is fixed (so that $\sigma_2 = 0$ and $\sigma_1 \neq 0$), the position resolution of the reconstructed vertex is given by [40]

$$\frac{\sigma_{\text{vtx},1}}{\sigma_1} = \frac{r_2}{r_2 - r_1} \implies \sigma_{\text{vtx},1} = \frac{r_2}{r_2 - r_1} \sigma_1$$

by the law of similar triangles. This situation is shown in Figure 2.2(b). In the same way, assuming the position on the first layer is fixed, the position resolution of the reconstructed vertex is

$$\sigma_{\text{vtx},2} = \frac{r_1}{r_2 - r_1} \sigma_2.$$

This situation is shown in Figure 2.2(c).

The individual resolutions of the first two layers are a combination of the segmented detector spatial resolution defined in Section 2.2.1, and the uncertainty introduced by multiple scattering as the particle traverses them, defined in Section 2.1.3. For the first layer multiple scattering has only occurred in the beampipe at distance r_0 before the detector is hit. This gives a single multiple scattering term. Assuming both layers have the same segmentation, giving rise to an intrinsic error of σ , and adding errors in quadrature, the first layer resolution thus becomes

$$\sigma_1 = \sqrt{\sigma^2 + (r_1 - r_0)^2 \cdot \sigma_{\theta,0}^2}. \quad (2.14)$$

The 0 in $\sigma_{\theta,0}$ here indicates that the multiple scattering comes from the beampipe, and the total positional error comes from multiplying the angular error with the distance. For the second layer, two multiple scattering terms are present; one from the beampipe, and one from the first layer. The resolution thus becomes

$$\sigma_2 = \sqrt{\sigma^2 + (r_2 - r_1)^2 \cdot \sigma_{\theta,1}^2 + (r_2 - r_0)^2 \cdot \sigma_{\theta,0}^2}. \quad (2.15)$$

Since tracking detectors are purpose-built to have a low material budget multiple scattering from the first layer can be assumed to be small compared to the multiple scattering from the beampipe, leading to the approximation

$$\sigma_2 \simeq \sqrt{\sigma^2 + (r_2 - r_0)^2 \cdot \sigma_{\theta,0}^2}. \quad (2.16)$$

The total pointing resolution for the vertex position, σ_{vtx} , is given by combining $\sigma_{\text{vtx},1}$ and $\sigma_{\text{vtx},2}$. Their multiple scattering terms are correlated however, giving

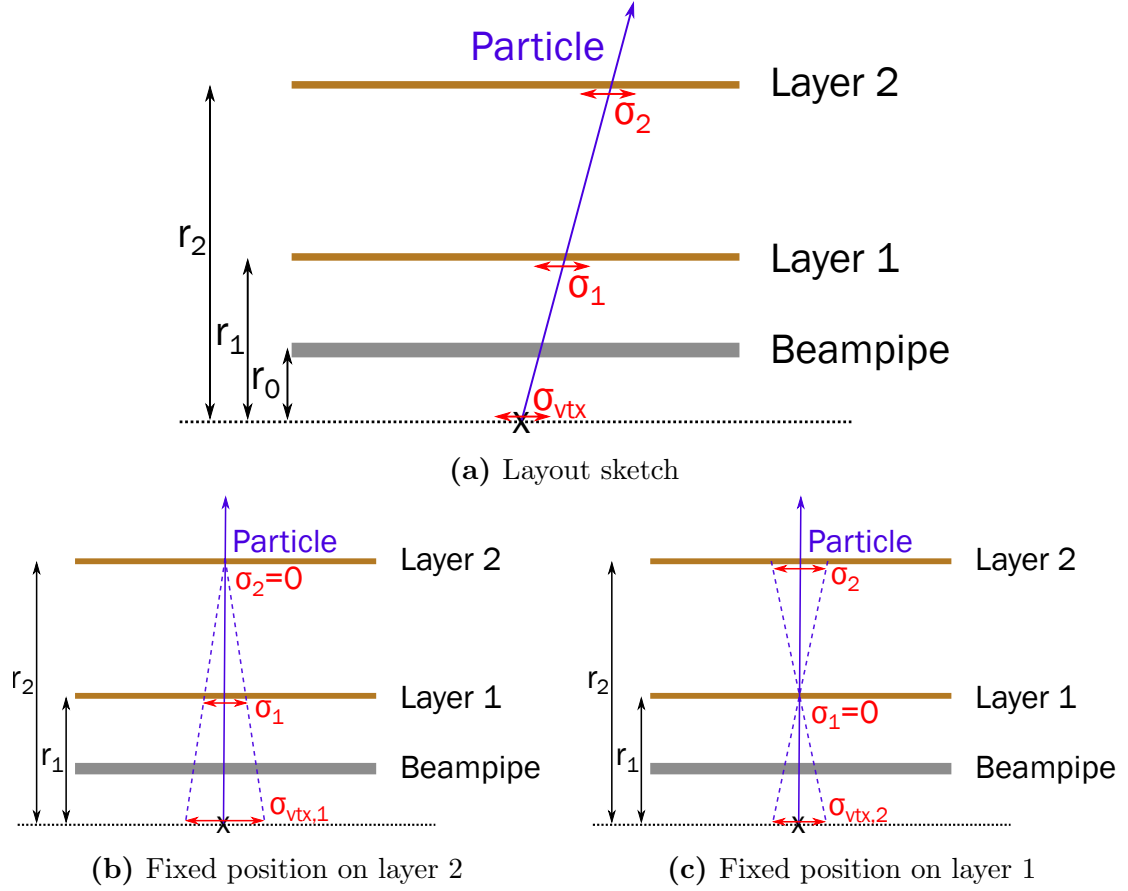


Figure 2.2: Sketches of the simplified two-layer detector used in deriving the equation for pointing resolution. Figure 2.2(a) shows the detector layout, with a particle track drawn. The layers have intrinsic resolutions σ_1 and σ_2 , and the full pointing resolution is labelled σ_{vtx} . Figures 2.2(b) and 2.2(c) show the uncertainties in vertex measurement that arise from errors in position measurements on layers 1 and 2, respectively.

rise to a third term in the expression. With the sum in quadrature, including the correlation term, the pointing resolution is given by

$$\begin{aligned}
 \sigma_{\text{vtx}} &= \sqrt{\sigma_{\text{vtx},1}^2 + \sigma_{\text{vtx},2}^2 + \sigma_{\text{correlation}}} \\
 &= \sqrt{\left(\frac{r_2}{r_2 - r_1}\sigma_1\right)^2 + \left(\frac{r_1}{r_2 - r_1}\sigma_2\right)^2 + \frac{2r_1r_2}{(r_2 - r_1)^2}(r_2 - r_0)\sigma_\theta(r_1 - r_0)\sigma_\theta} \\
 &= \sqrt{\frac{r_2^2 + r_1^2}{(r_2 - r_1)^2}\sigma^2 + \frac{r_2^2(r_1 - r_0)^2 + r_1^2(r_2 - r_0)^2 + 2r_1r_2(r_2 - r_0)(r_1 - r_0)}{(r_2 - r_1)^2}\sigma_\theta^2} \\
 &= \sqrt{\frac{r_2^2 + r_1^2}{(r_2 - r_1)^2}\sigma^2 + \frac{(2r_1r_2 - (r_1 + r_2)r_0)^2}{(r_2 - r_1)^2}\sigma_\theta^2}.
 \end{aligned} \tag{2.17}$$

With the assumption $r_2 \gg r_1$, this can be written

$$\sigma_{\text{vtx}} \simeq \sqrt{\left(\frac{r_1^2}{(r_2 - r_1)^2} + 1\right) \sigma^2 + (2r_1 - r_0)^2 \cdot \sigma_\theta^2}. \quad (2.18)$$

With $\sigma = d/\sqrt{12}$ where d is the segmentation size of the detector (see Section 2.2.1), and the multiple scattering term as $\sigma_\theta \simeq (13.6 \text{ MeV}/c \cdot \sqrt{x/X_0})/(p \cdot \beta)$ (see Section 2.1.3), an approximative formula for the pointing resolution can be written

$$\sigma_{\text{vtx}} \simeq \sqrt{\left(\frac{r_1^2}{(r_2 - r_1)^2} + 1\right) \cdot \frac{d^2}{12} + (2r_1 - r_0)^2 \cdot \frac{(13.6 \text{ MeV}/c)^2 x}{p^2 \cdot \beta^2 X_0}}. \quad (2.19)$$

The last term describes the contribution from multiple scattering, and at low momenta and velocities (small p and β), this is dominant. This term also dominates at high detector material thickness, as can be seen by the proportionality to x/X_0 . The term also includes a part relating to the tracker barrel layout; to minimise the pointing resolution, the innermost layer should be kept as close as possible to the beampipe, to minimise the factor $(2r_1 - r_0)^2$.

The first term dominates at higher momenta, and shows the linear dependence on the segmentation size d . A smaller segmentation size thus improves pointing resolution, as it reduces the vertex position uncertainty σ_{vtx} . The term also shows the importance of keeping r_1 small, i.e. having the innermost layer close to the vertex. There is also an inverse proportionality to the difference between r_2 and r_1 , indicating that a long detector lever arm is desired, with the outermost layer far away from the innermost one.

This derivation is made for a two-layer detector, but the principles hold true for more layers as well. Thin detector layers with small segmentation are desired, and an innermost layer close to the beampipe with an outermost layer far away to give a long lever arm.

2.2.3 Relative momentum resolution

To study the relative momentum resolution of a detector, a study of $N + 1$ equally spaced detector layers can be used to give a good indication of the behaviour and parameters involved [41]. The layers are placed at distances r_0, r_1, \dots, r_N from the interaction point, and will correspond to $N + 1$ equally spaced measurement points of the track. The length (i.e. total lever arm) of the detector is thus given by $L = r_N - r_0$, and the resolution of a detector layer is denoted σ (and given by Section 2.2.1 for a segmented detector). The detector is assumed to be in a solenoidal magnetic field of strength B , directed along the beam direction of the accelerator.

The total relative momentum resolution consists of two parts, summed in quadrature; one stemming from the detector layout, and one from multiple scattering within the detector. In this derivation, the transverse momentum p_T is considered, which is an interesting momentum component as it is orthogonal to the

magnetic field. This thus gives the momentum in the plane where the particles curve. Calling the two parts of the relative momentum resolution “geom” and “MS” respectively, it can be written as

$$\frac{\sigma_{p_T}}{p_T} = \sqrt{\left(\frac{\sigma_{p_T}}{p_T}\right)_{\text{geom}}^2 + \left(\frac{\sigma_{p_T}}{p_T}\right)_{\text{MS}}^2}. \quad (2.20)$$

At low momenta the multiple scattering part dominates, while the geometric part dominates at higher momenta.

The first part, coming from the detector geometry, is given by [42]

$$\left(\frac{\sigma_{p_T}}{p_T}\right)_{\text{geom}} = p_T \cdot \frac{\sigma}{|q| \cdot B \cdot L^2} \cdot \sqrt{\frac{720N^3}{(N-1)(N+1)(N+2)(N+3)}}. \quad (2.21)$$

The charge of the tracked particle is denoted q , and no assumption is made here concerning the units of the different parameters. In literature a factor of 0.3 is frequently present in the denominator, which stems from assuming that q is given in terms of the elementary charge, and p_T in units of GeV/c.

The second part of Equation 2.20 gives a contribution from multiple scattering, which can be written as [42]

$$\left(\frac{\sigma_{p_T}}{p_T}\right)_{\text{MS}} = \frac{1}{|q|B} \frac{13.6 \text{ MeV/c}}{\beta} \sqrt{\frac{C_N}{X_0 L}}, \quad (2.22)$$

where $\beta = v/c$ is the velocity of the tracked particle, q its charge, and C_N a dimensionless coefficient dependent on the number of layers in the detector. It is related to the curvature uncertainty of the track, and ranges from 1.25 (with 3 layers) to 1.43 (with an infinite number of layers) [41]. The coefficient C_N is thus often said to be equal to 1.3 within 10% accuracy [41, 42]. This part of the relative momentum resolution dominates at low momenta.

From the part stemming from the detector geometry, Equation 2.21, it is clear that a large lever arm L is very important for achieving good resolution; the resolution depends quadratically on the lever arm length. A high magnetic field also improves the resolution, as does a fine segmentation and low-noise detectors (decreasing σ). This part is also directly proportional to p_T , indicating that the resolution deteriorates as momentum increases. This is due to the curvature of the track decreasing as momentum increases. There is also a weak dependence on the number of detector layers ($\propto 1/\sqrt{N}$). A large number of measurement points improves the resolution of the track curvature. However, more detector layers commonly increase the material budget, and thus the multiple scattering contribution. More registered hits are also beneficial for the pattern recognition used in track reconstruction, however, so more layers can be useful despite the weak $1/\sqrt{N}$ dependence.

For the multiple scattering part presented in Equation 2.22, there is no momentum dependence, but a dependence on the particle velocity β . This part dominates

at low momenta. Again, a stronger magnetic field can be seen to improve the resolution. There is also a weak dependence on the detector size, with the inverse proportionality to \sqrt{L} .

In total, relative momentum resolution improves with stronger magnetic fields and larger detectors. The formulae presented here are valid for equal spacing between detector planes, but they give a clear indication for the behaviour of a layered detector in the general case.

2.2.4 Detector coordinate system

The detector concepts for the EIC are all centred around a beampipe, and most detectors in collider experiments have a radial symmetry. A cylindrical coordinate system is thus commonly used to describe positions within a detector. The z axis of the cylindrical system is defined as being in the beam direction (and hence also known as the “beam axis”), and the r and ϕ coordinates are used to define points away from this axis. This is shown schematically in Figure 2.3. The origin of the

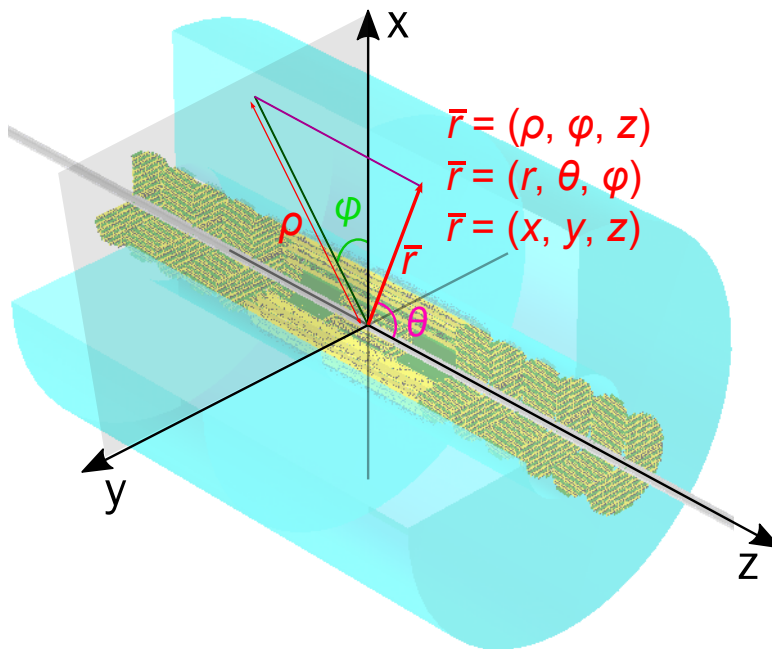


Figure 2.3: Detector coordinate system, overlaid on a simulated detector. The coordinates of the point \vec{r} are given in three different ways. ρ is the radial distance of the point from the z axis, $r = |\vec{r}|$, and the angles θ and ϕ are marked.

coordinate system is normally taken to be the nominal interaction point (IP). For a particle track, the polar angle of the track to the beam is of interest. This is labelled θ , and is also included in the figure. In simulation software a Cartesian coordinate system is often used, with a z axis and origin common to that of a cylindrical system.

In an accelerator where collisions are made between particles travelling along a common axis, the parameters of the outgoing particles are commonly separated

into transverse (i.e. in the x - y / r - ϕ plane) and longitudinal (i.e. in the z direction) components. This is useful for example when a solenoidal magnetic field is present and directed along the beam axis, so that only the transverse momentum p_T will contribute to the track curvature. The transverse momentum is also invariant under Lorentz boosts along the z axis, which makes it a useful quantity to measure as it will be the same in the centre-of-mass frame and the lab frame.

In a collision the centre-of-mass frame will in most cases be Lorentz boosted along the z axis compared to the lab frame, with the result that the measured exiting angles of final-state particles are different from the centre-of-mass exiting angles. To decouple the centre-of-mass measurement of angles between outgoing particles from the Lorentz boost, the variable rapidity is introduced. Rapidity is labelled y , and defined by

$$y = \frac{1}{2} \ln \left(\frac{E + p_z c}{E - p_z c} \right) \quad (2.23)$$

where E is the energy of an outgoing particle, and p_z its longitudinal momentum [43]. This variable is akin to the polar angle θ in that it pertains to the angle of the particle track to the beam axis. Rapidity is useful due to the property that differences in rapidity are invariant under Lorentz boosts, making the angular separation of two particles (expressed in azimuthal angle ϕ and rapidity y) independent of the frame of measurement.

For highly relativistic particles with a small angle to the beam axis, it can be difficult to get accurate measurements of p_z [43]. In this region, it also holds that $p_z c \approx E \cdot \cos(\theta)$. The quantity pseudorapidity, labelled η , is therefore defined as

$$\eta = -\ln \left(\tan \left(\frac{\theta}{2} \right) \right), \quad (2.24)$$

where θ is the angle of the particle relative to the beam axis. For massless particles rapidity and pseudorapidity are equal. In describing angles of particle tracks in collider detectors, the pseudorapidity η is commonly used instead of the polar angle θ , but they contain the exact same information. The pseudorapidity is also used to define detector regions; positive η is commonly called the “forward” region, and negative η is called the “backward” region, while small values of η (generally approximately $-1 \leq \eta \leq 1$) is known as the “central” region. For electron-proton collisions, the positive z direction is frequently taken to be the original proton-going direction.

2.3 Kalman filter track reconstruction

Reconstruction of particle tracks in a detector is commonly performed using a Kalman filter [44, 45]. This method utilises all detector hits to create a smooth particle track that can be used to estimate the particle position at any time since the collision. It can thus also be used to find the particle creation vertex. Mathematically, the Kalman filter is the optimal track reconstructing solution in most cases, as it minimises the mean square estimation error.

The core of Kalman filter track reconstruction is to view the particle position and trajectory as a “state vector” that evolves in time. The Kalman filter algorithm can be used for “filtering” (i.e. estimating the present state vector, based upon all past known measurements), “prediction” (i.e. estimating the state vector at a future time), and “smoothing” (estimating the state vector at a past time, based on all known measurements at the present time). The algorithm can intrinsically handle combinations of different detectors, hit types, and resolutions. It also takes measurement error into account, as well as angular divergences caused by multiple scattering, making it ideal for particle track reconstruction in detectors.

When reconstructing a particle track, all measurement points are known, and in a collider experiment such as the EIC the particle is assumed to originate from inside the beampipe. The track reconstruction is therefore made from the outside, pointing in towards the particle vertex. The reconstruction is made in two steps; filtering followed by smoothing. After the smoothing, the optimal track parameter estimation can be found at any point along the track. A single point can also be easily removed from the estimation once the track is smoothed, making it possible to identify outlier measurements at detector positions, which is useful for determining detector resolution and alignment.

The filtering process is shown schematically in Figure 2.4, for a detector with six layers.

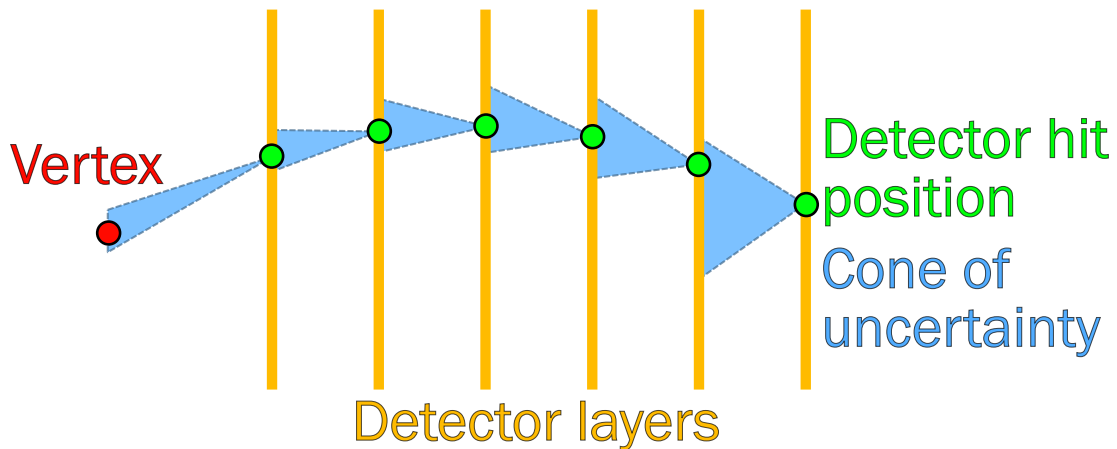


Figure 2.4: Kalman filter algorithm illustration using a multi-layer detector. A particle has been created at the vertex, and traversed the six detector layers to the right, leaving hit positions (marked in green). The Kalman filter algorithm starts with the rightmost hit, and iteratively predicts the position on the previous detector layer. As more physical hits are included in the filter, the projection error decreases (shown in blue). The algorithm thus gives the most accurate result close to the vertex.

The filtering starts at the outermost hit (the rightmost detector plane in the figure), and makes a prediction of where the next hit will be, within a region of uncertainty. As the position at the next detector plane is measured, the prediction for the next layer is refined, and the error matrices of the filter are updated. In this iterative

fashion, the elements of the covariance matrix of the filter shrinks as more hits are included, thus reducing the impact of a single hit position on the total state vector. In the figure, the size of the uncertainty is represented by the width of the “cone” originating at each hit. This cone shrinks the more hits are included in the filter, making the position estimation most accurate close to the vertex.

Once the filtering process is finished, smoothing is performed, utilising all the data points and the information from the filtering. This gives an optimal estimate of the full particle track.

For the work presented here, a Kalman filter implementation in the GENFIT framework is used [46].

2.4 Silicon detectors

2.4.1 Silicon properties

Silicon is a crystalline semiconductor, and its electrical properties can thus be described using band theory [47]. An ionising particle travelling through silicon transfers energy to the silicon (see Section 2.1.1), and the energy can excite electrons in the silicon valence band to the conduction band, creating electron-hole pairs. The silicon band gap is approximately 1.1 eV, but the average energy needed to generate an electron-hole pair is approximately 3.65 eV [36]. Some energy goes into lattice excitations rather than electron excitations, which makes the required energy higher than the band gap energy.

The conduction properties of silicon can be altered by introducing different atoms into its lattice. This is known as “doping”. Introduction of donor atoms which have an extra electron, for example phosphorous, arsenic, or antimony, creates an excess of electrons in the silicon. This is known as “n-doping”. Similarly, introduction of acceptor atoms such as boron, aluminium, and gallium leads to an excess of holes. This is known as “p-doping”.

2.4.2 p-n junction

The basis of a semiconductor detector is frequently a so-called “p-n junction”, which is a p-doped material in contact with an n-doped material. When such a contact is made, the free charge carriers (i.e. electrons for the n-doped material and holes for the p-doped material) move by diffusion to even out the charge distribution. The free electrons move into the p-doped material and combine with holes there, and the holes move to the n-doped material and combine with electrons. The combination of electrons and holes leaves a region depleted of free charge carriers. In this depleted region, the doping atoms that remain thus have no free charges balancing out their excess charge, leaving the p-doped material negatively charged and the n-doped material positively charged. As there is now a difference in charge on opposite sides of the junction, an electric field is present from the n-doped material to the p-doped material. This field pushes diffusing

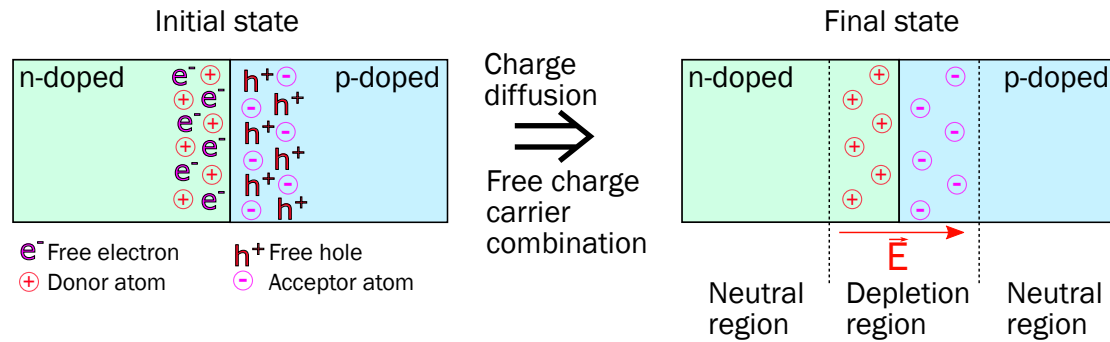


Figure 2.5: Illustration of an unbiased p-n junction. Before the materials are in contact (initial state), both the n-doped and the p-doped materials are electrically neutral. The n-doped material has free electrons, and the p-doped has free holes. Only the carriers closest to the junction are shown here. On contact, the electrons diffuse into the p-doped material, and the holes into the n-doped material, and the free electrons and holes combine. This leaves the charged donor and acceptor atoms, creating a charged region. This charged region gives rise to an electric field that works against further diffusion, until an equilibrium is reached. The right figure shows the equilibrium, where a depletion region (i.e. a region with no free charge carriers) is surrounded by remaining neutral regions.

electrons back in the n-doped material, and holes back into the p-doped material, balancing out the diffusion. Thus an equilibrium is reached, with a depleted region in the junction. This process is illustrated in Figure 2.5. The material outside the depletion region remains electrically neutral as each doping atom is balanced by an electron or a hole. The depleted region remains free of free charge carriers. In the electrically neutral region charges move by diffusion, whereas they move by drift in the electric field in the depleted region.

A reverse biasing (i.e. applying a negative voltage on the p-doped side compared to the n-doped side) can be applied to the p-n junction to increase the electric field strength, and thus the size of the depleted region. This is normally done in semiconductor detectors since charge movement by drift is preferable to charge movement by diffusion.

2.4.3 Basic silicon sensor operation

As an ionising particle travels through silicon, electron-hole pairs are created along its path from the energy lost by the incident particle. A silicon detector works by registering the movement of these created electrons and holes by the current induced on collection electrodes, in accordance with the Shockley-Ramo theorem [48]. For this to be possible, the electrons and holes must be separated to prevent immediate recombination. Charges in silicon move by either diffusion or by drift. Movement by diffusion is due to the charge carrier density gradient, and it is the most prominent method of movement in undepleted volumes. Diffusion is relatively slow, and diffusing charges are therefore more prone to getting trapped and recombining before they are collected. In depleted areas, charges move pri-

marily by drift in the electric field present. This is faster than diffusion, so the collection time of the signal of particles traversing a depleted region is shorter. The charge cloud around the particle track also has less time to spread out, and is thus smaller, which makes smaller pixels viable. Smaller pixels are favourable for the resolution of a full detector (see Section 2.2.1).

As silicon is exposed to ionising radiation, defects in the crystal lattice can appear. Those defects can act as traps for charges moving in the silicon, reducing the size of the collected signal. As charges moving by diffusion are slower than charges moving by drift, they are more prone to getting caught in those traps while traversing the silicon. Depleted detector areas are thus more radiation tolerant and suffer less signal loss from radiation exposure.

It is thus desirable to collect as much charge as possible via drift, as it increases signal collection speed, signal size, and signal uniformity, and reduces charge cloud spread and signal loss from radiation damage of the sensor. This implies that detectors should have as much of the sensitive volume depleted as possible. A silicon sensor is thus generally reverse biased to deplete as large a region as possible. The drift speed generally also increases with the electric field strength, which increases with reverse bias voltage.

A charged ionising particle that traverses a silicon detector leaves electron-hole pairs all along its track. A photon on the other hand will penetrate a certain length into the silicon, and then be fully absorbed. The charge will thus be left in a very localised “ball”, rather than along a track [49]. This is of particular importance for the study presented in Section 4.3.2.

2.4.4 Detector noise

Both signal generation and signal processing in readout electronics gives rise to noise in silicon detectors. The signal generation noise mainly gives rise to fluctuations in signal amplitude, whereas readout electronic noise is a source for “fake hits” in a detector (i.e. the detector registering a hit without a particle interacting with it). The noise from the readout electronics comes from three main sources; thermal noise, shot noise, and flicker noise [36]. Thermal noise stems from the random movement of free charge carriers due to their thermal kinetic energy, and is always present when free charge carriers are present. Shot noise comes from a statistical fluctuation in the number of free charge carriers in the sensitive volume, e.g. via spontaneous electron-hole pair creation in the silicon. Shot noise is directly proportional to the sensor leakage current [36]. The flicker noise mainly arises from the capture and release of charge carriers within the readout electronics. So-called “trapping centres” can appear at silicon oxide boundaries, where charge carriers frequently get trapped and released, which leads to an increase in flicker noise [50]. The so-called “random telegraph signal” (RTS) or “popcorn” noise is a kind of flicker noise that frequently appears in silicon pixel sensor electronics. All of these electronic noise effects appear in the readout electronics of silicon pixels, and can thus cause fake hits. Shot noise is less prevalent than thermal noise and flicker noise however, and both thermal noise and flicker noise increase with

increased detector capacitance [36].

Silicon detectors commonly consist of a large number of small pixels, which means that careful design of the pixel readout electronics is needed to minimise the amount of noise in a full detector. The silicon vertex tracker at the EIC will contain approximately 10^{10} pixels in total, so it is important to keep the fake hit rate low to be able to accurately identify hits coming from particles, and reconstruct particle tracks. A large fraction of fake hits in the detector will make track identification difficult and reduce the efficiency of the track reconstruction algorithms. At the EIC, the fake hit rate for a silicon sensor must be below 10^{-5} hits per pixel and event to be at a level where track reconstruction is still possible [51]. The total detector noise is frequently reduced by setting different thresholds of detection for different pixels, and masking very noisy pixels (and thereby removing them from the active detector). Different pixels always have slight variations due to inhomogeneities in sensor production which makes their noise characteristics differ slightly, requiring different thresholds.

2.4.5 Monolithic Active Pixel Sensors

In the work presented here, monolithic active pixel sensors (MAPS) are the sensor type under investigation. In MAPS, the readout electronics and the detector volume are in the same silicon wafer, which reduces the complexity of connections compared to hybrid sensors. The difference between MAPS and hybrid sensors is illustrated in Figure 2.6; a hybrid sensor consists of two chips bonded together,

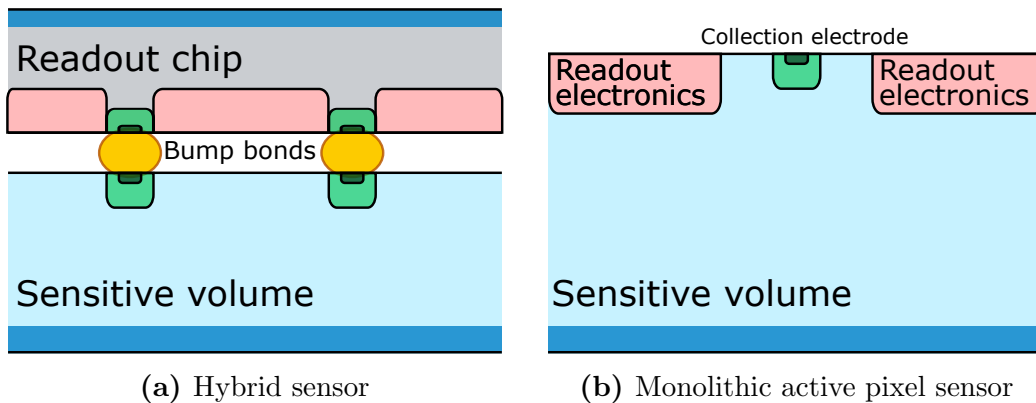


Figure 2.6: Sketch of a bump-bonded hybrid sensor and a monolithic active pixel sensor. In the hybrid sensor, the sensitive volume is on a separate silicon wafer to the readout electronics. In the monolithic active pixel sensor, the readout electronics are embedded in the same wafer as the sensitive volume.

separating sensitive volume and readout electronics. Up until now this is the most common type of sensor used in silicon vertex trackers. MAPS sensors have the benefits of being cheap and relatively easy to mass produce with commercial CMOS (complementary metal–oxide–semiconductor) technologies, as well as having lower material budget than hybrid sensors.

2.4.5.1 MAPS sensor evolution

The first use of MAPS sensors in a collider experiment is for the heavy flavour tracker (HFT) in the STAR experiment at RHIC [52, 53], installed for the 2014 heavy ion runs. This sensor, known as ULTIMATE or MIMOSA-28, collects charge only by diffusion. The ALICE experiment at CERN uses MAPS for its silicon vertex tracker as of the latest shutdown and upgrade [29, 54]. This sensor, known as ALPIDE, is partially depleted and thus collects charge by both diffusion and by drift. It is discussed in more detail in Section 2.4.5.2.

In particular, depleted monolithic active pixel sensors (DMAPS) are under investigation in the work presented here. “Depleted” in this case means that the depletion region is intended to be as large as possible. DMAPS is a relatively new detector concept, utilising the technology of high voltage and high resistivity CMOS (HV/HR-CMOS). High voltage CMOS implies that the in-pixel CMOS electronics are shielded, and a higher voltage can thus be applied over the sensitive volume, which increases the size of the depleted region [36]. High resistivity CMOS implies that the silicon making up the sensitive volume has a high resistivity, which increases the depletion for a given voltage and thus allows higher depletion at lower voltages than silicon with lower resistivity. Various aspects of both high voltage and high resistivity CMOS are frequently combined in current sensor developments.

In most sensor designs the depleted region grows from the interface between the n-doped collection electrode and the p-doped epitaxial layer. Full depletion can thus be reached by maximising the size of this interface by having a large collection electrode, comparable in size to the pixel size. Commonly, the in-pixel CMOS electronics are located inside the collection electrode in those cases, shielding them from the sensitive volume and allowing a higher voltage to be applied. In a collaboration between CERN and the TowerJazz foundry (a company producing semiconductors), a new method for achieving full depletion with a small collection electrode has been developed [55]. In this method, a deep planar junction is introduced in the sensitive volume, and the depletion grows from this junction. The in-pixel CMOS electronics are in this case located in a deep p-well, separate from the collection electrode in order to keep the electrode small while shielding the electronics from the sensitive volume. Figure 2.7 shows sketches of the large and small collection electrode DMAPS variants.

Having a larger collection electrode increases detector capacitance, which results in a lower signal gain for a given power consumption, meaning the sensor needs more power to generate a clear signal. The higher capacitance also increases noise and charge collection time. A large collection electrode thus leads to a large sensor power consumption, which increases the need for cooling and larger cables to the sensors. The total material thickness of the sensor and services thus increases with increased capacitance, which is detrimental to detector performance due to multiple scattering. A smaller collection electrode gives a smaller sensor capacitance, resulting in lower noise and faster charge collection time for a given power consumption. The in-pixel CMOS electronics needed for amplification can

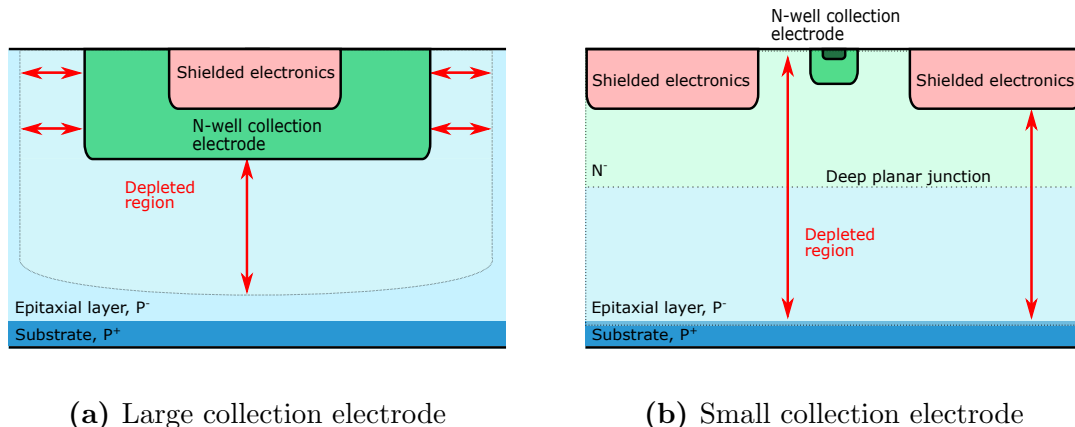


Figure 2.7: Schematic view of different ways to reach full depletion of a MAPS sensor, with large or small collection electrode. Cross sections of single pixels are shown.

also be made smaller due to the increased signal-to-noise ratio brought by the small capacitance, which allows the pixel size to be smaller while maintaining performance.

An example of a DMAPS sensor using a large collection electrode to reach high depletion is the MuPix, to be used in the Mu3e experiment [56]. No experiment currently uses the new small collection electrode DMAPS development, but it has been discussed for use in upgrades to the ATLAS experiment. The development enables the detector capacitance to be kept low while the depletion region is large, both of which are beneficial to the sensor characteristics. It is investigated in the context of the work presented here, and discussed further in Chapter 4.

2.4.5.2 The ALPIDE sensor

The sensor used for the inner tracking system of the ALICE experiment since the last upgrade (ALICE ITS2) is a MAPS sensor called ALPIDE (ALICE Pixel Detector). The ALPIDE sensor is made using the TowerJazz 180 nm CMOS imaging process, with a high resistivity epitaxial layer [57], allowing a larger depletion growth than previous MAPS sensors with a small sensor capacitance. A pixel of this sensor consists of a small n-doped collection electrode in a p-doped epitaxial layer, which is deposited on a p-doped substrate. The collection electrode is surrounded by a p-doped region called a “p-well”, which holds the full CMOS readout electronics. The sensor is reverse biased from the substrate and the p-well to the collection electrode, and the depletion region thus grows both from the collection electrode to the p-well and from the collection electrode to the substrate. An artistic view of a cross section of a group of four pixels is shown in Figure 2.8, indicating the depleted region, as well as a charged particle track and the electron-hole pairs generated along the track. Charge collection in this sensor occurs both by diffusion and by drift; primarily by diffusion in the undepleted region, and primarily by drift in the depleted region.

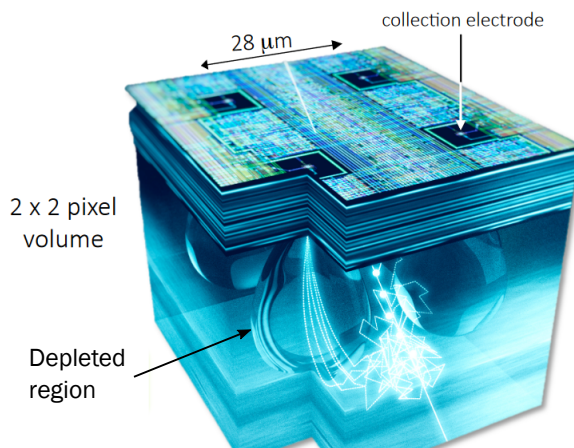


Figure 2.8: Artistic view of the ALPIDE chip, showing a cross section of four adjacent pixels. The depleted region is indicated by “bubbles” in the silicon, and a particle track and electron-hole pairs created along it are shown in white. Figure from [58].

The pixel size of the ALPIDE chip is approximately $27 \times 29 \mu\text{m}^2$ [59], and the chip is the initial baseline for the work described here. Further developments to increase depletion and decrease pixel size have been made, and tests carried out on those developments are shown in Chapter 4. The ALPIDE sensor itself is a current state-of-the-art pixel sensor, but it is not suitable for the EIC since its readout time is too long and a smaller pixel size is desired. A lower material budget for a sensor layer than what is possible with the power consumption of the ALPIDE sensor is also desired for the EIC [60].

2.4.5.3 ALICE ITS3 sensor developments

For the next upgrade of the ALICE Inner Tracking System, dubbed “ITS3”, a new technology is suggested for the three innermost layers of the silicon vertex tracker [61]. This is intended to have some distinct improvements over the ALPIDE sensor. A new feature available in CMOS technology is called “stitching”, which makes it possible to form a chip with a large sensitive area by connecting multiple sensor substructures directly on a silicon wafer [62]. In such a sensitive area, power distribution and data readout can be handled internally, which will help shift material to the edge of the detector. This will also reduce the power density in the sensitive region, reducing the need for cooling. In contrast, several smaller sensors are tiled together to form detector staves in the current ALICE ITS2 silicon vertex tracker, and power and data cabling is distributed all along the staff to the individual sensors. This leads to larger dead area between sensors and more material causing multiple scattering in the sensitive region. The current innermost layers in the ALICE silicon vertex tracker have material budgets of approximately 0.3% X/X_0 per layer. The proposed new design will be thinned to 20-40 μm , and thus have a material budget contribution from the silicon of approximately 0.02-0.04% X/X_0 . Silicon this thin is also flexible, and the sensors can thus be

bent [63]. The new design is intended to consist of large stitched sensors bent around the beampipe, removing most of the support material currently used to form detector staves. Since the power density is lower, it is also envisioned that air cooling will be sufficient, thus removing the cooling structures as well. This leads to an estimated total material budget of the bent sensor layers of 0.05% X/X_0 per layer, i.e. a factor of 6 improvement compared to the current innermost detector layers. The material will also be more uniformly distributed along the sensor, which reduces systematic errors arising from material irregularities.

The sensors for the ITS3 are proposed to be fabricated using the TowerJazz 65 nm CMOS imaging process. This has smaller transistors than the 180 nm process used for the ALPIDE chip, and can thus have a smaller pixel size (envisioned to be $10 \times 10 \mu\text{m}^2$) while retaining performance [64]. The 180 nm process is considered a backup solution however, with a slight increase in complexity and material budget. Sensors in the 65 nm process are estimated to be more expensive to develop, and the process properties for use in particle physics experiments is unknown, so R&D is ongoing to determine whether it is viable. If it is, the smaller pixel size and the lower material budget compared to existing sensors is estimated to greatly improve the performance of the silicon vertex tracker. The improvement of performance from utilising this technology in the context of the EIC silicon vertex tracker is further investigated in Section 6.2, using simulations.

Chapter 3

EIC physics theory

This chapter gives an overview of the physics of electron-proton collisions in general, and specifics concerning the main physics goals of the EIC. The impact of the physics goals on tracking detector performance requirements is also discussed. In particular the physics of charm quarks is discussed, as heavy quark detection imposes strong requirements on vertex resolution performance, and is the main physics channel investigated in this work. A comparison between tracker performance given by simulations and the detector requirements from the physics goals is carried out in Chapter 6, along with studies of the open charm reconstruction performance for different tracker configurations.

3.1 Electron-proton collisions

To probe the internal structure of a proton, electron-proton scattering is a useful tool. The dominant scattering process depends on the energy of the collision; at low, non-relativistic energies, elastic scattering dominates. This gives a probe to the global properties of the proton such as the charge distribution radius, and the proton remains intact after the collision. At higher energies inelastic scattering comes into play, which leaves the proton in an excited state. At even higher energies, deep inelastic scattering (DIS) dominates. In DIS, the interaction is with a quark or gluon inside the proton, and the proton breaks up into a multiparticle final state.

The electron-proton scattering can be described by the Feynman diagram shown in Figure 3.1. The interaction happens through exchange of a virtual photon (γ^*), with four-momentum q . The outgoing hadron X is a proton in the case of elastic scattering, and an excited state or a shower of hadrons in the inelastic and deep inelastic cases, respectively.

Labelling the four-momenta of this interaction with P_e and P'_e for the incoming and outgoing electron, and P_p and P_X for the incoming proton and hadronic final state, the square of the virtual photon four-momentum (q^2) can be written as

$$q^2 = (P_e - P'_e)^2 = P_e^2 + P_e'^2 - 2P_e \cdot P'_e = 2m_e^2 - 2E_e E'_e + 2p_e p'_e \cos(\theta), \quad (3.1)$$

using the initial and final states of the incoming electron. Factors of c are omitted here. The electron mass is given by m_e , and p_e indicates the three-momentum of

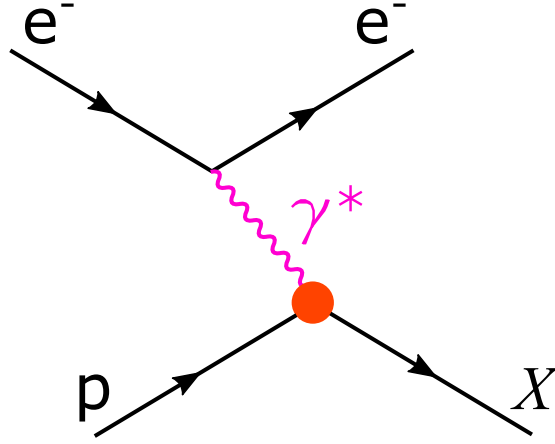


Figure 3.1: Electron-proton scattering. X indicates the hadronic final state, the characteristics of which vary with the collision energy (proton for elastic scattering, excited state of proton for inelastic scattering, and shower of hadrons for deep inelastic scattering).

the electron. The angle θ is the angle between the initial and final three-momenta of the electron (i.e. the electron scattering angle). Energy and three-momentum are related by

$$p = \sqrt{E^2 - m^2},$$

leading to

$$q^2 = 2m_e^2 - 2E_e E'_e + 2\sqrt{(E_e^2 - m_e^2)(E'_e{}^2 - m_e^2)} \cdot \cos(\theta) \approx -2E_e E'_e (1 - \cos(\theta)), \quad (3.2)$$

where the final approximation comes from neglecting the electron mass. This is valid when the energy is sufficiently high; $E_e \gg m_e c^2$. According to Equation 3.2, the virtual photon will always be constrained by $q^2 \leq 0$. The positive Lorentz invariant kinematic variable Q^2 is thus introduced, defined via

$$Q^2 = -q^2. \quad (3.3)$$

The value of Q^2 can be interpreted as relating to the wavelength of the virtual photon via $\lambda \sim hc/|Q|$, and thus to the transverse resolution scale of the collision. A higher value of Q^2 indicates a finer resolution. This can also be understood by utilising the Heisenberg uncertainty principle; the transverse resolution scale Δr will be proportional to the photon momentum, as $\Delta r \sim 1/|Q|$. The value of Q^2 also represents the virtuality of the photon; the smaller the Q^2 is, the closer the photon is to being real.

The differential cross section for elastic scattering of an electron and a proton is given by the Rosenbluth formula as [43]

$$\frac{d\sigma}{d\Omega} = \frac{\alpha^2}{4E_e^2 \sin^4(\theta/2)} \frac{E'_e}{E_e} \left(\frac{G_E^2 + \tau G_M^2}{(1 + \tau)} \cos^2\left(\frac{\theta}{2}\right) + 2\tau G_M^2 \sin^2\left(\frac{\theta}{2}\right) \right). \quad (3.4)$$

The variable τ relates to Q^2 via

$$\tau = \frac{Q^2}{4m_p^2} \quad (3.5)$$

where m_p is the proton mass in GeV/c^2 , and α is the fine-structure constant. The factors G_E and G_M are form factors for the elastic scattering, and functions of Q^2 . These form factors pertain to the charge distribution and magnetic moment of the proton, respectively. Since Q^2 can be measured from the outgoing electron energy and angle (see Equation 3.2), the Q^2 dependence of the form factors can be studied by observing the cross sections at different scattering angles and electron energies. The data from several experiments show that the form factors decrease with increasing Q^2 [65]. This proves that the proton has a finite size, rather than being pointlike, as for a pointlike particle the impact of electromagnetic properties would be independent of the resolution scale given by Q^2 [66].

As Q^2 increases, the elastic cross section decreases, as can be seen from Equation 3.4 when G_E and G_M decrease. This means that the elastic cross section falls off rapidly the smaller the wavelength of the virtual photon is, and elastic scattering becomes more unlikely as the transverse resolution scale decreases. Inelastic scattering interactions thus dominate here, which probe deeper into the proton. In this case, the virtual photon interacts with a parton within the proton.

The invariant mass of the hadronic final state is often labelled W , and given by

$$W^2 = P_X^2 = (P_p + q)^2 = m_p^2 - Q^2 + 2P_p \cdot q, \quad (3.6)$$

where m_p is the proton mass. This can be a useful quantity for characterising the electron-proton collisions.

For deep inelastic collisions, the Lorentz invariant dimensionless quantity x is also frequently used, defined as

$$x = \frac{Q^2}{2P_p \cdot q}. \quad (3.7)$$

As $Q^2 \geq 0$, x has a lower bound of 0. The definition of W can be used to find an upper bound; the baryon number must be conserved in the interaction, so the hadronic final state must contain at least one baryon. As the proton is the lightest baryon, the invariant mass of the final-state hadronic system must be greater than or equal to the proton invariant mass; $W \geq m_p$. Hence the 4-momentum product $2P_p \cdot q$ conforms to $2P_p \cdot q \geq Q^2$ (via Equation 3.6), which puts an upper bound of 1 on x . The values of x are thus in the interval $0 \leq x \leq 1$. When the invariant mass of the hadronic final state is equal to the proton mass (i.e. in an elastic collision where the proton remains intact), $x = 1$. The variable x can thus be seen as the ‘‘elasticity’’ of the electron-proton collision. In deep inelastic scattering in a frame where the proton energy is much higher than the proton mass, the variable x can be identified as the fraction of proton momentum carried by the struck parton [43]. Experimental measurements of x can thus give information about the momentum distribution among the constituent quarks of a proton.

A Lorentz invariant dimensionless variable representing the inelasticity of the collision is also frequently used, defined as

$$y = \frac{P_p \cdot q}{P_p \cdot P_e}. \quad (3.8)$$

In the initial proton rest frame, this reduces to

$$y = 1 - \frac{E'_e}{E_e}, \quad (3.9)$$

i.e. the fractional energy loss of the electron. As the electron will always lose energy in the collision in this frame, y can take values in the interval $0 \leq y \leq 1$. The variable ν is often used instead of y , defined as

$$\nu = \frac{P_p \cdot q}{m_p}. \quad (3.10)$$

In the initial proton rest frame, this reduces to $\nu = E_e - E'_e$, i.e. the energy lost by the electron.

For a fixed centre-of-mass energy \sqrt{s} , the collision kinematics are completely defined by any two of the independent kinematic variables Q^2 , x , and y or ν (not only y and ν however, as they are dependent).

The variable x is related to Q^2 and ν via

$$x = \frac{Q^2}{2m_p\nu}, \quad (3.11)$$

which can immediately be seen by the variable definitions. The centre-of-mass energy of the collision s is given by

$$s = (P_e + P_p)^2 = m_e^2 + m_p^2 + 2P_e \cdot P_p. \quad (3.12)$$

As $m_p^2 \gg m_e^2$, the approximation $2P_e \cdot P_p \simeq s - m_p^2$ is frequently used. Inserting this into the expression for y , it can be seen that y is directly proportional to ν as

$$y = \frac{2m_p}{s - m_p^2}\nu. \quad (3.13)$$

Combining this with the expression for x , it can be found that

$$x = \frac{Q^2}{y(s - m_p^2)}. \quad (3.14)$$

The variable Q^2 is thus related to x and y via $Q^2 = (s - m_p^2)xy$ [43]. Hence knowing two of the kinematic variables (and the centre-of-mass energy), the remaining ones can be found. The values of Q^2 and y can be found from measuring the angle and energy of the scattered electron. Equation 3.2 gives Q^2 , and y can for example be found via [67]

$$y = 1 - \frac{E'_e}{E_e} \cos^2\left(\frac{\theta}{2}\right), \quad (3.15)$$

where the angle θ once again is the electron scattering angle with respect to its original direction. From this, the rest of the variables can be calculated (for a given centre-of-mass energy \sqrt{s}). The variables can also be calculated from the hadronic final state, using the Jacquet-Blondel method [68].

For inelastic scattering, the differential cross section in terms of the two kinematic variables x and Q^2 can be written [43]

$$\frac{d^2\sigma}{dx dQ^2} = \frac{4\pi\alpha^2}{Q^4} \left(\left(1 - y - \frac{m_p^2 y^2}{Q^2} \right) \frac{F_2(x, Q^2)}{x} + y^2 F_1(x, Q^2) \right). \quad (3.16)$$

This is a generalisation of the Rosenbluth formula (Equation 3.4) for inelastic scattering. The two functions $F_1(x, Q^2)$ and $F_2(x, Q^2)$ are called structure functions, and they are dimensionless functions parameterising the interaction of the virtual photon with the proton. They can be seen as a generalisation to the inelastic scattering region of the functions $G_E(Q^2)$ and $G_M(Q^2)$ in Equation 3.4. The structure functions describe the internal configuration of the proton. The function $F_1(x, Q^2)$ can be identified as having purely magnetic origins, whereas $F_2(x, Q^2)$ has both electric and magnetic origins [43].

In 1968 the phenomenon known as ‘‘Bjorken scaling’’ was predicted from theory [69]. Bjorken scaling means that, for a given value of x , the structure functions F_1 and F_2 are approximately independent of the value of Q^2 . This behaviour was first shown experimentally at experiments at the Stanford Linear Accelerator Center in 1969 [70]. The interpretation of this behaviour is that what is observed is scattering from point-like objects within the proton.

The structure functions were also used to predict the spin of the partons; if they were spin-0 particles, the purely magnetic structure function F_1 would be equal to zero. However, if they were spin-1/2 particles, the so-called Callan-Gross relation should hold [71];

$$F_2(x) = 2xF_1(x). \quad (3.17)$$

This implies that the electric and magnetic contributions to the scattering are related by the fixed magnetic moment of a spin-1/2 particle. This was found to be the case in the experiments at SLAC, implying that what is observed is elastic scattering off point-like spin-1/2 constituent particles inside the proton. These partons have been identified as quarks. The structure functions can be decomposed into different contributions from different quarks, such as different quark flavours, or valence and sea quarks. The contribution from charm quarks, $F_2^{c\bar{c}}$, is discussed briefly in Section 3.3.1.1.

Measuring the structure functions via the differential cross sections gives access to the parton distribution functions (PDFs), which represent the probability of a certain parton carrying a certain fraction of the proton momentum. In this way, the PDFs can describe the parton distributions and their interactions. The PDFs cannot be found analytically, but must be found through experiments. If a proton only consisted of three non-interacting quarks, each carrying a third of the proton momentum, the plot of a parton distribution function versus the momentum fraction x would be a delta function at $x = 1/3$ [72]. If the quarks interact however, and there is a ‘‘sea’’ of quark-antiquark pairs, the total PDF becomes a continuum. This is what is observed in experiments; at high x the valence quark contribution dominates, with a peak at approximately $x = 1/3$. At smaller x however, the gluon contribution dominates, together with the sea quark

contribution. Parton distribution functions are determined from global fits using data from a range of experiments, as different experiments and physics channels can focus on the interactions of different partons (charm photoproduction gives access to the gluon contribution for example; see Section 3.3.1). Figure 3.2 shows the current state of the proton PDFs, at two different energy scales [31]. The gluon contribution in the figure is scaled by a factor of 1/10. There is a clear dependence

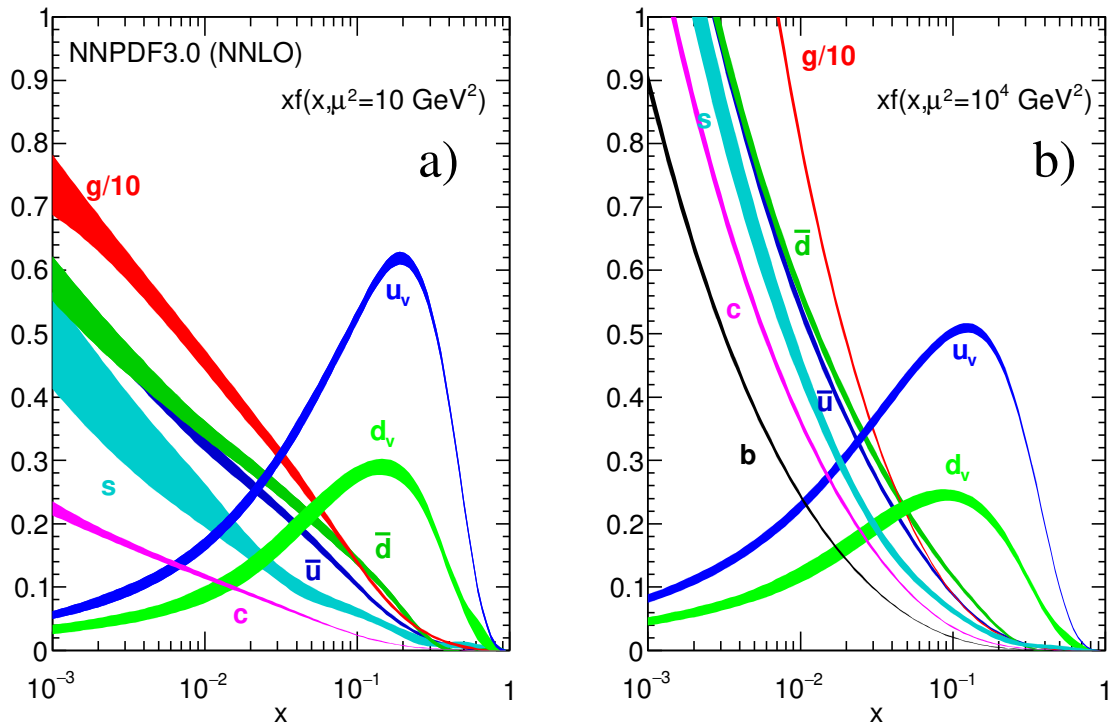


Figure 3.2: Proton parton distribution functions for two different energy scales (10 GeV^2 (a) and $10\,000 \text{ GeV}^2$ (b)). The colours correspond to different partons. It can be seen that the valence quarks (subscripted with “v” in the figure) dominate at higher momentum fractions x , and gluons and sea quarks at lower. The gluon contribution is shown scaled by a factor of 1/10. Figure from [31].

of the distributions on the energy of the resolving particles, but the general trends of the parton distribution dependence on x remains the same.

In experiments, it has been seen that the Bjorken scaling is not exact, especially at very large and very small values of x [43]. This can be seen in Figure 3.3, which shows measurements of the structure function $F_2(x, Q^2)$ from several experiments for different values of x plotted versus Q^2 [31]. If Bjorken scaling were exact, all data points for a given x would be constant in Q^2 . However, at low x values (below approximately $x \approx 0.05$), the proton structure function F_2 increases with increasing Q^2 , and at high x values (above approximately $x \approx 0.25$) it decreases. This behaviour is known as “scaling violations”. The implication of it is that the proton is observed to have more low- x partons at higher values of Q^2 , while the number of medium- x partons remains the same. This is an expected behaviour; at high values of Q^2 , more of the proton substructure can be resolved. The deep inelastic scattering process is thus more sensitive to the effects of quarks irradiating

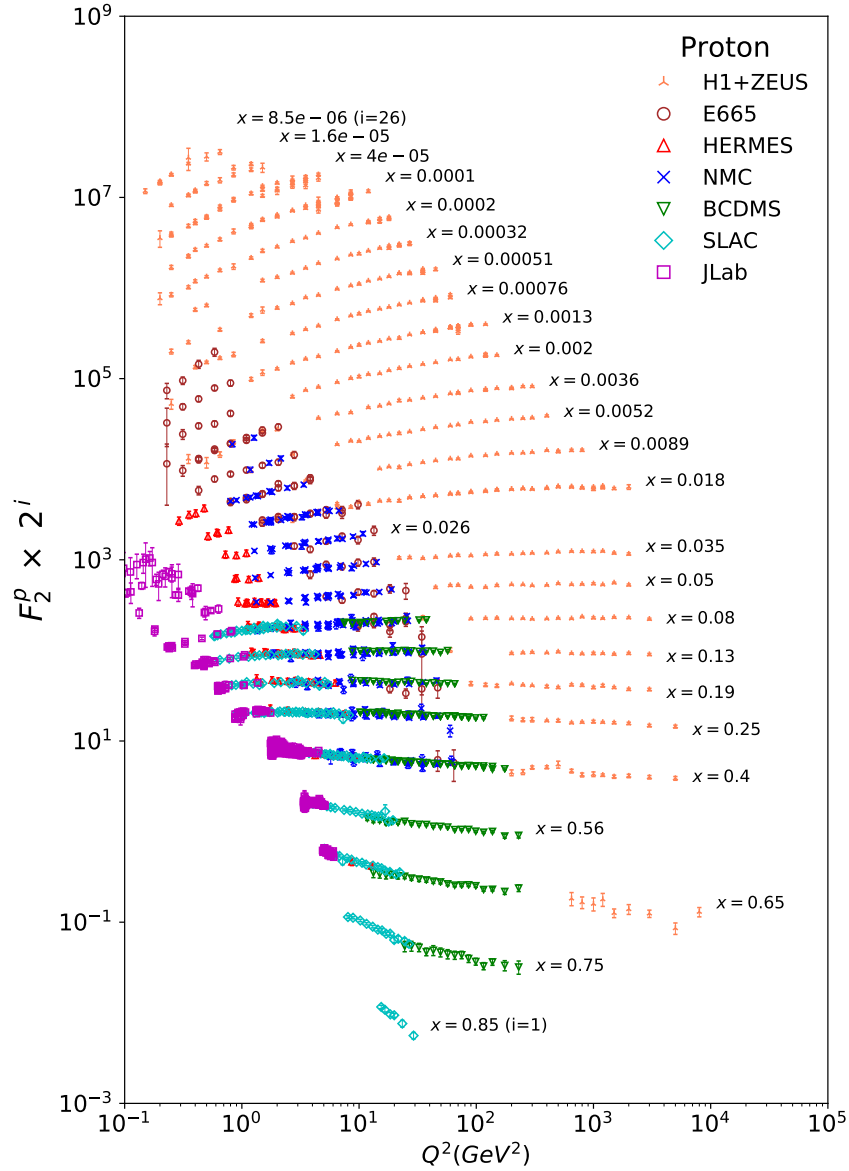


Figure 3.3: The proton structure function F_2 from several experiments, plotted versus Q^2 for different fixed values of x . The values for different x have been scaled by a factor (shown as 2^i in the axis label) in order to show them all without overlapping. Figure from [31].

off gluons over short distances. The gluon carries off some of the initial momentum of the quark before the interaction with the photon, leaving the quark with a lower proton momentum fraction x . The effective observable quark distribution thus shrinks towards smaller x as Q^2 increases. This can also be seen by comparing the left and right plots of Figure 3.2; the low- x parts of the individual PDFs all become more important at higher energy scales. As gluons are more readily emitted at higher Q^2 there are also more observable sea quark-antiquark pairs that can interact with the photon available, and these carry a low momentum fraction x . All in all, this means that fewer high- x partons will be observed as Q^2 increases, and more low- x partons will be observed. The Bjorken scaling violations that have been observed in experiments are thus expected.

3.2 EIC physics goals and tracking detector requirements

In this section, an overview of the main physics goals of the EIC is given, along with the constraints they put on tracking and vertexing performance. Details of the required performance are shown in Section 6.3, along with the estimated performance of different tracking detector designs given by simulation studies.

3.2.1 Nucleon structure

One of the main goals of the EIC is to find accurate descriptions for the internal structure of nucleons; the spatial distributions and motions of quarks and gluons. The EIC has the potential to map out the distributions in three dimensions [16].

The 3D momentum distributions of quarks and gluons can be described by transverse momentum dependent parton distributions (TMDs). Via polarisation of the beams, and a large available range of x and Q^2 , the EIC will be able to map out the TMDs for different quark flavours and gluons over an unprecedented kinematic range. An example of a TMD that will be investigated is the gluon Sivers function [73]. This can be done by studying open charm events, which can be aided by separation of the collision vertex and the charmed meson decay vertex. This sets a constraint on the silicon vertex tracker pointing resolution of approximately $5 \mu\text{m}$ [74]. The TMD investigations also require a good transverse momentum coverage in the detector.

The spatial distributions of partons can be found through the so-called generalised parton distributions (GPDs) [75]. Apart from the spatial distribution, GPDs can also give access to the total angular momentum of quarks and gluons, and thus the QCD energy-momentum tensor, which will help elucidate the origins of nucleon mass. The GPDs also contain information about the internal forces inside nucleons [76]. These features make measurements of GPDs an attractive prospect, and the EIC will be able to perform the measurements over a large range in x , and with high integrated luminosity. For the EIC detector as a whole, the measurement of GPDs is one of the most demanding processes [17]. For the tracking detectors however, it imposes no other constraint than a large detector acceptance (i.e. as large a detector coverage as possible). Most information about GPDs comes from particles at small angles however (such as the scattered proton), and they are thus more likely to be detected by beamline instrumentation.

The sea quark content of the proton can be used to probe its strangeness, but also as a measurement of gluon density. The density of gluons has been seen to increase as x decreases, and the gluons and sea quarks dominate the proton structure at $x < 0.1$ [23]. As the gluon density grows higher, a balance between gluon radiation and recombination is expected to be reached, making the density saturate. The saturation is commonly described by the colour glass condensate formalism [77], which can be seen as a theorised new type of matter. The EIC

will be able to study the gluon saturation regime with higher precision than any previous experiment, leading to both observation of the state (and thus confirmation of its existence) and study of its properties [78]. Saturation is a crucial test for the existing models of QCD, and thus an important property to measure at the EIC. The sea quarks and gluon density at the EIC can be measured using heavy meson production. Charmed jets can be used to probe the strangeness, and this requires excellent pointing resolution for separating the collision vertex from charmed meson decay vertices [79]. This puts a requirement of the silicon vertex tracker pointing resolution to be down to $5 \mu\text{m}$ in the central region, and $20 \mu\text{m}$ in the forward and backward regions (see Section 2.2.4 for region definitions). Jet reconstruction also requires excellent momentum resolution, giving a requirement of a relative momentum resolution down to 0.5% in the central region, and 1-2% in the forward and backward regions.

Production of the ϕ meson has been found to be sensitive to gluon saturation [78]. Tagging of ϕ production involves detection of a low-momentum kaon, which sets a threshold of the lowest detectable transverse momentum for the tracking detectors of 135 MeV/c for kaons. This also implies the need for particle identification to be possible in this low-momentum region.

3.2.2 Nucleon mass

The nucleon mass cannot be explained purely by mass given by the Higgs mechanism; summing up the three valence quark masses for a proton gives a total mass that is approximately 1% of the observed proton mass [31]. Calculations using quantum chromodynamics increases the contribution from quark masses, but it still cannot fully explain the origins of the nucleon mass. The mass thus has to come from interactions and movements of the quarks and gluons inside a nucleon. The contributions to the mass can be separated into contributions from quark and gluon kinetic and potential energies, quark masses, and the so-called “trace anomaly” of the QCD energy-momentum tensor [80]. The different contributions can then be extracted from different experiments.

The measurements of the gluon contribution puts the most stringent demands on the tracking detectors, as the proposed studies for it utilise production and detection of heavy quarkonia such as the J/Ψ meson [81] which interacts with hadrons primarily via gluon exchange. The Υ meson is also considered, for the same reason. Previous experiments have not been able to reach the energies needed for Υ production, but the EIC will be able to. Heavy quarkonium event reconstruction requires excellent momentum resolution to be able to separate different states. This puts a requirement on relative momentum resolution down to 0.5% for the tracking detector. However, decay products from heavy quarkonia most often go in the far-forward region outside of the silicon vertex tracker acceptance, putting the requirements on beamline instrumentation further away from the interaction point. The ϕ meson is a lighter quarkonium particle that also interacts mainly with the gluons in a nucleon. A ϕ meson decay gives a low-momentum kaon, setting a requirement of the minimum detectable transverse momentum of 135 MeV/c for kaons [31].

3.2.3 Nucleon spin

The spin of a nucleon can be decomposed as [82]

$$\frac{1}{2} = \frac{1}{2}\Delta\Sigma + \Delta G + L_q + L_g, \quad (3.18)$$

where $\Delta\Sigma$ is the spin contribution from quarks and antiquarks, ΔG the contribution from gluons, and L_q and L_g the spin contributions from the quark and gluon angular momenta. Before 1987, the leading theory was that the quarks carried almost all of the nucleon spin. However, in 1987 the European Muon Collaboration showed that the quarks carry less than 25% of it [83], a result that became known as the “proton spin crisis”. Recent results from the RHIC spin program [84] have shown that the gluon contribution ΔG is nonzero. To determine spin contributions, the collided particles have to be polarised, and measurements performed over a large range in momentum fraction x . One of the main goals of the EIC is thus to elucidate the origin of nucleon spin by using the highly polarised beams and large kinematic range available [16]. This will help reduce the errors on measurements of both $\Delta\Sigma$ and ΔG , and constrain the orbital angular momentum sum $L_q + L_g$ [17].

The main silicon vertex tracker requirements from study of the nucleon spin comes from the usage of heavy quarks as a probe of ΔG . Such a measurement has been performed at COMPASS, using measurements of the spin asymmetry of D^0 mesons generated in the collision [85]. Tagging of events containing production of heavy flavour mesons benefits greatly from being able to resolve the heavy meson decay vertex from the primary collision vertex, which leads to strict demands in tracker pointing resolution. These demands are summarised to be a resolution down to $5 \mu\text{m}$ in the central pseudorapidity region [74]. Further tagging of D mesons also requires detection of a low-momentum pion, leading to a minimum transverse momentum requirement on the tracking detectors of $100 \text{ MeV}/c$. Reconstruction of D mesons is discussed further in Section 6.6.

3.2.4 Nuclear effects

At the EIC, it will be possible to collide electrons with a wide range of atomic nuclei, ranging from protons to lead. This enables study of the effect a collision with a nucleus has, compared to single nucleons, giving access to information about interactions between nucleons. These interactions are described by nuclear parton distribution functions (nPDFs). From studying the cross section ratio of electron collisions compared to the expected behaviour from a collection of individual nucleons, different behaviour is found for different values of x . At $x < 0.1$, the cross section of ion collisions is smaller, due to a nuclear shadowing effect. Interactions between nucleons in a nucleus here reduce the parton densities [86]. At higher x , in the range $0.1 < x < 0.3$, there is instead an anti-shadowing effect, enhancing the electron-ion cross section. In the range $0.3 < x < 0.7$, the so-called “EMC effect” dominates, lowering the electron-ion cross section again [87]. The exact mechanisms behind shadowing, antishadowing, and the EMC effect are currently

unknown, and one of the big questions in nuclear physics [88]. The EIC has the opportunity to elucidate this better than any previous experiment, due to the large kinematic coverage and high luminosity available. Due to the large range of ions available, and the ability to investigate several ion species at the same energies, the EIC will be able to find the mass number dependence of the nuclear PDFs with unprecedented accuracy.

Electron-ion collisions can also give information about both the quark-gluon plasma and cold QCD matter in atomic nuclei, along with their transport properties. The study of transport properties imposes strict requirements on the silicon vertex tracker, as it is favourably studied using heavy flavour production since heavy quarks form early in the collision and then propagate through the nuclear material and interact with it. The heavy flavour production can also be used as a probe of the nuclear gluon distributions [89]. Heavy flavour reconstruction requires excellent pointing resolution, in order to separate heavy flavour decay vertices from primary collision vertices, for efficient heavy flavour tagging. This gives requirements of pointing resolution down to $5 \mu\text{m}$ in the central region, and down to $20 \mu\text{m}$ in the forward and backward regions. Excellent momentum resolution is also needed for accurate jet reconstruction and studies of jet substructure, giving a minimum relative momentum resolution of 0.5% in the central region, and 1-2% further forwards and backwards. Study of the nuclear effects also puts strict requirements on the minimum detectable momentum. For reconstruction of D^{*+} mesons from charm quark production, a low-momentum pion needs to be detected [31], giving a minimum detectable momentum requirement for pions of 100 MeV/c. Creation and decay of the ϕ meson is also used here, which decays to low-momentum kaons. This gives a requirement of the lowest detectable kaon momentum of 135 MeV/c.

3.3 Open charm physics

In the work presented here, open charm physics is the main interest. The term “open charm” is used for particles that have a non-zero charm flavour quantum number (i.e. most commonly contain only one charm quark). In contrast, “hidden charm” refers to particles containing charm quarks, but equal numbers of charm and anticharm, for example the J/Ψ meson. The open charm mesons are known as D mesons, and contain a charm quark and an up, down, or strange quark.

Study of open charm physics requires excellent detector performance in terms of vertex resolution and particle identification, which makes it a suitable subject of study for the work carried out in this thesis. The performance of the silicon vertex tracker will have a large impact on the D meson invariant mass resolution that can be achieved, and this is studied for different tracker configurations in Section 6.6 using simulations. Open charm events are commonly used as benchmarking physics channels for studying tracker performance [29, 90], and they are thus necessary to have a good handle on as a figure of merit for tracker comparisons.

3.3.1 Charm production

There are two main models for charm quark production in electron-proton scattering; the first is excitation of an intrinsic charm quark within the proton (i.e. from charm existing as part of a charm-anticharm sea quark pair), where the charm quark gets knocked out of the proton by the incoming virtual photon. The second is charm production at the interaction of a gluon in the proton with the incoming photon, in a process known as photon gluon fusion (or boson gluon fusion) [91]. In leading order QCD, the photon-gluon fusion process dominates. The intrinsic charm production mechanism only contributes at high values of x [92].

The photon-gluon fusion cross section is largest at low values of Q^2 , i.e. when the photon virtuality is low. Figure 3.4 shows the leading order Feynman diagram of the charm photoproduction process. A higher order process can also

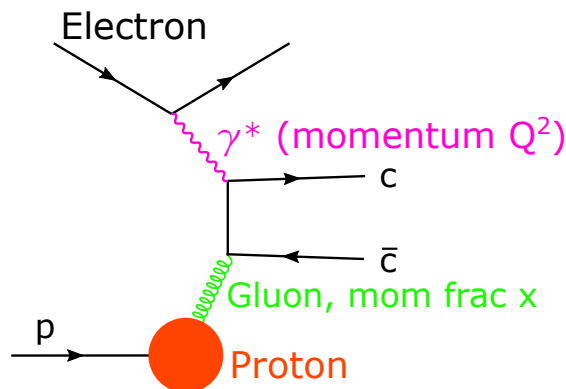


Figure 3.4: Feynman diagram showing the leading order process (with a direct photon) of photon-gluon fusion to $c\bar{c}$.

occur, wherein the photon fluctuates to a quark-antiquark pair which radiates off a gluon, leading to a gluon-gluon fusion interaction with the proton. The photon is labelled “resolved” in this case, and “direct” in the leading order case. As the charm production process depends on the gluons of the proton, the cross section is expected to increase at smaller x where the gluon density is higher. Charm can also be produced via decay of b flavoured hadrons, but the b production cross section is small due to its large mass, so this contribution is negligible.

Results from electron-proton collisions at HERA indicate that photon-gluon fusion is the dominant process for charm production [93]. This process is thus the focus of the physics simulation work presented in Chapter 6.

3.3.1.1 The charm structure function

The charm contribution to the proton structure function is commonly denoted $F_2^{c\bar{c}}$. As charm is produced in an electron-proton collision either by interaction with a charm sea quark or a gluon, measurement of $F_2^{c\bar{c}}$ provides detailed information about the charm production mechanism, and thus constrains the models used for calculating the expected interaction cross sections, including the treatment of the charm mass. The charm structure function can be found by measurement of the

interaction cross sections, which are found by reconstructing the charmed mesons produced after hadronisation of the charm quarks (see Section 3.3.2).

As the dominant charm production process involves interactions with gluons, measurements of the charmed mesons from electron-proton scattering gives a sensitive probe to the gluon distribution of the proton [94]. As such, measurements of $F_2^{c\bar{c}}$ can favourably be used to test different parton distribution function parametrisations, both for gluons and charm sea quarks.

The photon-gluon fusion charm production can also be mistaken for other scattering processes under certain circumstances [95]. This makes the process a background that is important to have a good understanding of, which comes from accurate knowledge of $F_2^{c\bar{c}}$.

From measurements at HERA, it has been found that in the low- x region (over the interval $0.0008 \leq x \leq 0.008$) the charm structure function $F_2^{c\bar{c}}$ makes up up to 23.7% of the proton structure function F_2 [92]. It is thus of great interest to know the charm structure function accurately in order to model the proton structure at low x . Figure 3.5 shows the current experimental knowledge of the charm structure function, for different values of x and Q^2 . The EIC will help elucidate this further, over a large range of x and Q^2 .

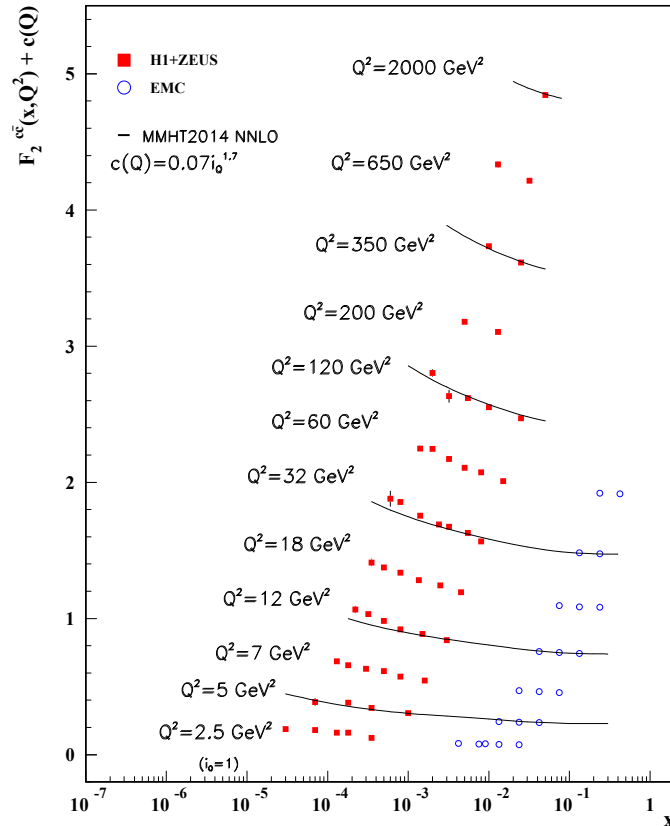


Figure 3.5: The charm structure function $F_2^{c\bar{c}}$ from HERA (combined data from the H1 and ZEUS experiments) and the EMC experiment, plotted versus x for different fixed values of Q^2 . The values for different Q^2 have been modified by a constant $c(Q)$ in order to show them all without overlapping. Figure from [31].

Results from HERA have shown that a high precision vertex resolution can be used to improve the measurements of heavy flavour structure functions [96]. To get the best possible measurements of the charm structure function at the EIC, it is thus desirable to have a high-performing silicon vertex tracker, to better be able to reconstruct charmed particle production events.

3.3.2 Hadronisation

As colour-singlet states cannot exist, the charm quarks themselves cannot be experimentally observed. Through hadronisation, the charm quarks combine with other quarks and form D mesons (in the case of open charm). The other quarks can come either from the proton remnant or from quark-antiquark pairs created from the excess potential energy present as the charm-anticharm pair moves apart [43]. The precise process of hadronisation is not analytically understood, but it can be described using fragmentation functions, which describe the transfer of a quark's energy into a given hadron [72]. One example of a phenomenological description of hadronisation using fragmentation functions is the Lund string model [97], which is used in the particle generator PYTHIA (see Section 6.1.2.2) to generate hadrons from quarks created in collision events.

Fragmentation ratios are used to describe the probability of a quark forming a particular hadron. These ratios can be measured in experiments, and compared to theoretical predictions to form fragmentation models. The fragmentation fractions of open charm particles have been measured at HERA [98] and at electron-positron colliders [99]. A summary of the fragmentation ratios of charm quarks to D mesons (taken from [100]) is shown in Table 3.1. The table also shows the quark composition of each meson. The values in the table are the average fragmentation

D meson	Fragmentation ratio
D^0 ($c\bar{u}$)	$56.43 \pm 1.51\%$
D^+ ($c\bar{d}$)	$22.56 \pm 0.77\%$
D^{*+} ($c\bar{d}$)	$22.87 \pm 0.56\%$
D_s^+ ($c\bar{s}$)	$7.97 \pm 0.45\%$

Table 3.1: Fragmentation ratios of c quarks to D mesons [100].

ratios from all included datasets. Other possible charmed particles (such as the Λ_c baryon) are left out, as the main focus of this work is the D mesons. Direct production of a D^0 is thus the most common hadronisation channel for a charm quark.

3.3.3 Decay

Charmed mesons are heavy particles, and thus unstable. They will all decay within a picosecond of their creation at the collision, meaning they will never reach the sensitive detector volume at the EIC. The charmed mesons can thus only be observed by reconstruction of their decay products. The mean lifetime of

a D^0 meson is $\tau = (4.101 \pm 0.015) \cdot 10^{-13}$ s [31], giving a decay length in the D^0 rest frame of $c\tau \approx 122.9$ μm .

In the work presented here, only three hadronic decays of the D^0 , D^+ , and D^{*+} mesons into final states containing charged pions and kaons are investigated (see Section 6.6). These events have low multiplicity (and thus low combinatorial background), and contain only charged particles which is crucial for detection in the tracking detectors. The decay channels used in this work are $D^0 \rightarrow K^- + \pi^+$, with a branching ratio of $3.95 \pm 0.031\%$, $D^+ \rightarrow K^- + \pi^+ + \pi^+$ with a branching ratio of $9.38 \pm 0.16\%$, and $D^{*+} \rightarrow \pi^+ + D^0$ with a branching ratio of $67.7 \pm 0.5\%$ [31]. The decays are shown as Feynman diagrams in Figure 3.6.

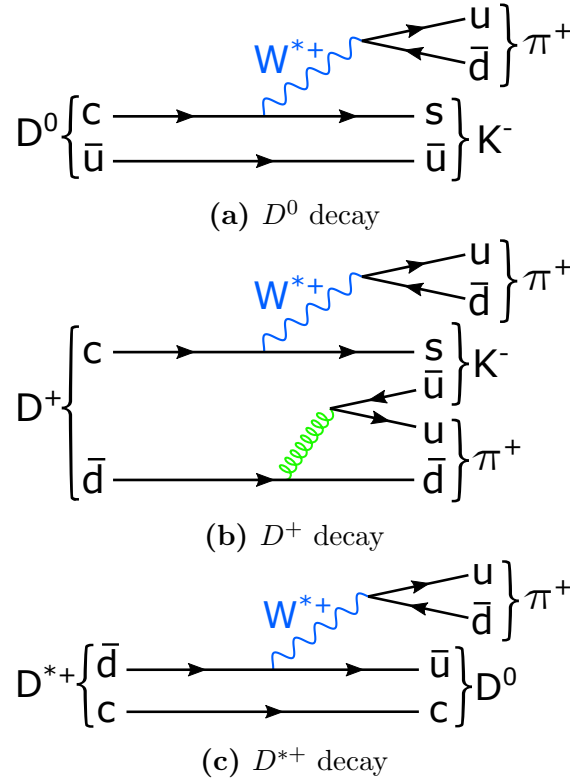


Figure 3.6: Leading order Feynman diagrams for the decay channels for D^0 , D^+ , and D^{*+} mesons investigated in the work presented here.

For the D^+ decay, the gluon can radiate from any of the two quarks. It can also be replaced by a photon, but the gluon exchange is favoured. The D^{*+} has a short mean lifetime of approximately $7.9 \cdot 10^{-21}$ s [31], and will thus decay very close to the original charm creation point. In the observed channel, it also decays to a D^0 , which will then decay according to for example Figure 3.6(a). The total decay chain for a D^{*+} used in this work is thus $D^{*+} \rightarrow \pi^+ + D^0 \rightarrow \pi^+ + K^- + \pi^+$, with a branching ratio of $2.67 \pm 0.03\%$.

Chapter 4

Sensor studies

4.1 Introduction

In this chapter, the experimental work carried out on silicon pixel sensors is discussed. The aim of the work carried out is to compare the performance of fully depleted MAPS sensors (i.e. DMAPS) to partially depleted MAPS sensors with regard to charge collection properties, and to find a suitable technology for development of a DMAPS sensor for the EIC. Two kinds of studies are presented here; studies using a radioactive source on test chips in the cleanrooms of the Birmingham Instrumentation Laboratory for Particle physics and Applications (BILPA), described in Section 4.2, and studies of data from a testbeam carried out at the Diamond Light Source, described in Section 4.3. The studies in this chapter thus pertain to single sensors, rather than a complete silicon vertex tracker. Simulation studies of full tracker geometries, performed taking potential sensor technologies into account, are presented in Chapters 5 and 6.

4.2 TowerJazz Investigator studies

4.2.1 TowerJazz Investigator test chips

The chips tested as part of this study are different versions of the TowerJazz Investigator monolithic prototype test chip. The chips are produced in the TowerJazz 180 nm CMOS imaging process, and were originally developed in a collaboration between CERN and the TowerJazz foundry for tests pertaining to the ALICE Inner Tracker upgrade (“ITS2”) [101]. The tested chips have the same geometries and available pixel flavours, but some differences in the sensitive volume and the biasing scheme. Each chip is divided up into 134 mini-matrices, each containing pixels of different design [102]. Each mini-matrix consists of 8×8 active pixels, surrounded by 2 rows of dummy pixels. The analogue signal from each active pixel can be read out individually.

The pixels are fundamentally of the same design as in the ALPIDE chip (see Section 2.4.5.2) consisting of an octagonal n-doped collection electrode in a p-doped

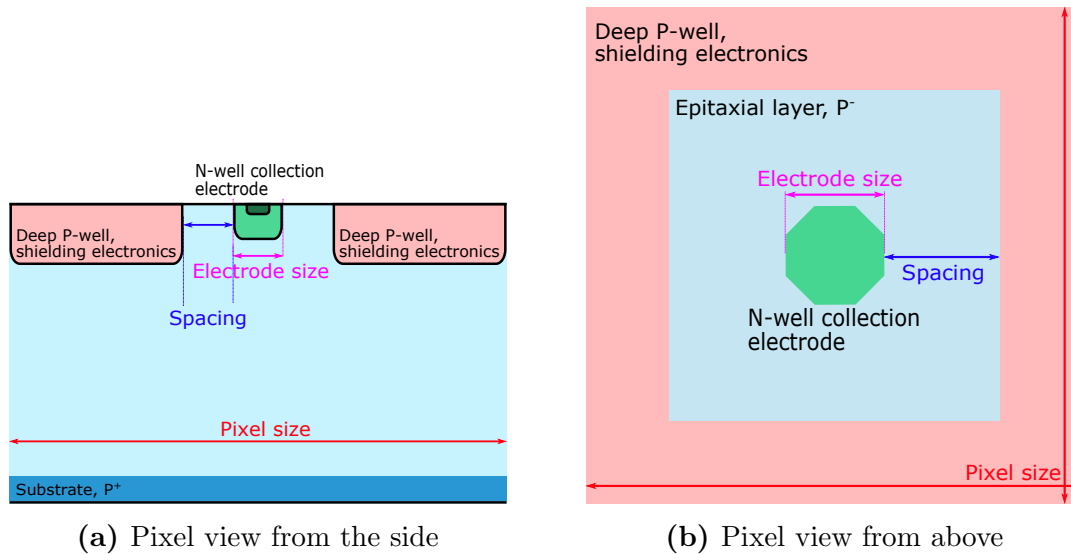


Figure 4.1: Schematic view of a pixel, from the side and from above. Definitions of the pixel dimensions that vary between different mini-matrices in the test chips are shown in both views.

epitaxial layer deposited on a p-doped substrate, with an approximately square deep p-well containing the CMOS readout electronics surrounding the collection electrode. Figure 4.1 shows a sketch of the pixel layout, both from the side and as a top-down view. The pixels of different mini-matrices differ in pixel size, collection electrode size, and spacing between the deep p-well and the collection electrode. These parameters are marked in the figures. All tested chips have an epitaxial layer thickness of $25\ \mu\text{m}$.

Three different versions of the TowerJazz Investigator are tested in the work presented here; the TowerJazz Investigator 1 in the so-called “standard process” and in the “modified process”, and the TowerJazz Investigator 1B. The standard process is used in the ALPIDE chip (see Section 2.4.5.2), while the modified process is a more recent development in an effort to reach full depletion of the sensitive volume with a small collection electrode [55]. Figure 4.2 shows a schematic view of the two processes side by side, for comparison. The depleted region in the standard process grows from the collection electrode, extending out as the bias voltage (between the substrate and p-well, and collection electrode) is increased. The region below the p-well will thus largely remain undepleted. The modified process has been developed to amend this, by introducing a deep planar n-p junction in the epitaxial layer. The depleted region grows from this junction in the modified process, which theoretically depletes the full sensitive volume when a reverse bias is applied. Introduction of the deep planar junction requires no changes to other parts of the pixel, which makes it possible to directly compare the performance of the standard and modified processes for different mini-matrices in the TowerJazz Investigator 1 chips.

The TowerJazz Investigator 1B is produced using the modified process, and has the same pixel mini-matrices available as the TowerJazz Investigator 1. The main

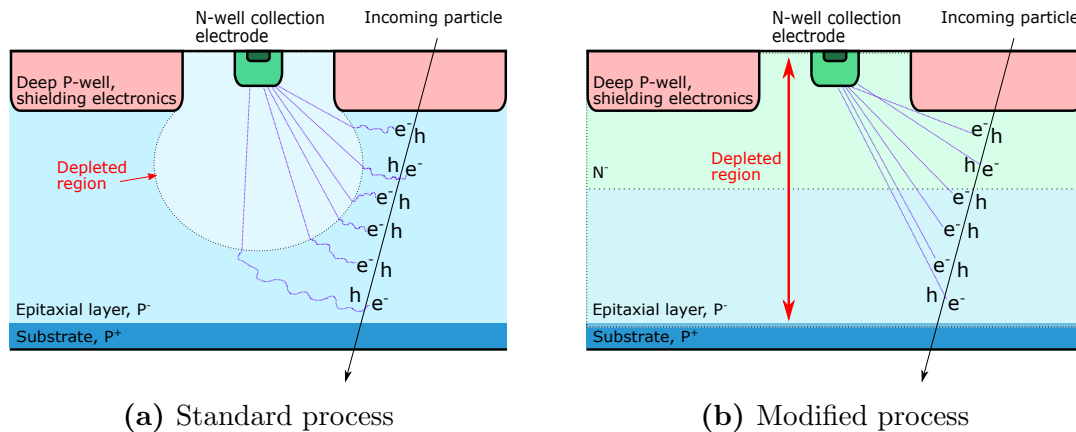


Figure 4.2: Schematic view of a pixel of the TowerJazz Investigator in the standard process (a) and modified process (b). Doping types, depleted regions, and an example particle track are shown. Figure adapted from [55].

feature of the TowerJazz Investigator 1B is that it makes it possible to bias the p-well and the substrate separately, which enables study of how different biasing settings change the charge collection properties for different pixels. The chip is mounted on a different carrier board than the TowerJazz Investigator 1 chips, and thus requires a different experimental setup. Direct comparisons between the TowerJazz Investigator 1 chips and the 1B chip will not be viable due to the large difference in experimental setup, but different biasing settings of the 1B can be compared to each other.

4.2.2 Comparing the standard and modified processes

Comparisons are made of the charge collection properties of the TowerJazz Investigator 1 chips in the standard process and the modified process. The figures of merit used pertain to the charge collection; the signal amplitude and the signal rise time (i.e. charge collection time) are extracted.

4.2.2.1 Experimental setup

The chip under investigation is wirebonded to a carrier board, which has connections for providing voltages to the chip and reading it out. The carrier board is connected to a passive readout board, where the signal from a pixel in the currently selected mini-matrix can be extracted. The passive readout board is in turn connected to two control boards developed by SiLab in Bonn [103]; a General Purpose Analog Card (GPAC), and a Multi-Input-Output (MIO) board, containing a field-programmable gate array (FPGA) used for chip configuration. The experimental setup is shown schematically in Figure 4.3. All control signals and all but one of the chip biases are provided by the MIO and GPAC, controlled by a computer connected to the MIO. A computer program can thus be used to power the setup on and off, and select the active mini-matrix (and thus the investigated pixel flavour). The MIO board also provides a periodic reset pulse to the investigated chip, which is needed since the readout of the TowerJazz Investigator is

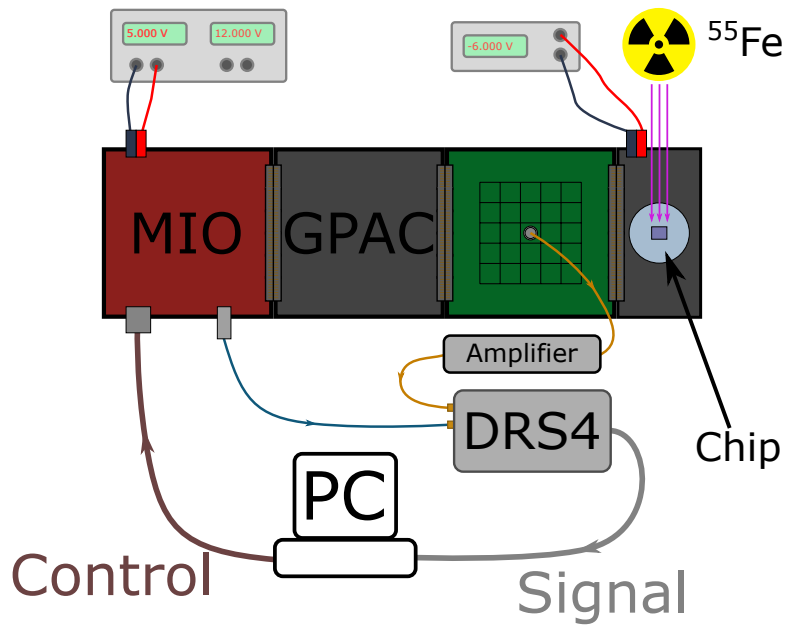


Figure 4.3: Schematic view of the TowerJazz Investigator 1 experimental setup. The carrier board on the right can be exchanged without altering the rest of the setup, enabling direct comparisons between different chips.

integrating. In order to reduce the risk of damage to the pixel electronics, the reverse biasing of the sensitive area is provided separately [104], directly from a power supply to the carrier board. For the TowerJazz Investigator 1 this biasing can have values between 0 V and -6 V , and biases the substrate and the p-well relative to the collection electrode. It thus affects the size of the depleted region in the pixels. For the results presented here, the bias voltage is always set to -6 V .

The analogue output of a pixel is connected from the passive readout board to an amplifier, and then to a fast USB oscilloscope called a DRS4 Evaluation Board [105]. The amplifier is an inverting CIVIDEC C1 2 GHz 20 dB broadband amplifier [106], modified by CIVIDEC to have a decay time of approximately $20\ \mu\text{s}$. As the signal from a pixel is integrating, the registered signal is expected to continuously rise due to the leakage current. The decay time of the amplifier changes this however, making the signal after amplification constant before a hit in the detector, and exponentially decay back to the constant value after a hit.

Two inputs on the DRS4 oscilloscope are used; one is used for the amplified output signal of a pixel, and another for the reset signal (output from the MIO board). The DRS4 is connected to a computer which runs specific DRS4 readout software. As the chip responds to the reset pulse (sent every $25\ \mu\text{s}$), a trigger is set up in the readout software to avoid fake hits coming from this reset response. The DRS4 oscilloscope provides a high time resolution, due to its capability of sampling up to $5 \cdot 10^9$ times per second. The trigger level is also set high enough that the majority of the intrinsic noise of the chip is rejected, so that only sensor hits coming from a radioactive source are registered.

To study the chips, an ^{55}Fe source is used. The source is placed as close as possible on top of the chip, and a single pixel is read out. The isotope ^{55}Fe decays via electron capture, and through that emits x-rays or Auger electrons. The electrons are stopped in the casing of the source before they reach the chip under investigation, but the x-rays are not. The signal registered in the pixels will thus be that of x-rays. The x-rays emitted from the ^{55}Fe source are mainly of the types K_α and K_β , with energies of 5.9 keV and 6.5 keV, respectively [107]. Not all decays emit an x-ray, however. There are two separate K_α and K_β x-rays that can be emitted for this isotope, but the energies of them are close together, so both peaks of each type are considered to have the same energy. A K_α x-ray occurs in 24.4% of decays, and a K_β x-ray occurs in 2.85% of decays [107].

Tests with the x-rays from ^{55}Fe are carried out for different pixel flavours by changing the active mini-matrix in the chip under investigation. This enables study of varying pixel sizes and parameters, for both the standard and the modified process. The investigated pixels and their parameters are shown in Table 4.1.

Pixel size	Coll. el. size	Spacing
$20 \times 20 \mu\text{m}^2$	$3 \mu\text{m}$	$3 \mu\text{m}$
$28 \times 28 \mu\text{m}^2$	$2 \mu\text{m}$	$3 \mu\text{m}$
$30 \times 30 \mu\text{m}^2$	$3 \mu\text{m}$	$3 \mu\text{m}$
$40 \times 40 \mu\text{m}^2$	$3 \mu\text{m}$	$13.5 \mu\text{m}$
$50 \times 50 \mu\text{m}^2$	$3 \mu\text{m}$	$18.5 \mu\text{m}$

Table 4.1: Pixel properties of the investigated mini-matrices of the TowerJazz Investigator. Figure 4.1 shows the definition of the listed dimensions.

The different parameters of the pixels give them different gains, which makes comparison between different pixel flavours complicated. However, the goal of the study is to investigate the performance difference of the standard and modified processes, which is possible for any of the pixel sizes. All tests are carried out at room temperature in an ISO-7 cleanroom environment, using unirradiated chips.

The data from the DRS4 oscilloscope is saved in a binary format [105], which is decoded and plotted using a program written in Python 3.6. This program analyses the data by doing a curve fit for each registered hit, and extracting the signal amplitude and signal rise time. As the output signal is flat before a hit, has a sharp rise at the hit, and decays slowly after the hit, a double exponential function is needed for the fit. The function used to fit the signal is shown in Equation 4.1. It consists of two parts; one before the signal start at time t_0 , and one after:

$$t \leq t_0 : f(t) = a \quad (4.1a)$$

$$t > t_0 : f(t) = a - b \cdot \left(e^{-\frac{t-t_0}{c}} - 1 \right) \cdot e^{-\frac{t-t_0}{d}} \quad (4.1b)$$

where the fitting parameters are labelled t_0 , a , b , c , and d . The constant offset of the signal is given by a , and comes from the leakage current. If the decay time is

very long the parameter d is large, and the last exponential term tends to 1. In this case, the parameter b corresponds directly to the signal amplitude, and c is related to the signal rise time [104]. However, if the parameter d is not large, the amplitude and rise time have to be calculated rather than taken directly from the parameters. The amplitude of the signal can be found by taking the derivative of the fit function, finding an expression for the maximum, and subtracting the constant background offset a . The amplitude is thus given by

$$\mathbf{amplitude} = f_{max} - a = b \cdot \left(1 - \frac{c}{d+c}\right) \cdot \left(\frac{c}{d+c}\right)^{c/d}. \quad (4.2)$$

The rise time is taken to be the time it takes for the signal to rise between 10% and 90% of the maximum amplitude value. The time values for 10% and 90% amplitude are found numerically from the fitted function, and the registered rise time for a hit is taken to be the difference between them.

Events are rejected where the amplitude is negative, the rise time is less than 1 ns, or the decay time is an order of magnitude shorter than the expected value. Such events can come from bad fits, or signals arising from induction of charge movement in an adjacent pixel. After extraction of the signal amplitude and rise time from the fits, the data are read by a script written in ROOT 6 [108] to make plots using binned histograms. A Gaussian fit is also made to the rise time distributions to extract their mean values and widths.

4.2.2.2 Results

The results are separated by pixel flavour (labelled by pixel size, as given in Table 4.1), and compare the standard process with the modified process. Figures 4.4, 4.5, and 4.6 show superimposed plots for the standard and modified process signal amplitude and rise time for the $20 \times 20 \mu\text{m}^2$ pixel, the $28 \times 28 \mu\text{m}^2$ pixel, and the $50 \times 50 \mu\text{m}^2$ pixel, respectively. The standard process histograms are blue, and the modified process histograms are red. The histograms are normalised on the total number of entries.

When the x-ray photons from the ^{55}Fe interact with the silicon, they are expected to be completely absorbed and create electron-hole pairs (as the photoelectric effect is the dominant interaction mode for these relatively low photon energies [35]). As most photons have an energy of either 5.9 keV or 6.5 keV, there should be clear peaks in the amplitude spectra if all charge is collected in the pixel. This can be seen clearly in the amplitude spectra for both the standard and modified processes in Figures 4.4 and 4.5. The tested $50 \times 50 \mu\text{m}^2$ pixel has a much lower gain (the scale of the amplitude axis is an order of magnitude smaller than for the other pixels), and in the amplitude spectra in Figure 4.6(a), the K_β peak cannot be distinguished. If the x-ray hits a pixel near the pixel edge, charge can also be shared with adjacent pixels giving rise to a continuum of amplitudes lower than the peak values. This feature is also clearly seen in all the amplitude plots. Parts of this continuum can also arise from incomplete charge collection from hits at the pixel edges, where the charge is not collected in any of the pixels. The sharp

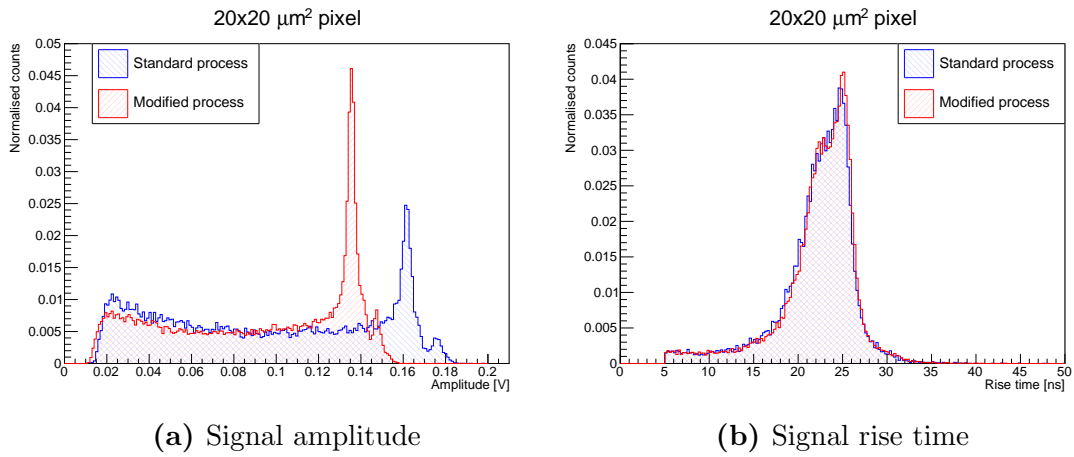


Figure 4.4: Comparison of the signal amplitude and rise time for the standard and modified process, using a $20 \times 20 \mu\text{m}^2$ pixel.

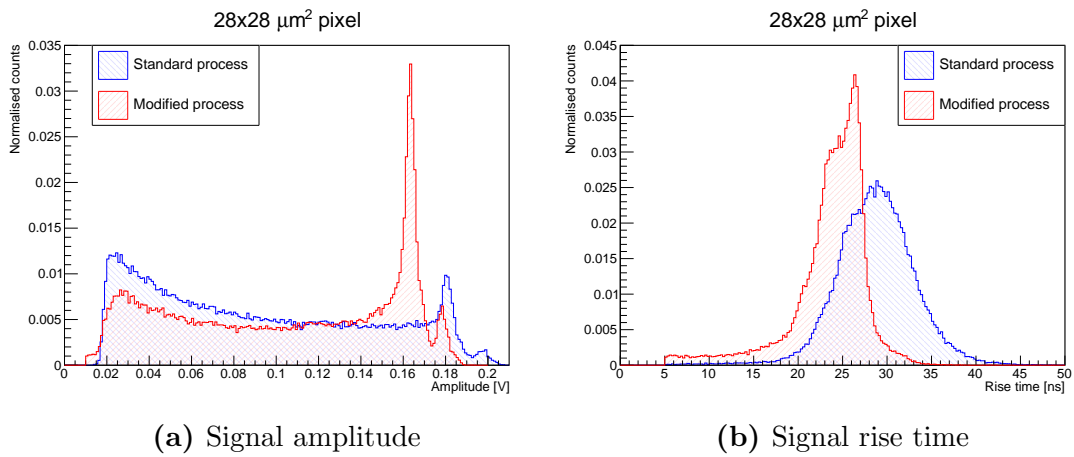


Figure 4.5: Comparison of the signal amplitude and rise time for the standard and modified process, using a $28 \times 28 \mu\text{m}^2$ pixel.

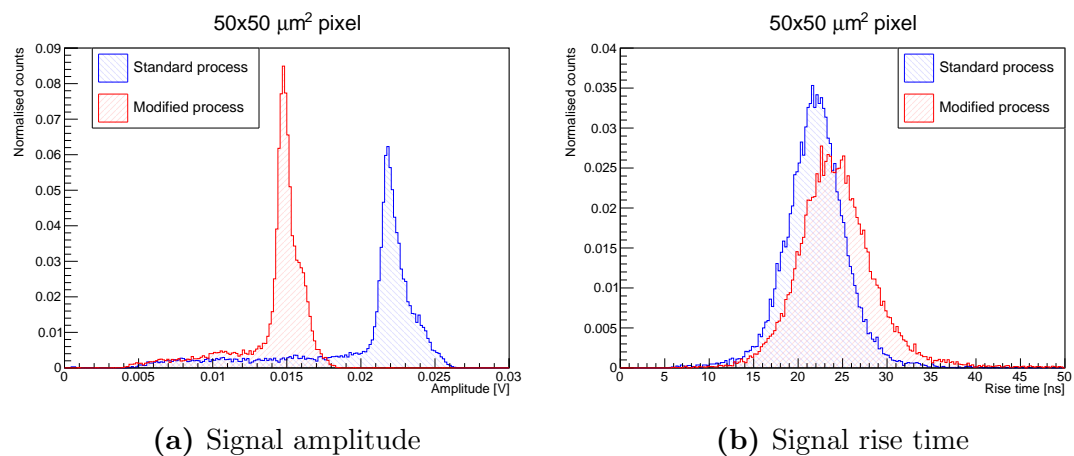


Figure 4.6: Comparison of the signal amplitude and rise time for the standard and modified process, using a $50 \times 50 \mu\text{m}^2$ pixel.

edge of the spectra at low amplitude comes from the trigger level used at the data acquisition stage, which sets a lower limit on the possible signal amplitudes that can be recorded.

In all three amplitude plots, the peak positions are located at lower amplitudes for the modified process, compared to the standard process. This is due to an increased capacitance in the pixel that stems from the deep planar junction introduced in the modified process, which reduces the signal gain slightly. Comparing the peak height relative to the background (i.e. the continuum) for the amplitude spectra, it is clear that the modified process improves the signal-to-background ratio for all pixel sizes. The background arises from hits at pixel edges that are not completely collected by the single investigated pixel, indicating that the modified process has a higher charge collection efficiency. This is especially visible in Figure 4.5(a) (i.e. for the $28 \times 28 \mu\text{m}^2$ pixel). The difference is smaller for the $20 \times 20 \mu\text{m}^2$ pixel. There is also a clear difference for the $50 \times 50 \mu\text{m}^2$ pixel, but the spectra have a much lower amplitude and a different shape than the spectra from the smaller pixels. Discussions with chip designers from CERN have revealed that pixels where the spacing is large (i.e. pixels of a size of $40 \times 40 \mu\text{m}^2$ or larger) are significantly different from other pixels. Results from them can differ significantly to results from smaller pixels, and they are not representative for developments used in future sensors [109]. Large spacing causes a region around the collection electrode to remain undepleted, and thus increases the pixel capacitance, which decreases the signal amplitude [110]. A higher signal-to-background ratio indicates a more complete charge collection, as more of the hits from the ^{55}Fe x-rays are fully registered by the pixel. This indicates a smaller charge cloud, and fewer trapped charges, and thus a larger depleted region in the modified process compared to the standard process.

The rise time distributions for the $20 \times 20 \mu\text{m}^2$ pixel size show very little difference between the standard and modified process. For a $28 \times 28 \mu\text{m}^2$ pixel however, the rise time distribution for the modified process is clearly shifted to lower values than the distribution for the standard process. This indicates that charge generated by the incident x-ray is collected faster in the modified process in this pixel. The distribution for the modified process is also narrower than the standard process distribution, which indicates a more uniform charge collection mechanism for all charge sizes, i.e. for hits at any point in the pixel. Charges in silicon are collected either by diffusion or by drift (see Section 2.4.3), and collection by drift is faster and dominates in depleted regions. The narrower rise time distribution located at lower times thus indicates that the modified process has a larger depleted volume for a $28 \times 28 \mu\text{m}^2$ pixel. For a $20 \times 20 \mu\text{m}^2$ pixel there is little difference, which indicates that the depletion does not change as much between the standard and modified processes. This can be understood by considering the relative depleted volume; for a smaller pixel size, the fraction of the sensitive volume that is depleted will be larger for the standard process, compared to the standard process for a larger pixel size. Using the modified process may thus not deplete a small pixel significantly more than what is already depleted in the standard process. The rise time distributions for the $50 \times 50 \mu\text{m}^2$ pixel show that the modified process in

this case has a slightly higher mean rise time, and a wider distribution. This likely stems from the large spacing causing a region around the collection electrode to be undepleted [110], which makes charge collection slower. As already mentioned pixels with large spacing differ significantly from the ones with smaller spacing, and conclusions from them are less clear [109]. This is also evident in that the amplitudes for a pixel with large spacing are much lower than for the pixels with smaller spacing, making the signal response characteristics differ significantly.

Both rise time distributions for the $20 \times 20 \mu\text{m}^2$ pixel size, and the modified process rise time distribution for a $28 \times 28 \mu\text{m}^2$ pixel size, show a “shoulder” to the left of the highest peak. Hits giving rise to this shoulder likely stem from hits very close to the collection electrode, whereas the main peak stems from hits in other places in the depleted region. Hits close to the collection electrode are expected to result in shorter signal rise times than hits further away.

Figure 4.7 shows 2D histograms of amplitude and rise time for the $28 \times 28 \mu\text{m}^2$ pixel, for the standard and modified processes. The standard process plot shows a downwards slope as amplitude increases, indicating that larger signals get collected faster. Larger signals come from hits in the centre of the pixel, and smaller signals primarily from hits near the pixel edges where the charge gets shared with other pixels. As charge collection by drift is faster than charge collection by diffusion, this indicates that charges at the pixel edges are collected primarily by diffusion and charges in the centre are collected primarily by drift. The depleted region in the standard process does thus not seem to extend to the pixel edges [111]. In the modified process however, there is no distinct slope in the amplitude-rise time plot, which indicates a uniform charge collection mechanism and thus full depletion throughout the pixel.

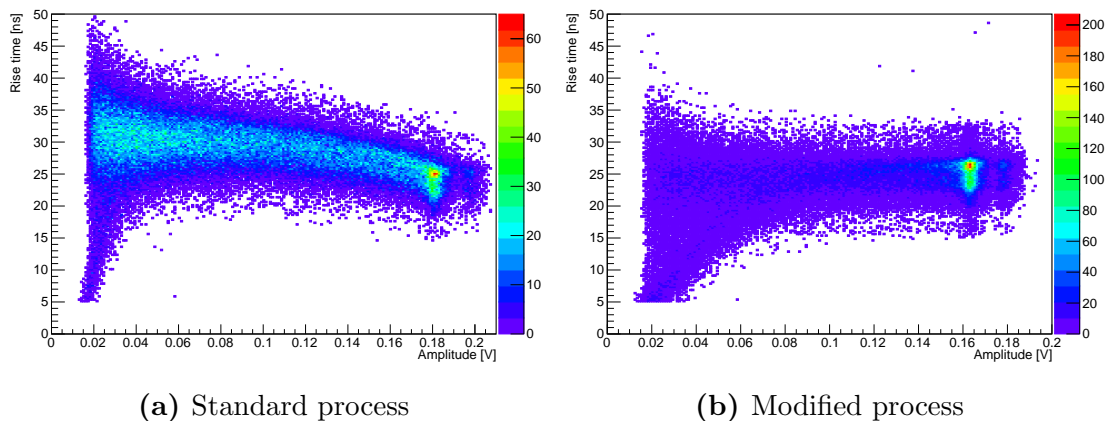


Figure 4.7: Plots of signal rise time versus amplitude, for the standard and modified process using a $28 \times 28 \mu\text{m}^2$ pixel.

The rise time distributions are studied by using Gaussian fits, and extracting the mean value and distribution width. A Gaussian approximation is used as the fits give a good indication of the centroid position (i.e. mean rise time) and the width of the distributions even when they are not purely Gaussian in shape. Using a

Gaussian fit also enables direct comparisons with results from colleagues at other institutions. The results are shown in Table 4.2 for the different pixel flavours labelled by the pixel size (see Table 4.1). The distribution width given in the table is the standard deviation of the Gaussian fit.

Pixel size	Mean rise time [ns]		Distribution width [ns]	
	Standard	Modified	Standard	Modified
$20 \times 20 \mu\text{m}^2$	22.78 ± 0.12	22.23 ± 0.11	3.15 ± 0.15	2.96 ± 0.12
$28 \times 28 \mu\text{m}^2$	29.72 ± 0.14	23.25 ± 0.11	4.09 ± 0.11	2.81 ± 0.12
$30 \times 30 \mu\text{m}^2$	27.71 ± 0.15	23.78 ± 0.10	4.05 ± 0.16	2.64 ± 0.09
$40 \times 40 \mu\text{m}^2$	22.29 ± 0.09	23.21 ± 0.11	2.61 ± 0.07	3.32 ± 0.11
$50 \times 50 \mu\text{m}^2$	22.87 ± 0.09	24.70 ± 0.10	3.15 ± 0.08	3.87 ± 0.10

Table 4.2: The mean rise times, and the width of the rise time distributions (defined as the standard deviation of the Gaussian fit), for the standard and modified process in the TowerJazz Investigator 1. The table contains results for five different pixel flavours, labelled by their sizes. Details of the differences between the pixels can be found in Table 4.1.

For the $20 \times 20 \mu\text{m}^2$, $28 \times 28 \mu\text{m}^2$, and $30 \times 30 \mu\text{m}^2$ pixels, the modified process reduces both the mean rise time and the rise time distribution width, both indications of a larger depleted region compared to the standard process. The difference is smallest for the $20 \times 20 \mu\text{m}^2$ pixel, as can also be seen in Figure 4.4(b). For the $40 \times 40 \mu\text{m}^2$ and $50 \times 50 \mu\text{m}^2$ pixels however, both the mean rise time and the rise time distribution width is higher in the modified process compared to the standard process. For these pixels the spacing between the p-well and the collection electrode is large ($13.5 \mu\text{m}$ and $18.5 \mu\text{m}$) which makes the behaviour of the pixels significantly different compared to pixels with smaller spacing (i.e. around $3 \mu\text{m}$) [109]. The pixels with large spacing have an order of magnitude lower signal amplitude than the others, and it is theorised that this also affects the rise time distributions. A large spacing also gives rise to an undepleted region around the collection electrode [110]. In developments building on from results from the TowerJazz Investigator chips, the modified process and a small spacing is used. The pixels with large spacing are thus not considered representative of desired future developments.

The absolute numbers of the pixel rise times show some discrepancies to results presented by collaborators at CERN, and in an effort to find the source of the differences tests using different cables in the setup were performed. These tests showed that the absolute numbers are impacted by the length of cable used between the passive board pixel output and the amplifier. Tests were also performed using a nominally identical amplifier borrowed from colleagues at the University of Glasgow [112], and the amplifier was also found to be a source of difference. The amplifiers have been modified by CIVIDEC to have a very long decay time, but the modifications yield slightly different results for the different amplifiers despite them being of the same type originally. While the absolute values of the mean rise time and the rise time distribution width depend on details of the experimental

setup, the comparative measurements using the same setup are still valid, and the conclusions that the modified process gives a larger depleted region and thus better charge collection properties has been shown in all the setups.

4.2.3 Comparing different biasing configurations

The TowerJazz Investigator 1B allows separate biasing of the p-well and the substrate, with respect to the collection electrode. This makes it possible to change the electric field strength within the pixel, and study how this affects the charge collection properties. The TowerJazz Investigator 1B is only available in the modified process, with the deep planar n-p junction as illustrated in Figure 4.2(b).

4.2.3.1 Experimental setup

The chip under investigation is mounted to a carrier board containing connections for powering the chip, providing a reset signal, and reading out the analogue signal of four pixels, and pins for selecting the active mini-matrix. Three power supplies are used; one to power the on-chip electronics, one to bias the p-well, and one to bias the substrate. The p-well biasing is labelled “PWELL” in parts of this section, and the substrate biasing is labelled “HV” (for “high voltage”). A reset signal is provided by an Arduino board via a voltage divider. The voltage divider is needed as the reset signal to the chip is supposed to be 1.8 V, and the Arduino outputs a 5 V signal. A schematic view of the experimental setup can be seen in Figure 4.8. The analogue signal from a single pixel is connected to the same

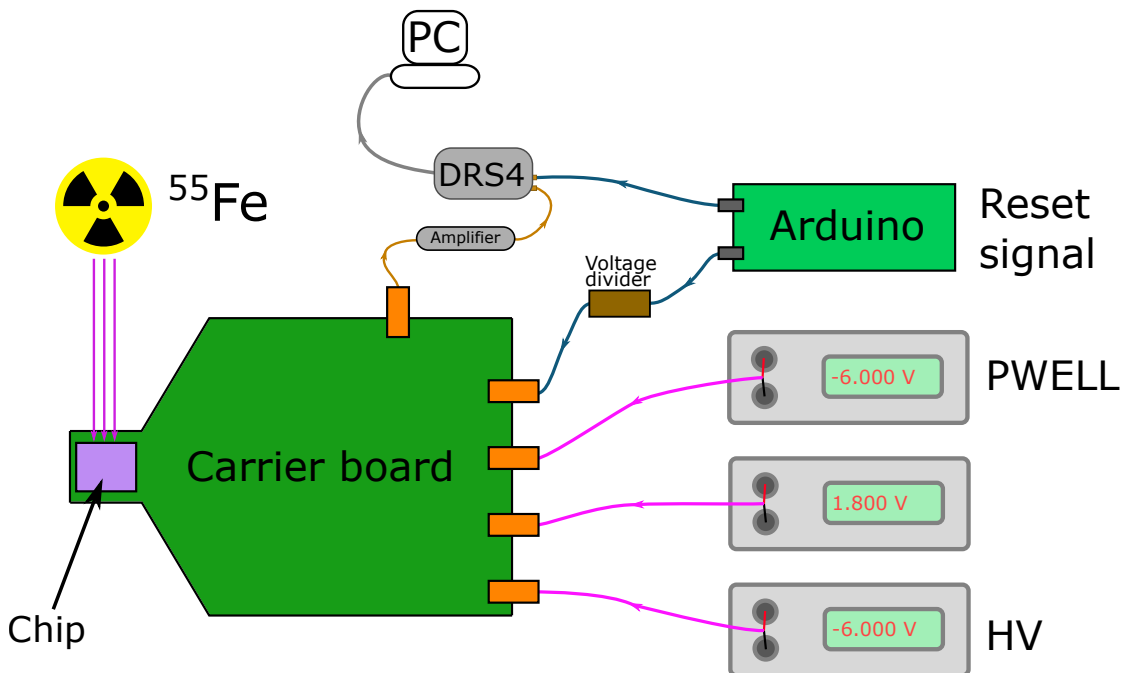


Figure 4.8: Schematic view of the TowerJazz Investigator 1B experimental setup. The substrate (“HV”) and the p-well (“PWELL”) are biased separately. The active mini-matrix is selected by bridging pins on the carrier board.

amplifier used for the TowerJazz Investigator 1 studies (see Section 4.2.2), and the amplified signal is sent to the DRS4 oscilloscope. A reset signal is also provided to the DRS4 from the Arduino, to enable setting up a trigger to avoid fake hits from the reset response of the chip.

An ^{55}Fe source is used to produce the investigated signal. The active mini-matrix (i.e. pixel flavour) is selected by bridging pins on the carrier board. The signal amplitudes from the TowerJazz Investigator 1B are generally smaller than the amplitudes of the TowerJazz Investigator 1, and a signal for pixels with large spacing cannot be found. As pixels with large spacing are not used in future developments [109], this is not considered a significant problem. The focus of the studies is the $28 \times 28 \mu\text{m}^2$ pixel, with dimensions as described in Table 4.1. This pixel was found in investigations of the TowerJazz Investigator 1 to give clear signals with high amplitude.

The possible bias voltages for the p-well are between -3 V and -8 V . If the voltage is between 0 V and -3 V , the signal is too small to register. If it is below -8 V the leakage current becomes too high, and there is a risk of damaging the sensor. The substrate voltage always has to be equal to or lower than the p-well voltage. For a p-well voltage of -6 V , tests are performed with substrate voltages between -6 V and -15 V . With a substrate voltage below -15 V , the current again becomes too large for safe sensor operation due to punch-through between the substrate and the p-well.

To extract the signal amplitude and rise time, a fit using Equation 4.1 is used, and the same method as described in Section 4.2.2.1 is used to extract the parameters of interest. The amplitude and rise time are then plotted as histograms for different biasing voltages. Gaussian fits are made to the rise time distributions to extract the mean rise times and the rise time distribution widths.

4.2.3.2 Results

The main results shown are for a $28 \times 28 \mu\text{m}^2$ pixel, with different biasing of the p-well and the substrate. Figure 4.9 shows the amplitude and rise time for different substrate voltages with a fixed p-well voltage of -3 V . Figure 4.10 shows the same for a fixed p-well voltage of -6 V . The spectra are normalised by the total number of counts present.

For the signal amplitude plots, the expected K_α and K_β peaks are always visible. With a p-well biasing of -3 V the signal amplitudes are relatively low, and close to the trigger level. At a p-well biasing of -6 V the amplitudes are higher, and the continuum from shared hits is easier to see. For both p-well bias voltages, two things are immediately apparent; a larger substrate bias voltage increases the gain (i.e. the signal amplitude), and the signal-to-background ratio of the peaks decreases with a larger substrate bias voltage (where the background is taken to be the continuum from shared hits).

The signal rise time plots show that the rise time distribution widens and gets a higher mean value as the substrate bias voltage grows. At a substrate bias voltage

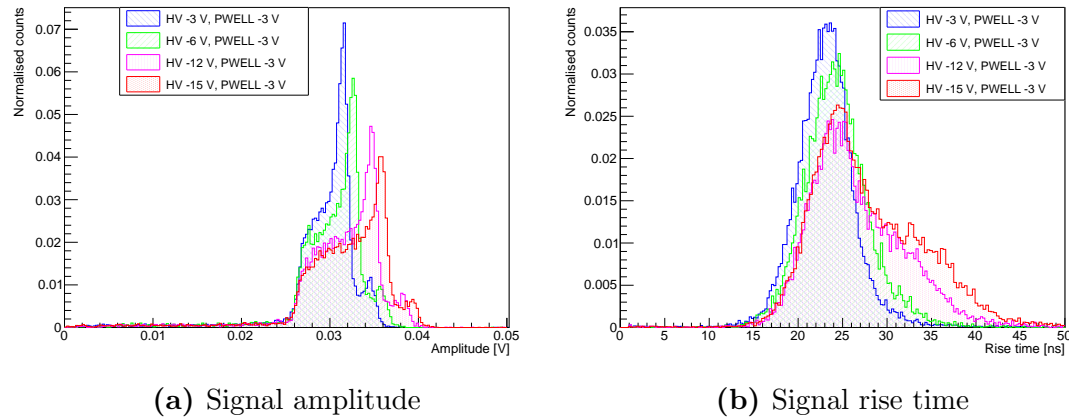


Figure 4.9: Comparison of the signal amplitude and rise time for a fixed p-well biasing of -3 V (labelled “PWELL”), and varying substrate biasing (labelled “HV”).

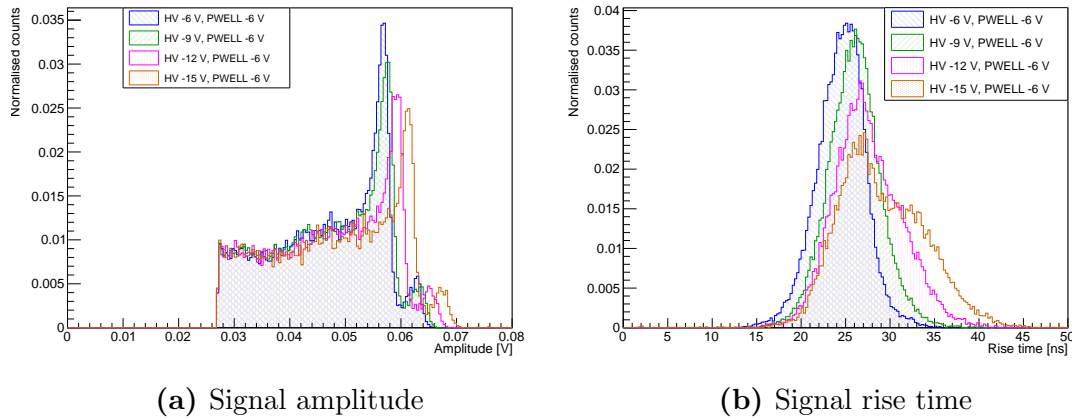


Figure 4.10: Comparison of the signal amplitude and rise time for a fixed p-well biasing of -6 V (labelled “PWELL”), and varying substrate biasing (labelled “HV”).

of -15 V, the rise time distribution tends to a double normal distribution. The same trends have also been seen in studies using a p-well voltage of -8 V. The variations are smaller in that case however, as the voltage difference between the p-well and the substrate is smaller.

Figure 4.11 shows a 2D histogram of rise time versus amplitude, for a p-well bias voltage of -6 V and a substrate bias voltage of -15 V. A downwards slope as the signal amplitude increases is visible, indicating that smaller charges are collected slower in this case. A plot where the substrate voltage is -6 V shows no downwards slope, which indicates that when the substrate voltage is increased while the p-well voltage is kept at -6 V, charges at the pixel edges get collected slower.

Table 4.3 shows the fit results to the rise times, extracting the mean signal rise time and the rise time distribution width for different substrate bias voltages and

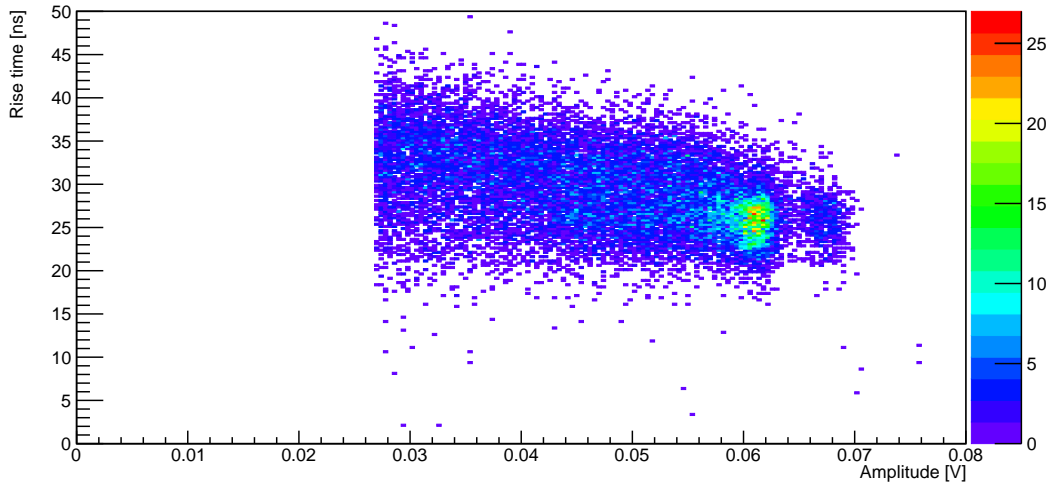


Figure 4.11: Signal rise time versus amplitude, for a p-well biasing of -6 V and a substrate biasing of -15 V.

Substrate voltage:	Mean rise time [ns]	Distribution width [ns]
-6 V	24.34 ± 0.09	2.87 ± 0.07
-9 V	25.95 ± 0.09	2.97 ± 0.08
-12 V	27.52 ± 0.12	3.94 ± 0.10
-15 V	29.42 ± 0.17	4.89 ± 0.12

Table 4.3: The mean rise times, and the width of the rise time distributions (defined as the standard deviation of the Gaussian fit), for a p-well bias voltage of -6 V and varying substrate bias voltage.

a p-well bias voltage of -6 V. These results clearly show what is indicated by Figures 4.9 and 4.10; as the substrate voltage increases, the charge collection gets slower and becomes less uniform.

Tests are also performed using a $20 \times 20 \mu\text{m}^2$ pixel with dimensions as shown in Table 4.1. Results from this, with a p-well bias voltage of -6 V and substrate bias voltages of -6 V and -15 V are shown in Figure 4.12. The differences in rise time distributions are smaller for this pixel compared to the $28 \times 28 \mu\text{m}^2$ pixel. There is a slight shift to higher mean rise time as the substrate bias voltage increases, but the rise time distribution width remains approximately constant. The signal amplitude shows the same trend for this smaller pixel as well however; the signal-to-background ratio of the peak decreases as the substrate bias voltage increases, indicating a less complete charge collection.

In conclusion, it can thus be seen that the signal-to-background ratio for the peaks decreases with increased difference between p-well and substrate bias voltage, and the rise time characteristics deteriorate. These results are unexpected; a larger potential difference between the substrate and the p-well results in a higher electric field strength within the pixel, which naïvely is expected to improve the charge

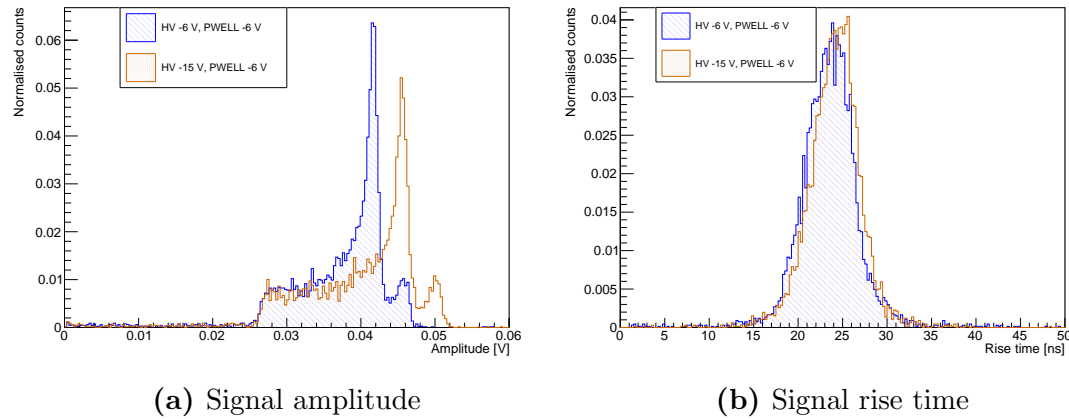


Figure 4.12: Comparison of the signal amplitude and rise time for a fixed p-well biasing of -6 V (labelled “PWELL”), and substrate biasing (labelled “HV”) of -6 V and -15 V, for a $20 \times 20 \mu\text{m}^2$ pixel.

collection properties. Figure 4.11 however shows that as the substrate bias voltage increases, charges from the edge of the pixel get collected slower. A slower charge collection increases the chance of charges being trapped and recombining before being collected, reducing the signal-to-background ratio of the peaks. The background stems from hits not being completely collected in the investigated pixel, and the charge collection is thus shown to be less complete the higher the bias voltage difference between the p-well and the substrate is. Tests with a smaller pixel size show that the effect of different biasing is smaller in that case.

Detailed simulations of the electric field within the pixels carried out by colleagues at CERN have shown that the modified process has an electric field minimum between pixels, below the p-well [113]. Figure 4.13 shows an illustration of the electric field lines within a pixel, with the electric field minimum marked by a magenta star. Charges at the pixel edge get pushed into this minimum, resulting

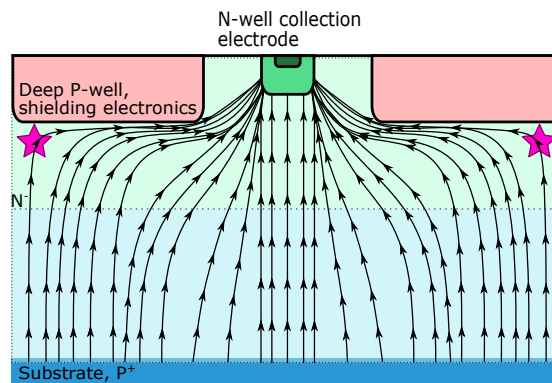


Figure 4.13: Sketch of the electric field lines (marked as black lines with arrows) within a pixel. The magenta stars indicate an electric field minimum at the pixel edges. As the voltage difference between the substrate and the p-well increases, the electric field lines under the p-well become straighter. Figure adapted from [113].

in entrapment or slow collection. There is thus an area under the p-well where charge has a higher probability of not being collected. The simulations have also shown that this effect gets more prominent as the bias voltage between the p-well and the substrate increases; the electric field lines under the p-well get straighter, making charge move more towards the minimum under the p-well than towards the collection electrode. The charges in a larger area thus get transported to the p-well, and then have to drift laterally along a longer path to reach the collection electrode. This explains the presented results well: a higher substrate bias voltage compared to the p-well bias voltage deteriorates the charge collection properties of the pixel, due to a slower charge collection near the pixel edge. The simulations also indicate that the effect of the electric field minimum decreases as the area under the p-well decreases, i.e. as the pixel size gets smaller. This also matches the presented results from the lab measurements.

To improve the charge collection performance, further process modifications are suggested [113]. These modifications are made to shape the electric field to push charges from the pixel edges toward the collection electrode. The modifications are implemented in the MiniMALTA chip, and are discussed in more detail in Section 4.3.1.

4.3 MiniMALTA studies

The modified process described in Section 4.2.1 was developed into a fully monolithic MAPS sensor with integrated analogue and digital signal processing, intended as a candidate for the outermost layer of the ATLAS experiment inner tracker in a future upgrade. The new sensor is named MALTA (“Monolithic pixel detector from ALICE to ATLAS”) [114], and was intended to have a high timing resolution and a high radiation tolerance. From tests of the chip carried out at testbeams and labs at CERN however, it has been observed that the radiation tolerance is low, with detection inefficiencies being observed under the p-well (at the pixel edges) after irradiation [114]. After simulation studies by colleagues at CERN [113] this is theorised to come from the same pixel edge effect as was observed in the study presented in Section 4.2.3, i.e. an electric field minimum under the p-well. To amend the reduction in hit detection efficiency at high irradiation doses and high substrate biasing, two pixel modifications have been implemented in a test chip called MiniMALTA. This section describes the MiniMALTA chip and studies of the performance of the pixel modifications at a testbeam using x-rays.

4.3.1 MiniMALTA test chip

The MiniMALTA test chip is a sensor prototype produced in the TowerJazz 180 nm CMOS imaging process, based on developments of the MALTA chip [115]. The chip has eight different sectors with different characteristics, and each sector consists of 8×16 square pixels with a pixel size of $36.4 \times 36.4 \mu\text{m}^2$. The collection electrode size is $3 \mu\text{m}$, and the spacing is $4 \mu\text{m}$. Figure 4.14 shows the layout of

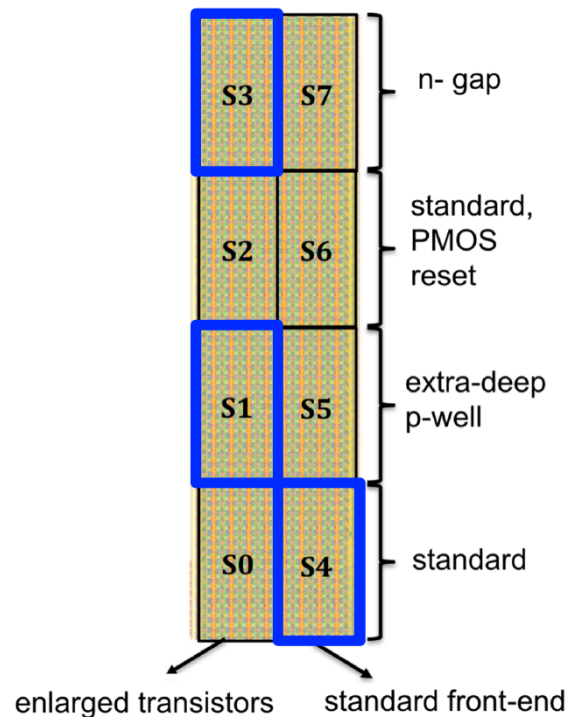


Figure 4.14: MiniMALTA chip sector layout. Sectors under investigation are marked by blue boxes, i.e. “S1”, “S3”, and “S4”. Figure from [115].

the MiniMALTA chip, with the sectors explored in this work marked with blue boxes. The sectors are arranged in pairs, with one of the pairs having enlarged transistors in the in-pixel analogue electronic circuitry in order to reduce the noise level of the pixels (and thus enabling lower threshold values to be set). There are four different sector designs; “standard” is the same design as that of the MALTA chip [114] (i.e. the so-called “modified process” from Section 4.2), and “standard, PMOS reset” is the same as the MALTA chip design with a different reset signal structure. This sector is not studied in this work. The sectors labelled “extra-deep p-well” and “n-gap” contain process modifications to funnel the electric field lines more towards the collection electrode (compared to the MALTA-like situation shown in Figure 4.13), and the main purpose of this study is to compare the performance of pixels containing these process modifications to the performance of the pixel layout of the MALTA chip, which is the “modified process” described in Section 4.2.1.

Figure 4.15 shows the extra deep p-well and n-gap modifications. The extra deep p-well modification has an added deep p-well at the pixel edges, whereas the n-gap modification leaves a gap in the n-layer at the pixel edges. Both modifications introduce junctions to prevent the electric field lines from being vertical under the p-well, pushing charges more towards the collection electrode. The schematic views exaggerate the size of the features. The modifications thus help reduce the effect of the electric field minimum shown in Figure 4.13 by funnelling the field lines towards the collection electrode.

The MiniMALTA chip also allows separate biasing of the p-well and the substrate,

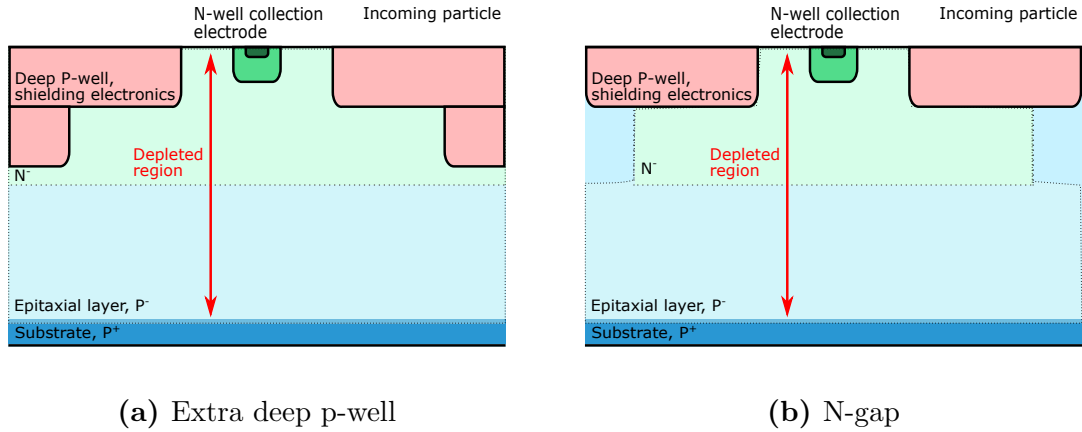


Figure 4.15: Schematic view of a pixel of the MiniMALTA chip with the extra deep p-well modification (a) and the n-gap modification (b). Both process modifications have the purpose of funnelling the electric field at pixel edges towards the collection electrode. Figure adapted from [113].

so the impact of the performance of the process modifications can be studied with different bias configurations in the same way as was done for the Tower-Jazz Investigator 1B, described in Section 4.2.3. However, the p-well biasing of the MiniMALTA version used in the tests described in this section cannot go beyond -2 V.

4.3.2 Diamond Light Source testbeam

The effect on the in-pixel particle detection efficiency given by the new modifications shown in Figure 4.15 was studied using data from a testbeam of the MiniMALTA chip carried out at the Diamond Light Source in the spring of 2019. The testbeam was carried out in collaboration with the University of Oxford, and results were published in 2020 [116]. The Diamond Light Source synchrotron was used to produce monochromatic x-rays, chosen to have an energy of 8 keV (to roughly approximate the signal of a minimum ionising particle in the chip), and a beamspot size of $2 \times 2 \mu\text{m}$. The tested MiniMALTA chips were mounted on a cooling jig on a motion stage in the beamline, making it possible to make fine adjustments to the beamspot position on the chip by activating the motion stage. The cooling jig kept the chips at a constant temperature of -13 °C. For the measurements, the beamspot was moved across the chip in $2 \mu\text{m}$ steps. After each movement of the beamspot data were acquired for 1 s, giving approximately 10 000 photons per step. In this way, different sectors of the chips were scanned in great detail. Each scan covered an area of $100 \times 100 \mu\text{m}^2$. For every step, the number of hits for each pixel in the chip was registered and saved.

The beam intensity changed slightly over time. This was corrected for in each step by normalising to a value measured by an ion chamber further down the beamline, which measures the beam intensity. The low-energy beam halo arising from focusing of the x-rays was removed during data acquisition by a filter based on artificial intelligence methods.

A minimum ionising particle traversing silicon will create electron-hole pairs along its entire track, creating a “tube” of charges to be collected. An x-ray will instead deposit all charge in a small volume, giving rise to a “charge ball” [49]. The implication of this is that x-rays will be fine probes of local inefficiencies within a pixel, as the charge collection from an x-ray hit will be strongly related to the pixel performance at the hit position. Due to the difference in charge deposit mechanism, the results from this study are not directly comparable to studies of in-pixel efficiency carried out using MIPs. The efficiency is thus termed “pixel photon response” here, to avoid confusion.

Several MiniMALTA chips were tested during the testbeam, irradiated to different doses. For the work carried out as part of this thesis, the data from two chips are investigated; one unirradiated chip, and one irradiated to a level of $1 \cdot 10^{15}$ 1 MeV neutron equivalents per cm^2 [36]. Such high irradiation doses are not of great interest for the EIC, where the expected level of irradiation is of the order of $1 \cdot 10^{10}$ 1 MeV neutron equivalents per cm^2 [51]. Irradiated chips are useful in demonstrating the charge collection properties of different pixel modifications however, as the effect of a low electric field region will be more evident with an increased radiation dose. Trapping and recombination becomes more frequent after irradiation, and more charge will thus be lost in regions where the electric field (and thus charge movement speed) is lower. The pixel modifications may thus have a more noticeable impact for irradiated sensors. Both of the chips investigated here have an epitaxial layer thickness of $30 \mu\text{m}$.

Three sectors of the MiniMALTA chips are investigated, as can be seen in Figure 4.14. First of all, the MALTA-like sector (marked “S4” in the figure) is looked at. The pixels in this sector have no modifications other than the deep planar junction, and the in-pixel analogue circuitry transistors used are the same size as in the MALTA chip. This sector thus represents the baseline that the pixel modifications can be compared to, and is of the same design as the modified process of the TowerJazz Investigator 1 and 1B presented in Section 4.2 (albeit with a pixel size of $36.4 \times 36.4 \mu\text{m}^2$). The extra deep p-well sector and the n-gap sector investigated (marked “S1” and “S3” in the figure) carry the new designs that should theoretically improve the charge collection efficiency. Both of those sectors have enlarged transistors to reduce noise.

4.3.2.1 Data analysis

The number of counts in each pixel can be extracted individually for each $2 \mu\text{m}$ beam step from the data. As the beamspot size is $2 \times 2 \mu\text{m}^2$, and the step length for a single step is $2 \mu\text{m}$, the pixel response is plotted in a 2D histogram of x and y position with a bin size of $2 \times 2 \mu\text{m}^2$. Due to charge sharing, a pixel will frequently have a response even when the beam is located just outside the pixel edge. As the absolute pixel position is not known with sufficient precision compared to the beamspot position, the location of the pixel edges are not initially known. A fit is therefore made to find them; a histogram of the counts of each of the pixels for different beamspot positions is looked at, and projections are made in the x and y directions. The projected distributions are then fitted with a generalised Gaussian

distribution (also known as an exponential power distribution), and from this the centre position of the pixel in x and y can be extracted. Using the extracted centre value, and the fixed pixel size of $36.4 \times 36.4 \mu\text{m}^2$, the pixel edges can be determined. The generalised Gaussian used for the fit is given by

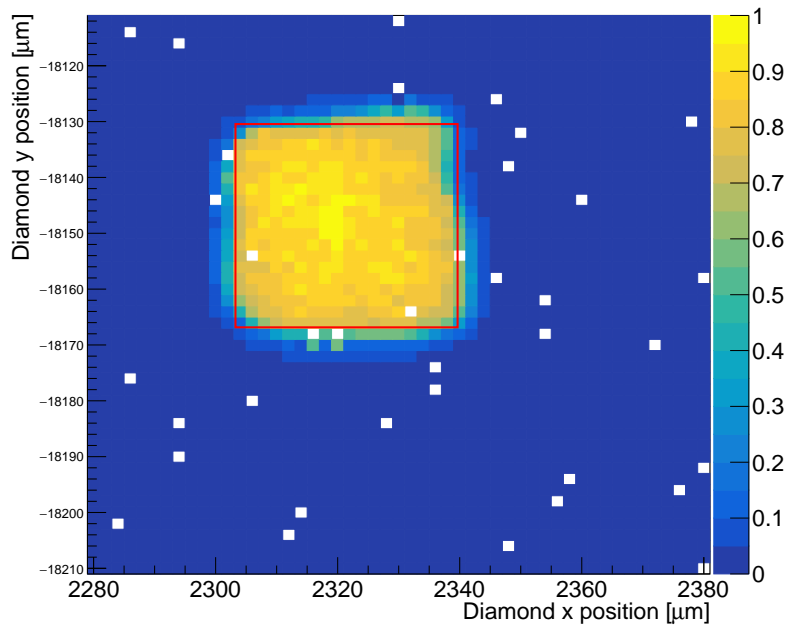
$$f(x) = \frac{\beta}{2\alpha\Gamma(1/\beta)} e^{-(|x-\mu|/\alpha)^\beta}. \quad (4.3)$$

The parameter β is a measure of how “square” the function is; at $\beta = 2$ it has the shape of a regular Gaussian distribution. The function $\Gamma(1/\beta)$ is the generalised factorial function, and the fit parameter μ will give the pixel centre position in this case.

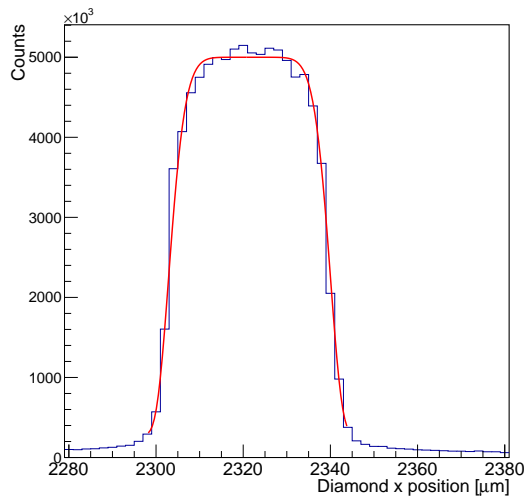
The pixel boundaries are required to be able to normalise the in-pixel response, and calculate the average photon response across the pixel. Figure 4.16 shows an example of a (normalised) pixel response, plotted versus the beamspot position given in the Diamond Light Source coordinate system. The pixel edge from the fits is shown as a red square, and the projections and fits in the x and y direction used to extract the pixel edges are shown in the separate subfigures. The white spots in the pixel response map are bins without data, where the data taking failed to start after the beam step. These bins are ignored in all calculations.

Once the pixel borders are known, the pixel response can be normalised. It is assumed that the pixel will be 100% efficient near the centre, and hence the bin with the maximum number of counts is used as the basis of normalisation. All other bins for the pixel are divided by the number of counts in the maximum bin, giving a pixel response map between 0% and 100%. The normalisation is performed individually for each pixel in the scanned area. In the square space defined by the pixel edges the full pixel response is averaged using each bin within the pixel, where bins on the edge of the pixel border are calculated as fractions of a bin. This averaging is performed individually for each pixel, and the total average photon response for a sector of the chip is finally taken as the average value for all the visible pixels in the sector.

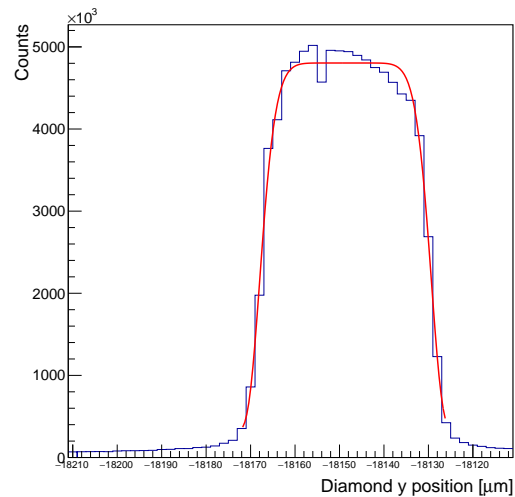
The amount of charge sharing and the extent of the charge sharing region is also calculated. Charge sharing is defined as the fraction of registered hits in a pixel that are outside of the nominal pixel area. Bins with a fraction of less than 5% of the maximum number of counts in a pixel are exempt from the charge sharing calculation, as this level is found to correspond to the noise level of the chips. The charge sharing percentage is then averaged over all pixels in the sector where a charge sharing calculation can be performed (i.e. excluding partial pixels), to give the charge sharing percentage for a full sector. The charge sharing extent is calculated for each pixel side individually as the maximum distance from the pixel edge at which the fraction of counts drops below 5% of the maximum number of counts. An average is then taken for all available pixel sides in the sector, to give an average extent of the charge sharing.



(a) Single pixel normalised response



(b) x projection



(c) y projection

Figure 4.16: Example pixel response, with pixel border from fit (a). The colour corresponds to the normalised photon response, between 0% and 100%. The projections and fits for this pixel, using a generalised Gaussian distribution, are shown in (b) and (c). The axes give the Diamond Light Source reference coordinate system. Each bin is the same size as the beamspot; $2 \times 2 \mu\text{m}^2$.

4.3.2.2 Results

Figure 4.17 shows a visual comparison of the photon response for the three unirradiated MiniMALTA sectors. The axes in the figure show the position in the scanned $100 \times 100 \mu\text{m}^2$ area, and each bin has a size of $2 \times 2 \mu\text{m}^2$, with the colour corresponding to the photon response (i.e. the number of counts in the bin, normalised for each pixel). In this figure each pixel has been normalised individually,

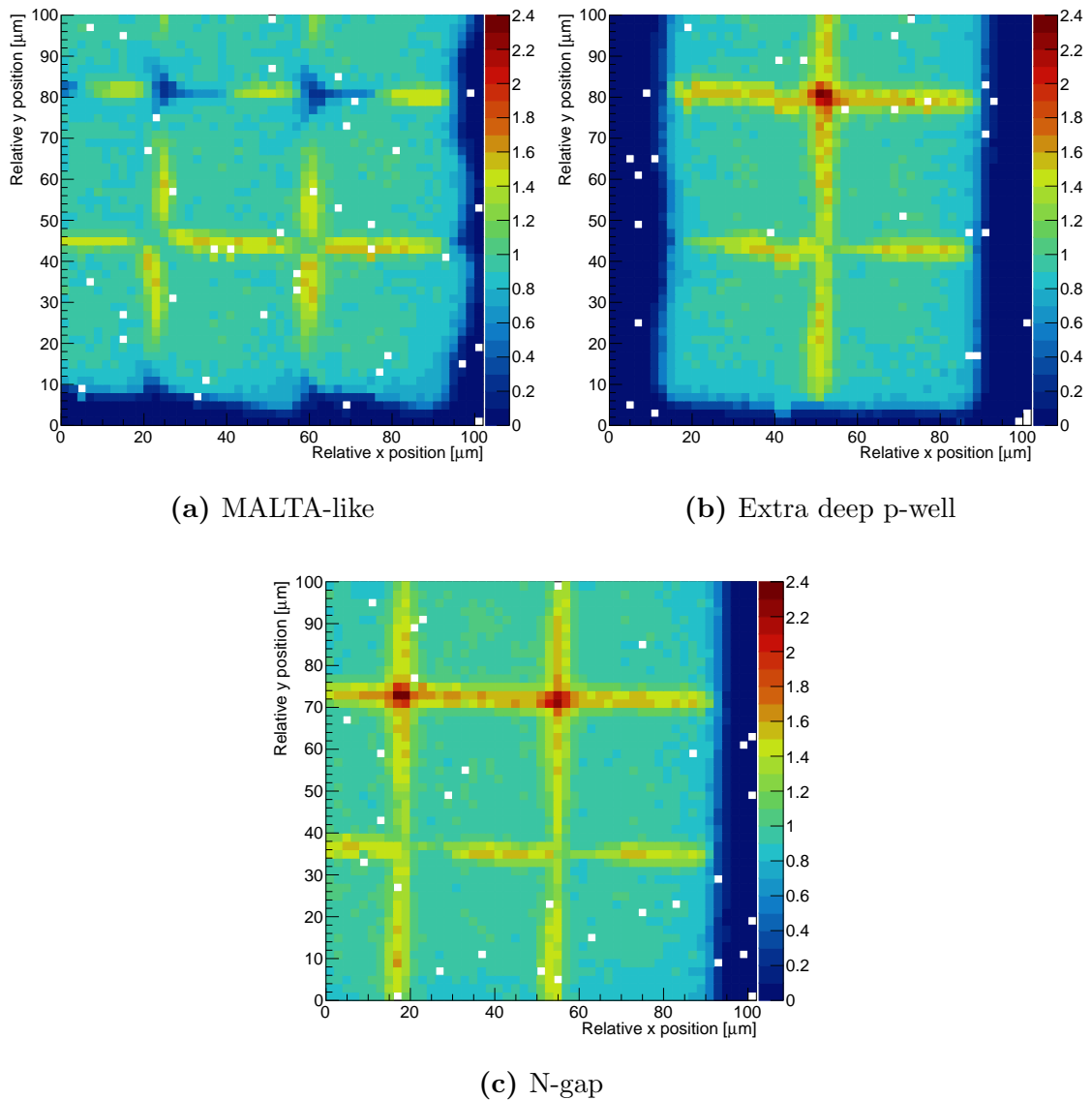


Figure 4.17: Total (summed) photon response maps for all available pixels in the three different sectors, for the unirradiated chip. The substrate voltage used is -6 V, and the p-well voltage is -2 V.

and the photon responses of all available pixels have been summed up. In the charge sharing regions the highest visible response values are thus much higher than 100%, as more than one pixel registers a hit in those regions. The charge sharing between pixels can thus be seen as yellow lines, where several pixels register hits for a beam step. The MALTA-like sector and the n-gap sector have 9 active pixels each, and the extra deep p-well sector has 6 active pixels. The colour scale for all three subfigures is the same, and by comparing the colours it is thus immediately obvious that both the maximum and minimum summed response values for the MALTA-like sector are lower than for the extra deep p-well and n-gap sectors. The MALTA-like sector has an inefficiency in the pixel corners, leading to a total photon response below 15% in that area. The sectors with the process modifications for improved charge collection instead see an increase in efficiency

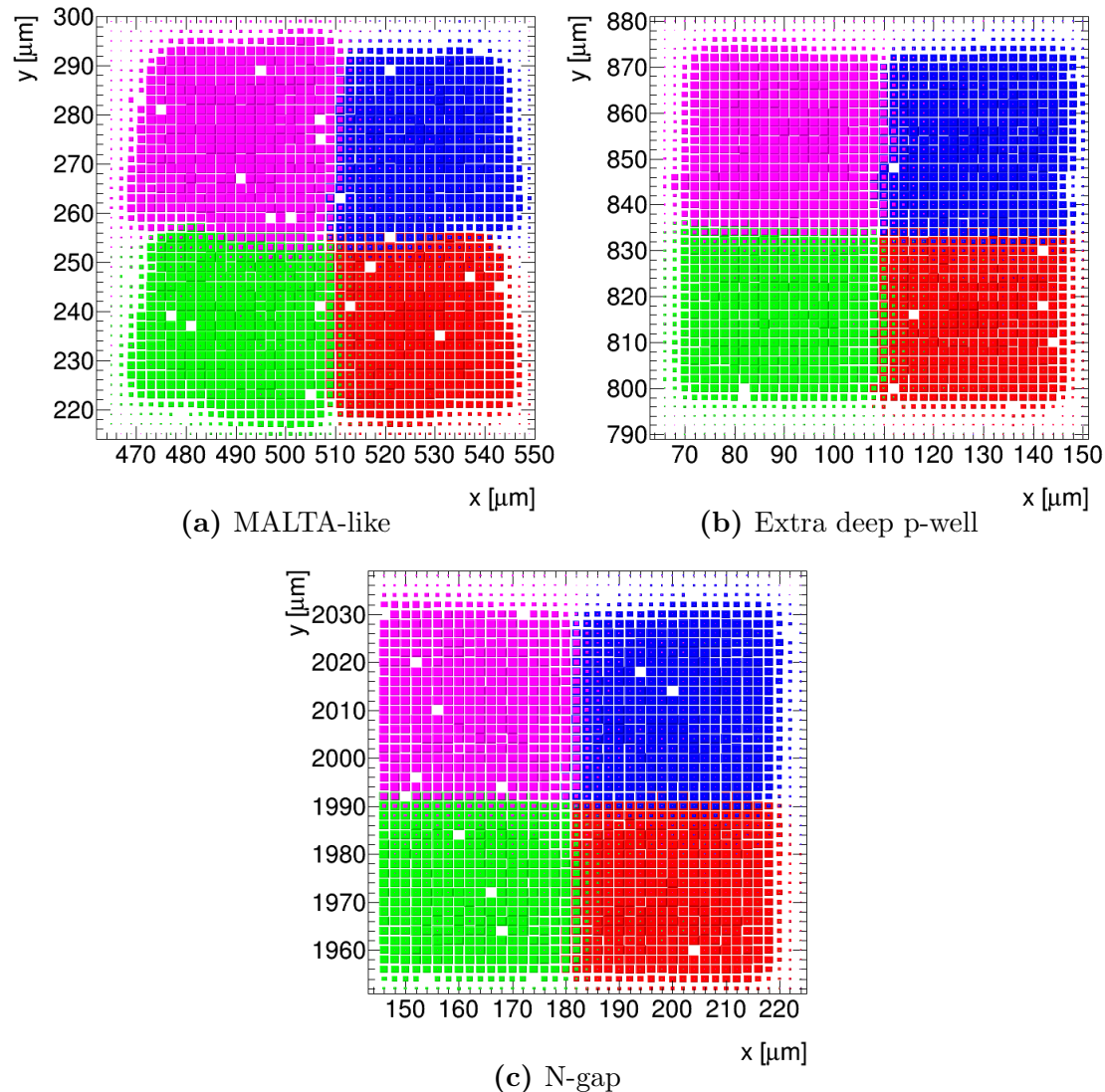


Figure 4.18: Normalised in-pixel photon response per pixel for four different pixels in the three different sectors, for the unirradiated MiniMALTA chip. The substrate voltage used is -6 V, and the p-well voltage is -2 V. The size of a coloured square in a bin corresponds to the normalised photon response value, between 0% and 100%.

at the pixel corners due to charge sharing, giving a summed response of up to 240% where several pixels register a hit. It is clear from this figure that there are some irregularities in the pixel response at corners; some corners have a lower summed response than others. This is due to the shape of the p-well within the pixels, which is not a symmetric square, and the pixel orientation which varies to accommodate the readout system. This effect has also been observed in the MALTA chip [114].

A different visual comparison of the unirradiated results is shown in Figure 4.18. Here, each bin contains a coloured square, where the size of the square represents the normalised photon response, taking values between 0% and 100%. A smaller square indicates a lower response. Four pixels for each MiniMALTA sector

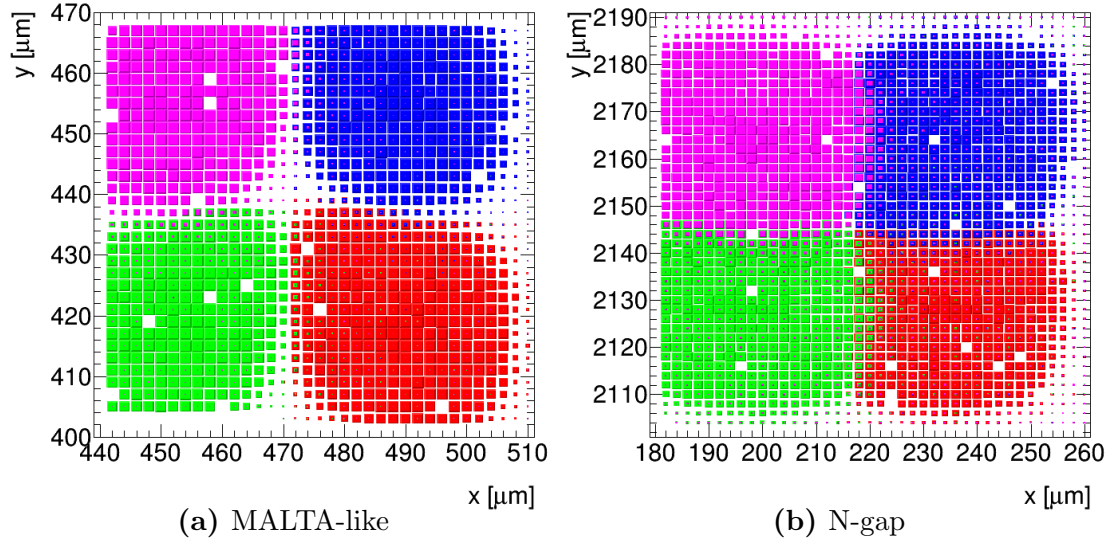


Figure 4.19: Normalised in-pixel photon response per pixel for four different pixels in the MALTA-like sector and the n-gap sector, for the MiniMALTA chip irradiated to 1 MeV neutron equivalents per cm^2 . The substrate voltage used is -6 V, and the p-well voltage is -2 V. The size of a coloured square in a bin corresponds to the normalised photon response value, between 0% and 100%.

are plotted in different colours, and there is no summation of the pixel responses in this plot. The axes indicate the position relative to the bottom left corner of the sensitive area of the MiniMALTA chip (see Figure 4.14). The pixel size is $36.4 \times 36.4 \mu\text{m}^2$. It can immediately be seen that the pixel photon responses have a more regular shape in the extra deep p-well and the n-gap sectors compared to the MALTA-like sector. This also causes the charge sharing between pixels to be more asymmetric in the MALTA-like sector. There appears to not be a significant difference between the responses in the two sectors with process modifications.

Figure 4.19 shows the same kinds of plot for the irradiated chip, with a bias voltage of -6 V on the substrate and -2 V on the p-well. There are no data available for the extra deep p-well sector for this configuration, so only the MALTA-like sector and the n-gap sector are shown. After irradiation, it is clear that the n-gap pixel modification improves pixel photon response compared to the MALTA-like pixels. The responses for the pixels in the n-gap sector retain a roughly square shape, whereas the inefficiencies at the pixel edges in the MALTA-like sector are obvious. The pixel photon response for this sector becomes “pear shaped”, and drops to almost 0% at pixel corners. By comparing Figures 4.19(a) and 4.18(a), it can be seen that this is an effect of the irradiation. Radiation damage increases the likelihood of charges being trapped before being collected, and the effect is mainly seen on slow-moving charges. In the studies performed in Section 4.2.3 it was concluded that the pixels in the MALTA-like layout (i.e. the so-called “modified process”) have an electric field minimum at pixel edges (under the p-well), causing charge created in those positions to be collected slower. It is thus theorised that the same effect is seen here; the electric field minimum causes inefficiencies at the pixel edges

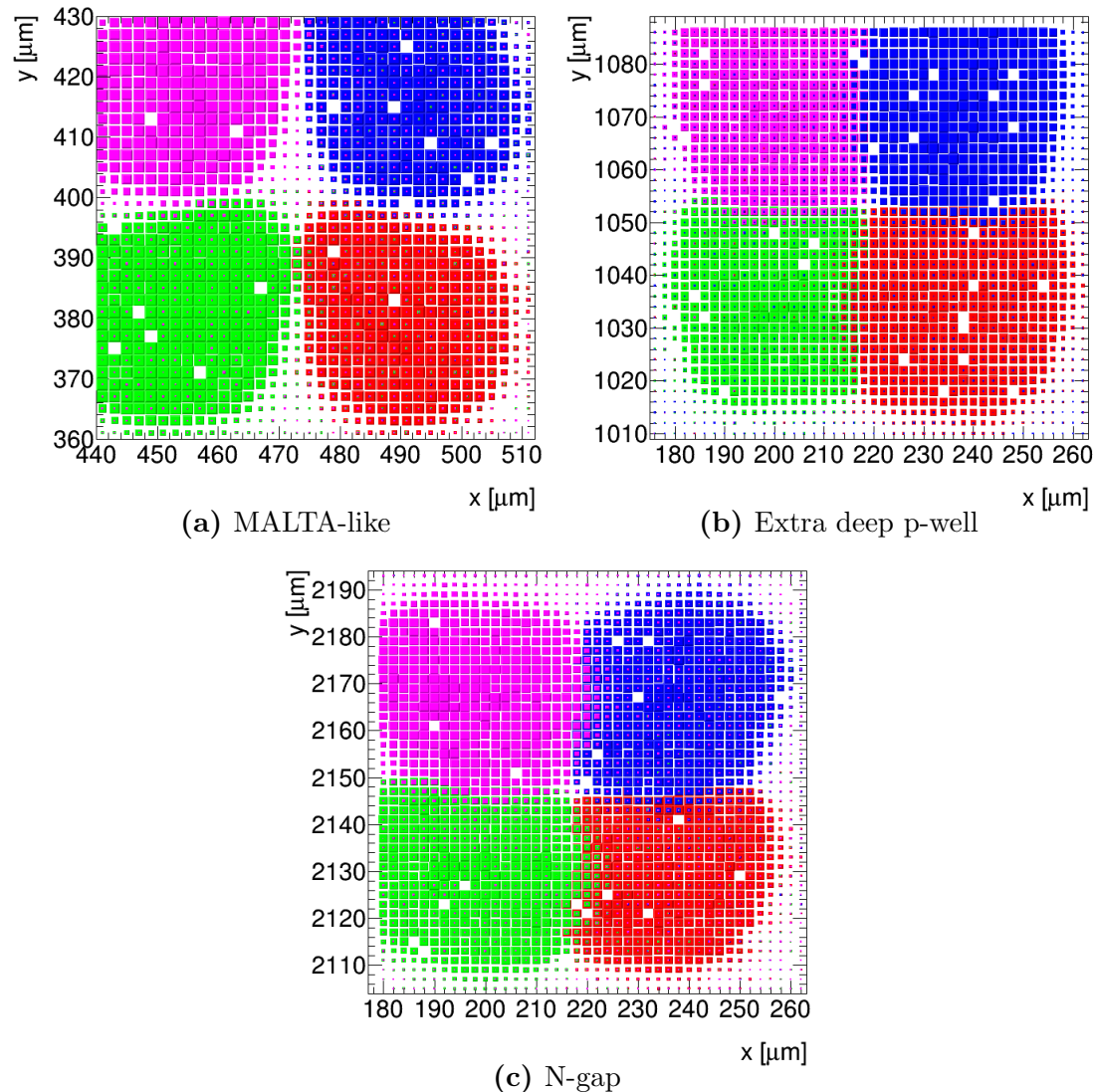


Figure 4.20: Normalised in-pixel photon response per pixel for four different pixels in the three different sectors, for the MiniMALTA chip irradiated to 1 MeV neutron equivalents per cm^2 . The substrate voltage used is -20 V, and the p-well voltage is -2 V. The size of a coloured square in a bin corresponds to the normalised photon response value, between 0% and 100%.

for the MALTA-like sector, but the n-gap modification successfully removes this minimum and thus the inefficiency. The “pear shape” matches results seen from testbeam studies of the MALTA chip [114], and the shape comes from the layout of the p-well which is not a symmetric square in this chip. The particle detection efficiency is found to be highest where the p-well is not present [114].

The photon response results for the irradiated chip with a bias voltage of -20 V for the substrate and -2 V for the p-well are shown in Figure 4.20. All three investigated sections are available for this configuration. The “pear shape” of the pixel response in the MALTA-like sector appears even stronger here than at a substrate bias voltage of -6 V. This matches the expectations from the studies presented in Section 4.2.3; a higher potential difference between the substrate and

the p-well makes charge collection from the pixel edges less efficient. By comparing the n-gap sector performance shown in Figure 4.20(c) with Figure 4.19(b), it can be seen that the shape of the pixel photon response in this region becomes less square at a higher bias voltage, and the response at the intersection of the four pixels appears to decrease. A benefit of the measurements presented in Figures 4.19 and 4.20 is that the chip was not relocated between them, so the scans were performed over exactly the same area. A direct visual comparison can therefore be made of the extent of the photon response regions for the pixels for the different biasing settings, and the extent of charge sharing for the n-gap sector can thus be seen to appear to increase at a higher bias voltage.

The numerical values for the average photon response of pixels in a sector, the charge sharing percentage, and the average charge sharing extent are extracted. Results for the unirradiated chip are shown in Table 4.4. The photon response value is averaged over the full pixels, and inefficiencies at the pixel edges thus reduce this value. It can be seen that the extra deep p-well and the n-gap sectors are not significantly different from each other in any of the presented figures of merit. They have a slightly higher photon response than the MALTA-like sector, and significantly more charge sharing. The charge sharing extent is not significantly different for any of the sectors however. This indicates that while charge sharing is present above the background level outside of the pixels in the MALTA-like sector, those pixels are less efficient than the modified pixels at collecting the charges far away from the pixel centre.

Sector	Average ph. response [%]	Charge sharing [%]	Average extent of charge sharing [μm]
MALTA-like	83.43 ± 1.36	14.92 ± 2.92	6.05 ± 1.06
Extra deep p-well	85.82 ± 0.69	19.17 ± 0.51	6.93 ± 0.49
N-gap	86.00 ± 0.69	19.44 ± 0.59	7.32 ± 0.66

Table 4.4: Analysis results for the unirradiated chip, with a bias of -6 V on the substrate and -2 V on the p-well. Results are shown for each sector.

Table 4.5 shows the results for the irradiated chip, with a bias voltage of -6 V on the substrate and -2 V on the p-well. The difference in photon response is within errors for the two available sectors in this case. There is a vast difference in charge sharing however; the pixels in the n-gap sector can register charge a lot

Sector	Average ph. response [%]	Charge sharing [%]	Average extent of charge sharing [μm]
MALTA-like	74.50 ± 3.54	4.16 ± 1.25	4.00 ± 1.71
N-gap	78.90 ± 2.84	24.19 ± 1.01	10.89 ± 2.03

Table 4.5: Analysis results for the irradiated chip, with a bias of -6 V on the substrate and -2 V on the p-well. Results are shown for the two available sectors; MALTA-like and n-gap.

more efficiently outside the pixel edge, and a lot further away than the pixels in the MALTA-like sector. This is mainly due to the low efficiency of the MALTA-like sector charge collection at the pixel edges, making the photon response drop to zero near the edge.

Finally, the results for the irradiated chip with a bias voltage of -20 V on the substrate and -2 V on the p-well are shown in Table 4.6. In this case, the average photon response is significantly higher in the extra deep p-well and n-gap sectors, compared to the MALTA-like sector. This indicates that the modifications work

Sector	Average ph. response [%]	Charge sharing [%]	Average extent of charge sharing [μm]
MALTA-like	64.73 ± 3.67	5.41 ± 2.16	5.48 ± 2.24
Extra deep p-well	79.40 ± 2.50	18.61 ± 1.14	11.01 ± 2.71
N-gap	77.78 ± 2.50	23.98 ± 1.88	12.13 ± 2.59

Table 4.6: Analysis results for the irradiated chip, with a bias of -20 V on the substrate and -2 V on the p-well. Results are shown for all three investigated sectors.

as intended, and reduce the inefficiency arising from an electric field minimum at pixel edges as the bias difference between the substrate and the p-well increases. The difference in photon response between the extra deep p-well and the n-gap sectors is within errors. The charge sharing is again much lower for the MALTA-like sector than for the other two, due to the charge collection inefficiency at pixel edges. This inefficiency appears to be amended by both the extra deep p-well and the n-gap modifications. The n-gap modification yields a higher charge sharing percentage than the extra deep p-well modification in this case, while the charge sharing extents for the two modifications are within errors of each other.

Tables 4.7 and 4.8 show a summary of all results for the MALTA-like sector and the n-gap sector, respectively. From this, it can be seen that there is a significant decrease in both photon response and charge sharing for the MALTA-like sector after irradiation. This matches what has been seen at testbeams of the MALTA chip [114], and stems from poor charge collection efficiency at the pixel edges giving rise to a “pear shaped” pixel response (as can be seen in Figure 4.19(a)). As the substrate bias voltage changes from -6 V to -20 V, there is a further

Chip	Sub. bias	Average ph. response [%]	Charge sharing [%]	Average extent of charge sharing [μm]
Unirrad.	-6 V	83.43 ± 1.36	14.92 ± 2.92	6.05 ± 1.06
Irradiated	-6 V	74.50 ± 3.54	4.16 ± 1.25	4.00 ± 1.71
Irradiated	-20 V	64.73 ± 3.67	5.41 ± 2.16	5.48 ± 2.24

Table 4.7: Summary of results from the MALTA-like sector, for both the unirradiated and irradiated chip and different substrate bias voltages. The p-well bias voltage is -2 V for all studies.

Chip	Sub. bias	Average ph. response [%]	Charge sharing [%]	Average extent of charge sharing [μm]
Unirrad.	-6 V	86.00 ± 0.69	19.44 ± 0.59	7.32 ± 0.66
Irradiated	-6 V	78.90 ± 2.84	24.19 ± 1.01	10.89 ± 2.03
Irradiated	-20 V	77.78 ± 2.50	23.98 ± 1.88	12.13 ± 2.59

Table 4.8: Summary of results from the n-gap sector, for both the unirradiated and irradiated chip and different substrate bias voltages. The p-well bias voltage is -2 V for all studies.

significant decrease in the average photon response, mimicking the effect seen in the study of the TowerJazz Investigator 1B chip presented in Section 4.2.3. The charge sharing remains within errors of the value from using the smaller substrate bias voltage however. The n-gap sector also shows a significant decrease in photon response after irradiation. For this sector however, the charge sharing increases rather than decreases. As the substrate bias voltage is changed to -20 V, there is no significant difference in either photon response or charge sharing for this sector, indicating that the process modification works as intended in removing the electric field minimum under the p-well which causes charge collection inefficiencies at higher bias voltages.

To quantify the difference in pixel photon response and charge sharing brought on by irradiation and change of substrate bias voltage, ratios of the values from different configurations are calculated and presented in Table 4.9. From this table,

Sector	Ratio (sub. bias and chip)	Average response	Charge sharing	Extent of charge sh.
MALTA-like	-6 V irr. / -6 V unirrad.	0.89 ± 0.04	0.28 ± 0.1	0.66 ± 0.31
	-20 V irr. / -6 V irr.	0.87 ± 0.06	1.30 ± 0.65	1.37 ± 0.81
N-gap	-6 V irr. / -6 V unirrad.	0.92 ± 0.03	1.24 ± 0.06	1.49 ± 0.31
	-20 V irr. / -6 V irr.	0.99 ± 0.05	0.99 ± 0.09	1.11 ± 0.32
E.d.p-well	-20 V irr. / -6 V unirrad.	0.93 ± 0.03	0.97 ± 0.06	1.59 ± 0.41

Table 4.9: Ratios of the figures of merit for different configurations. The irradiated chip is denoted by “irr.”, and the unirradiated by “unirr.”. The extra deep p-well sector is labelled “E.d.p-well”.

it is clear that the photon response for pixels in the MALTA-like sector decreases significantly both after irradiation and when using a larger substrate bias voltage. For the pixels in the n-gap sector, there is a decrease in pixel photon response after irradiation, but no significant decrease when the substrate voltage grows larger. The charge sharing percentage and extent decrease after irradiation for pixels in the MALTA-like sector, and increase for pixels in the n-gap sector. There is however no significant change in charge sharing for either sector when the substrate bias voltage changes from -6 V to -20 V. The photon response for pixels in the extra deep p-well sector match those of the n-gap sector. The charge sharing fraction is smaller than for the n-gap sector however, but the charge sharing extent is compatible within errors.

Table 4.10 shows the ratios for the different sectors for the unirradiated chip, for a bias voltage of -6 V on the substrate and -2 V on the p-well. The data used as a basis for this table are presented in Table 4.4. This shows that the

Ratio	Average response	Charge sharing	Extent of charge sharing
E.d.p-well / MALTA-like	1.03 ± 0.02	1.28 ± 0.25	1.15 ± 0.21
N-gap / MALTA-like	1.03 ± 0.02	1.30 ± 0.26	1.21 ± 0.24
N-gap / E.d.p-well	1.00 ± 0.01	1.01 ± 0.04	1.06 ± 0.12

Table 4.10: Ratios of the figures of merit for the different sectors in the unirradiated chip, at a substrate bias voltage of -6 V and a p-well bias voltage of -2 V. The extra deep p-well sector is labelled “E.d.p-well”.

extra deep p-well and the n-gap modifications slightly improve the average photon response compared to the MALTA-like sector, and increase the fraction of charge shared. There is however no significant difference in the charge sharing extent in this unirradiated case. It can also be seen that there is no significant difference in any of the figures of merit between pixels with the extra deep p-well or n-gap modifications.

The conclusions that can be drawn from this testbeam study is thus that the process modifications introduced to funnel the electric field more towards the collection electrode seem to function as intended, and improve charge collection properties at the pixel edges. The results from pixels in the MALTA-like sector qualitatively match results from previous testbeams of the MALTA chip [114], and the new pixel modifications improve both the pixel response and the charge sharing properties at higher bias voltages and after irradiation. There is little to no difference visible between the extra deep p-well modification and the n-gap modification in these studies, but data for the extra deep p-well are not available for the full investigated parameter space, making a complete comparison difficult.

4.4 Conclusions and discussion

The conclusions from the studies presented in this chapter are that the so-called “modified process” with a deep planar junction collects charge more efficiently than the “standard process”, which indicates a higher level of depletion. The difference is smaller for smaller pixel sizes however, where the standard process appears to already deplete a large fraction of the pixel volume, but the signal-to-background ratio is still significantly higher for the modified process. Increasing the potential difference between the substrate and the p-well in the modified process deteriorates the charge collection performance, as this increases the effect of an electric field minimum trapping charges at the pixel edges. Modifications to the pixel edge geometry are introduced to remove the electric field minimum and funnel the electric field towards the collection electrode [113], and it is found that adding an extra deep p-well or a gap in the n-layer improves the charge collection performance and maintains the performance as the bias voltage increases.

Simulations and studies of the MiniMALTA chip carried out by colleagues at CERN have shown that the extra deep p-well modification and the n-gap modification both lower the highest bias voltage that it is possible to have in the sensor due to punch-through between the substrate and the p-well [113]. Having a higher bias voltage theoretically reduces the charge collection time, which is desirable for a fast sensor. Further studies of the impact on charge collection time in pixels with the modifications are required, as they may not be necessary for smaller pixels where the region with an electric field minimum is smaller.

The studies in this chapter show that a sensor utilising the modified process provides an improvement compared to the current state-of-the-art MAPS sensor known as the ALPIDE (see Section 2.4.5.2), with regard to charge collection properties and pixel size. It is thus a viable alternative for development of an EIC-specific sensor, allowing more charge to be collected in a smaller pixel. This improves the silicon vertex tracker resolution compared to what is currently possible with existing sensors, which is necessary to meet the requirements brought by the EIC physics goals. Further developments in this 180 nm CMOS imaging process are thus considered as a path forward for the EIC detector. The timeline for the ALICE ITS3 upgrade described in Section 2.4.5.3 aligns well with the EIC however, and the specifications of the proposed ITS3 sensor meets the EIC requirements [51]. The current plan is for the EIC to partake in the ITS3 upgrade developments, and fork off a specific EIC sensor at a later date. This development is intended to use the 65 nm CMOS imaging process, and is hence quite different to the sensors made in the 180 nm CMOS imaging process investigated in this chapter. The initial costs necessary for developing a sensor in this new technology are larger than the costs of developing a sensor in the 180 nm technology, and the technology is as of yet untested for use in particle physics experiments. It is thus currently a high cost and high risk development. A new sensor design in the 180 nm technology utilising results from the studies presented here and in work by collaborators is thus kept as a fallback solution for the EIC silicon vertex tracker. The modified process would be used in such a sensor, possibly incorporating further modifications such as the extra deep p-well or the n-gap, depending on the pixel size used. For the small pixel size required for the EIC physics programme, the results from this chapter indicate that the area with an electric field minimum will be small and the extra modifications may thus not be needed. Further studies are required however, once development of a bespoke EIC sensor starts.

In the following two chapters, simulation studies investigating the performance of a full silicon vertex tracker are presented. These studies utilise results from the sensor studies presented here in order to investigate the performance impact of different silicon sensor technologies and possible pixel sizes. Chapter 5 contains general detector simulations, whereas Chapter 6 contains more specific simulations taking into account the (now better known) EIC boundary conditions. Section 6.2 in particular shows a comparative study of the impact of different silicon sensor technologies on the detector vertex resolution, using the latest available EIC beampipe.

Chapter 5

General detector layout simulations

5.1 Introduction

Before January 2020 and the official approval of the EIC project by the US Department of Energy, some significant details of the project implementation were unknown. Two different sites (the Thomas Jefferson National Accelerator Facility and the Brookhaven National Laboratory) were possible, before Brookhaven was decided on as host. The two sites have different impacts on the detector design, most notably in beamline layout, beampipe design, and interaction rate. These parameters all affect the detector design. General simulations were thus made, giving comparisons that remain valid across the different possible external constraints. These general simulation studies are presented in this chapter. The focus in these simulations is comparisons between different detector layouts and parameters, rather than comparisons to the actual EIC requirements. Simulations carried out after site selection for the EIC are presented in Chapter 6, when both external constraints on detector design and the detector requirements imposed by the EIC physics case were better known. These more focused simulations are based on the results from the work presented in this chapter.

In the work presented here, a combination of the ALICE Inner Tracker upgrade (ITS2) [29] and the inner tracker of the BeAST detector [24] is used as a baseline. At the silicon vertex tracker level however, all proposed detector concepts are similar. The purpose of the simulations is to determine the most efficient silicon vertex tracker layout, with respect to resolution of momentum and point of origin (vertex position) of the tracked particles. In the EIC, the vertex position is of interest, as heavy flavour particles will be created in the collision and decay within a short distance ($\sim 100 \mu\text{m}$) from the collision vertex. It is thus important to be able to reconstruct the point of origin for the tracked particles, and be able to separate the primary collision vertex from the secondary decay vertex to accurately describe the physics of the collision. The momentum resolution is used for particle

identification and separation, and invariant mass reconstruction, and is thus an important tool for reconstructing events. The figures of merit observed in the presented simulations in this chapter are the relative momentum resolution and the pointing resolution, which is a measurement of how well the particle creation vertex can be found. The theory behind those figures of merit can be found in Sections 2.2.2 and 2.2.3. The work presented in Chapter 4 indicate that a pixel size of $20 \times 20 \mu\text{m}^2$ is viable, and the impact of pixel size on tracking resolutions is studied in this chapter, thus investigating how the sensor technology investigated in the previous chapter can affect the EIC.

In some of the simulations a time-stamping layer is added, to investigate the effects it would have on the resolutions. Such a layer may have different properties to the rest of the silicon vertex tracker, and would have the possibility of time-stamping bunch crossings and thus help keep track of the beam polarisations in the detected interactions, as described in Section 1.3. The simulations study whether adding such a time-stamping layer would be detrimental to the detector performance, without considering the possible benefits the time-stamping would bring to event separation and reconstruction.

5.2 Experimental setup

Simulations are made using EICROOT, which is a Monte Carlo framework for detector simulation specifically developed for the EIC collaboration [117]. At the time the simulations were started, this was the main framework in use in the collaboration. EICROOT is based on the PandaRoot framework, which in turn is based on the FairRoot framework [118]. The ROOT version used in the simulations is ROOT 5.34/36, and GEANT3 is used for the particle interactions and Monte Carlo part of the simulations. The data analysis is performed using ROOT 6 [108].

At the start of the simulation, the detector geometry to be investigated is defined; the silicon vertex tracker pixel size, the thickness of the detector layers, and the detector layout are selected. The parameter space for the Monte Carlo simulation is then defined; the particle type, the pseudorapidities in which the particles are generated, their generated momentum (or transverse momentum) range, and the number of events to be generated. The pseudorapidity η is defined as $\eta = -\ln(\tan(\theta/2))$, where θ is the angle of the particle relative to the beam axis (see Equation 2.24). Each event consists of one particle, created at the centre of the defined geometry, with momentum that places it within the defined parameter space. The particles are created using a “box generator” in EICROOT. The generator has been modified to create a uniform distribution of particles in terms of transverse momentum p_T or momentum p , across a given uniform pseudorapidity range. A magnetic field is also defined to be uniformly 1.5 T or 3 T along the beam direction in the detector. The 1.5 T field is the same as the field strength in the existing BaBar solenoid, and the suggested solenoid for the ePHENIX concept [26]. A solenoid with a field of 3 T is discussed in the EIC White Paper [16], and in the JLEIC concept [119].

The Monte Carlo simulation is performed for the geometry and parameters given, creating and propagating particles through the detector. The information about the propagation of the particle is saved, and makes up a “true track” that the particle has taken. Details of the interaction of the particle with the geometry is also saved, and where it hit the sensitive areas of the detector.

The detector hits are then digitised, with a smearing around the hit position determined by the currently selected pixel size. The pixels in the vertex tracker are defined to be square, and the smearing is Gaussian with a standard deviation given by the pixel side length divided by $\sqrt{12}$ (see Section 2.2.1). The smeared hit positions are stored.

A reconstruction is then made, using the digitised hits on the active detector area. A Kalman filter is used as part of an ideal tracker using the digitised detector hits [45]. This forms a reconstructed track.

Finally, analysis code is executed to compare the simulated “true track” to the reconstructed track. This makes it possible to compare parameters of the tracks, and thus see how good the defined detector is at reconstructing the truth. In particular, the relative momentum resolution and the pointing resolution are studied in the transverse plane. This plane is perpendicular to the magnetic field, so it is the plane in which the tracked particles curve, making it relevant for momentum measurements. The relative momentum resolution is found by comparing generated and reconstructed momenta via the equation

$$\frac{\sigma_{p_T}}{p_T} = \frac{p_{T,\text{rec}} - p_{T,\text{gen}}}{p_{T,\text{gen}}} \quad (5.1)$$

where “rec” and “gen” represent reconstructed and generated momenta, and extracting the resolution at different momentum values by fitting a Gaussian to the distributions at those values. The resolution is taken to be the standard deviation of the Gaussian fit. For the transverse pointing resolution, the reconstructed vertex position in the transverse plane (x and y, given that z is the beam direction) is treated in the same way for different values of the momentum. The same is also done for the longitudinal pointing resolution (in the z direction).

The interval used for the Gaussian fit is set to 1.5 standard deviations around the peak centre position. This range was deemed to be the best way of extracting data reliably from the central peak, avoiding the tails of the distributions. Tests have been made using different intervals, which showed that the absolute numbers extracted vary slightly, but the trends remain the same. Comparative measurements using the same interval are thus considered valid.

The particles used in the simulations presented here are mainly positive pions, π^+ , in the barrel region. Pions are used because they have hadronic interactions, and are a decay product of the D^0 which is an interesting charmed meson in this context (see also Chapter 6). At higher pseudorapidities (more forward regions), electrons are used instead of pions as the scattered electron is the main particle of investigation in those regions. The pseudorapidity range investigated is $-0.5 \leq \eta \leq 0.5$ for the central barrel studies (using pions), $\eta = 3$ for the silicon disk

studies, and $0 \leq \eta \leq 2.5$ for the simulations using both barrel and disks. The tested detector concepts are all symmetric around the interaction point, so the results for the forward region will be equally valid in the backward region (i.e. at negative pseudorapidities). The simulated momenta cover a range from 0 to 50 GeV/c. This range stems from the projected EIC physics case [16] and discussions with colleagues at the Lawrence Berkeley National Laboratory (LBNL). Particles with very low transverse momentum (below approximately 0.4 GeV/c) spiral in the magnetic field within the full-radius detector, which makes track reconstruction difficult. Measurements in this very low momentum region are thus frequently of poor quality.

All simulations contain the same beampipe configuration in the centre, made up of beryllium, with a radius of 18 mm and a thickness of 0.8 mm. The beryllium section is 800 mm long, and further out (i.e. at $|z| > 400$ mm) the beampipe is made of aluminium with a 20 mm radius and a thickness of 0.8 mm. This beampipe is based on the ALICE Long Shutdown 2 beampipe upgrade [29]. Outside the investigated silicon vertex tracker is a time projection chamber (TPC). This starts at a radial distance of 225 mm from the centre, and ends at a radial distance of 775 mm. The TPC has a length of 1960 mm along the beam axis, and is centred around the “interaction point” where the simulated particles are created. The TPC used in the simulations is the baseline TPC present in EICROOT. It has an intrinsic transverse resolution of 200 μm , and intrinsic longitudinal resolution of 500 μm . The charge dispersion, with the drift length D given in centimetres, is $15.0 \mu\text{m}/\sqrt{D}$ in the transverse direction and $1.0 \mu\text{m}/\sqrt{D}$ in the longitudinal direction.

Between the beampipe and the TPC the silicon vertex tracker is situated. This is the main detector part under investigation in the work presented here. The structure of layers in the tracker is based on the ALICE Inner Tracker upgrade design [29]. The innermost layers thus have a thickness of (in radiation lengths, see Section 2.1.2) 0.3% X_0 , and the outer layers 0.8% X_0 .

The starting point for the inner tracker geometry is the BeAST silicon vertex tracker. This tracker consists of four layers; two of the inner layer types for the ALICE upgrade, and two of the outer layer types. The positioning of these layers is modified from the standard BeAST layout to match the spacing of the upgraded ALICE inner tracking system [29]. This ensures that the layout is physically viable when support structures and services are included in the construction. A detector layer consists of several detector staves, each made up of a row of individual sensor chips. The staves contain a support structure for the chips, cables for powering them and reading them out, and a cooling system. The chips constitute the sensitive area of the detector, while the other staff parts only add inactive material. The individual detector staves in EICROOT are highly detailed, containing water cooling pipes, cooling plates, and support truss structures, based on the detailed layout of the ALICE inner tracking system upgrade staves. The inner layers have a length in the beam direction of 270 mm, and the outer layers have a length

of 840 mm. In the configuration used as a BeAST-based “standard” barrel, the innermost layer is placed at a radius of 23.4 mm (i.e. 23.4 mm from the centre of the beampipe, where the particles are created in the simulations), and consists of 12 staves of chips, tilted by 12 degrees to have an overlap to cover the full area. The second layer is at a radius of 46.8 mm, and consists of 24 staves. The third layer is of the ALICE outer cell type, with a thickness of $0.8\% X_0$. It is located at a radius of 87.6 mm, and consists of 10 staves. The outer cell staves are wider than the inner ones (twice as wide), and hence fewer staves are needed to cover the full area. The fourth and outermost layer consists of 16 staves, and resides at a radius of 133.8 mm. This leaves space for a time-stamping layer, located at a radius of 180.0 mm.

Where not otherwise stated, the time-stamping layer has a thickness twice that of an outer barrel layer, i.e. $1.6\% X_0$, and a pixel size matching the rest of the barrel. The increased thickness stems from that a higher time resolution may require a higher power to the chips in the layer. This means that the power cable size has to increase and that more cooling is needed to keep the layer operational, and the material thickness will thus increase. Larger pixels might also be needed to accommodate the circuitry required for the time-stamping, and to keep power density low. Results of investigations of different thicknesses and pixel sizes for the time-stamping layer are presented in Section 5.3.5.

In the forward and backward regions of the detector, silicon disks are placed. The disks are made up of the same kind of detector staves as the inner barrel layers, with varying stave lengths adjacent to each other to form an approximately circular shape. The first disk is frequently placed inside the outer barrel layers, and thus has to have a smaller radius than the other disks. The starting point is again the BeAST tracker, with seven disks each in the forward and backward regions. The disks are placed equidistantly at positions between 250 mm and 1210 mm from the interaction point. The layouts and positions of the disks for different studies are discussed in more detail in Sections 5.3.6 through 5.3.10.

Figure 5.1 shows a sketch of the simulated detector, with the different silicon vertex tracker barrel layer distances marked. A time-stamping layer is also present, as the outermost line in the barrel part of the sketch. A basic disk layout consisting of 7 disks in the forward region and 7 disks in the backward region is also shown in the sketch. It is however important to note that the inner holes of the disks are not shown, and neither is the beampipe. In Section 5.3.1 the radiation lengths of the different detector parts in the barrel region are shown as a function of pseudorapidity.

Simulations were first performed focusing on the silicon vertex tracker barrel. The region in the interface between the barrel and the silicon disks was later studied as well, and finally the possibility of an all-silicon tracker replacing the gas TPC was investigated. The results are presented below in that order, starting with radiation length scans.

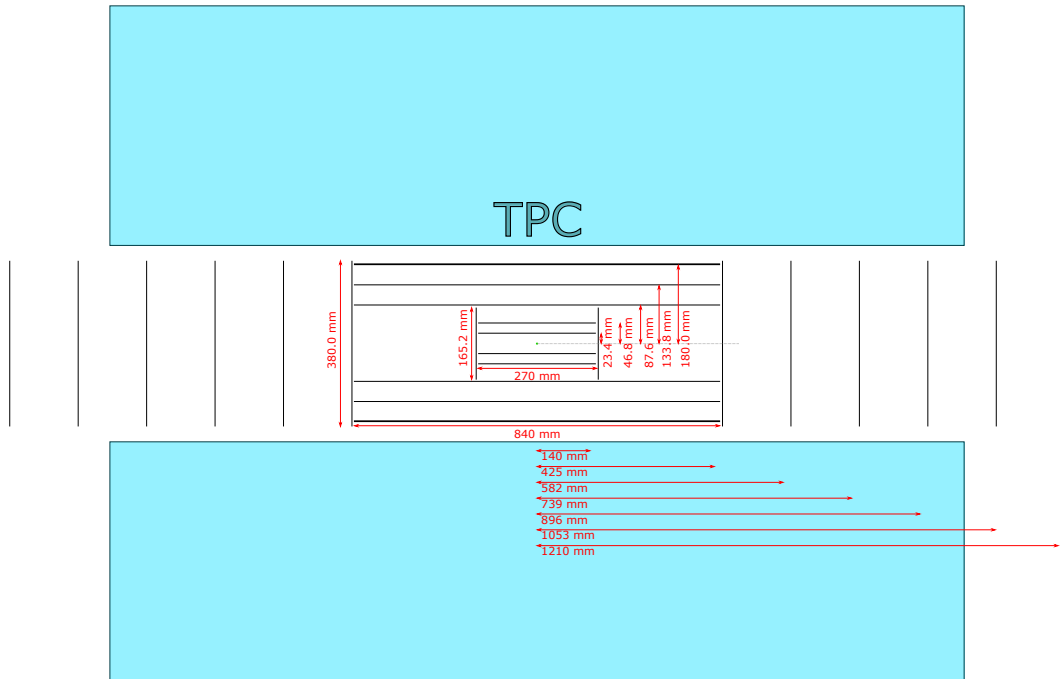


Figure 5.1: Sketch of a cross section along the beam direction of the “standard” simulated silicon vertex tracker barrel, with surrounding TPC and silicon disks. A beampipe runs through the centre of the detector, but is not included in the figure.

5.3 Results

The resolutions shown in the results are the relative momentum resolution and the transverse pointing resolution for the discussed detector variations. The longitudinal (beam direction) pointing resolution is also investigated, but its results often mimic those of the transverse pointing resolution, and the longitudinal pointing resolution plots are in those cases not presented.

5.3.1 Radiation length scan

Scans are performed to determine the radiation length of the different parts of the detector used in the simulations. The standard BeAST-like 4-layer barrel layout is used, with no disks present. The plots show the radiation length plotted versus the pseudorapidity η . The resulting plots for the standard barrel with beampipe and TPC, and the same with an added time-stamping layer $1.6\% X_0$ thick are shown in Figure 5.2. The contribution from the TPC is split into two parts; the TPC gas (labelled “TPC_TpcGas”), and the TPC inner field cage (labelled “TPC_TpcIfc”).

The different detector layers are clearly visible here, and the pseudorapidities at which they are no longer hit by a particle. There are some small irregularities present that likely stem from the tilt and non-uniformity of the individual staves, and their overlap.

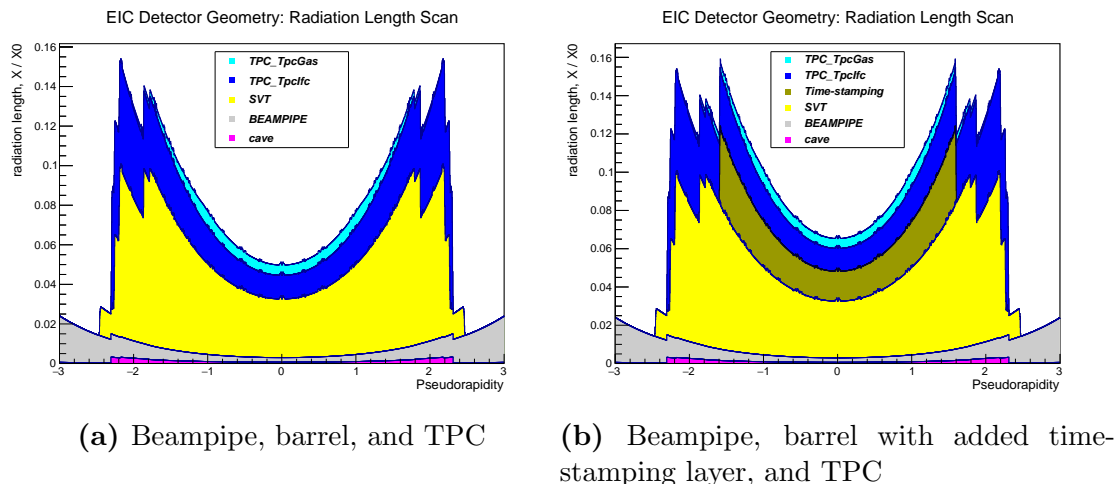


Figure 5.2: Radiation length scans for detector setups. The standard beampipe and TPC are in place in both scans.

5.3.2 Comparison no SVT/SVT+TPC

First of all, a study of the impact of having a silicon vertex tracker present is performed. The parameters for the simulations are shown below.

- Particle: π^+
- Transverse momentum range: 0 to 50 GeV/c
- Pseudorapidity range: $-0.5 \leq \eta \leq 0.5$
- Number of events: 100 000
- 5 layer barrel (two inner, two outer, one time-stamping layer)
- Magnetic field: 1.5 T

Pions are used as they are one of the main particles of interest for the open charm physics described in Chapter 3. They are also the lightest hadrons, and will thus have a large probability of being created in collisions and heavy particle decays at the EIC.

For the run with no silicon vertex tracker, the TPC inner radius is extended to cover the otherwise empty volume. The TPC in this case thus has an inner radius of 23.4 mm and an outer radius of 775.0 mm, compared to the regular inner radius of 225.0 mm. Figure 5.3 shows the resulting resolutions. It is clear from both the relative momentum resolution and the transverse pointing resolution that adding a silicon vertex tracker barrel has great benefits. Having only the TPC is better for the relative momentum resolution only at very low transverse momenta (below approximately 2 GeV/c), due to multiple scattering being dominant there (and thus the lower material budget of a gas TPC gives a better resolution). For the pointing resolution, not having a finely segmented innermost layer is clearly detrimental at all momenta.

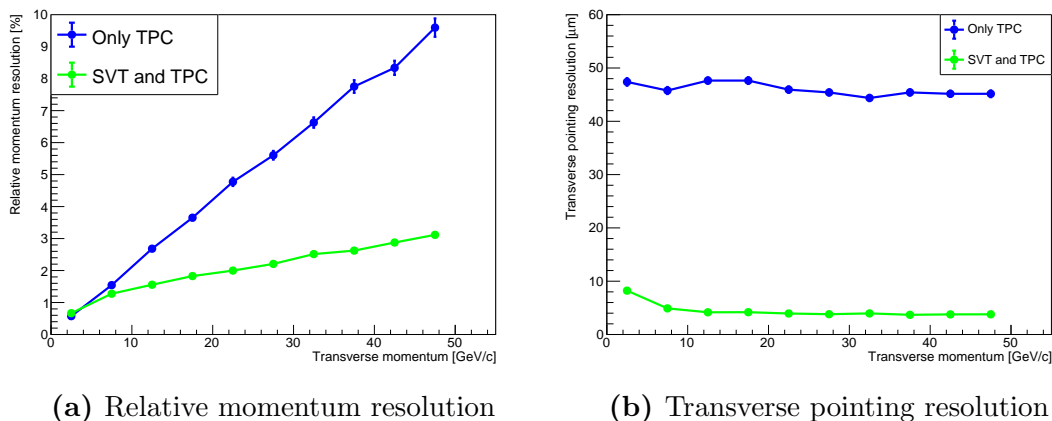


Figure 5.3: Relative momentum resolution and transverse pointing resolution, comparing having a standard barrel with a $20 \times 20 \mu\text{m}^2$ pixel size with a TPC outside, and just having a TPC extending all the way to the same innermost radius as the silicon barrel.

5.3.3 Barrel pixel size

To investigate the effect of pixel size in the barrel region on the resolutions, the parameters below are used for simulations;

- Particle: π^+
- Transverse momentum range: 0 to 5 GeV/c
- Pseudorapidity range: $-0.5 \leq \eta \leq 0.5$
- Number of events: 100 000
- 5 layer barrel (two inner, two outer, one time-stamping layer)
- Magnetic field: 1.5 T

Results of varying the pixel size are shown in Figure 5.4. The results for the pointing resolutions are in agreement with theory (see Equation 2.19); smaller pixel size improves the resolution. At the lowest momentum point the difference is small, due to the dominance of multiple scattering and the larger errors on the measurements at this point. Equation 2.21 indicates a linear dependence on pixel size for the relative momentum resolution. The equation is however derived for a detector layout with all layers having the same pixel size, whereas the simulated case has different resolution in the silicon layers and the TPC. The behaviour of the relative momentum resolution might thus not match the approximate theory, as the “pixel size” is not altered in the whole detector. The discrepancy with theory might also be due to the multiple scattering part of the relative momentum resolution dominating at the relatively low momenta used in this simulation, rather than the geometric part. Studies at higher momenta show that the expected pixel size dependence appears there. This can be seen in Figure 5.5, which shows the relative momentum resolution results for momenta between 0 and 50 GeV/c. The depen-

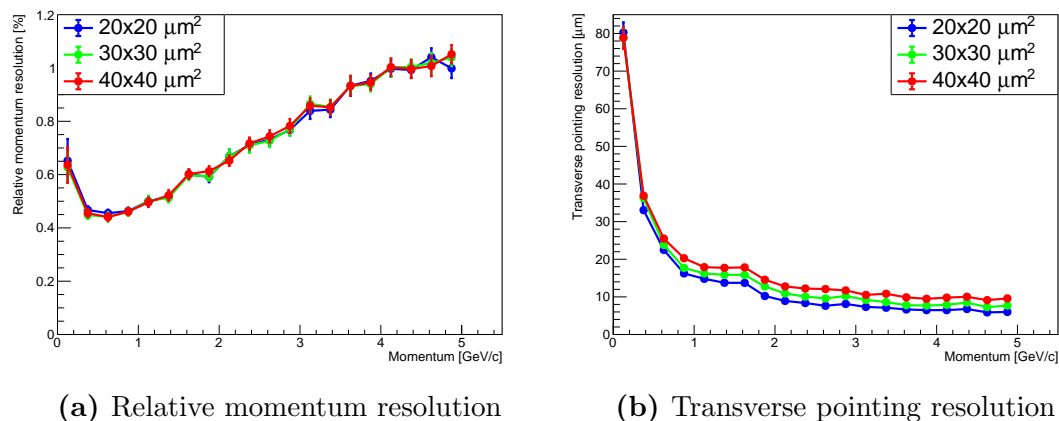


Figure 5.4: Relative momentum resolution and transverse pointing resolution for different pixel sizes in the silicon vertex tracker barrel.

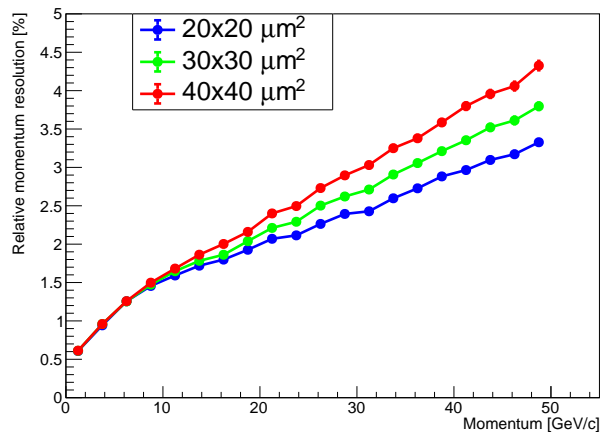


Figure 5.5: Relative momentum resolution for different pixel sizes in the silicon vertex tracker barrel, for momenta between 0 and 50 GeV/c.

dence thus starts becoming significant at momenta of approximately 10 GeV/c. The rise of relative momentum resolution at momenta below 0.4 GeV/c in Figure 5.4(a) stems from the inverse proportionality on particle velocity of multiple scattering which dominates here. The measurements at the lowest momenta are also of poor quality, and the error bars are relatively large. There is no visible rise of the relative momentum resolution at momenta below 0.4 GeV/c in Figure 5.5, due to the wider bins used.

5.3.4 Barrel layout studies

Figure 5.6 shows the relative momentum resolution and the transverse pointing resolution for different barrel layer layouts, in a transverse momentum range of 0 to 50 GeV/c. The pixel size for all layers is kept at $20 \times 20 \mu\text{m}^2$, and the innermost and outermost barrel layers are always present and unchanged while intermediate layers are added or removed. The parameters used in the simulations are:

- Particle: π^+
- Transverse momentum range: 0 to 5 GeV/c, and 0 to 50 GeV/c
- Pseudorapidity range: $-0.5 \leq \eta \leq 0.5$
- Number of events: 100 000
- Pixel size: $20 \times 20 \mu\text{m}^2$
- Magnetic field: 1.5 T

When present, the thickness of the time-stamping layer is $1.6\% X_0$, and its pixel size is $20 \times 20 \mu\text{m}^2$. A study of varying the thickness and pixel size of the time-stamping layer is presented in Section 5.3.5.

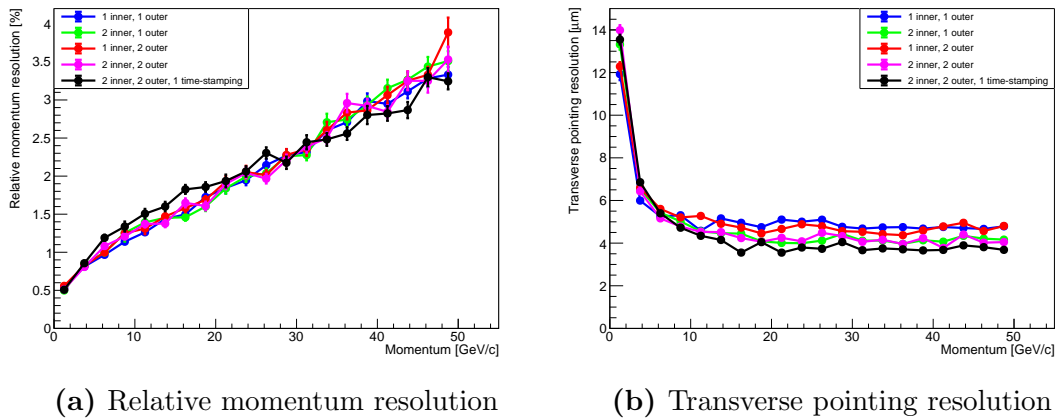


Figure 5.6: Relative momentum resolution and transverse pointing resolution for different silicon vertex tracker barrel layouts, for transverse momenta between 0 and 50 GeV/c. The number of layers is varied, with the innermost and outermost layers always the same and present.

Figure 5.7 shows results from the same simulation carried out at transverse momenta between 0 and 5 GeV/c (i.e. in a low transverse momentum region).

For the relative momentum resolution, there is no significant difference for the different layouts at most momenta, apart from when a time-stamping layer is present. The relative momentum resolution depends heavily on the lever arm of the detector, and since the outer and inner layers of the detector do not change, it is expected that the resolution will not be significantly altered. The standard TPC is also always present, keeping the maximum lever arm at a constant length. In Figure 5.7, it can be seen that after reaching a minimum the relative momentum resolution grows worse with increasing transverse momentum, which also corresponds to theory. At very low momenta, having two inner layers and only one outer layer seems to be the best (this is not seen in Figure 5.6, since the binning there is not as fine in the low momentum region). Multiple scattering dominates the resolution at low momenta, so removing material without changing the lever arm is expected to improve the resolution. The outer layers have a thickness of $0.8\% X_0$ while the inner layers have a thickness of $0.3\% X_0$, so removing an outer

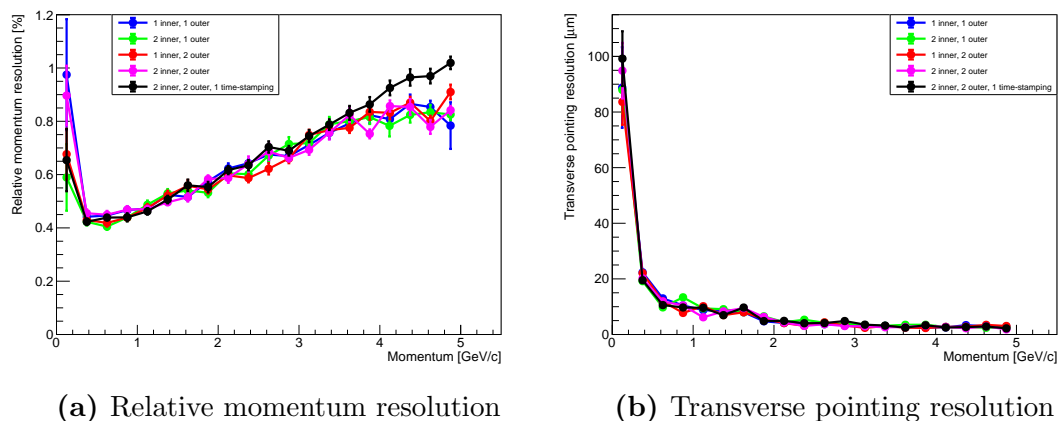


Figure 5.7: Relative momentum resolution and transverse pointing resolution for different silicon vertex tracker barrel layouts, for transverse momenta between 0 and 5 GeV/c.

layer removes a relatively large amount of material. The measurements in this very low momentum region are of poor quality however, as particles with very low transverse momentum (below approximately 0.4 GeV/c) spiral in the magnetic field within the detector. The errors are large within this region, and the difference between several of the layouts are within errors. No strong conclusion about the optimal layout can thus be drawn from these simulations at the lowest presented momentum point.

When the time-stamping layer is present, there is a significant deterioration of relative momentum resolution above 4 GeV/c. This likely stems from the added material of the layer; it is equivalent to the material two outer layers would add. At higher momenta, above 28 GeV/c, the addition of a time-stamping layer appears to slightly improve momentum resolution however. This possibly stems from the number of layers increasing (see Equation 2.21), an effect which becomes more important at higher momenta. It is however important to note that the difference in relative momentum resolution between all the tested layouts is small (at most of the order of 0.1%), and frequently within errors.

At low momenta (i.e. p_T less than 10 GeV/c), the transverse pointing resolution does not change significantly between the different geometries. This is in agreement with theory (see Equation 2.19), since the total lever arm does not change, nor the distance from the beampipe to the innermost layer. At low momenta, the layouts with the lowest material close to the beampipe (i.e. just one inner layer) have marginally the best pointing resolution. At higher momenta there is a separation between the layouts, with the one containing a time-stamping layer giving the best resolution. The reason for this separation is not obvious in the parametrisation presented in Section 2.2.2. The results in Figure 5.6 show that having two inner layers seems to be better than having one, regardless of whether there are one or two outer layers. There is possibly a dependence on the number of layers that does not show up in the theory derived from a two-layer case. There is also clearly in

the equations a dependence on the lever arm for a two-layer case, with a longer arm giving better resolution. This may explain why the layout containing the time-stamping layer has the best pointing resolution at high momenta. The gas TPC is always present, keeping the maximum lever arm constant. However, the TPC has a different resolution than the silicon layers, and the silicon lever arm may have an effect separate from the lever arm given by the gas TPC. Having two layers close to the interaction point likely aids in reducing errors in reconstruction by providing more data points, and thus increases the accuracy of the reconstructed vertex point.

Studies are also made looking at having the innermost layer inactive. This would be representative of a worst case scenario during operation. The results of the investigation show that there is little impact on relative momentum resolution apart from at very low momenta, but big losses in pointing resolution. An inactive innermost layer would be worse than not having the innermost layer at all, which is in agreement with theory as an inactive layer will increase multiple scattering without providing any information.

5.3.5 Time-stamping layer thickness and pixel size

Investigations are made concerning how adding a separate time-stamping layer would affect the detector performance. The standard 4-layer barrel is used, and the time-stamping layer is placed outside of it. The parameters below are used for the simulations.

- Particle: π^+
- Transverse momentum range: 0 to 5 GeV/c
- Pseudorapidity range: $-0.5 \leq \eta \leq 0.5$
- Number of events: 100 000
- Barrel pixel size: $20 \times 20 \mu\text{m}^2$
- Magnetic field: 1.5 T

Results for altering the time-stamping layer thickness (in terms of radiation length) are shown in Figure 5.8. For these studies, the time-stamping layer pixel size is kept at $20 \times 20 \mu\text{m}^2$.

For the time-stamping layer pixel size investigations, the thickness of the time-stamping layer is kept at $1.6\% X_0$. The resulting resolutions from this investigation are shown in Figure 5.9.

In all the plots, the black line stems from simulations done without a time-stamping layer, and the standard barrel with a $20 \times 20 \mu\text{m}^2$ pixel size. It can be seen that time-stamping layer pixel size has little to no significant impact on either of the resolutions. Adding a time-stamping layer makes both the relative momentum resolution and the transverse pointing resolution worse at very low momenta ($p_T \leq 0.4$ GeV/c). This is due to it adding a significant amount of material, at a thickness of $1.6\% X_0$. At high momenta, the relative momentum resolution is

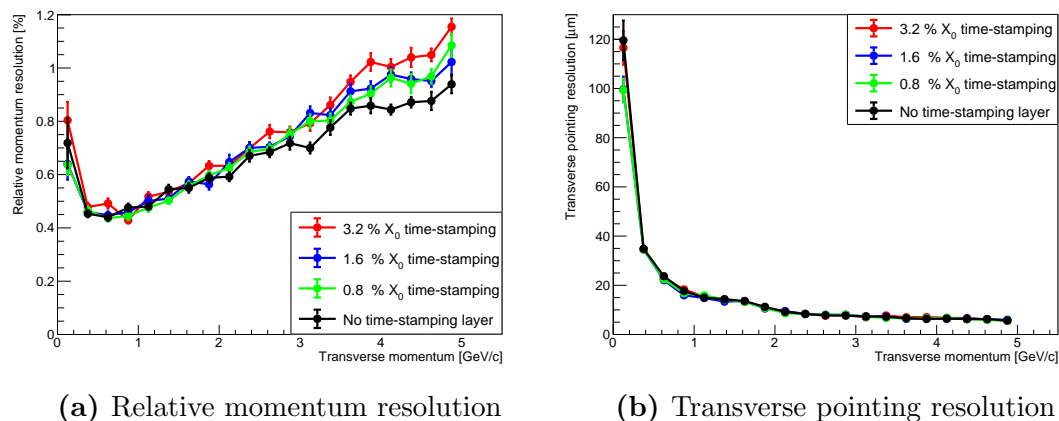


Figure 5.8: Relative momentum resolution and transverse pointing resolution for different time-stamping layer thicknesses.

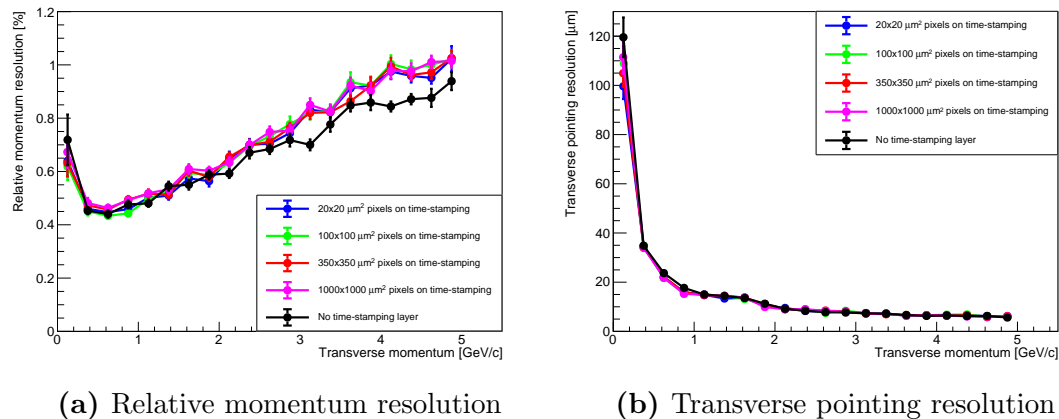


Figure 5.9: Relative momentum resolution and transverse pointing resolution for different time-stamping layer pixel sizes.

worse when a time-stamping layer is present. This likely stems from the increase in material, which is also indicated in the time-stamping layer thickness results; it is possible to see that a thinner time-stamping layer is better for the relative momentum resolution. There is however no significant difference between having a layer that is 0.8% X_0 thick and one that is 1.6% X_0 thick. For the transverse pointing resolution, the time-stamping layer thickness has no significant effect above very low momenta. It should once again be noted that the measurements at very low momenta are of a low quality, due to high multiple scattering effects and spiralling of particle tracks within the detector.

5.3.6 Disks, varying pixel sizes

A group at LBNL have focused mainly on the forward and backward regions of the inner tracking detector [120]. In a collaboration with this group, silicon disks are included in the forward and backward regions of the detector in the simulations.

As the detector is symmetric around the interaction point at this stage, the layout in both regions will be the same. This will likely change in the future as the detailed physics requirements in both regions becomes more clear, but it is a good approximation for these initial comparative simulations.

First of all, the resolutions are investigated in the forward region for different pixel sizes in the disks. The disks are made up of the same material as the inner barrel layers, with a thickness of $0.3\% X_0$. They are placed equidistantly between 250 mm (in the beam direction) and 1210 mm from the interaction point. These distances are based on the results of a preliminary study carried out by collaborators at LBNL, showing that this is a reasonable geometry for matching the silicon vertex tracker requirements available at the time [121].

The innermost disk is shrunk to have an outer radius of 82.6 mm, so that it fits within the outer barrel layers (with a 5 mm margin). The opening in the disk centred around the beampipe is square, with a side of 36 mm for the innermost disk, and 40 mm for the other disks. The square shape comes from that the disks are made up of individual staves, making a round shape difficult to form. The staves can be staggered slightly to mitigate this effect, but the hole cannot be made circular.

In the forward region, the main purpose for a deep inelastic scattering experiment is to detect the scattered electron. Hence electrons are used for these studies involving disks, rather than the pions used previously. It is also preferable to reconstruct the total momentum rather than the transverse momentum of the electron to be able to reconstruct the kinematic variables of an event, and hence the total momentum resolution is used in these studies. A uniform momentum distribution is also generated, rather than a uniform transverse momentum distribution.

For the studies of different pixel sizes in the forward region, the following parameters are used:

- Particle: e^-
- Momentum range: 0 to 50 GeV/c (uniform in p)
- Pseudorapidity: $\eta = 3$
- Number of events: 500 000
- Magnetic field: 1.5 T and 3 T

Since the pseudorapidity used is so high, there is no reason to have a silicon barrel or a TPC present in the simulations, as they will never be hit. This also means that the simulations are more light-weight, meaning a higher number of events can be simulated easily. Simulations are performed for magnetic fields of 1.5 T and 3 T. Figure 5.10 show the results for seven disks in a field of 1.5 T, and Figure 5.11 show the results for a field of 3 T.

The results once again show that a smaller pixel size improves all the resolutions, which is expected from theory. Since the momentum range is higher, there is more of a spread in the relative momentum resolution, as the geometric part of the

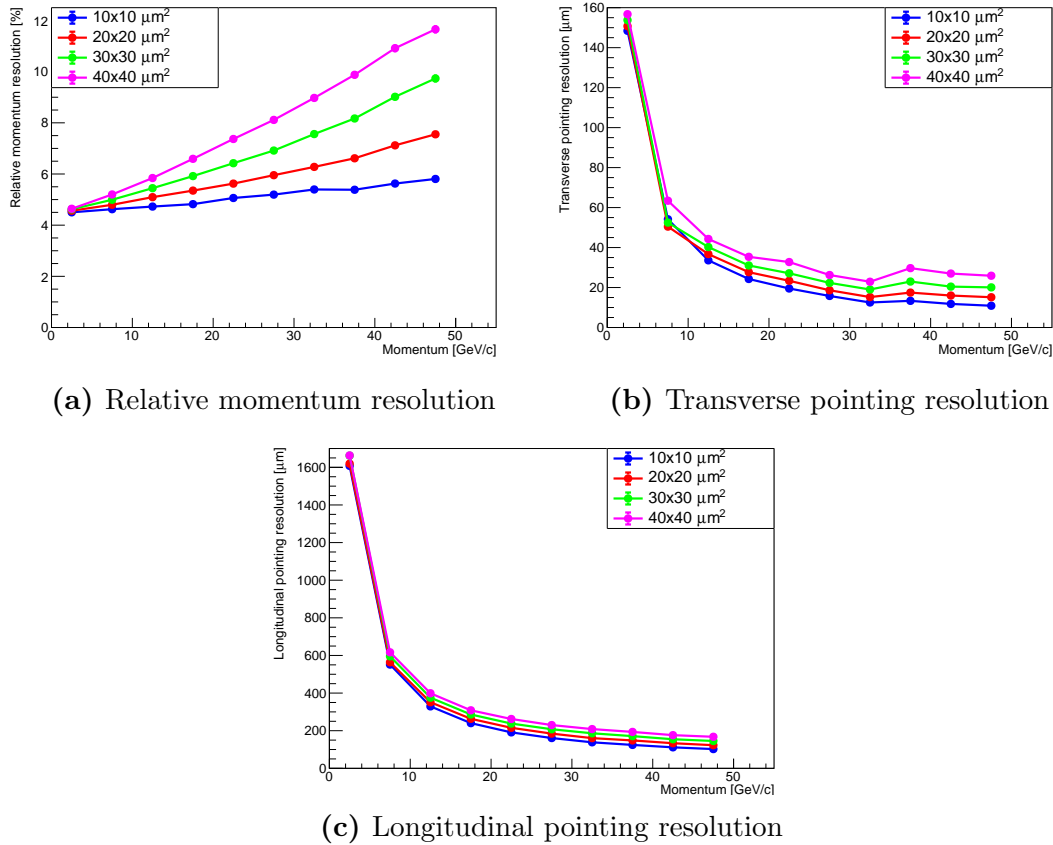


Figure 5.10: Relative momentum resolution and pointing resolutions for disk pixel size investigations. The results are from a 7 disk setup equidistant between 250 mm and 1210 mm from the centre point, in a magnetic field of 1.5 T.

theory dominates at higher momenta and this part is proportional to the pixel size (see Equation 2.21).

Comparing the results for the different magnetic field strengths, there is once again a close match with theory. The relative momentum resolution is inversely proportional to the magnetic field strength, and a factor of 2 difference can be seen in relative momentum resolution for the simulations. The pointing resolutions are largely unaffected by changing the magnetic field, again in agreement with theory.

The same simulation is also done for a setup with five disks, instead of seven. These simulations use the same parameters as before, but are only run for a magnetic field of 3 T. The five disks are placed equidistantly with the first one 250 mm from the centre point and the last one 1210 mm from the centre point. The results are shown in Figure 5.12.

These results are best compared to Figure 5.11, which is the 7 disk layout with a 3 T magnetic field. The relative momentum resolution plot contains a dashed line for the 7 disk layout with a $10 \times 10 \mu\text{m}^2$ pixel size to make this comparison easier. The difference between the two configurations is a near-constant offset of

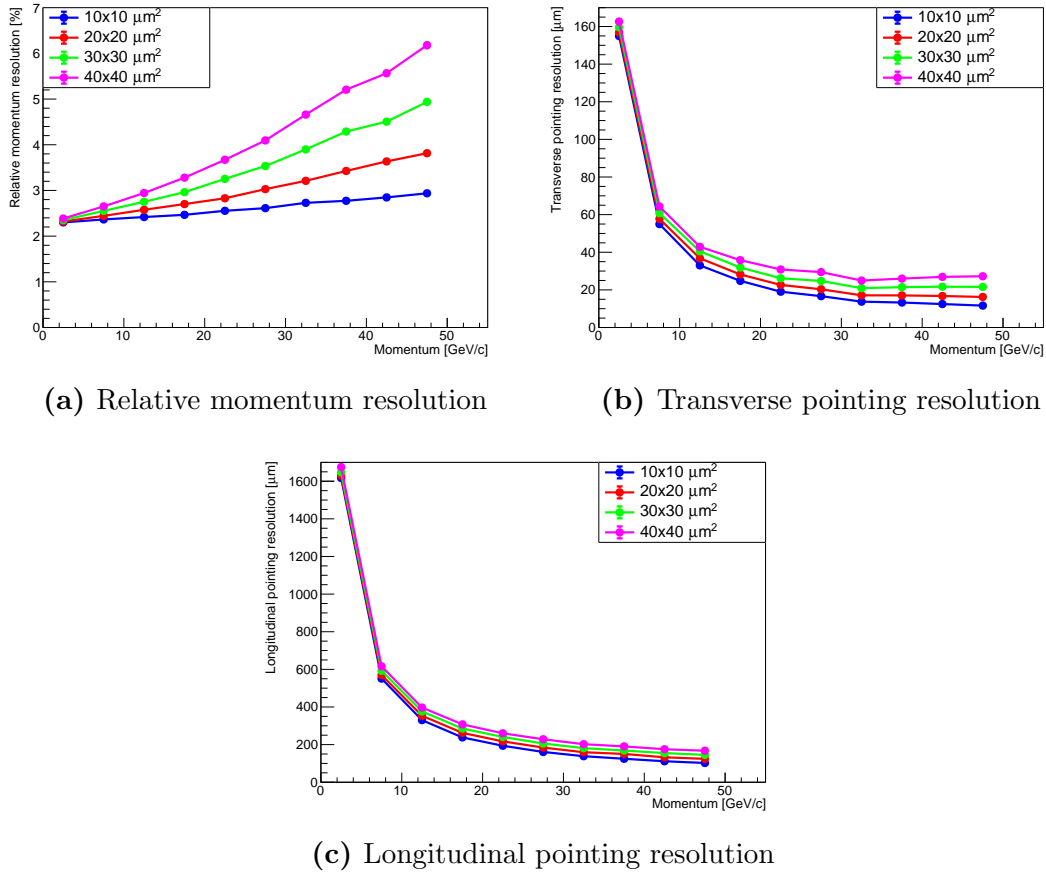


Figure 5.11: Relative momentum resolution and pointing resolutions for disk pixel size investigations. The results are from a 7 disk setup equidistant between 250 mm and 1210 mm from the centre point, at $\eta = 3$, in a magnetic field of 3 T.

approximately 0.2%. The relative momentum resolution for the 5 disk layout is slightly better, due to the decrease in material. The pointing resolutions show little to no change. This agrees with theory, where the innermost layer is most important for pointing resolution, and the length of the lever arm is the most important for momentum resolution. Neither of those two main parameters change between having 5 or 7 disks.

The question of whether to use 5 or 7 disks also becomes a question of detector coverage and redundancy, however. Particles may miss some of the disks, or not have hits registered in them due to local inefficiencies or inactive pixels. The number of disks to use will thus be a balance of keeping tracking performance, while having as little material as possible in the way of the particle.

5.3.7 Innermost disk position

Using seven disks, simulations are made testing the effect of changing the innermost disk position. The innermost disk is placed at different distances from the centre point, whereas the outer 6 disks are kept in the same positions as in the previously

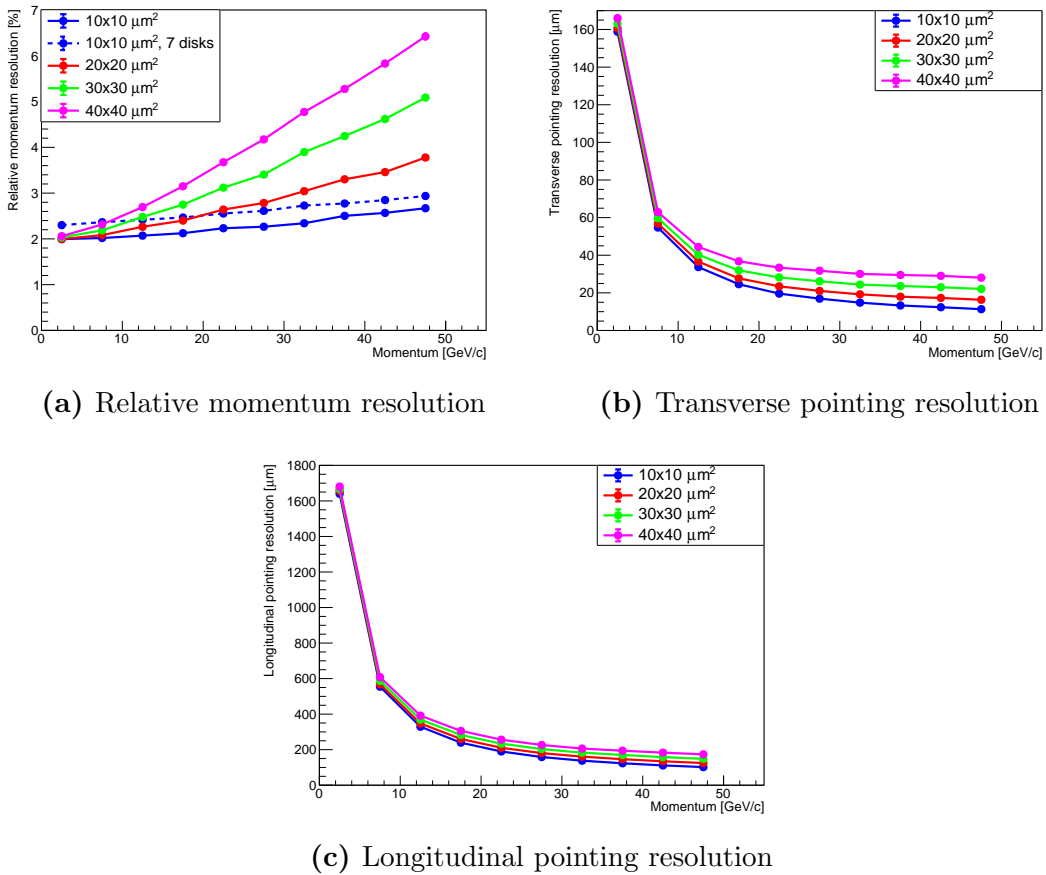


Figure 5.12: Relative momentum resolution and pointing resolutions with a 3 T magnetic field, for 5 disks equally spaced between 250.0 mm and 1210.0 mm from centre point. The relative momentum resolution plot shows a dashed line for the 7 disk layout (as presented in Figure 5.11) for comparison.

described pixel size studies; i.e. equally spaced between 410 mm and 1210 mm from the centre point. Simulations are run for innermost disk distances from the centre point of 140 mm (5 mm from the inner barrel layers), 195 mm, 225 mm, 240 mm, 250 mm (which is the standard position, used in the pixel size studies), 275 mm, and 305 mm. The simulation parameters used are shown below.

- Particle: e^-
- Momentum range: 0 to 50 GeV/c (uniform in p)
- Pseudorapidity: $\eta = 3$
- No barrel and no TPC present
- Number of events: 500 000
- Pixel size: $20 \times 20 \mu\text{m}^2$
- Magnetic field: 3 T

The results of the simulations are shown in Figure 5.13.

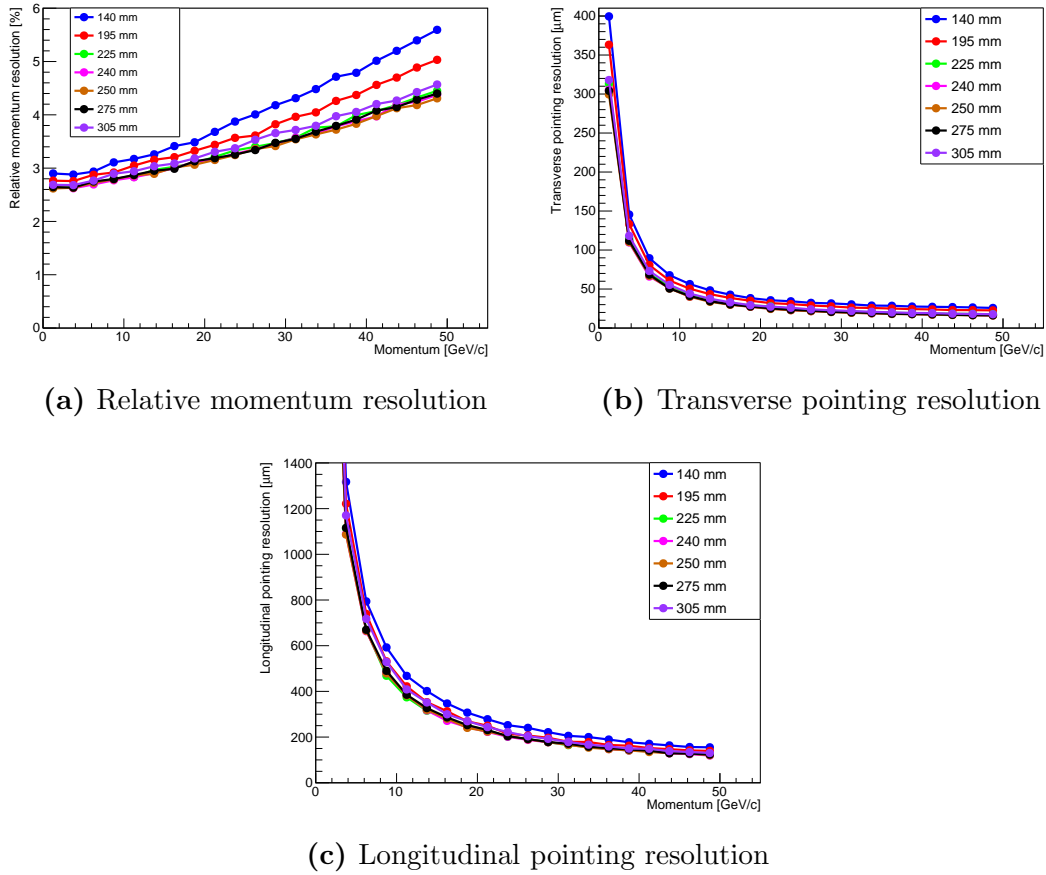


Figure 5.13: Relative momentum resolution and pointing resolutions for a 7 disk layout, with varying innermost disk positions.

At first glance, the results seem to indicate a discrepancy with theory. The shortest distance (140 mm) appears to be the worst one, whereas theory suggests that having the innermost layer closer to the interaction point ought to make it better. However, looking at how the disks are produced in simulations in conjunction with the disk positioning, this appears to be an effect of the disk inner radius. Table 5.1 shows the pseudorapidity for the inner radius edge for a selection of disk positions.

Disk position	η of inner radius
140 mm	2.75
195 mm	3.01
250 mm	3.33
305 mm	3.52

Table 5.1: Pseudorapidity location of the innermost disk inner radius, for different disk positions.

From this table, it can be seen that for a disk position of 140 mm, a particle with pseudorapidity 3 will completely pass through the hole in the centre of the disk. This explains why a disk position of 140 mm gives the worst pointing resolution in

this instance; it completely removes the innermost disk as an active detector part for the simulated particles.

For a disk position of 195 mm the particles should always just hit the disk. Disks will however be built up of staggered rectangular staves of silicon, so the inner holes will thus not be completely circular, and the simulations reflect this. This means that the particles with pseudorapidity 3 will hit the innermost disk when they emerge with certain azimuthal angles, and not with others. As the full results of the simulations make up an average of all simulated events, and the particle distribution is uniform in the azimuthal angle, this shows up as a worse average resolution than what would be expected if the innermost disk were always hit.

When the disk is hit, there are also some trends that can be observed. As the disk moves further away from the centre point the lever arm decreases, which deteriorates the relative momentum resolution. The first detector hit is also further away from the interaction point, deteriorating the spatial resolutions.

In conclusion, an innermost disk position of 250 mm from the centre appears best for momentum resolution at higher momenta. The difference is small between the positions where the disk is fully hit and close to the centre, however. As the disk moves further out, a deterioration can be seen. It is however worth reiterating that this is for the special case of $\eta = 3$. If the innermost disk is hit, theory indicates that having it closer to the centre would improve the resolutions, so at lower pseudorapidities a position closer to the interaction point is expected to be better. The disk should thus be placed as close as possible to the inner barrel layers.

5.3.8 Different inner barrel length, with disks

To study the impact of changing the interface region between barrel and disks, simulations are run in a range of pseudorapidities encompassing both. For these simulations the baseline used is the standard barrel with 7 disks and no time-stamping layer. The innermost disk is always placed 5 mm from the inner barrel edge (i.e. as close as possible to the interaction point, 140 mm from the centre), and the next disk is placed 5 mm outside the outer barrel edge (425 mm from the centre point). The remaining disks are placed equidistantly up to a distance of 1210 mm from the centre point. A simulation run is also made without disks. All simulation runs have the same beampipe and TPC. The parameters used in the simulations are shown below.

- Particle: e^-
- Momentum range: 0 to 50 GeV/c (uniform in p)
- Pseudorapidity range: $0 \leq \eta \leq 2.5$
- Number of events: 100 000
- Pixel size: $20 \times 20 \mu\text{m}^2$
- Magnetic field: 1.5 T

The length of the inner barrel is adjusted, moving the inner disk accordingly. Figure 5.14 shows a sketch of the situation where the inner barrel is 270 mm long. The results of this investigation, with resolutions plotted versus the momentum,

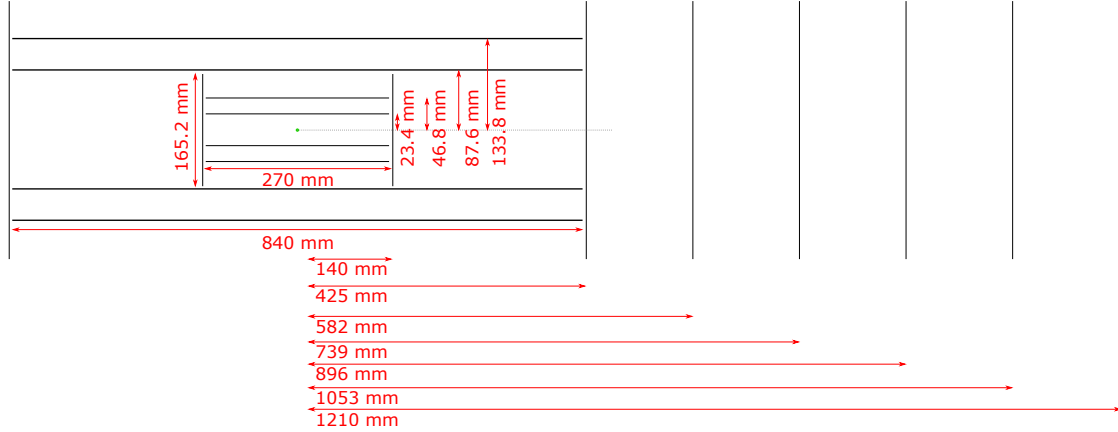


Figure 5.14: Sketch of the layout of the detector, including disks. The inner barrel length is adjusted, and the innermost disk moves accordingly. The green dot indicates the centre point.

are shown in Figure 5.15. In Figure 5.16, the resolutions plotted versus the pseudorapidity are shown.

From Figure 5.15 it can be seen that in this situation, both the relative momentum resolution and the pointing resolutions are largely unaffected by the length of the inner barrel layers, for different values of the momentum p .

The insensitivity to the changes likely stems from the averaging over the investigated pseudorapidity range. For a given momentum, different events will have hit different regions of the detector. Some will thus be strongly affected by the placement of the disks and extent of the layers, whereas some will only be sensitive to the radii the barrel layers are placed at. In plots versus momentum, this will not show up explicitly other than as a small change of the full average resolution.

Figure 5.16 shows the same simulation results, plotted versus the pseudorapidity. Figure 5.17 shows a sketch of the detector with an inner barrel length of 270 mm, with pseudorapidity edges marked. The pseudorapidity coverage for the inner barrel layers and the first disk will change for shorter or longer inner barrels.

In the plots of resolutions versus pseudorapidity the effect of changing the layer length is clear. Looking first at the relative momentum resolution, it can be seen that it begins to deteriorate as the track length in the TPC gets shorter. The outer radius of the TPC is missed at $\eta \geq 1.06$, which is where the curves start to turn upwards. This deterioration of resolution can be explained with the number of hit points along the track decreasing as the full radius of the TPC is not utilised. At large pseudorapidities ($\eta \geq 2.1$) the resolution improves however, as the lever arm increases when more disks are hit. In the simulation containing no disks (the

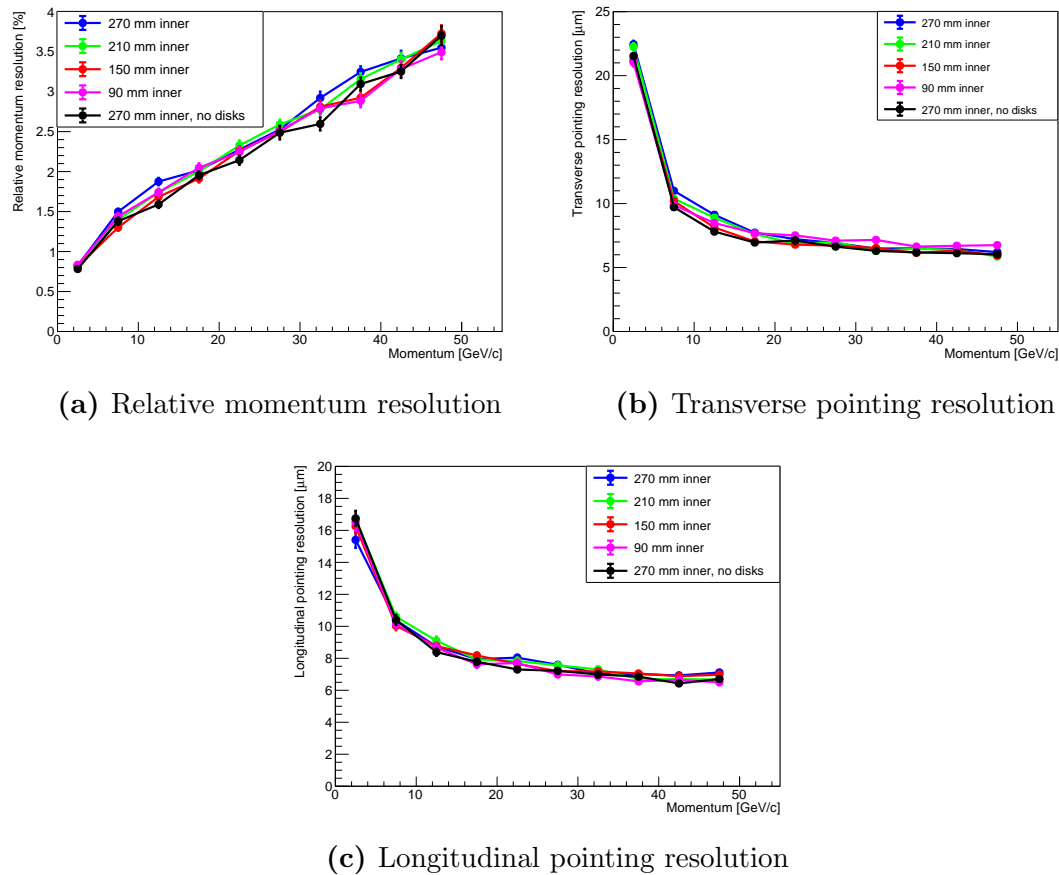


Figure 5.15: Relative momentum resolution and pointing resolutions versus momentum for different lengths of the inner barrel layers.

black points and line) no parts of the detector are hit after a point, cutting the graph off.

In the pointing resolutions, there is a very clear deterioration as layers are missed. The big jump happens when the innermost layer is no longer hit, which makes sense as the innermost layer position is the main variable affecting the pointing resolution. For the 90 mm long inner layer particles also travel through the inner hole of the innermost disk at pseudorapidities larger than 1.65, and for the 150 mm long inner layer this happens at pseudorapidities larger than 2.13, thus missing the first disk as well as the innermost layer. When the disks are not present and the TPC is no longer hit, there are no more data points when the innermost layer is the only one hit as that is not enough for reconstruction.

5.3.9 Different parameters on outermost disks

It can be of interest in the disk region to have different material thickness and/or pixel size on one of the disks, in order to either reduce cost or introduce additional functionality, such as precision time-stamping. A study is therefore made to investigate the impact of changing the pixel size and material thickness of the

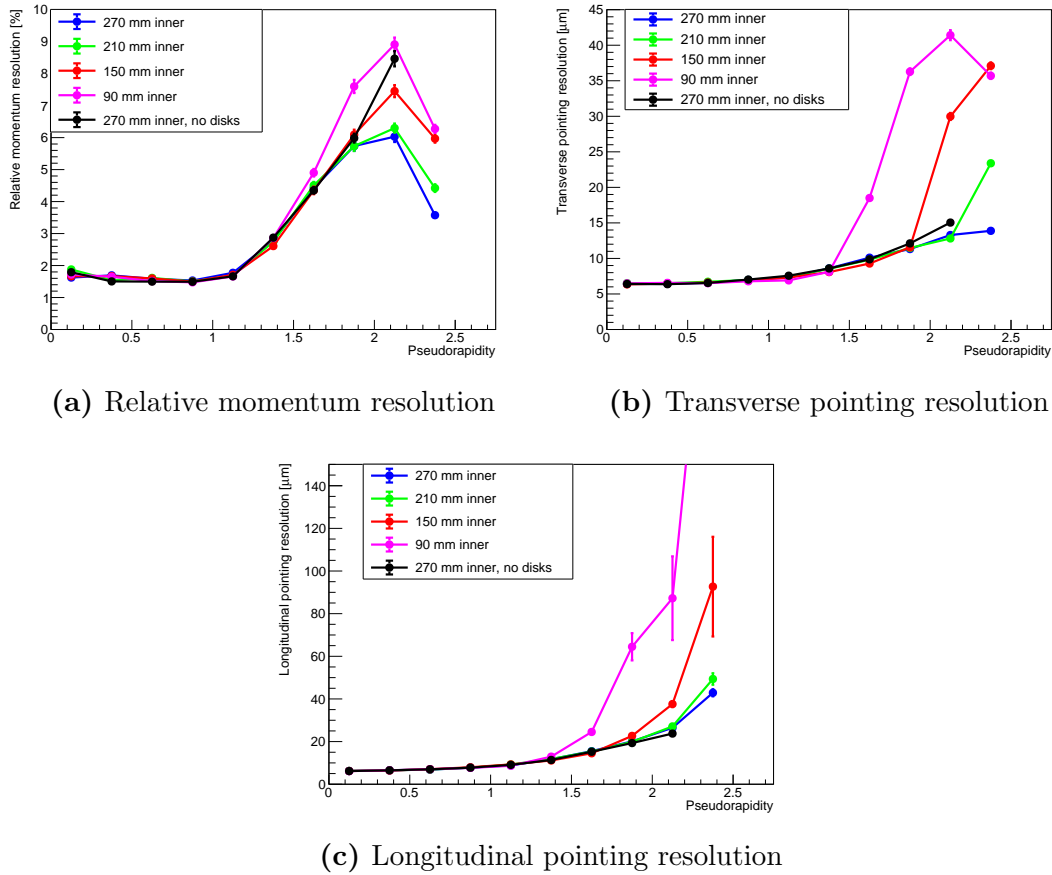


Figure 5.16: Relative momentum resolution and pointing resolutions versus pseudorapidity for different lengths of the inner barrel layers.

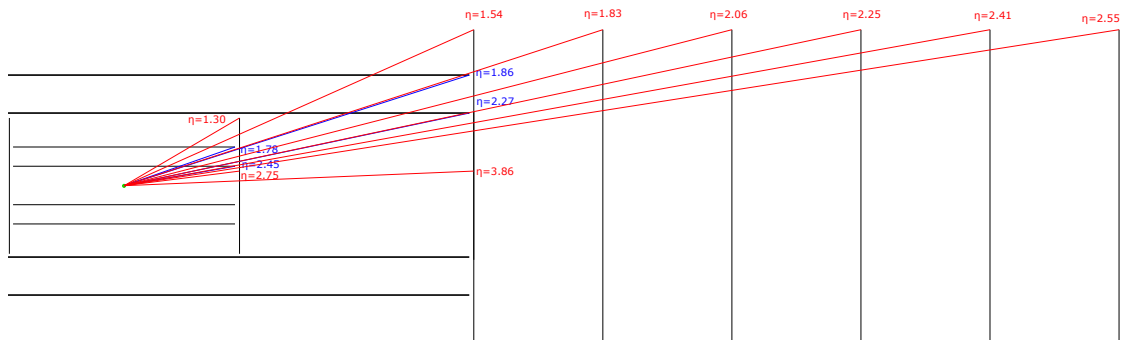


Figure 5.17: Detector sketch with pseudorapidity edges for different parts marked. Disk edges are marked in red, and barrel layer edges in blue. The sketch is for an inner barrel length of 270 mm.

final or the penultimate disk. It is desirable to have detectors with low material and high granularity near the interaction point in order to have a high tracking performance, and a possible time-stamping layer is thus best placed further away. As there is no tracking detector behind the final disk however, deterioration of the resolution in this “outer anchor point” of the reconstructed track may have a

significant negative impact on the full resolutions. Alteration of the penultimate disk while keeping the pixel size and material of the final disk low is therefore also investigated.

The simulations are preformed at $\eta = 3$, which means that the barrel layers and the TPC will never be directly hit. These detector parts are thus excluded from the simulations, to make them more light-weight and thus make it possible to use more events in the study. The disks are placed as in Section 5.3.8 with a 270 mm long inner barrel; the innermost disk is placed at 140 mm from the interaction point, and the remaining six disks are placed equidistantly between distances of 425.0 mm and 1210.0 mm from the interaction point. All simulations have the same beampipe. The parameters used for this study are shown below.

- Particle: e^-
- Momentum range: 0 to 50 GeV/c (uniform in p)
- Pseudorapidity: $\eta = 3$
- No barrel and no TPC present
- Number of events: 500 000
- Magnetic field: 1.5 T

The standard pixel size used is $20 \times 20 \mu\text{m}^2$, and the material thickness is $0.3\% X_0$. These two parameters are altered for the final and the penultimate disk, and the impact on resolutions studied.

Figure 5.18 shows the relative momentum resolution and transverse and longitudinal pointing resolutions when altering the pixel size and thickness of the final disk. The resulting resolutions for completely removing the final disk are also shown.

Since the transverse pointing resolution only differs at momenta larger than approximately 10 GeV/c, a plot is shown with this area of resolution zoomed in, to clearly show the present separation. The longitudinal pointing resolution has no significant difference between the variations, and a zoomed in view is thus not shown.

From both the relative momentum resolution plot and the transverse pointing resolution plot, it can be seen that the thickness of the final disk can be increased from $0.3\% X_0$ to $1.6\% X_0$ without any severe negative impact on the resolutions. Increasing the pixel size has a large negative impact, however, regardless of the thickness of the disk. If the pixel size is increased from the default $20 \times 20 \mu\text{m}^2$ to $100 \times 100 \mu\text{m}^2$, the resolutions are equally poor to not having the final disk in place at all, and using a shorter six disk layout. This strongly indicates that it is crucial to maintain high spatial resolution in the final data point used for tracking. This makes sense, as it is the first point used in the Kalman filter reconstruction (tracking from the outside towards the vertex position), and a high resolution here thus immediately constrains the track position well, reducing uncertainties. The material thickness can however be increased by a factor of five without a

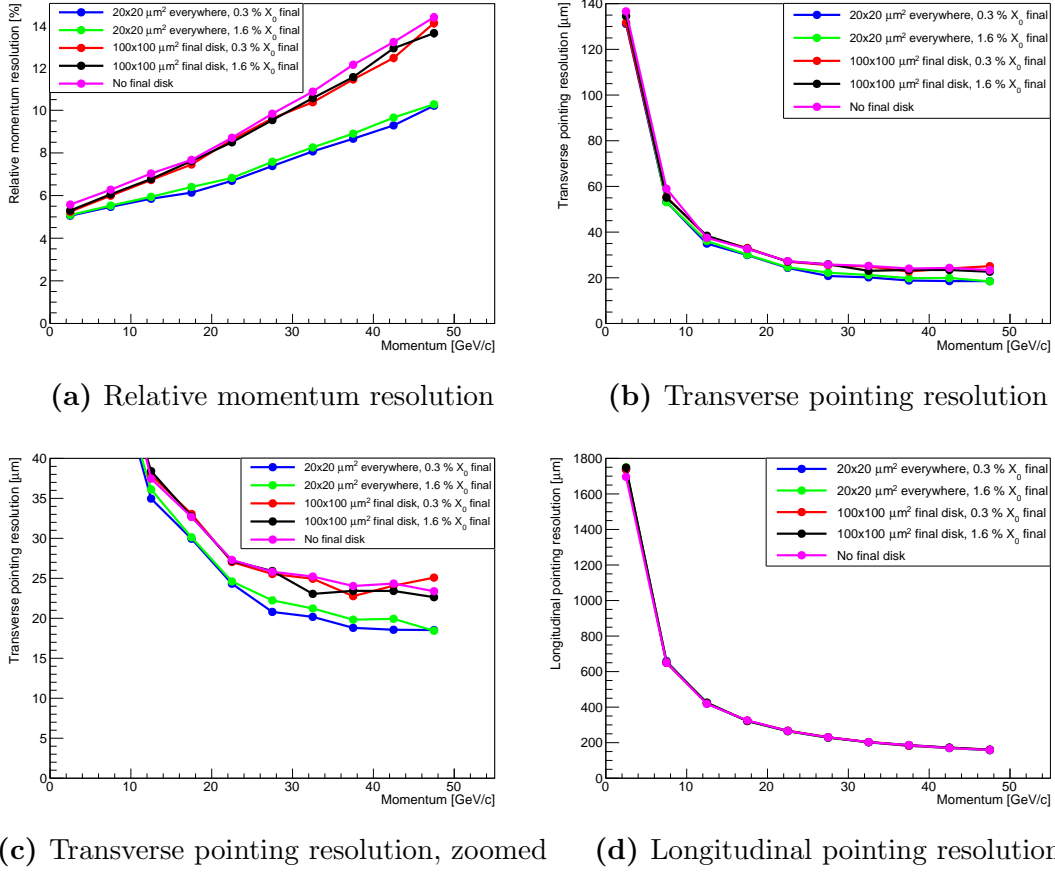
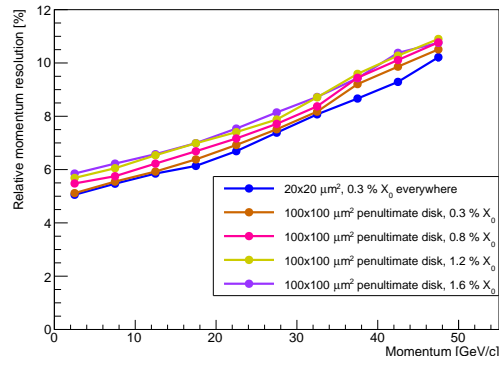


Figure 5.18: Relative momentum resolution and pointing resolutions versus momentum, for variations of the pixel size and material thickness of the outermost disk. The resolutions when no final disk is present (i.e. only six disks are used) are also shown.

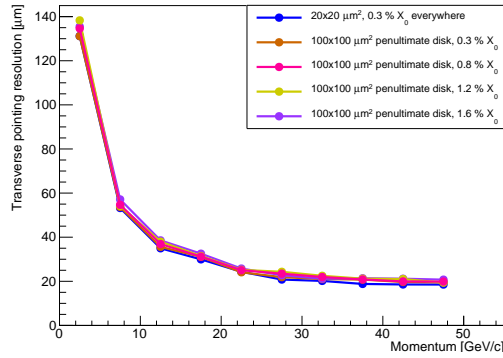
severely detrimental effect on the resolutions. The negative effect of increasing the pixel size does not appear in the barrel time-stamping layer study presented in Section 5.3.5, most likely due to that the TPC aids in tracking there, outside of the time-stamping layer. In the case of the disks, there are no further tracking detectors beyond the final disk.

Figure 5.19 shows the resulting relative momentum resolution and pointing resolutions when altering the pixel size and material thickness of the penultimate disk, while the final disk is kept at the default thickness and pixel size. Several material thicknesses are investigated here, for a constant pixel size of $100 \times 100 \mu\text{m}^2$.

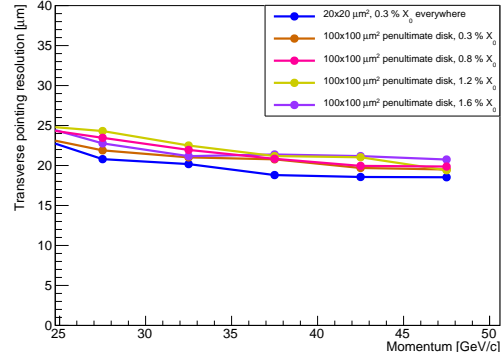
Looking at the zoomed in plots of the pointing resolutions in both the transverse and the longitudinal direction, it can be seen that there is little difference when varying the thicknesses. It is however always better to keep the pixel size as low as possible. The standard configuration with $20 \times 20 \mu\text{m}^2$ pixel size outperforms the $100 \times 100 \mu\text{m}^2$ pixel size layout. In the transverse direction the difference in resolution is up to $2 \mu\text{m}$ when comparing the standard disk layout to having the penultimate disk 1.6% X_0 thick with $100 \times 100 \mu\text{m}^2$ pixel size. In the longitudinal direction, the difference is up to $10 \mu\text{m}$.



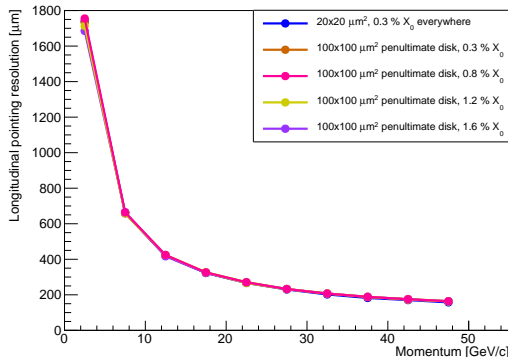
(a) Relative momentum resolution



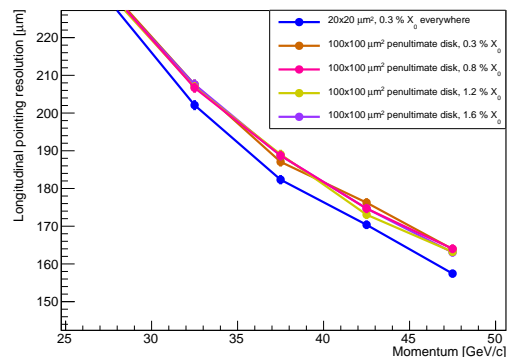
(b) Transverse pointing resolution



(c) Transverse pointing resolution, zoomed



(d) Longitudinal pointing resolution



(e) Long. pointing resolution, zoomed

Figure 5.19: Relative momentum resolution and pointing resolutions versus momentum, for variations of the pixel size and material thickness of the penultimate disk.

For the relative momentum resolution, there is a clear trend of deterioration as the thickness of the penultimate disk increases. The difference is however not larger than 1%, and approximately constant across the whole momentum interval. This can be compared to enlarging the pixels in the final disk, which leads to a larger deterioration as momentum increases. It is however clear that the combination of larger pixel size and thicker material is detrimental to the resolutions, and that it is thus important to keep the material thickness down if larger pixels are used in the penultimate disk.

5.3.10 Replacing gas TPC with silicon layers and disks

5.3.10.1 Different silicon layouts

In order to investigate the possibilities and potential benefits of an all-silicon tracker, simulations are made where the gas TPC is replaced with layers of silicon. Different layouts of this silicon replacement are tested, and results from the best basic layouts are combined into a final feasible design. In the simulations, the silicon vertex tracker barrel remains the same; the standard 4-layer barrel, with an added time-stamping layer. Seven disks are present in the forward region, at positions in z (along the beam axis) of 140.0 mm, 425.0 mm, 582.0 mm, 739.0 mm, 896.0 mm, 1053.0 mm, and 1210.0 mm. The radii of the disks are varied in the different layouts. The simulation parameters used are shown below. In the text that follows, the different layout names as presented in the resolution plots will be written in italics in parentheses. All layouts are shown as cross section sketches in Appendix B.

- Particle: e^-
- Momentum range: 0 to 50 GeV/c (uniform in p)
- $0 \leq \eta \leq 2.5$
- Number of events: 100 000
- Pixel size: $20 \times 20 \mu\text{m}^2$
- Magnetic field: 1.5 T

Electrons are used, as both the barrel and the disk regions are investigated and the scattered electron can end up in a large range of pseudorapidities [16]. The pseudorapidity range is selected as it incorporates both hits in all barrel layers and in all disks in the different layouts. First of all a reference run is made using the standard TPC (*With gas TPC*) with the regular basic disks. This is the layout shown in Figure 5.1. The first gas TPC replacement layout investigated keeps the standard disks, and replaces the gas TPC with four silicon layers (*2+2 layers, long*) with a thickness of $0.8\% X_0$ each and a length of 1960 mm, which is the same length as the gas TPC. The first silicon layer is placed at a radius of 225.0 mm, which is the same as the innermost TPC radius. The second layer is placed as closely as possible to this, 46.2 mm further out (i.e. at a radius of 271.2 mm). Having two layers close together will help in finding the direction a particle travels, if it hits both layers. The final two layers in this layout are placed at radii of 728.8 mm and 775.0 mm, which is the gas TPC outer radius. A sketch of the layout can be seen in Figure 5.20. Detector staves this long may in reality require a slightly higher material thickness, but $0.8\% X_0$ is used as an approximation in the simulations.

Tests are also done with a smaller radius replacement (*2 layers, long, small radius*), where the gas TPC is replaced by two silicon layers, at radii of 383.8 mm and 430.0 mm, and lengths of 1960 mm. This layout keeps the standard disks with their normal radii. A layout with shorter layers (840.0 mm long) is also tested at

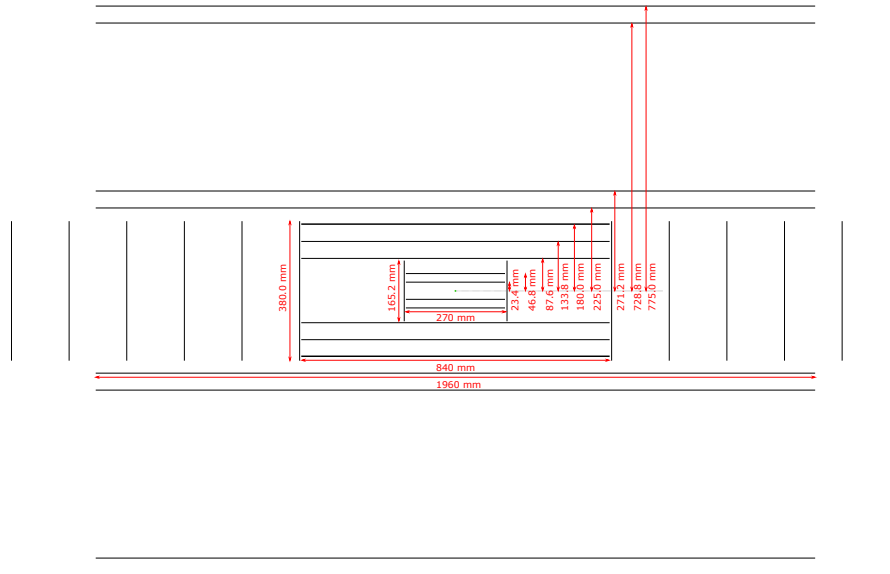


Figure 5.20: Sketch of the simulated layout with standard disks, where the gas TPC is replaced by two inner and two outer silicon layers (*2+2 layers, long*).

this radius (*2 layers, short, small radius; large disks*). This layout has enlarged disks, with a radius of 430.0 mm. The innermost disk radius is always kept the same, in order to fit inside the outer barrel layers.

Studies of the layouts with a smaller radius shows that larger disks improve momentum resolution in the investigated parameter space. More studies are therefore made with shorter layers (840.0 mm, the same length as the barrel outer layers) and larger disks. The full radius of 775.0 mm is used for the barrel region, and five silicon layers are used to replace the gas TPC. The layers are placed equidistantly between 225.0 mm and 775.0 mm. Five layers are used as a balance of tracking capability (which increases with number of detector hits) and material thickness. A study was made comparing the resolutions resulting from using two layers instead of five, and no significant deterioration was found from using five layers. Tests are made with enlarged disks, with a radius of 420.0 mm (*5 layers, short; large disks*), and an optimised disk layout. The radius of 420.0 mm is used as that will give a maximum length across the disk of 840.0 mm; the same length as an outer barrel layer. The optimised disk layout is a combination of smaller disks and larger rings, combining the best-performing elements while keeping a realistic configuration (*5 layers, short; optimised disks*). The sizes of the disks and rings can be trimmed to give close to full silicon detector coverage in central to forward pseudorapidities. The optimised disks offer many possibilities of fine-tuning coverage in certain pseudorapidity regions. A sketch of this layout can be seen in Figure 5.21.

Resolutions from the simulations are shown in Figure 5.22 versus momentum, and in Figure 5.23 versus pseudorapidity. From the plots, it can first of all be seen that the longitudinal pointing resolution is not significantly altered by changes in the TPC region. This is expected, as the inner barrel layers and the disks are the main detector parts affecting the longitudinal pointing resolution. Hence with

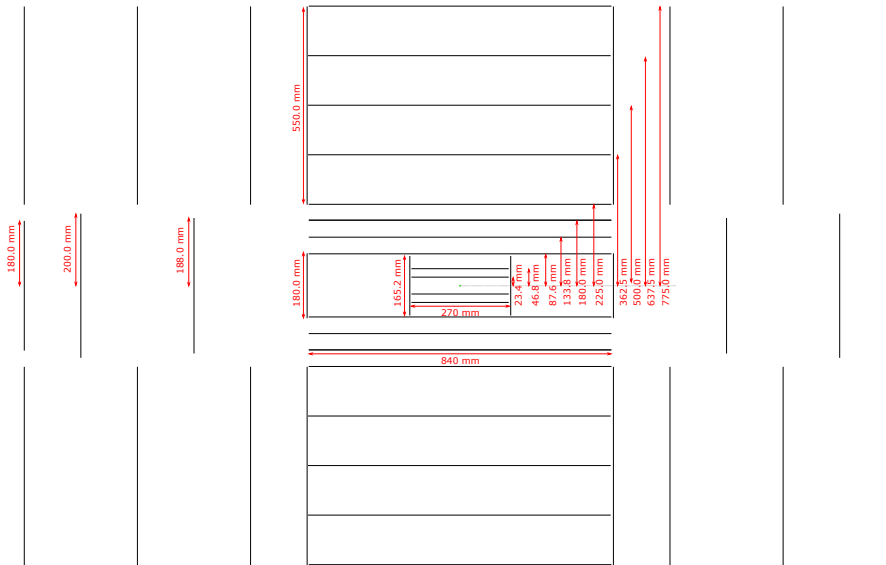


Figure 5.21: Sketch of the simulated layout with optimised disks (*5 layers, short; optimised disks*), where the gas TPC is replaced by five equidistant silicon layers, as well as disks and rings to give pseudorapidity coverage in the forward and backward regions.

disks of the same thickness, position, and pixel size in place, there is never much difference.

Looking at the relative momentum resolution versus momentum, it is first noteworthy that above momenta of around 5 GeV/c, some of the silicon configurations outperform the gas TPC. This is likely to a large extent due to the much smaller pixel size of the silicon layers, giving a better intrinsic resolution compared to the TPC. Only the long small radius layout with standard disks (*2 layers, long, small radius*) does not outperform the gas TPC at any point. This is due to the decrease in lever arm length, which strongly affects the relative momentum resolution. Decreasing the length and making room for a larger disk size improves the momentum resolution, as seen by comparing the two different small radius layout results (i.e. the curves labelled *2 layers, long, small radius* and *2 layers; short, small radius; large disks*).

In the plot of transverse pointing resolution versus momentum, there is no significant difference between any of the layouts. This is expected, since the innermost layers of the detector do not change.

Looking at the plot of relative momentum resolution versus pseudorapidity, more details of where the momentum resolution losses come from for the different layouts can be seen. The resolution of the gas TPC layout starts to deteriorate as the path length through the gas decreases. It then improves again once more disks are hit, at pseudorapidities $\eta \geq 2.1$. The layout with two inner and two outer silicon layers (*2+2 layers, long*) immediately loses momentum resolution when the outer two layers are no longer hit, at $\eta \geq 1.1$. Like the gas TPC layout, resolution is then improved again once disks are hit and the lever arm increases. In a pseudorapidity

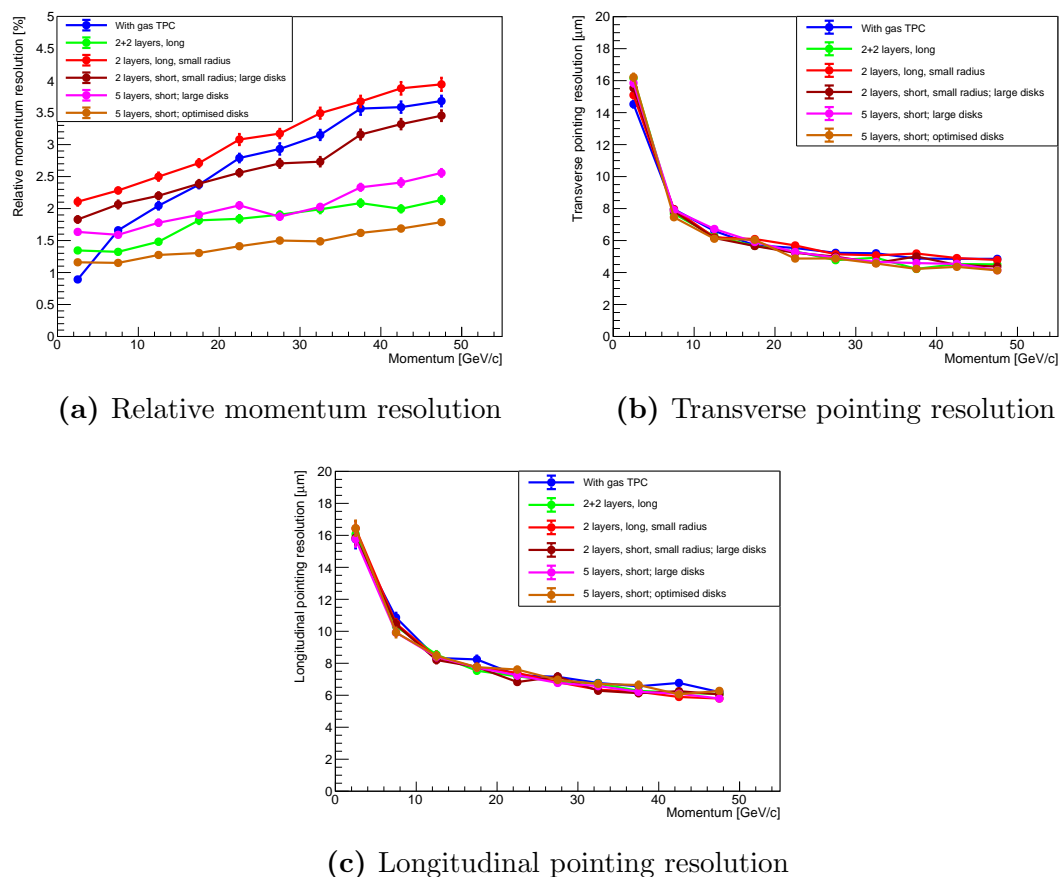


Figure 5.22: Relative momentum resolution and pointing resolutions versus momentum for different gas TPC replacement configurations.

interval of $1.1 \leq \eta \leq 2.3$ however, the relative momentum resolution for this layout is much worse than it is at central pseudorapidities.

The momentum resolutions of the small radius layouts follow each other well at $\eta \leq 1.5$. After this however, it becomes apparent that having shorter layers and larger disks improves momentum resolution due to the better pseudorapidity coverage.

Comparing the five layer layouts, their momentum resolutions are the same at $\eta \leq 0.5$. After that however, they diverge in the interval $0.5 < \eta \leq 1.9$, with the optimised disk layout having better resolution consistently. This is due to the detector gaps in pseudorapidity present in the 420 mm (large) disk layout, where layers are missed. These gaps are closed by disks and rings in the optimised disk layout.

Looking at the transverse pointing resolution versus pseudorapidity, most layouts have no significant difference. Only the long small radius layout with standard disks and the gas TPC layout are worse than the others, at $\eta \geq 1.6$.

In conclusion, the layout with disks and rings, that combines the best parts of the other tested layouts into a physically viable construction, outperforms the gas

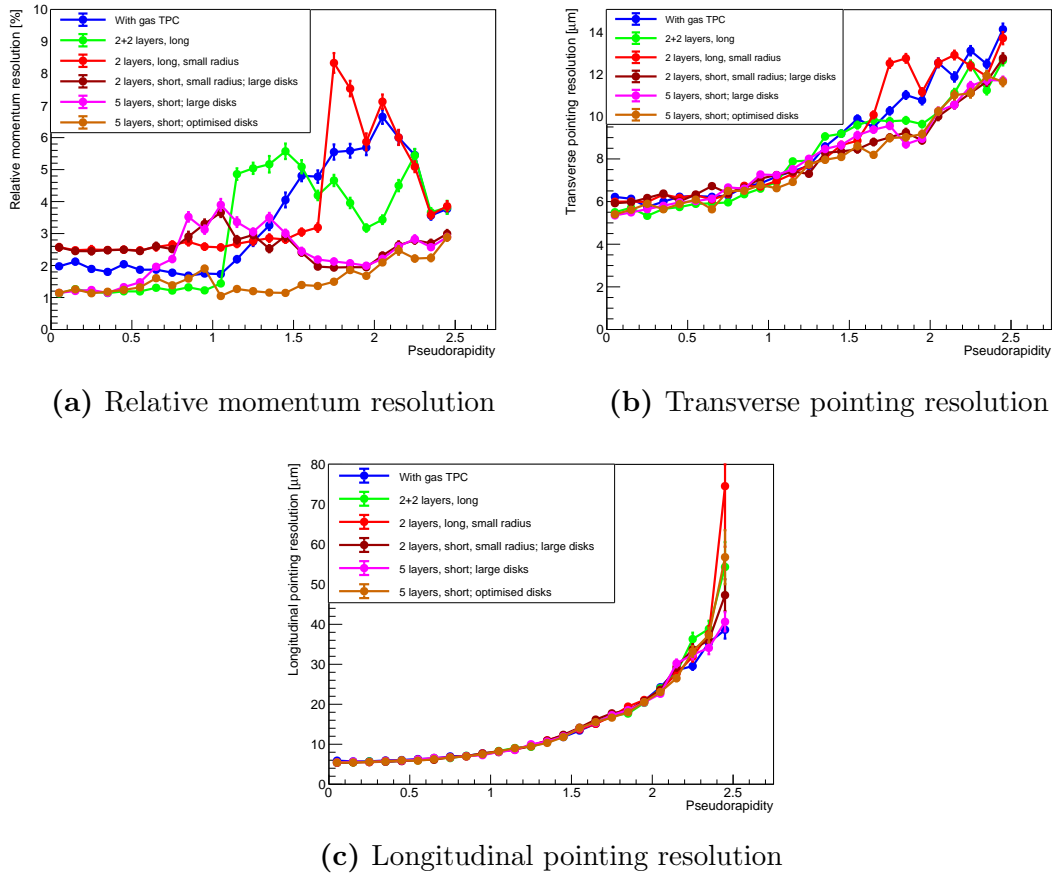


Figure 5.23: Relative momentum resolution and pointing resolutions versus pseudorapidity for different gas TPC replacement configurations.

TPC in all the studied parameter space, apart from at momenta below 5 GeV/c. While the layout with a large radius and long layers performs well, it may not be possible to construct such long barrel layers without significantly increasing the material budget. The same is true for large disks.

The ridges seen in the plots versus pseudorapidity have a direct correspondence to gaps in the detector coverage. Fine-tuning the layout can minimise the gaps and improve the resolutions. This can be done effectively for any of the proposed detector concepts for the EIC. Figure 5.24 shows a sketch of the five layer optimised disk layout (*5 layers, short; optimised disks*) with pseudorapidity edges marked, next to a fine-binned scan of relative momentum resolution versus pseudorapidity, using 500 000 events. From this figure, it is clear that the relative momentum resolution deteriorates in the “gaps” between disks (e.g. at $0.52 < \eta < 0.69$), only to be recovered when the next disk is hit.

Important to note in this study is that a gas TPC gives many points through which a track can easily be extrapolated, whereas a few silicon layers can make unambiguous track finding and reconstruction more difficult in a more realistic test (e.g. for full event reconstruction, rather than single particle). One solution would be to increase the number of silicon layers, while keeping in mind that an

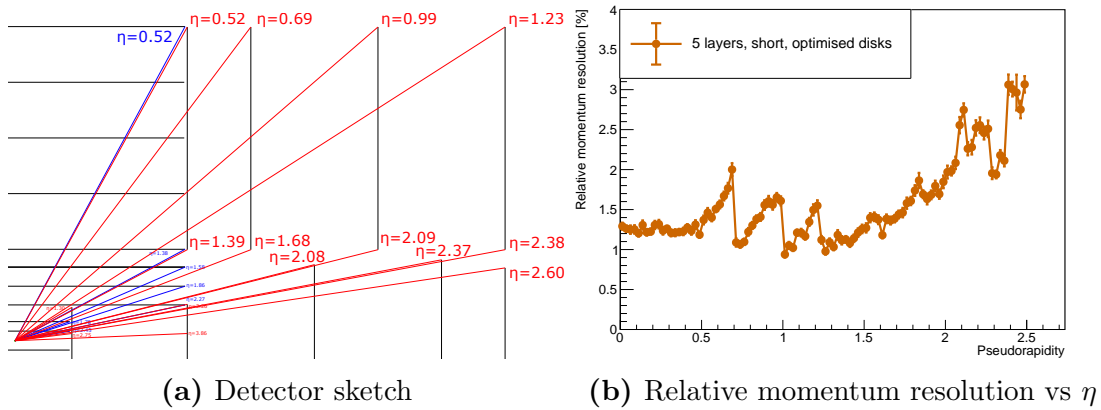


Figure 5.24: Sketch with pseudorapidity edges marked, and relative momentum resolution versus pseudorapidity for the optimised disks layout.

increased material thickness deteriorates resolution. The smaller pixel size possible with the silicon is also beneficial for the reconstruction however, so a balance can likely be reached between performance and material thickness. The five layer layout is an attempt at reaching this balance. In a study made comparing two silicon layers to five, it is found that having five silicon layers instead of two is not severely detrimental to any of the resolutions in this parameter space. A gas TPC can also help with particle identification by keeping track of the energy loss of the passing particle. This would need to be handled by other detectors if an all-silicon tracker layout is used. However, if a more compact layout is used, more space can be dedicated to improved bespoke particle identification detectors and calorimeters.

Comparing the two different five layer layouts, it can clearly be seen that the optimised disk layout has significantly better relative momentum resolution than the 420 mm disk layout. In the plot versus momentum, there is always a difference of approximately 0.5% between them, with the optimised disk layout being lower. In the plot versus pseudorapidity, the relative momentum resolution of the 420 mm disk layout is up to 2% higher than the optimised disk layout at certain pseudorapidities, and never lower. In the following studies, only the optimised disk layout will thus be considered.

5.3.10.2 Different silicon replacement outer radius

Using silicon layers instead of a gas TPC can potentially make it possible to reduce the overall tracker radius without severe loss of performance. Dedicated studies are therefore made for different outer radii of the detector, utilising the results from Section 5.3.10.1. The best-performing silicon configuration, shown in Figure 5.21, is simulated for different outer radii, keeping the five silicon layers equidistantly spaced between a radius of 225.0 mm and the currently investigated maximum outer radius. The minimum distance between layers is 46.2 mm, resulting in a smallest possible outer radius of 409.8 mm. Outer radii of 500.0 mm, 600.0 mm, and 775.0 mm (which is the standard radius as presented in Figure 5.21) are also

tested. The radius of the rings is changed to match the currently investigated outer radius, in order to keep the full tracker radius at the investigated level.

Studies are made both in the central region and in the forward region, with slightly different parameters. For the central region, the following parameters are used:

- Particle: e^-
- Momentum ranges: 0 to 5 GeV/c and 0 to 30 GeV/c
- Pseudorapidity ranges: $-1 \leq \eta \leq 1$ and $0 \leq \eta \leq 1$
- Number of events: 100 000
- 5 layer barrel (two inner, two outer, one time-stamping layer)
- Pixel size: $20 \times 20 \mu\text{m}^2$
- Magnetic field: 1.5 T

In the central region, the scattered electron is expected to carry momenta between approximately 0 and 30 GeV/c [16].

There is no significant difference in any of the pointing resolutions in this study, so only the relative momentum resolution results are shown. The inner barrel layers give the dominant effect on the pointing resolutions, and they remain the same in all the investigated layouts. The gas TPC layout used is the standard one, with an outer radius of 775.0 mm, as shown in Figure 5.1. Figure 5.25 shows the relative momentum resolution versus momentum and pseudorapidity in the momentum interval 0 to 5 GeV/c and pseudorapidity interval $-1 \leq \eta \leq 1$. In Figure 5.26, the same can be seen for the study performed in the momentum interval 0 to 30 GeV/c and pseudorapidity interval $0 \leq \eta \leq 1$.

The study of momenta between 0 and 5 GeV/c is made in order to observe the differences for very low momenta, whereas the 0 to 30 GeV/c study is made to investigate the detector performance at the most probable electron momenta in the central region [16].

At all momenta below 5 GeV/c, the gas TPC outperforms the silicon replacement in relative momentum resolution at all pseudorapidities between -1 and 1 . The largest difference when comparing to the smallest silicon replacement (with an outer radius of 409.8 mm) to the 775.0 mm outer radius gas TPC is 2%. At momenta approaching 5 GeV/c, the difference between the gas TPC and the silicon replacements decreases.

Looking at the higher momentum interval (0 to 30 GeV/c), it can be seen that the gas TPC loses performance faster with increasing momentum than the silicon layouts do. The points where the different silicon layouts start having better relative momentum resolutions than the gas TPC can be seen. The 775.0 mm outer radius silicon layout is better at momenta above 6 GeV/c. The 600.0 mm silicon layout is equally good or better at momenta above approximately 11 GeV/c. The 500.0 mm is equally good at 30 GeV/c. For the 409.8 mm radius silicon layout,

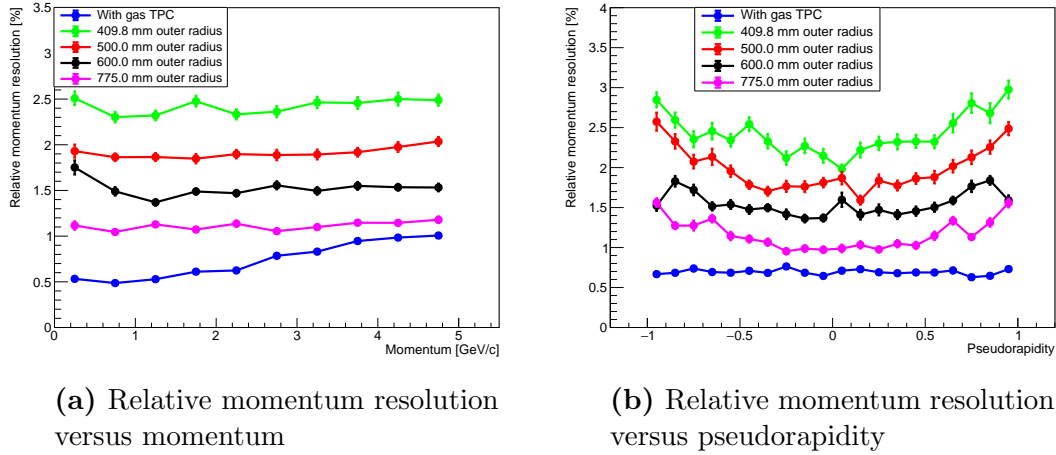


Figure 5.25: Relative momentum resolution versus momentum and pseudorapidity for different silicon TPC replacement outer radii, in the momentum range 0 to 5 GeV/c and pseudorapidity range $-1 \leq \eta \leq 1$.

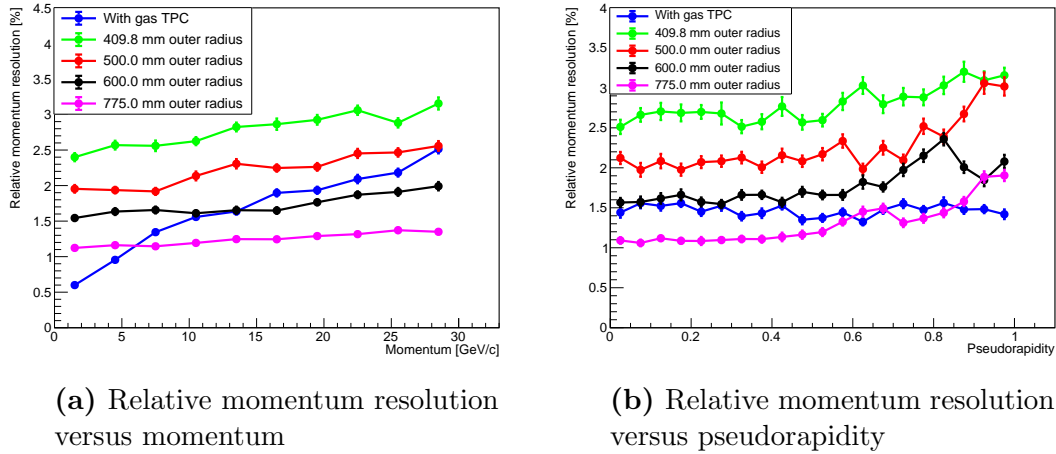


Figure 5.26: Relative momentum resolution versus momentum and pseudorapidity for different silicon TPC replacement outer radii, in the momentum range 0 to 30 GeV/c and pseudorapidity range $0 \leq \eta \leq 1$.

the difference to the gas TPC decreases from 2% at low momenta to approximately 0.5% at 30 GeV/c, but it never outperforms the 775.0 mm radius gas TPC.

Looking at the pseudorapidities for the higher momentum interval study, the 775.0 mm silicon layout is equal to or outperforms the gas TPC at $\eta \leq 0.9$. The 600.0 mm silicon layout matches the performance of the gas TPC at $\eta \leq 0.5$. The smaller radius layouts are always 0.5% to 1.5% worse in relative momentum resolution than the gas TPC in this parameter space.

Note again that for momenta below 5 GeV/c, the gas TPC has better relative momentum resolution than any of the investigated silicon layouts.

The same study is performed in the forward region, using the following parameters;

- Particle: e^-
- Momentum range: 0 to 50 GeV/c
- Pseudorapidity range: $1.0 \leq \eta \leq 2.5$
- Number of events: 100 000
- 5 layer barrel (two inner, two outer, one time-stamping layer)
- Pixel size: $20 \times 20 \mu\text{m}^2$
- Magnetic field: 1.5 T

In this study the longitudinal pointing resolution never differs significantly and is not shown. Figures 5.27 and 5.28 show the resolutions for different radii of the optimised disk layout versus momentum and pseudorapidity, respectively.

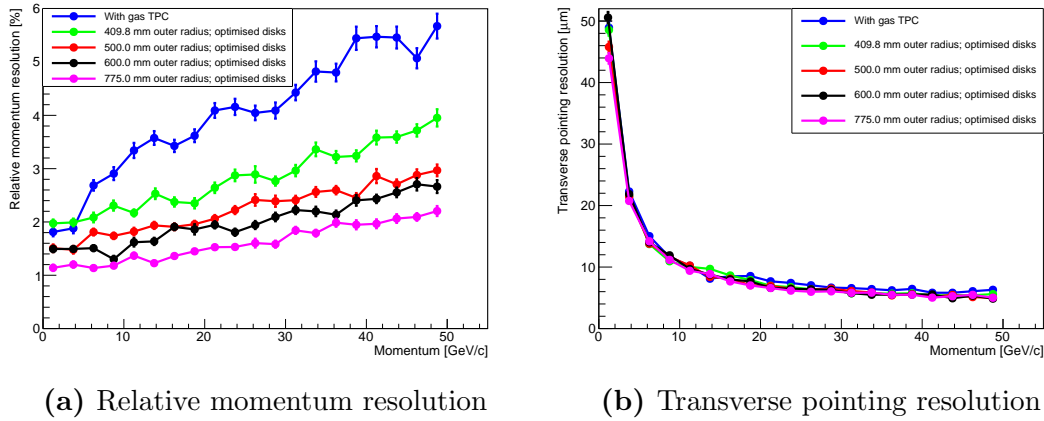


Figure 5.27: Relative momentum resolution and transverse pointing resolution versus momentum for different silicon TPC replacement outer radii, with optimised disk layout. Forward regions ($1 \leq \eta \leq 2.5$).

Looking at Figure 5.27, it can be seen that the optimised disk layout has better relative momentum resolution than the gas TPC at all momenta when the radius is 500.0 mm or larger. The layout with an outer radius of 409.8 mm only outperforms the gas TPC at momenta exceeding 5 GeV/c. The 775.0 mm outer radius is the best layout tested, but the difference in relative momentum resolution to the 500.0 mm layout is at most slightly less than 1%. The difference in transverse pointing resolution is small for all tested layouts.

In Figure 5.28, it can first of all be seen that for transverse pointing resolution, the gas TPC is worse than any radius of silicon for pseudorapidities between approximately 1.5 and 2.3. For the relative momentum resolution, the silicon layouts are different up until a pseudorapidity of 1.9, whereafter they are the same (as is expected, since the layouts are identical in this region of the disks). The 775.0 mm outer radius layout always has better relative momentum resolution than the gas

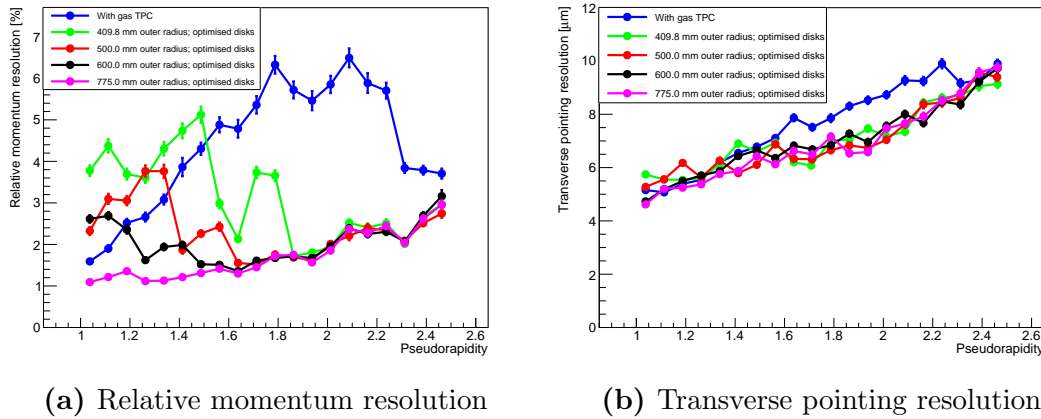


Figure 5.28: Relative momentum resolution and transverse pointing resolution versus pseudorapidity for different silicon TPC replacement outer radii, with optimised disk layout. Forward regions ($1 \leq \eta \leq 2.5$).

TPC in the investigated parameter space. The 600.0 mm layout has better momentum resolution than the gas TPC at $\eta \geq 1.2$, and the 500.0 mm layout has better resolution at $\eta \geq 1.4$. The 409.8 mm silicon layout outperforms the gas TPC at pseudorapidities larger than 1.55. The gas TPC relative momentum resolution is at most 2.5% lower than the 409.8 mm silicon layout relative momentum resolution.

To investigate at what radius silicon outperforms a gas TPC, different outer radii of the gas TPC are studied in the central region, and compared to the previously discussed all-silicon simulations with five silicon layers replacing the gas TPC. The parameters used are listed below.

- Particle: e^-
- Momentum range: 0 to 30 GeV/c
- Pseudorapidity range: $0 \leq \eta \leq 1$
- Number of events: 100 000
- 5 layer barrel (two inner, two outer, one time-stamping layer)
- Pixel size: $20 \times 20 \mu\text{m}^2$
- Magnetic field: 1.5 T

The radii tested mimic those of the silicon replacement layouts; 409.8 mm, 500.0 mm, 600.0 mm, and (the standard gas TPC outer radius) 775.0 mm. The results are compared to the simulations performed with the optimised disks layout.

Figure 5.29 shows the gas TPC (blue) superimposed on the 775.0 mm radius silicon replacement layout with optimised disks (green). The range of pseudorapidities between -1 and 1 are marked by purple dashed lines.

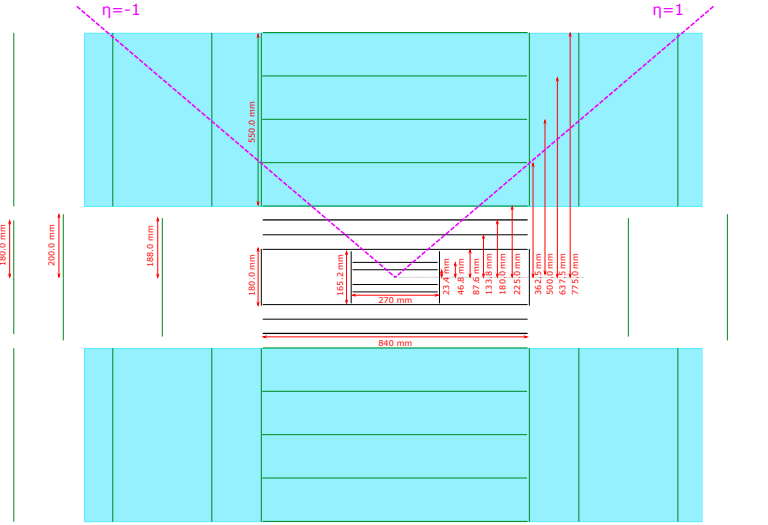


Figure 5.29: Sketch of the gas TPC (blue) superimposed on the 775.0 mm radius silicon replacement layout (green). The dashed lines indicate $|\eta| = 1$.

The resolutions resulting from these simulations can be seen in Figure 5.30 versus momentum, and in Figure 5.31 versus pseudorapidity. The longitudinal pointing resolution does not change significantly between the different layouts, and is thus not shown. In the figures, the colours match radii. A solid line with circular markers indicates that the data correspond to a silicon layout, and a dashed line with square markers indicates a gas TPC of the same radius.

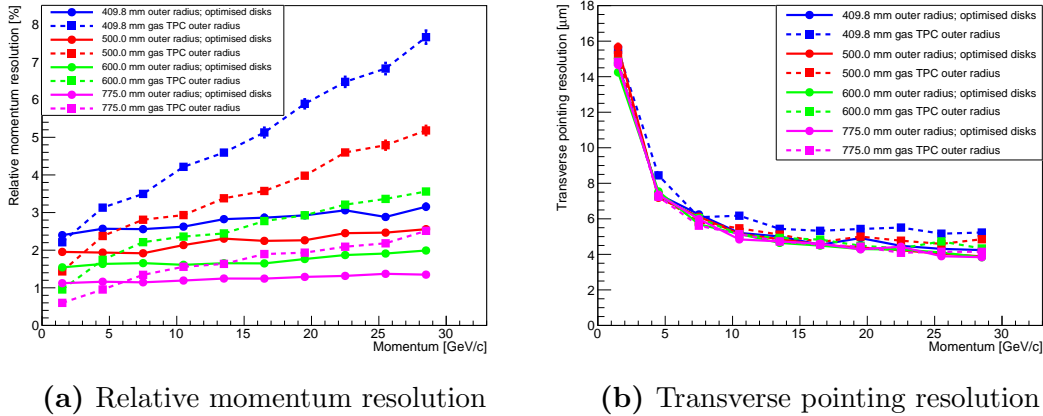


Figure 5.30: Relative momentum resolution and transverse pointing resolution versus momentum, comparing 5 layer silicon replacement with gas TPC for different maximum outer radii.

From the plot of transverse pointing resolution versus momentum, it can be noted that the transverse pointing resolution for a small-radius gas TPC is worse than the other tested layouts at most momenta. This is likely due to the decrease in lever arm, in combination with the relatively poor spatial resolution of the gas TPC (compared to silicon).

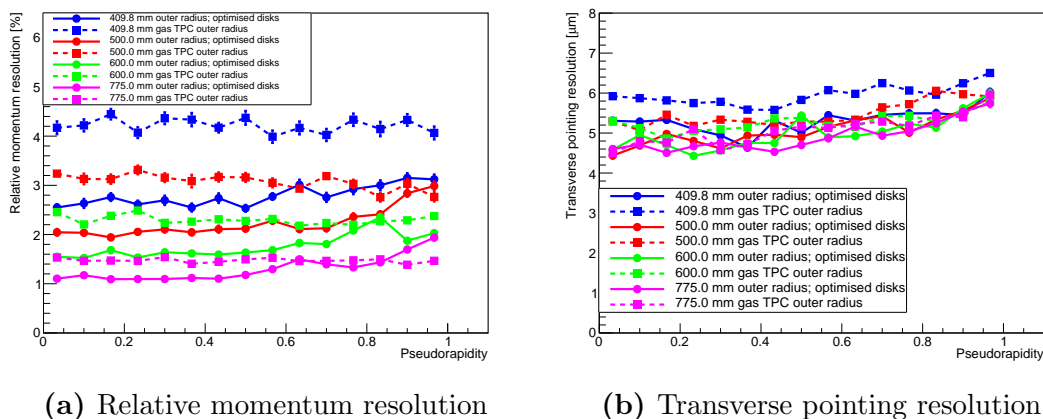


Figure 5.31: Relative momentum resolution and transverse pointing resolution versus pseudorapidity, comparing 5 layer silicon replacement with gas TPC for different maximum outer radii.

Looking at the relative momentum resolution versus momentum plot, it can be seen that silicon is always equal to or better than a gas TPC if they both have a maximum radius of 409.8 mm. In all cases, the relative momentum resolution for the silicon layout deteriorates slower with increasing momentum than it does for the gas TPC. The silicon layouts are thus always better than the gas TPC at high momenta. The location of the crossover point where silicon becomes better than gas depends on the radius. For the 500.0 mm radius, the gas TPC is better at momenta below 3 GeV/c. For the 600.0 mm radius, the gas TPC is better at momenta below approximately 4 GeV/c. At a radius of 775.0 mm, the gas TPC has a better relative momentum resolution at momenta below 6 GeV/c.

The transverse pointing resolution versus pseudorapidity plot in Figure 5.31 shows that the gas TPC at 409.8 mm radius has the worst pointing resolution in the whole investigated pseudorapidity range ($0 \leq \eta \leq 1$). In general the silicon layouts are shown to have the best transverse pointing resolution here, but the difference between silicon and gas for each radius is below 1 μm . The pointing resolution is dominated by the inner barrel layers, which do not change between the layouts.

Looking at the relative momentum resolution versus pseudorapidity, it can immediately be seen that the silicon layouts at 409.8 mm radius and 500.0 mm radius are better than their gas TPC counterparts across the full range investigated. The 500.0 mm radius silicon layout also outperforms or matches the 600.0 mm radius gas TPC at pseudorapidities smaller than 0.8. The silicon layout with radius 600.0 mm always outperforms or matches the 600.0 mm radius gas TPC. Finally, the 775.0 mm radius silicon layout has better or equal relative momentum resolution than the standard gas TPC layout at pseudorapidities below 0.85. In general, the difference between silicon layouts and gas TPC increases as the radius decreases, in favour of the silicon layout. In the investigated parameter space, an all-silicon layout has better performance than a gas TPC as soon as the radius is decreased from the baseline of 775.0 mm. In other words, if it is decided that the tracker radius is to be decreased from 775.0 mm, an all-silicon layout is preferable to a gas TPC.

5.4 Conclusions

In conclusion, the best silicon vertex tracker layout indicated by the performed general simulations is one with two inner layers (two are needed to keep redundancy, and having two improves pointing resolution at higher momenta), two outer layers, and seven disks in the forward and backward regions. Having two outer layers instead of just one makes little difference for the resolutions, but an extra layer may help in getting an accurate particle track for vertex reconstruction. A time-stamping layer does not have a severe negative impact on any of the resolutions, but can aid the detection in other ways. The detector benefits from keeping the pixel size in all layers as small as possible, and the material budget in each layer as low as possible. Having five disks is comparable to having seven disks, but seven are chosen to increase detector coverage. If a time-stamping layer is desired in the disk region, it is better to replace the penultimate disk with a technology using larger pixel size, rather than the final disk. The material of this disk must be kept low, however. If the pixel size of the last disk is kept the same, its thickness can be increased without severely affecting the resolutions. It is however essential to keep the pixel size low on the final disk.

The simulations indicate that for particles with momenta above around 5 GeV/c, the resolutions can benefit from replacing the gas TPC with silicon layers. The best silicon vertex tracker, as shown by the simulations, will thus be something similar to the sketch shown in Figure 5.21. This is a baseline layout that can be adapted to any of the suggested detector concepts with small alterations to accommodate different beampipes and fit in with other detector parts. If the detector is to be more compact than the baseline radius of 775.0 mm, the simulations indicate that it is beneficial to replace the gas TPC with layers of silicon and larger disks and rings.

In the next chapter, more targeted simulations are presented, utilising what was deduced from these general simulations and altering the layouts to fit with the detector constraints and collider parameters that are now known. The detector performance is also investigated with regard to the tracking requirements arising from the EIC physics programme.

Chapter 6

Focused detector layout simulations

6.1 Introduction

After the official selection of the Brookhaven National Laboratory (BNL) as host for the EIC, some parameters of the facility design are better known. An effect of this is that simulations can be more targeted and tailored to this facility, incorporating geometric constraints that were previously not fixed. The main piece of information that affects the simulations presented here is the more detailed layout of the central detector region. The simulations presented in this chapter build on from the simulation results presented in Chapter 5, while also taking sensor developments discussed in Chapter 4 into account.

In December of 2019, an effort was started to collate all relevant studies for the EIC in a “Yellow Report”, thus producing a base document at expert level from which further documents and studies can be made. The report was published in March of 2021 [17]. The EIC Yellow Report contains both physics studies and detector studies, and how they are connected (i.e. how desired physics investigations affect detector requirements, and how detector performance and possible coverage constrains the physics that can be observed). The work carried out as part of the Yellow Report initiative is largely split up into two collaborating groups; a Physics Working Group (PWG) and a Detector Working Group (DWG). The work presented here has been carried out in conjunction with the Yellow Report initiative, and reported to the groups and partially included in the final Yellow Report. Site selection for the EIC coincided with the Yellow Report initiative, and the Yellow Report is currently used as a basis for defining a reference detector for the EIC.

At the start of the EIC Yellow Report effort, it was suggested that the planned developments of silicon sensors for the EIC would benefit from joining the effort of sensor development for the ALICE ITS3 upgrade [122]. The new sensor developments are planned to enable a lower material budget and a smaller pixel size compared to existing MAPS sensors (see Section 2.4.5.3), thus theoretically improving detector performance. Projections made from the planned ITS3 developments are used for the baseline detectors in this chapter.

At the beginning of this chapter the current central detector region layout is presented, taking into account the constraints brought on by site selection. The simulation tools used are also presented, and Section 6.1.3 outlines the baseline layouts used for the studies in this chapter. Section 6.2 shows a comparison between the performance of the baseline layout presented in Chapter 5 and one of the new baseline layouts, taking possible new detector technologies based on the ALICE ITS3 technology developments into account. The performance of the baseline layouts of this chapter in terms of relative momentum resolution and transverse pointing resolution is quantified in Section 6.3, and compared to the EIC physics requirements provided by the Yellow Report PWG. An investigation of the minimum particle momentum that allows track reconstruction is presented in Section 6.4, providing a quantification of the detector acceptance both in terms of momentum and pseudorapidity. Finally, Sections 6.5 and 6.6 pertain to studies of physics events. First of all event generation is discussed, with a focus on open charm events. The particle distributions for different collision energies is shown, and the fraction of generated events within the detector acceptance is investigated. Finally, the generated events are propagated through a full simulation of the different detector layouts, and the reconstructed invariant masses of charmed D mesons are studied in detail.

6.1.1 Central detector region layout

In the central detector region, where the silicon vertex tracker is located, changes to the beampipe have a large effect on the available space. The interaction regions at BNL will have a larger crossing angle, and thus a larger beampipe radius, than what was assumed in the studies presented in Chapter 5, and this impacts the possible design of the tracker near the interaction point. The larger crossing angle aids in reducing parasitic collisions due to short bunch spacing, and enables placing of the final focusing quadrupoles closer to the interaction point. A larger crossing angle thus makes it possible to increase the luminosity of the experiment, but forces detectors to be located further from the interaction point.

The beampipe used in the previously presented studies (see Chapter 5) is assumed to be a cylindrical beryllium tube with aluminium extensions. The beryllium part has a radius of 18 mm, and the aluminium part has a radius of 20 mm. In the studies presented here, an updated beampipe adapted for the BNL interaction regions is used. This beampipe is shown as it appears in simulations in Figure 6.1. This is the beampipe model as of March 2020 [123]. It has an inner radius of 31 mm in the central region, and is in this region made of beryllium with a thickness of 760 μm . The beryllium section is 1466 mm long, and on each side the beampipe continues in widening shapes made of aluminium.

The implication of this is that the silicon vertex tracker inner radius has to increase in order to accommodate the new beampipe, compared to previous studies. A detailed description of the new SVT layout is shown in Section 6.1.3, and a study of the impact of the beampipe change is presented in Section 6.2. The beampipe extensions in the forward and backward regions also affect the possible inner radius of the disks, and thus limits the detector acceptance at high pseudorapidity.

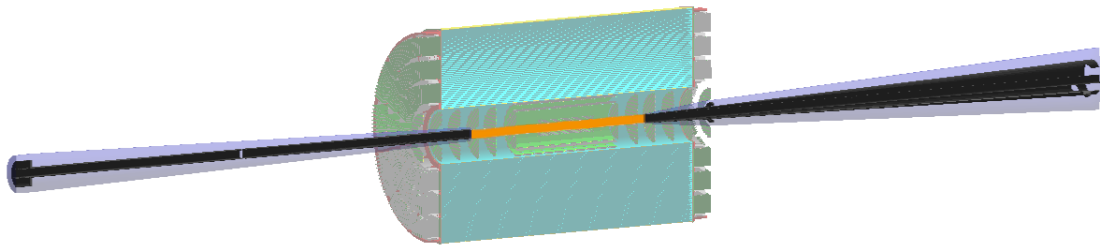


Figure 6.1: The full beampipe geometry in the central region, as of March 2020. A shadow of a full central tracking detector is also shown. The central beryllium part of the beampipe is marked in orange. Outside of this, the pipe is made up of aluminium. A blue shadow shows the maximum envelope of the beampipe.

6.1.2 Simulation tools

The simulations presented in this chapter utilise a variety of simulation tools, in order to generate, propagate, and reconstruct realistic physics events through realistic detector setups. The EICROOT framework (described in Section 5.2) is used for initial comparisons of sensor technologies and study of the effect on performance the new beampipe radius has. It is also modified to output GDML files containing the silicon geometry so that the exact same geometry can be imported into other frameworks. EICROOT has a framework for generating accurate silicon stave geometries, so it is used throughout to generate the silicon vertex tracker layouts. The EICROOT framework is insufficient for advanced studies using physics events, and is also being phased out by the EIC software community in favour of larger and more modern frameworks. The majority of simulations presented in this chapter thus utilise the “Fun4All” framework, described in Section 6.1.2.1.

6.1.2.1 Fun4All

The Fun4All framework is a further development of a data analysis framework originally built for the PHENIX experiment [124]. In 2015 the new developments separated into a full simulation and data analysis framework for the sPHENIX experiment, and it has since also been adapted to include simulation parameters for the EIC. The framework is built around compiled C++ code and steering macros utilising ROOT [108]. The major benefit of the Fun4All framework for the work presented here is the inclusion of multi-track reconstruction for a single event. Whereas EICROOT handles single particle tracks well, the framework is lacking in reconstructing multiple tracks and vertices. In Fun4All, GENFIT [46] is used for track reconstruction in the work presented here. Different track and vertex reconstruction software packages such as ACTS (“A Common Tracking Software”) [125] are also currently being integrated into the framework, but at the time of this work GENFIT was the main available alternative.

The framework is built around different modules that can be swapped out or altered. These modules are used to provide input to the simulations (such as a file from a particle generator), perform simulations, digitisation, and reconstruction, and construct output files for further analysis. Throughout the work presented

here, a module interfacing with GEANT4 [126] (PHG4Reco) is used to perform the simulations. A module interfacing with GENFIT (PHG4TrackFastSim) is used for digitising detector hits and reconstructing tracks from the digitised hits. The digitisation is performed as a Gaussian smearing of the hit position with a standard deviation given by the set pixel size divided by $\sqrt{12}$, and the reconstruction uses a Kalman filter algorithm (see Section 2.3).

Crucially, the Fun4All framework is officially supported by the EIC software community and as such it is frequently updated with the current official geometries for different structures, such as the current beampipe implementation. This makes for easy integration of the simulations into a more realistic setting. The framework also has the possibility of reading event generator output, making it possible to study physics events in it, and how different detector parameters affect physics observables from realistic particle collisions.

6.1.2.2 PYTHIA

To generate realistic particle distributions and investigate physics observables in simulations, PYTHIA 8.3 is used [127]. Pythia is a standard tool for simulating multiparticle final states from collisions of elementary particles, and it contains a wide range of physics models which have been verified by comparisons with experimental data to make sure the generation is as realistic as possible according to current physics knowledge [128].

As a collision is simulated in Pythia, a physics process is first selected. This is the most highly-energetic process in the event evolution. After this process the resulting particles are left to evolve, which involves radiation of gluons and photons as well as multiple parton-parton interactions. This evolution also contains the beam remnants (for example the remaining quarks of the proton, if one has been knocked out by the initial process). The objects carrying colour are connected together by “strings”. Once the “parton level” evolution is completed, hadronisation occurs via application of the Lund string model [97]. This forms both stable and unstable hadrons. In the final stage of the physics event generation, particle decays occur after some time from the initial collision. All the information of the event is then saved to an “event record”, which contains all the particles that have been generated in a single collision, along with data about them such as their energies and creation and decay vertex positions. In the work presented here, the HepMC2 event record format is used [129]. The HepMC2 files created when running Pythia can be input into the Fun4All framework, and thus the full event can be propagated through a simulated detector.

A number of physics processes are available in Pythia. These can be individually activated or deactivated before the event generation algorithm is run. In the work presented here, the photon-gluon fusion process is the main process under investigation. It is discussed further in Section 3.3.1.

Pythia can also be “tuned” to investigate how different parameters affect the match of generated events to experimental data, and thus create a more accurate event generator. In the work presented here, the default tunes are used unless

indicated otherwise. Electron-proton collisions are under investigation here, and thus the photons emitted from the electron must be modelled accurately. The flag `PDF:lepton2gamma` is thus activated in Pythia to ensure that both direct and resolved photon contributions are taken into account.

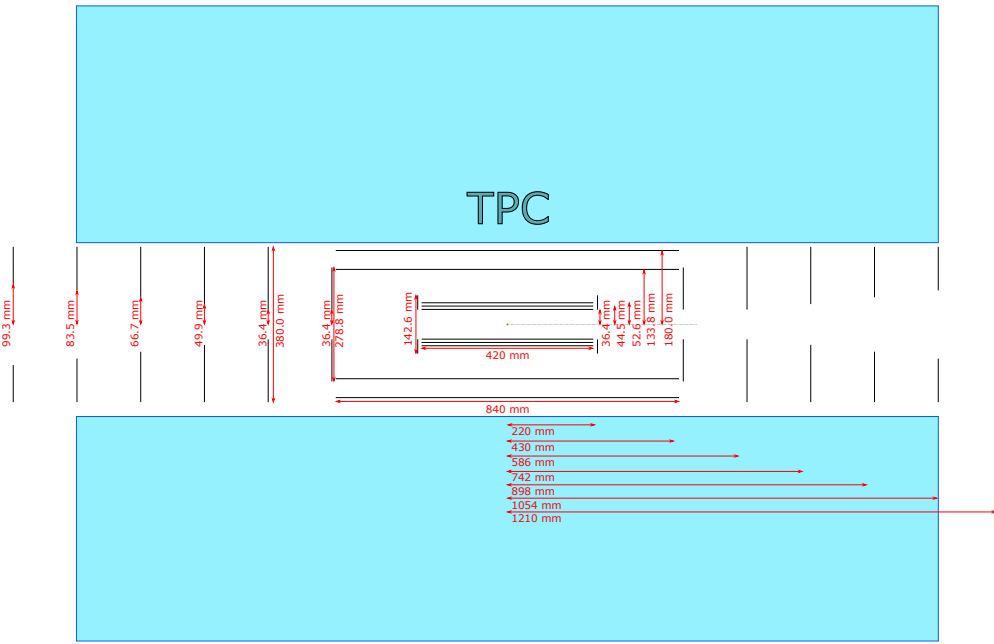
6.1.3 Baseline layouts

In the work presented in this chapter, three different layouts are mainly used. The “silicon plus TPC baseline” investigated in this work has been adopted as one of the two baselines present in the EIC Yellow Report, and the compact “all-silicon baseline” is based on the all-silicon tracker concept presented in the Yellow Report [17]. It is important to note that it has some differences compared to the Yellow Report all-silicon tracker, however. This is discussed in more detail in Section 6.1.3.2. A different all-silicon layout with a 600 mm outer radius based on the layouts presented and investigated in Section 5.3.10 is also used in this work.

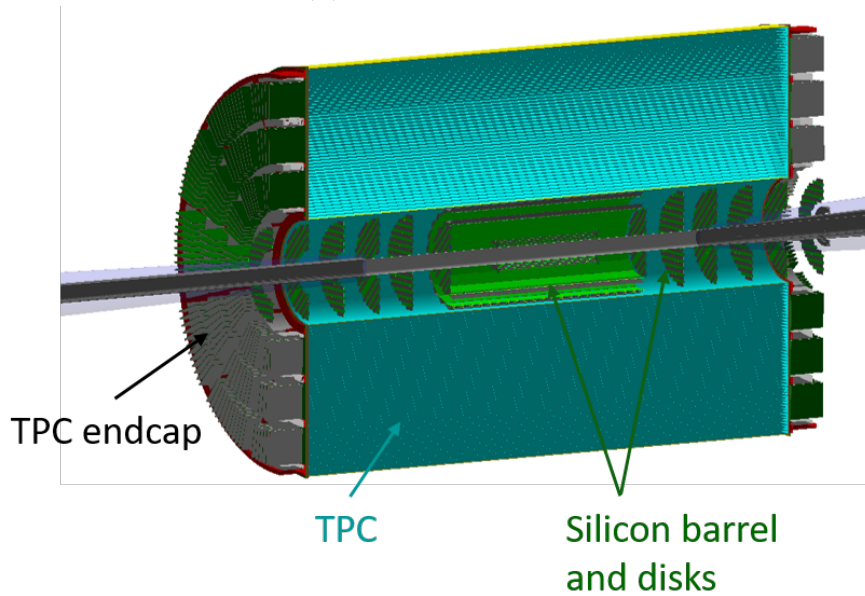
6.1.3.1 Silicon plus TPC baseline

Figure 6.2 shows a sketch of this baseline, along with an implementation of it in Fun4All. Here the beampipe that is to be used (as of March 2020) can also be seen. The silicon vertex tracker barrel in this layout consists of three inner layers and two outer layers, all constructed using the proposed ITS3 technology described in Section 2.4.5.3. Using this technology, the inner layers of the tracker have a material budget of 0.05% X_0 , the outer layers 0.55% X_0 , and the disks 0.24% X_0 . These material budgets are based on projections of the power consumption of sensors constructed using the ITS3 technology, performed by colleagues at the Lawrence Berkeley National Laboratory (LBNL) [130]. The projections take the varying sensor size and stave lengths into account. The ALICE ITS3 sensors are envisioned to have a pixel size of $10 \times 10 \mu\text{m}^2$. This layout is based on the studies presented in Chapter 5, altered to accommodate the larger beampipe. The three inner layers of the layout are located at radii of 36.4 mm, 44.5 mm, and 52.6 mm, where the distance between the layers comes from the minimum distance between the ALICE ITS2 layers [29], which ensures that the detector can be physically constructed in this layout using existing technologies. The inner layers have a length of 420 mm, which is needed to maintain the pseudorapidity coverage that was possible using the previously studied beampipe layout (with an 18 mm radius). Three inner layers are used instead of two in order to better be able to reconstruct low-momentum particles that spiral early. The two outer layers are placed at radii of 133.8 mm and 180.0 mm, and have a length of 840 mm.

Outside of the silicon layers, the default Fun4All implementation of an EIC TPC is located. This TPC is roughly based on the sPHENIX TPC [131], and is thus relatively compact, with an inner radius of 200 mm and an outer radius of 780 mm. The length of the TPC is 2110 mm, and in the simulations it is represented by 48 cylindrical layers of the sPHENIX TPC gas mixture (a mix of neon and carbon tetrafluoride) centred around the nominal interaction point. The 48 layers are



(a) Sketch of layout



(b) Implementation in Fun4All

Figure 6.2: The silicon plus TPC baseline layout. The top figure shows a schematic sketch of the detector parts, and the bottom figure shows the implementation of it in the Fun4All framework. The sketch omits the beampipe, and more clearly shows the inner radius tapering of the disks to fit around the pipe.

surrounded by a kapton field cage, emulating the non-gaseous material needed in a TPC. The transverse resolution (ϕ resolution) used is $200 \mu\text{m}$, and the longitudinal resolution is $500 \mu\text{m}$. At the longitudinal ends of the TPC, the sPHENIX representation of TPC endcaps is placed. The endcaps contain mockup structures of the readout electronics, adding a significant amount of material.

In the forward and backward regions, 14 silicon disks are placed (7 in each direction). The disks are tapered in both inner and outer radius, to account for the increasing beampipe radius at increasing z , and to not add material in regions already covered by the barrel layers. The disks consist of staggered staves of silicon similar to the barrel layers, creating roughly circular surfaces. Table 6.1 shows a summary of the positions and dimensions of the TPC baseline layout components.

Layer	Length	Radial position	Disk	z position	Inner radius	Outer radius
Layer 1	420 mm	36.4 mm	Disk 1	220 mm	36.4 mm	71.3 mm
Layer 2	420 mm	44.5 mm	Disk 2	430 mm	36.4 mm	139.4 mm
Layer 3	420 mm	52.6 mm	Disk 3	586 mm	36.4 mm	190.0 mm
Layer 4	840 mm	133.8 mm	Disk 4	742 mm	49.9 mm	190.0 mm
Layer 5	840 mm	180.0 mm	Disk 5	898 mm	66.7 mm	190.0 mm
TPC start	2110 mm	200.0 mm	Disk 6	1054 mm	83.5 mm	190.0 mm
TPC end	2110 mm	780.0 mm	Disk 7	1210 mm	99.3 mm	190.0 mm

(a) Barrel region

(b) Disk region

Table 6.1: Positions and lengths of detector parts in the barrel region and the disk region, for the silicon plus TPC baseline. In the disk region, the seven forward disks are shown, but this layout is symmetric so it is the same with reversed sign on the z position in the backward region.

In the simulations, the detector is encapsulated by an absorbing volume that stops particles from leaving the detector and spiralling back in. In reality there will be particle identification detectors and calorimeters outside the tracker which will stop particles from spiralling back.

Some investigations also include a layout with the same silicon parts, but with layers of micro-pattern gas detectors (MPGDs) replacing the TPC. The MPGD layers are 1880 mm long, and placed radially in a “2+2+2” configuration (i.e. three double layers). The radial positions for the MPGD layers are shown in Table 6.2.

Layer	Radial position
Layer 1	200.0 mm
Layer 2	218.6 mm
Layer 3	488.9 mm
Layer 4	507.5 mm
Layer 5	777.7 mm
Layer 6	796.4 mm

Table 6.2: Radial positions of the MPGD layers, each with a length of 1880 mm. The silicon parts of this layout are the same as presented in Table 6.1.

Both the transverse and longitudinal resolutions used are 150 μm for the layers. A drawback of the currently available MPGD layout is the lack of endcap detectors,

which leaves detector gaps in pseudorapidity. Studies with this layout are thus only performed in the central region.

6.1.3.2 All-silicon baseline

The all-silicon baseline layout used in this work is based on a concept developed in collaboration with colleagues at LBNL as part of the EIC Yellow Report effort. It is important to note that the layout used in the work presented in this chapter has some significant differences compared to the layout presented in the Yellow Report however, notably the usage of three inner layers, and material thicknesses based on projections from using the ITS3 technology. It is thus not the concept in the Yellow Report, but a layout based on the Yellow Report concept.

The silicon vertex tracker here consists of a total of seven barrel layers and ten disks (five in the forward direction and five in the backward direction). The barrel layers are arranged as three inner layers, two intermediate layers, and two outer layers. The inner layers each have a material budget of 0.05% X_0 , the intermediate and outer layers 0.55% X_0 , and the disks 0.24% X_0 [130], and a default pixel size of $10 \times 10 \mu\text{m}^2$. Table 6.3 shows a summary of the positions of the detector elements in this layout, and Figure 6.3 shows an implementation of the layout in Fun4All. The distance between the barrel layers is once again based on the minimum distance between ALICE ITS2 layers, to make sure construction is realistic using current technologies.

Layer	Length	Radial position	Disk	z position	Inner radius	Outer radius
Layer 1	420 mm	36.4 mm	Disk 1	250 mm	36.4 mm	170.0 mm
Layer 2	420 mm	44.5 mm	Disk 2	490 mm	36.4 mm	362.6 mm
Layer 3	420 mm	52.6 mm	Disk 3	730 mm	49.9 mm	432.3 mm
Layer 4	540 mm	180.0 mm	Disk 4	970 mm	66.7 mm	432.3 mm
Layer 5	600 mm	226.8 mm	Disk 5	1210 mm	99.3 mm	432.3 mm
Layer 6	1050 mm	385.5 mm				
Layer 7	1140 mm	432.3 mm				

(a) Barrel region

(b) Disk region

Table 6.3: Positions and lengths of detector parts in the barrel region and the disk region, for the all-silicon baseline. In the disk region the five forward disks are shown, but the layout is symmetric so it is the same with reversed sign on the z position in the backward region.

6.1.3.3 All-silicon, 600 mm outer radius

An all-silicon layout based on the work presented in Section 5.3.10 is also tested. This layout is in particular based on the layout shown in Figure 5.21, with some modifications. The main feature of this layout is that it has an outer radius

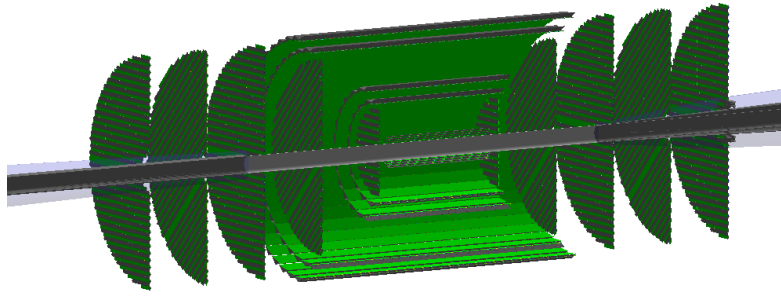


Figure 6.3: The all-silicon baseline layout implementation in the Fun4All framework.

of 600 mm, which is roughly in the middle of the TPC baseline outer radius of 780 mm and the all-silicon baseline layout outer radius of 432.3 mm. Figure 6.4 shows a sketch of the 600 mm outer radius all-silicon layout. It consists of nine

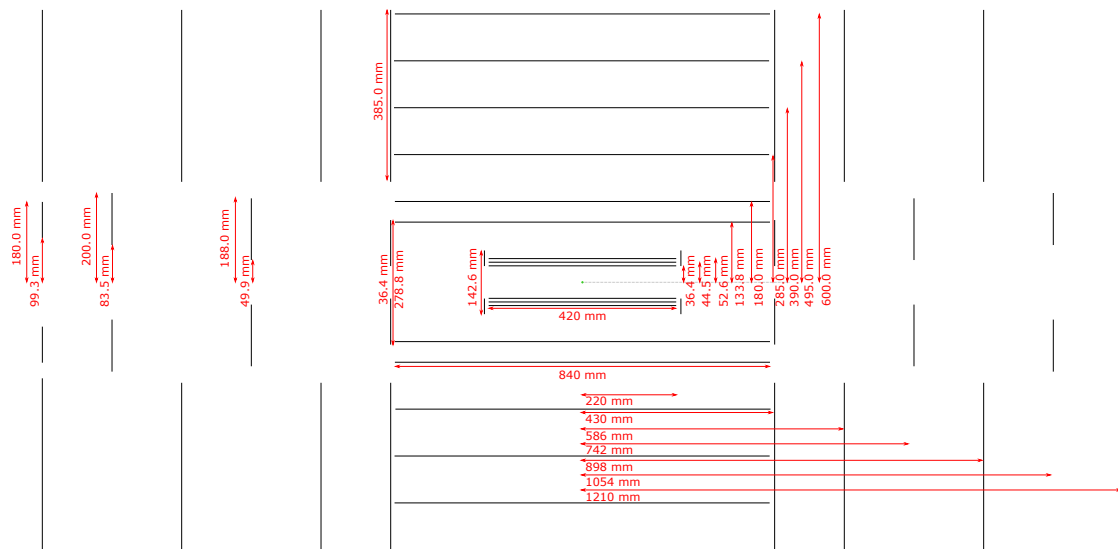


Figure 6.4: Sketch of the all-silicon layout with a 600 mm outer radius. The black lines represent different silicon layers.

silicon barrel layers, and fourteen disks and rings (seven in the forward direction and seven in the backward direction), where the rings have a large inner radius. The purpose of using a combination of disks and rings is that the size of them can be trimmed to give close to full pseudorapidity coverage while keeping the total material at a given pseudorapidity low. There are three inner barrel layers, two intermediate barrel layers, and four outer barrel layers. Four layers are used to aid track reconstruction by providing more hit points along the particle track, analogous with the five layer layouts presented in Section 5.3.10.1. The inner and intermediate layers are placed at the same radii as in the silicon plus TPC baseline layout, and have the same characteristics. The four outer barrel layers are placed equidistantly between radii of 285 mm and 600 mm. The inner barrel layers have a

material thickness of $0.05\% X_0$ each, the intermediate and outer layers $0.55\% X_0$, and the disks and rings $0.24\% X_0$.

Some studies are also made with an all-silicon layout with a 775 mm outer radius. This layout has the same five inner and intermediate barrel layers as the layout described above, but the outer barrel layers, disks, and rings have the positions as shown in Figure 5.21. It is thus the best-performing detector layout from the studies carried out in Section 5.3.10, adapted for a beampipe radius of 31 mm.

6.2 Comparison of silicon sensor technologies

After site selection in January 2020, further details of the interaction region are known. This has led to an increase in beampipe radius, further described in Section 6.1.1. The impact of the increased beampipe radius from 18 mm to 31 mm is investigated, along with the impact of utilising sensors based on the ITS3 technology instead of the previously studied ITS2-based sensors. The pointing resolution is expected to degrade as the innermost layers are moved to a larger radius. Since the ITS3 technology allows higher granularity and lower material budget however, using sensors in this technology may mitigate the loss of performance. This is investigated using these simulations. For these investigations, EICROOT is used in order to make an accurate comparison to previous studies. The study is made in the central region, and the parameters used are presented below.

- Particle: π^+
- Momentum range: 0 to 5 GeV/c
- Pseudorapidity range: $-0.5 \leq \eta \leq 0.5$
- Standard EICROOT TPC
- Inner layer material thickness: $0.3\% X_0$ for ITS2-based sensors, $0.05\% X_0$ for ITS3-based sensors
- Outer layer material thickness: $0.8\% X_0$ for ITS2-based sensors, $0.55\% X_0$ for ITS3-based sensors
- Magnetic field: Uniform 1.5 T

The “old baseline” layout used consists of two inner barrel layers, two outer barrel layers, and one time-stamping layer with a thickness of $1.6\% X_0$. This layout is described further in Section 5.2, and a sketch of it is shown in Figure 5.1. This layout has a beampipe with a radius of 18 mm. The “new baseline” layout is as described in Section 6.1.3.1, but using the default EICROOT TPC instead of the default Fun4All TPC. The silicon barrel in this layout has three inner layers and two outer layers, and accommodates the new beampipe with a radius of 31 mm.

A comparison of the transverse pointing resolution for the old baseline, new baseline with sensors based on ITS2 technology (using a $20 \times 20 \mu\text{m}^2$ pixel size), and new baseline with sensors based on ITS3 technology (using a $10 \times 10 \mu\text{m}^2$ pixel

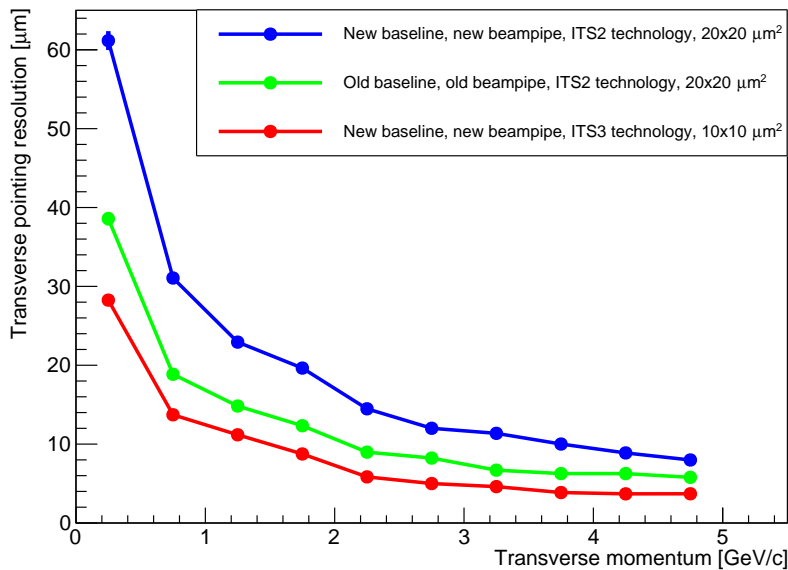


Figure 6.5: Transverse pointing resolution versus transverse momentum, comparing the old baseline layout (green), the new baseline layout with ITS2-based technology (blue), and the new baseline layout with ITS3-based technology (red).

size) is shown in Figure 6.5. The blue curve compared to the green curve represents mainly the effect of the increase of the beampipe radius. The detector technology and pixel size remain the same, but there is a severe deterioration of pointing resolution, especially at the lowest momenta. However, comparing the red curve to the blue curve shows the improvement gained from changing to sensors based on the ITS3 technology and a $10 \times 10 \mu\text{m}^2$ pixel size. The red curve lies underneath the green curve everywhere, showing that the pointing resolution performance can be regained, and even improved upon, with the updated beampipe radius by switching to ITS3-based sensors.

Figure 6.6 shows the relative momentum resolution and the transverse and longitudinal pointing resolutions, decoupling the sensor type (i.e. material thickness, given by whether the sensor technology is ITS2-based or ITS3-based) and pixel size of the silicon layers. The green curve again shows the old baseline layout, with the old beampipe (labelled “Old BP” in the legend) and ITS2-based sensors with a $20 \times 20 \mu\text{m}^2$ pixel size. The blue and magenta curves are results from using ITS2-based sensors, and the black and red curves from using ITS3-based sensors, all with the new baseline layout and the new beampipe radius.

There is no significant difference in relative momentum resolution. This is due to the relatively small difference in total detector lever arm when changing the inner detector radius, and the same TPC being used in all configurations. The transverse and longitudinal pointing resolutions both show the same trends; as momentum increases the resolutions of all tested configurations approach each other, while the differences are larger at lower momenta. Comparing the blue curve to the magenta

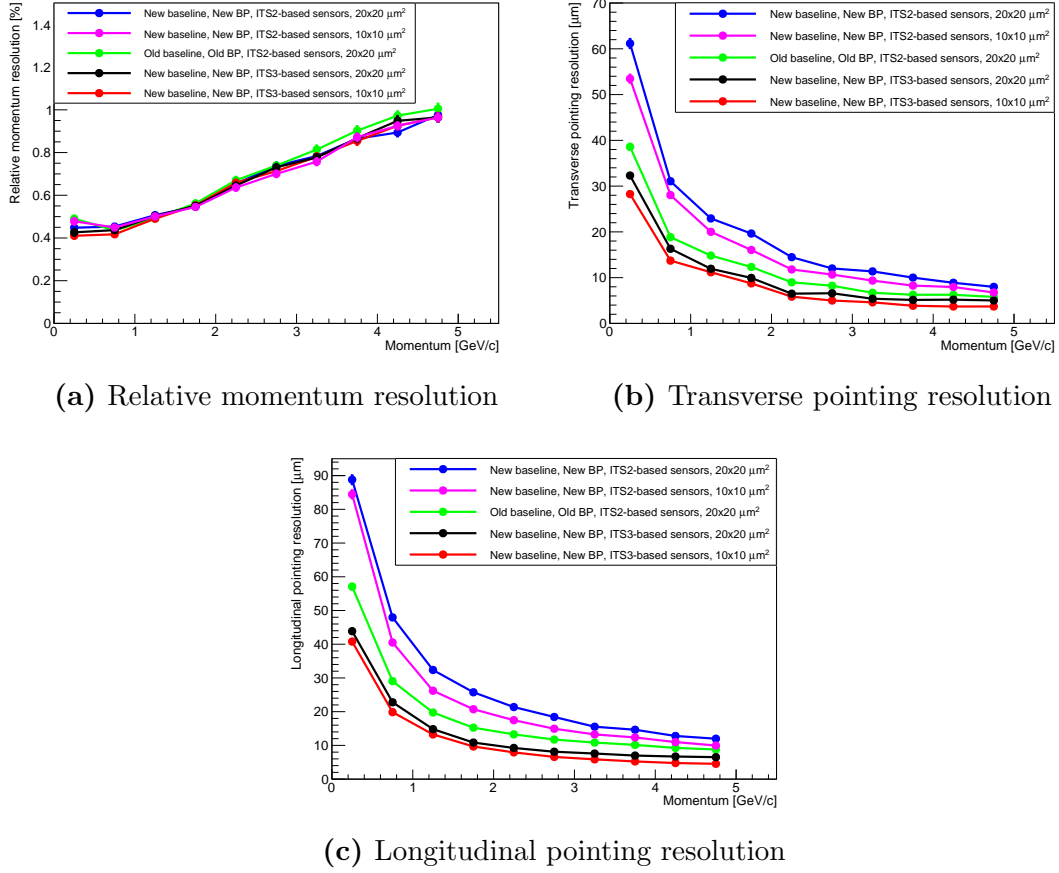


Figure 6.6: Relative momentum resolution and pointing resolutions versus momentum, comparing the old baseline layout with the new baseline layout and beampipe radius. The green curve represents the old baseline layout, and the other curves represent the new baseline layout with different sensor thicknesses and pixel sizes.

curve, and the black curve to the red curve, it is clear that a smaller pixel size improves pointing resolution. Comparing the blue curve to the black curve (or the magenta curve to the red curve), it is clear that a lower material thickness improves the pointing resolutions more than a decrease in pixel size does. Even with a pixel size of $20 \times 20 \mu\text{m}^2$, the ITS3-based sensors outperform the old baseline layout in spite of the increased beampipe radius. The projected ITS3 sensor pixel size is $10 \times 10 \mu\text{m}^2$, so a sensor with a $20 \times 20 \mu\text{m}^2$ pixel size based on the ITS3 technology will likely not be available, but it is useful to determine that a low material budget is more important than a small pixel size in this configuration.

Using the same dataset and analysis method, a comparison is also made of the angular resolutions at the vertex position for the different configurations, in both the θ and φ angles (see Section 2.2.4 for their definitions). A good angular resolution is of importance for the performance of particle identification detectors, and it is also of interest for reconstruction of the kinematic variables of a collision (see Section 3.1). The results of the angular resolution study are shown in Figure 6.7.

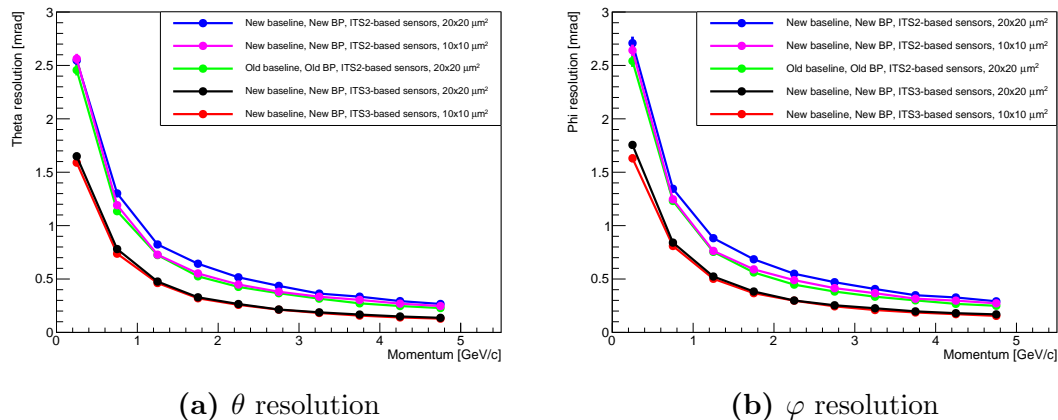


Figure 6.7: Angular resolutions versus momentum, comparing the old baseline layout with the new baseline layout and beampipe radius. The green curve represents the old baseline layout, and the other curves represent the new baseline layout with different sensor thicknesses and pixel sizes.

From these results, it can be seen that the inner detector radius only has a small impact (by comparing the three curves using ITS2-based sensors). The pixel size also appears to only have a small impact on the angular resolutions, while the detector material budget has a significant impact; the red and black curves (i.e. the results from using ITS3-based sensors) have the best angular resolution in both θ and φ out of the tested layouts, for both of the tested pixel sizes.

In conclusion, it is essential to keep the sensor material thickness low in order to maintain the resolutions with a large-radius beampipe at low momenta. The simulations show that the projected performance of the ALICE ITS3 sensor technology will remove the degradation of performance induced by the larger beampipe radius.

6.3 Detector resolution parametrisation

The EIC Yellow Report PWG has produced requirements on the tracking resolutions, taken from the strictest requirements of the currently investigated physics channels. The study presented here investigates the performance of different tracker layouts, and compares it to these requirements. Numerical values of the detector resolutions are extracted by fitting functions to the resolution data, giving parametrisations of the detector performances. The resulting functions are then presented to the PWG, to be implemented in “fast simulations” (i.e. analytical simulations using parametrisations of detector performances, rather than fully simulated detectors) to evaluate the impact of different tracker designs on the EIC physics capabilities. Studies are again made for relative momentum resolution and transverse and longitudinal pointing resolution, analogous to the studies presented in Chapter 5.

6.3.1 Experimental setup

The resolution studies are carried out in the central ($-1.0 \leq \eta \leq 1.0$), forward ($1.0 \leq \eta \leq 2.5$), and far-forward ($2.5 \leq \eta \leq 3.5$) regions, using the following parameters:

- Particle: π^+
- Transverse momentum range: 0 to 30 GeV/c (uniform in p_T)
- Number of events: 1 000 000
- Magnetic field: 1.5 T and 3.0 T, uniform
- Silicon pixel size: $10 \times 10 \mu\text{m}^2$

Studies are made for relative momentum resolution in both full momentum and transverse momentum (henceforth referred to as “relative transverse momentum resolution”), and both transverse and longitudinal pointing resolution. The study is performed for the three main layouts presented in Section 6.1.3. The layout with MPGD layers is only investigated in the central region, as endcaps for it are not yet implemented in the simulation framework, making measurements in the forward region unrepresentative of a realistic layout. Studies of the forward region of this layout are a subject for future work, once endcap detectors for it are implemented.

Equations 6.1 and 6.2 show the fitting functions used for the relative momentum resolution and the transverse pointing resolution, respectively. The fitting parameters are called A and B , and are the parameters used in this form to approximate detector performance for future fast simulations.

$$\frac{\sigma_p}{p} = A \cdot p \oplus B = \sqrt{(A \cdot p)^2 + B^2} \quad (6.1)$$

$$\frac{\sigma_{xy}}{p_T} = \frac{A}{p_T} \oplus B = \sqrt{\left(\frac{A}{p_T}\right)^2 + B^2} \quad (6.2)$$

For the fit of relative transverse momentum resolution, the momentum in Equation 6.1 is replaced with the transverse momentum. Equation 6.2 is also used to fit the longitudinal pointing resolution.

The requirements presented by the EIC Yellow Report PWG relevant to the inner tracking system are summarised in Table 6.4 [74]. The fit results are compared to these to determine whether the resolutions achieved by the different detector concepts are adequate.

As the tested detector concepts are all symmetric around the interaction point, the performance in the forward and backward regions will be identical. Only the forward region is thus studied and presented here. When the PWG requirements differ in the forward and backward regions, the strictest requirement is used for performance comparisons.

η interval	Relative momentum resolution [%]	Transverse pointing [μm]
$-3.5 \leq \eta \leq -2.5$	$A = 0.1, B = 0.5$	$A = 30, B = 40$
$-2.5 \leq \eta \leq -1.0$	$A = 0.05, B = 0.5$	$A = 30, B = 20$
$-1.0 \leq \eta \leq 1.0$	$A = 0.05, B = 0.5$	$A = 20, B = 5$
$1.0 \leq \eta \leq 2.5$	$A = 0.05, B = 1.0$	$A = 30, B = 20$
$2.5 \leq \eta \leq 3.5$	$A = 0.05, B = 2.0$	$A = 30, B = 40$

Table 6.4: Physics Working Group requirements on relative momentum resolution and transverse pointing resolution. There is no requirement on longitudinal pointing resolution. The requirement on relative transverse momentum resolution is the same as for relative momentum resolution. A and B are parameters of Equations 6.1 and 6.2.

6.3.2 Results

Results are presented in the form of resolution plots here, drawn along with the curve that would arise when using the PWG requirement parameters in Equation 6.1 or 6.2. Detailed tables with the fit results for the different configurations are presented in Appendix C. Figure 6.8 shows the relative momentum resolutions (i.e. using the full momentum p), and Figure 6.9 shows relative transverse momentum resolutions. Figure 6.10 shows transverse pointing resolution. In all plots, both results for 1.5 T and 3.0 T are present. The colours represent different detector layouts, and the 1.5 T results are continuous lines whereas the 3.0 T results are dashed lines and a darker colour. A red dashed line without data points indicates the PWG requirement parametrisation. Each figure has three subplots, indicating the different pseudorapidity intervals tested. As the MPGD layout only has results in the central region, and the longitudinal pointing resolution has no PWG requirements, those results are not shown here but can be found tabulated in Appendix C.

The plots of relative momentum resolution show that the TPC baseline layout is the best at low momenta in the central and forward regions (i.e. at momenta below 5 GeV/c in the central region, and below 2.5 GeV/c in the forward region). It is not the case in the far-forward region however, where the TPC is no longer a factor (the furthest TPC edge is at $\eta = 2.36$). Here the all-silicon concepts outperform the TPC concept, due to their larger-radius disks. This matches the conclusions drawn from the work presented in Section 5.3.10. Compared to the PWG requirements in the central region, a 1.5 T magnetic field is insufficient for all the tested layouts; the relative momentum resolution is worse than the requirement over most of the investigated momentum range. A 3 T field makes all layouts perform within the requirement, however. This is also true in the forward and far-forward regions. In the forward region, the all-silicon layouts match the requirement already at 1.5 T, whereas the TPC baseline only does so at momenta below 3 GeV/c.

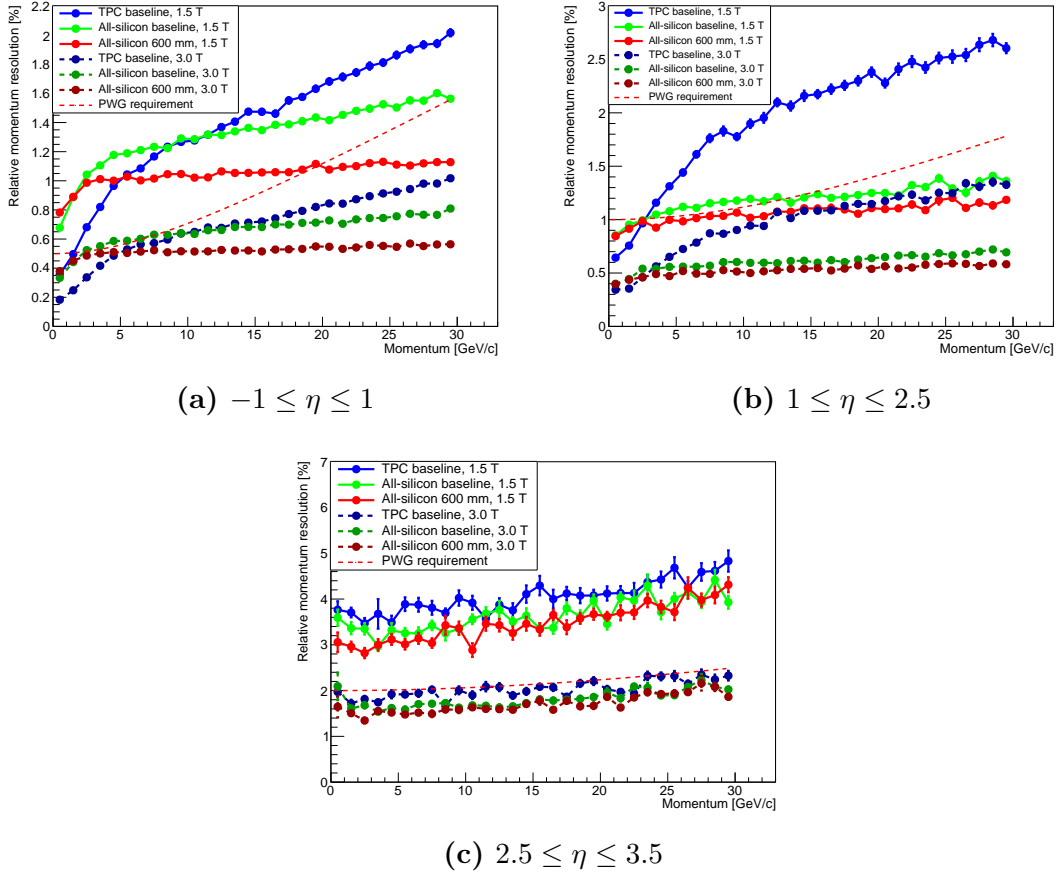


Figure 6.8: Relative momentum resolution for the TPC baseline, the all-silicon baseline, and the 600 mm outer radius all-silicon layout, for 1.5 T and 3.0 T magnetic fields. The PWG requirement is also shown, as a dashed red line.

The relative transverse momentum plots show the same trends in the central region. In the forward region however, the TPC baseline is worse than the PWG requirement at transverse momenta above 5 GeV/c. In the far-forward region, none of the concepts can satisfy the PWG requirement, even with a 3 T magnetic field.

From looking at the transverse pointing resolution, it is immediately clear that there is no significant difference between the different concepts, and they all outperform the PWG requirements by a large margin in all of the investigated regions.

6.3.3 Discussion

The transverse pointing resolution far exceeds the requirements in the investigated intervals. This indicates that a larger pixel size than $10 \times 10 \mu\text{m}^2$ could potentially be used, if it is necessary in order to keep the detector material budget low. A larger pixel size can give a lower power density in the sensor, thus lowering the material. However, the ITS3 technology is predicted to have a pixel size of $10 \times 10 \mu\text{m}^2$, so

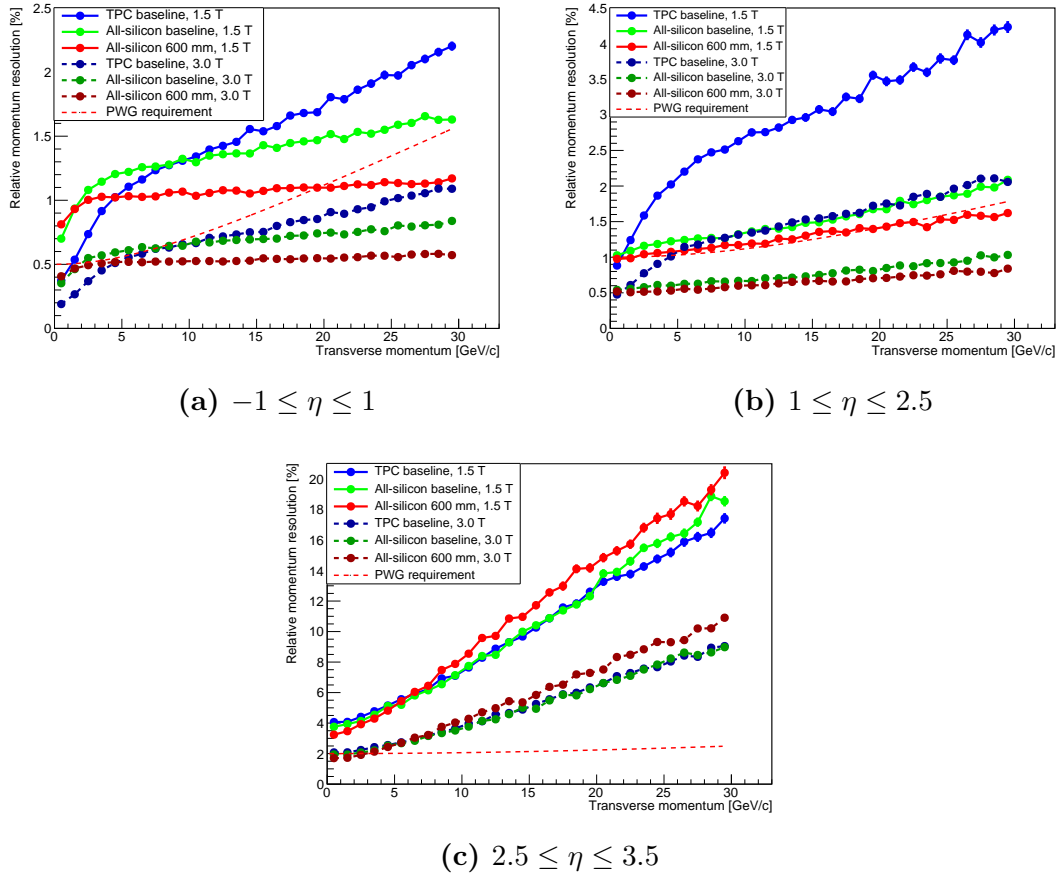


Figure 6.9: Relative transverse momentum resolution for the TPC baseline, the all-silicon baseline, and the 600 mm outer radius all-silicon layout, for 1.5 T and 3.0 T magnetic fields. The PWG requirement is also shown, as a dashed red line.

a larger pixel sensor with the projected low material budget may not be available. For the relative momentum resolution to be within the requirements in all regions, a 3.0 T magnetic field is required for all the investigated detector configurations, which has implications for the detector design and possible need for a tuneable magnet that can provide multiple different field strengths for different physics focuses.

The beampipe used in the simulations is the model that was current in March 2020. There are discussions ongoing about changes to the beampipe, which could include an extended central beryllium section. This would allow for better detector coverage in the far-forward and far-backward regions, while also reducing the material brought on by the beampipe in those regions. The beampipe updates are not available in simulations currently however, so the far-forward results presented here may be different in future studies.

In these studies the magnetic field used is uniform, which is not realistic in the far-forward region, where the field lines are more curved in real solenoidal magnets. The far-forward results might thus differ when a realistic magnetic field map is

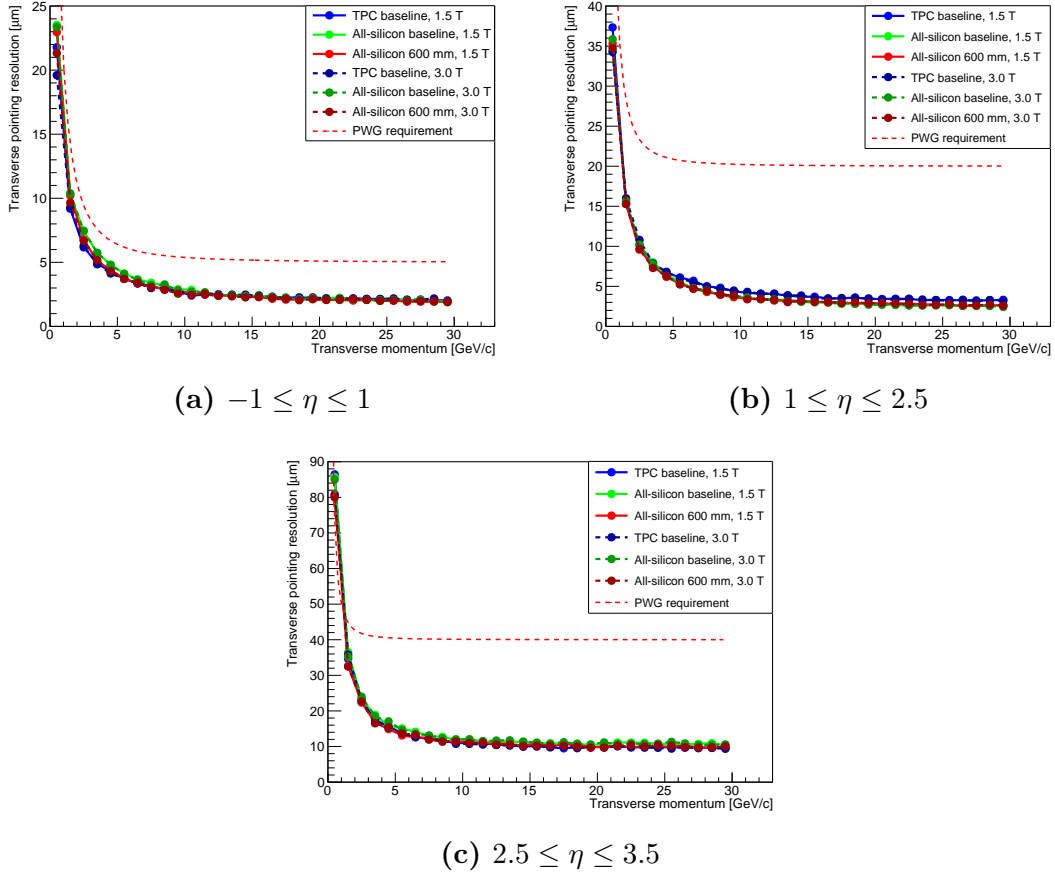


Figure 6.10: Transverse pointing resolution for the TPC baseline, the all-silicon baseline, and the 600 mm outer radius all-silicon layout, for 1.5 T and 3.0 T magnetic fields. The PWG requirement is also shown, as a dashed red line.

used. This was not possible at the time of the simulations, but it is an important subject for future work.

The resolutions of a TPC will also change with the magnetic field strength [36], which is not reflected in these simulations. The charge dispersion will decrease with an increased field, and the resolution will thus improve. In the simulations carried out here the TPC resolution is kept constant regardless of the magnetic field.

The simulations are thus not optimised, and present an idealised scenario neglecting effects that can both improve and deteriorate the resolutions. The results presented here give a good impression of the possible resolutions that can be reached and how they compare for different tracker layouts, but further work is required to get more accurate results. The impact of the different tracker layout performance with regard to open charm reconstruction is studied in Section 6.6, using simulations with the same limitations on magnetic field and TPC performance as discussed here.

6.4 Minimum momentum investigation

The minimum momentum that can be detected is an important parameter of a detector as certain physics channels, such as certain ϕ meson decays and D^{*+} decays, produces “slow” decay products with low transverse momentum (down to the order of 10 MeV/c) [31]. An investigation is thus made of the reconstruction efficiency of different detector concepts at low transverse momentum.

6.4.1 Experimental setup

Two detector concepts are investigated here; the silicon plus TPC baseline (see Section 6.1.3.1) and the all-silicon baseline (see Section 6.1.3.2). The study is made using both positive pions and positive kaons, since charged pions and kaons are the main low-momentum particles expected to be created in EIC collisions. The particles are generated in the following parameter space:

- Transverse momentum range: 0 to 0.5 GeV/c
- Pseudorapidity range: $-4.0 \leq \eta \leq 4.0$
- Number of events: 1 000 000
- Magnetic field: 1.5 T and 3.0 T

The detector coverage in pseudorapidity is smaller than this range, and this study will aid in determining the pseudorapidity edges of detector efficiency. Both of the magnetic field strengths considered for the EIC detectors, 1.5 T and 3.0 T, are investigated. Section 6.3 showed that a 3 T field is needed to reach adequate momentum resolution for the strictest physics channels of the EIC, but such a high field may result in a higher minimum momentum that can be detected, which is detrimental to several physics channels. Four runs are thus made for each detector layout; kaons and pions individually, for the two magnetic fields. The full possible pseudorapidity range is investigated to find the minimum reconstructable momentum in different pseudorapidity regions, and indicate where effective detector coverage ends in the tested layouts.

Reconstruction of the particle tracks is made with a basic Kalman filter algorithm built into Fun4All. This algorithm is relatively simplistic, and better performing EIC-specific tools will be developed as the project moves forward, but it gives a good indication of the reconstruction efficiency possible with the generic algorithms that currently exist. The results of this study can thus be viewed as a worst case scenario of the minimum reconstructable momentum.

For each generated particle, a check is made of whether or not the track can be reconstructed. Histograms of the generated number of non-reconstructed events are made, in bins of transverse momentum and pseudorapidity. These are then divided by histograms containing all generated events, giving a fraction of reconstructed events between 0 and 1 for each bin. Projections are then made in bins of pseudorapidity, and the point in transverse momentum where at least 90% of tracks are reconstructed is extracted.

6.4.2 Results and discussion

Figure 6.11 shows a map of the reconstructed fraction, with pseudorapidity on the x-axis and transverse momentum on the y-axis, for the silicon plus TPC baseline. The colour indicates the reconstructed fraction, from 0 to 1.

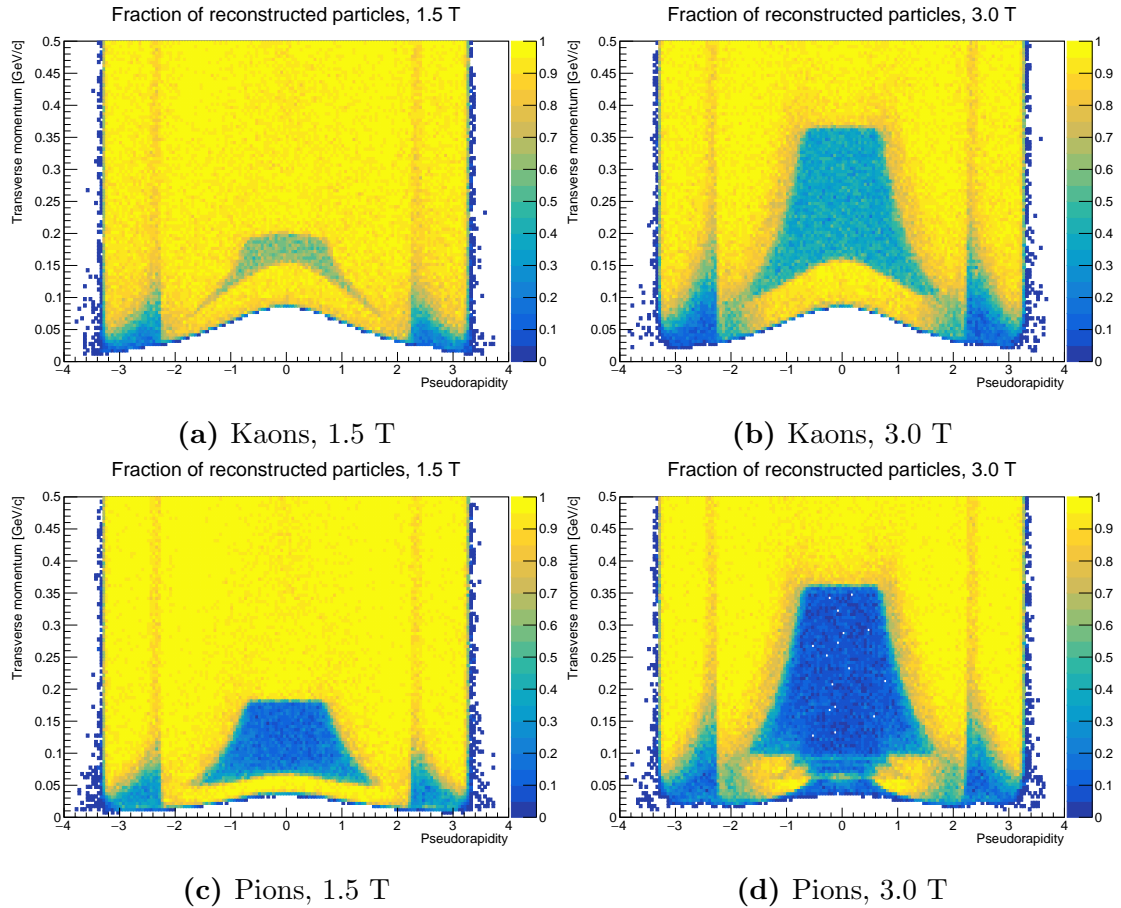


Figure 6.11: Reconstructed fraction of particles, versus transverse momentum (y-axis) and pseudorapidity (x-axis), for kaons and pions, using the baseline silicon plus TPC layout.

The plots show some features that can be explained by looking at the geometry of the detector in more detail. Table 6.5 shows the transverse momentum limits for spiralling within the detector. This is shown with lines drawn on the reconstructed fraction for kaons in a 1.5 T field in Figure 6.12(a). In Figure 6.12(b), lines indicating the pseudorapidity edges of different detector parts are shown. As the detector is symmetric around the interaction point, only half of the investigated pseudorapidity range is shown here in order to show the separation of the vertical lines better. Figure 6.13 shows a sketch of the forward region of the detector, with the pseudorapidity edges marked. The line colours in Figures 6.12 and 6.13 represent different detector parts; blue lines indicate the five barrel layers, magenta is the TPC inner and outer edges, and green and red indicate disk outer and inner radii, respectively. The pseudorapidity range between green and red lines are thus

Place	Radius	Spiralling p_T , 1.5 T	Spiralling p_T , 3.0 T
Layer 1	36.4 mm	8.18 MeV/c	16.4 MeV/c
Layer 2	44.5 mm	10.0 MeV/c	20.0 MeV/c
Layer 3	52.6 mm	11.8 MeV/c	23.7 MeV/c
Layer 4	133.8 mm	30.1 MeV/c	60.2 MeV/c
Layer 5	180.0 mm	40.5 MeV/c	80.9 MeV/c
TPC start	200.0 mm	45.0 MeV/c	89.9 MeV/c
TPC end	780.0 mm	175.4 MeV/c	350.8 MeV/c

Table 6.5: Transverse momentum for spiralling at different detector parts of the TPC baseline, for fields of 1.5 T and 3.0 T. All momenta below the presented values will spiral within the radius of the given detector layer.

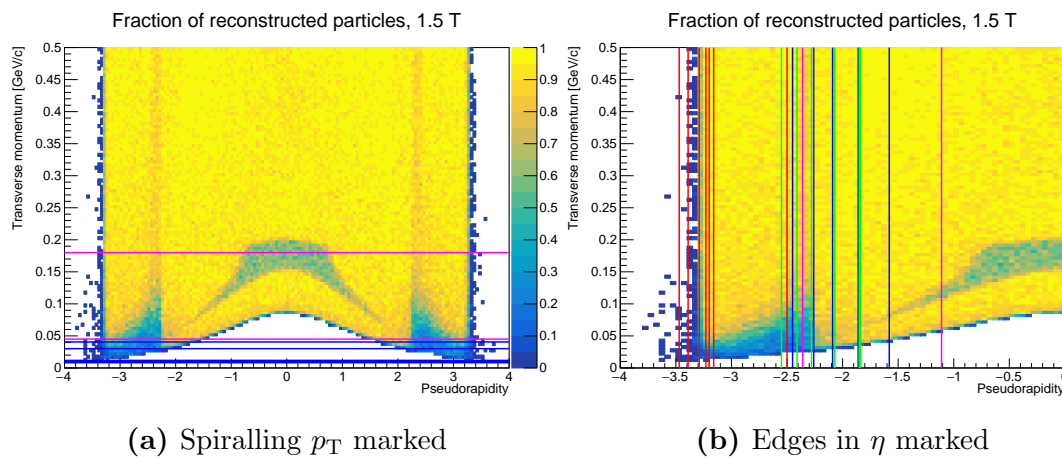


Figure 6.12: Reconstructed fraction of particles, versus transverse momentum (y-axis) and pseudorapidity (x-axis), for kaons in a 1.5 T magnetic field using the silicon plus TPC baseline layout. Spiralling momentum and pseudorapidity edges are marked by lines, where blue indicates silicon barrel layers, magenta indicates TPC inner and outer edges, green indicates disk outer radii, and red indicates disk inner radii. Lines in pseudorapidity are only drawn in the negative direction, as the detector is symmetric around zero.

where disk material is present. All three of the disks closest to the interaction point have the outer edge at $\eta = 1.84$. The low-efficiency region in the centre of the reconstructed fraction maps comes from spiralling within the TPC. Such spiralling creates a high density of hit points, which the basic reconstruction algorithm used is occasionally unable to utilise for reconstructing a track. It is important to note that the y-axis is the generated momentum rather than the reconstructed momentum. As the particles lose energy when traversing material, spiralling will occur within the detector for particles with slightly higher generated p_T than what is shown in Table 6.5. The central inefficiency arising from spiralling within the TPC thus extends slightly above the magenta line indicating the spiralling momentum at the TPC outer radius in Figure 6.12(a).

The yellow “band” of efficiency under the central inefficiency from the TPC comes

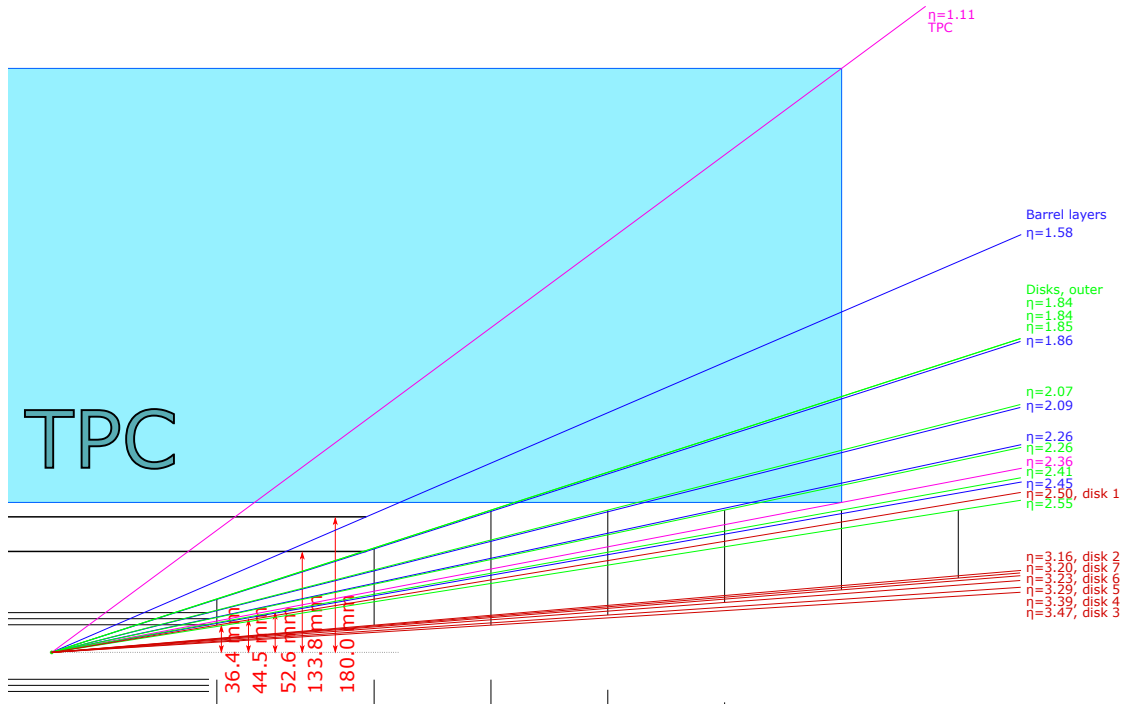


Figure 6.13: Sketch of the forward region of the silicon plus TPC baseline layout, with pseudorapidity edges of different detector parts marked.

from the silicon vertex tracker barrel layers. This has been verified by running the analysis without the silicon vertex tracker present (i.e. with just the TPC) and comparing the results. In the white regions, no events are reconstructed. This region goes to higher p_T in the central region than further out in pseudorapidity. This is due in part to the increase in total momentum as the pseudorapidity increases (as the p_T remains the same, but the direction of the total momentum is more in the longitudinal direction), but also due to the track of a spiralling particle being more “extended” in the longitudinal direction. As the spiral is extended further, it becomes easier to unambiguously separate the detector hit points and extract a track.

In the pseudorapidity direction, it can be seen that reconstruction efficiency is decreased when all but one of the barrel layers are missed, and several disks are hit, increasing the material.

Looking at the reconstructed fraction for 1.5 T and 3.0 T magnetic fields, it is clear that the inefficiency regions are larger when using a 3.0 T field. This is due to the increased number of spiralling particles as the magnetic field increases. The upper edge of the central inefficiency region doubles as the field doubles, which is in agreement with theory. For kaons, the “band” of efficiency below the TPC-induced inefficiency region remains almost the same however, indicating that the used silicon vertex tracker design (with three inner layers) is good at handling spiralling kaons.

Comparing the fraction of reconstructed particles for kaons and pions, it can be

seen that the central inefficiency regions are larger for pions. The lowest detectable transverse momentum is lower however. At a magnetic field strength of 3.0 T, reconstruction efficiency for pions decreases at the lowest p_T near $\eta = 0$, despite the presence of the silicon vertex tracker layers. For a fixed momentum pions move faster than kaons due to their smaller mass, which likely gives rise to more hits in a narrow spiral in the central region, making track reconstruction more difficult. The pions also scatter less, and lose less energy, leading to more detector hits in a small region.

Figure 6.14 shows the same reconstruction efficiency maps for an all-silicon baseline. Comparing these results to the TPC baseline results, it is clear that the

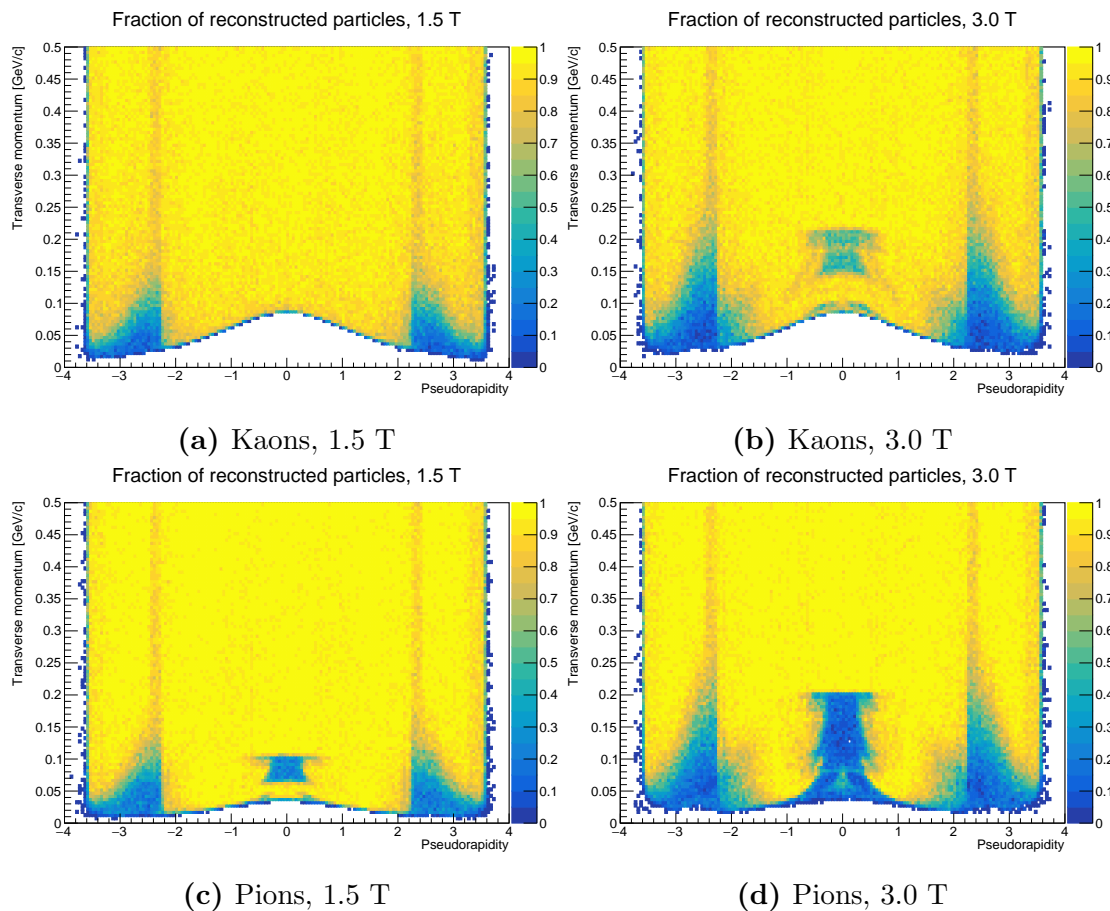


Figure 6.14: Reconstructed fraction of particles, versus transverse momentum (y-axis) and pseudorapidity (x-axis), for kaons and pions, using the all-silicon baseline layout.

central inefficiency comes mainly from the TPC. For a 3.0 T magnetic field a central inefficiency appears for kaons with the all-silicon baseline layout as well, but it is much less severe. The minimum reconstructable momenta are very similar, due to the three inner barrel layers being identical for the two different layouts. The central inefficiency again increases for pions and increasing magnetic field strength, due to an increased number of hit points from spiralling particles reducing the efficiency of the simple reconstruction algorithm used.

For the TPC baseline layout, projections are made in bins of pseudorapidity in order to find numerical values of the minimum reconstructable transverse momentum in different detector regions. Two projection examples for kaons in the TPC baseline are shown in Figure 6.15, for pseudorapidity intervals of $0.0 \leq \eta \leq 0.5$ and $2.0 \leq \eta \leq 2.5$. The metric for minimum detectable momentum is taken as

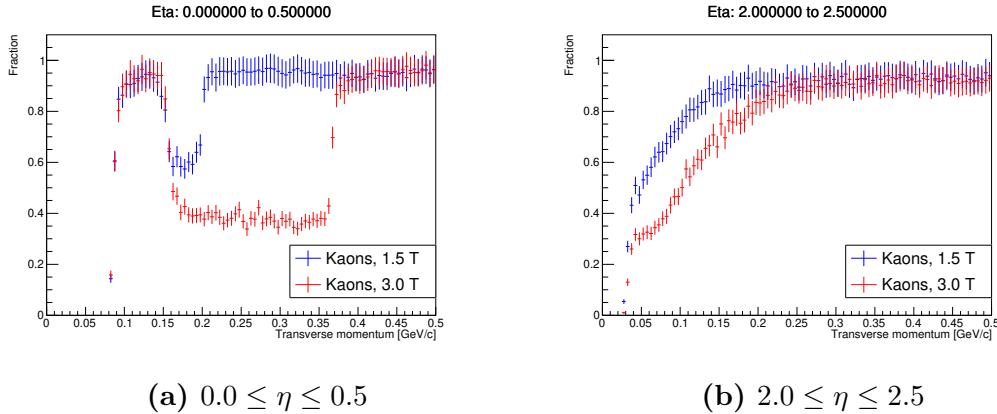


Figure 6.15: Fraction of reconstructed particles versus transverse momentum for kaons in the two investigated magnetic fields using the TPC baseline layout, for different pseudorapidity intervals.

the points where at least 90% of the particles are reconstructed. It is however important to note that a lower fraction of particles are always reconstructed once a clear threshold value in momentum is passed (i.e. at 80 MeV/c in the interval $0.0 \leq \eta \leq 0.5$, and 30 MeV/c in the interval $2.0 \leq \eta \leq 2.5$). In the projection at central pseudorapidities, the inefficiency from the spiralling in the TPC is obvious. There are thus two regions where at least 90% of particles are reconstructed. Table 6.6 shows the resulting minimum reconstructable transverse momenta for different pseudorapidity intervals for kaons using the TPC baseline layout, and Table 6.7 shows the same for pions.

The reconstruction algorithm used needs a particle mass assumption, and it has been left at the default value of the pion mass for the studies carried out. A test has been made comparing results for kaons when using the kaon mass assumption instead, and the difference is negligible for this study.

The main conclusion that can be drawn from this study is that it will be challenging to reconstruct the lowest momentum particles with high efficiency with a beampipe of the current radius, especially if a 3.0 T magnetic field is used. Improved reconstruction algorithms may be able to improve the minimum transverse momentum thresholds though, by handling track spiralling better. This should also make it possible to remove the inefficiency from spiralling in the central region, which would make it possible to detect particles with transverse momenta above 140 MeV/c with high efficiency across the full pseudorapidity range, for a 1.5 T magnetic field (and much lower p_T in some pseudorapidity regions).

η interval	Min- p_T , 1.5 T	Min- p_T , 3.0 T
$0.0 \leq \eta \leq 0.5$	$100 \text{ MeV}/c \leq p_T \leq 150 \text{ MeV}/c$ $p_T \geq 210 \text{ MeV}/c$	$100 \text{ MeV}/c \leq p_T \leq 150 \text{ MeV}/c$ $p_T \geq 380 \text{ MeV}/c$
$0.5 \leq \eta \leq 1.0$	$90 \text{ MeV}/c \leq p_T \leq 120 \text{ MeV}/c$ $p_T \geq 200 \text{ MeV}/c$	$90 \text{ MeV}/c \leq p_T \leq 120 \text{ MeV}/c$ $p_T \geq 380 \text{ MeV}/c$
$1.0 \leq \eta \leq 1.5$	$70 \text{ MeV}/c \leq p_T \leq 80 \text{ MeV}/c$ $p_T \geq 130 \text{ MeV}/c$	$70 \text{ MeV}/c \leq p_T \leq 100 \text{ MeV}/c$ $p_T \geq 290 \text{ MeV}/c$
$1.5 \leq \eta \leq 2.0$	$p_T \geq 50 \text{ MeV}/c$	$p_T \geq 160 \text{ MeV}/c$
$2.0 \leq \eta \leq 2.5$	$p_T \geq 140 \text{ MeV}/c$	$p_T \geq 220 \text{ MeV}/c$
$2.5 \leq \eta \leq 3.0$	$p_T \geq 110 \text{ MeV}/c$	$p_T \geq 180 \text{ MeV}/c$
$3.0 \leq \eta \leq 3.25$	$p_T \geq 100 \text{ MeV}/c$	$p_T \geq 110 \text{ MeV}/c$

Table 6.6: Transverse momentum regions where over 90% of particles are reconstructed, for different pseudorapidity intervals. The table shows results for positive kaons in the silicon plus TPC baseline layout. The highest pseudorapidity interval is smaller, since no transverse momenta reach 90% reconstruction efficiency above $\eta = 3.25$.

η interval	Min- p_T , 1.5 T	Min- p_T , 3.0 T
$0.0 \leq \eta \leq 0.5$	$50 \text{ MeV}/c \leq p_T \leq 65 \text{ MeV}/c$ $p_T \geq 190 \text{ MeV}/c$	$p_T \geq 370 \text{ MeV}/c$
$0.5 \leq \eta \leq 1.0$	$50 \text{ MeV}/c \leq p_T \leq 60 \text{ MeV}/c$ $p_T \geq 190 \text{ MeV}/c$	$p_T \geq 380 \text{ MeV}/c$
$1.0 \leq \eta \leq 1.5$	$40 \text{ MeV}/c \leq p_T \leq 50 \text{ MeV}/c$ $p_T \geq 120 \text{ MeV}/c$	$50 \text{ MeV}/c \leq p_T \leq 60 \text{ MeV}/c$ $p_T \geq 280 \text{ MeV}/c$
$1.5 \leq \eta \leq 2.0$	$30 \text{ MeV}/c \leq p_T \leq 50 \text{ MeV}/c$ $p_T \geq 70 \text{ MeV}/c$	$p_T \geq 160 \text{ MeV}/c$
$2.0 \leq \eta \leq 2.5$	$p_T \geq 130 \text{ MeV}/c$	$p_T \geq 200 \text{ MeV}/c$
$2.5 \leq \eta \leq 3.0$	$p_T \geq 100 \text{ MeV}/c$	$p_T \geq 150 \text{ MeV}/c$
$3.0 \leq \eta \leq 3.25$	$p_T \geq 60 \text{ MeV}/c$	$p_T \geq 110 \text{ MeV}/c$

Table 6.7: Transverse momentum regions where over 90% of particles are reconstructed, for different pseudorapidity intervals. The table shows results for positive pions in the silicon plus TPC baseline layout. The highest pseudorapidity interval is smaller, since no transverse momenta reach 90% reconstruction efficiency above $\eta = 3.25$.

6.4.3 Resolution study

Utilising the dataset generated for the minimum momentum study, an investigation can be made into the detector resolution at very low momenta across the full pseudorapidity range. The relative transverse momentum resolution and the transverse and longitudinal pointing resolutions are extracted versus pseudorapidity for the silicon plus TPC baseline detector. This is done for both kaons and pions in the same way as is described in Section 5.2, and the results for both particle flavours and magnetic fields are plotted in the same figure.

Figure 6.16 shows the relative momentum resolution and the transverse pointing resolution versus pseudorapidity. Figure 6.17 shows the longitudinal pointing resolution versus pseudorapidity, along with a zoomed-in version of the same results. A dashed line connecting the data points indicates a 3 T magnetic field.

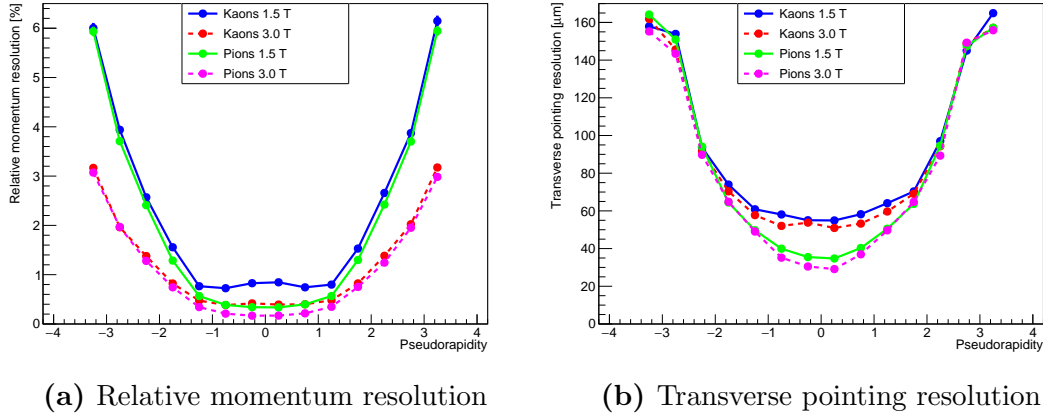


Figure 6.16: Relative momentum resolution and transverse pointing resolution versus pseudorapidity for pions and kaons and two different magnetic fields; 1.5 T and 3.0 T.

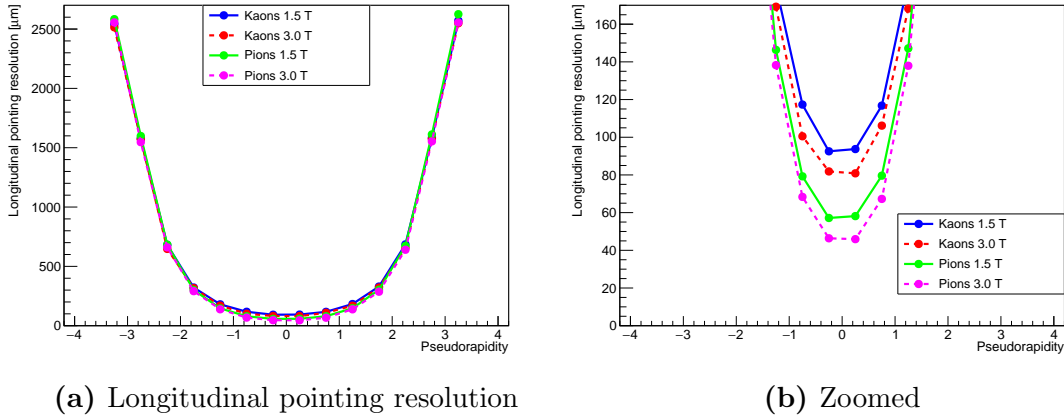


Figure 6.17: Longitudinal pointing resolution versus pseudorapidity for pions and kaons and two different magnetic fields; 1.5 T and 3.0 T.

In all the resolutions, it can be seen that pions are better resolved than kaons. This is due to the higher mass of the kaons, meaning they are slower (for a given p_T), and thus experience more multiple scattering which is inversely proportional to β (see Section 2.1.3). The relative momentum resolution for all curves deteriorates faster outside of $|\eta| = 1.11$, indicating a strong correlation with track length within the TPC, as $|\eta| = 1.11$ is the pseudorapidity of the TPC upper corners. It can also be seen that the magnetic field strength has little impact on pointing resolution outside of the central region where the TPC is fully involved, but affects relative momentum resolution over the full investigated pseudorapidity interval.

In the central region the transverse pointing resolution for these very low transverse

momenta is down to $30 \mu\text{m}$ for pions and $50 \mu\text{m}$ for kaons. As pseudorapidity increases the resolution deteriorates however, going up to $160 \mu\text{m}$ at the highest detectable regions.

The longitudinal pointing resolution is very poor at large pseudorapidities, going up to a millimetre at $\eta \sim 2.5$. In the zoomed-in plot of the central region however, it can be seen that the resolution goes down to $50 \mu\text{m}$ for pions and $80 \mu\text{m}$ for kaons. The deterioration is severe as η increases, however.

The conclusion of this study is that while the reconstruction efficiency is good in the far-forward region above transverse momenta of approximately $100 \text{ MeV}/c$, the detector resolution is very poor in this region for particles with low transverse momenta. This is important to keep in mind, as physics channels require both a minimum reconstructable momentum and a resolution with which particles can be reconstructed.

6.5 Event generation

Physics events for studies of detector performance under more realistic conditions than the single-particle simulations are generated using Pythia 8 (see Section 6.1.2.2). This enables the study of reconstruction of realistic physics observables in a realistic background environment. This section describes studies made at the event generator level. The effect of propagating the generated events through different detector layouts is described in Section 6.6.

6.5.1 Experimental setup

As discussed in Section 3.3, studies of open charm physics are heavily affected by tracker performance, and are frequently used as benchmarking studies for trackers. For these reasons, open charm is a suitable subject for study as part of this work. The main process under investigation here is charm quark production via photon-gluon fusion (see Section 3.3.1). In particular, the D^0 mesons produced via this process and subsequent hadronisation are studied, as they provide a good signal for reconstruction studies (i.e. a decay with a good branching ratio, and low multiplicity). The physics process for this (named `PhotonParton:ggm2ccbar` in Pythia) is thus activated. Events are generated for four different energy combinations of electrons and protons, as suggested by the EIC Yellow Report PWG [132]. The energy combinations are presented in Table 6.8, and include the lowest possible EIC energy, the highest possible EIC energy, and two intermediate energies.

Electron energy	Proton energy	Centre-of-mass energy (\sqrt{s})
5 GeV	41 GeV	28.65 GeV
5 GeV	100 GeV	44.73 GeV
10 GeV	100 GeV	63.25 GeV
18 GeV	275 GeV	140.72 GeV

Table 6.8: Beam energies used in generating Pythia events.

For each of these energies, 500 000 events are generated. Data from the event generation are saved, and can either be studied directly or used as input in simulations in the Fun4All framework.

6.5.2 Particle distributions

Studies have been made of the distributions of D^0 mesons and D^0 decay products, in terms of several different variables. The decay product distributions in pseudorapidity and transverse momentum are shown in Figure 6.18, and utilised in Section 6.5.3 to determine the fraction of events that are within the detector acceptance. The figure shows both all D^0 decay products, and specifically the pion-kaon pairs created in the main decay channel of interest ($D^0 \rightarrow K^- + \pi^+$ and its charge conjugate).

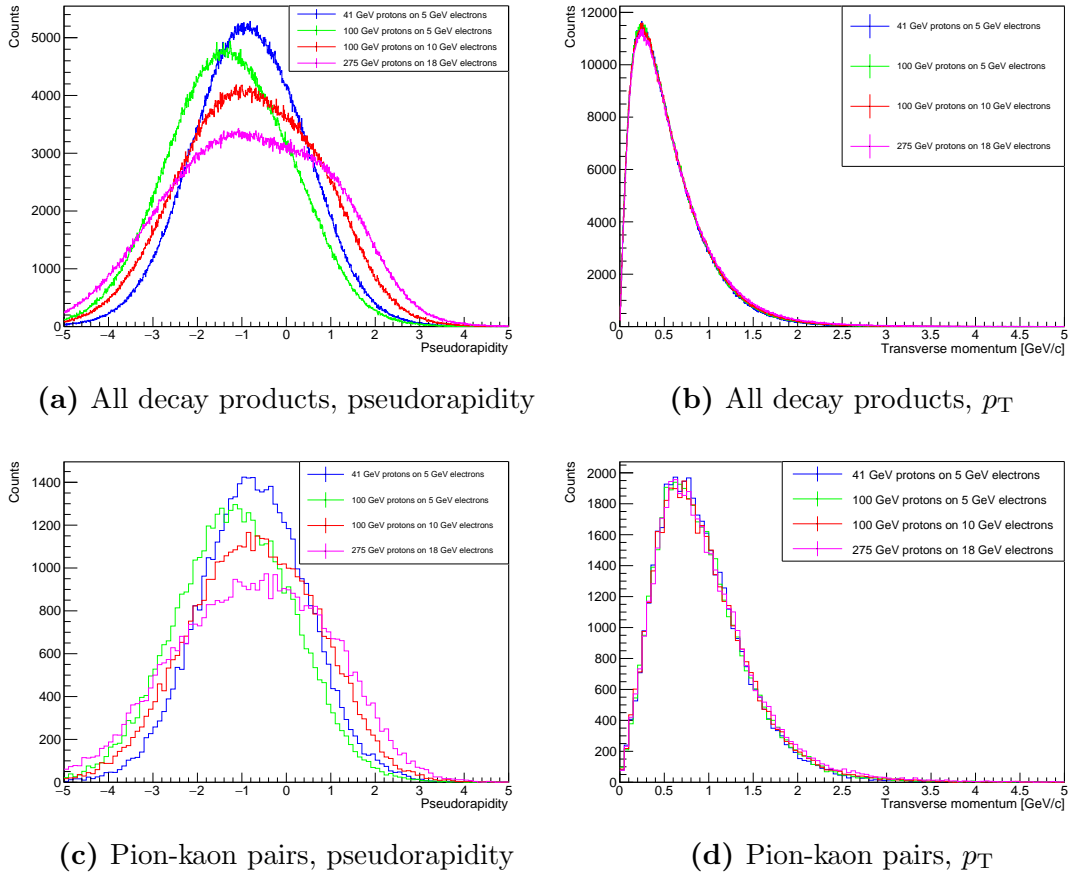


Figure 6.18: Pseudorapidity distributions and transverse momentum distributions of D^0 decay products, for the four investigated collision energies. In the top two plots all decay products are shown, and in the bottom two the pion-kaon pairs are shown.

In the generated events, the incoming electrons travel in the positive direction, and the protons in the negative direction. As the energy asymmetry grows in favour of the proton, it is thus natural that more decay products are boosted in the negative direction. This is most evident by comparing the green pseudorapidity

curve (for the collision of 5 GeV electrons and 100 GeV protons) to the others; this pseudorapidity distribution is shifted more into negative pseudorapidities than both the blue curve and the red curve, which have the same energy in one of the beams. The pseudorapidity distributions for pion-kaon pairs look similar to the distributions containing all decay products (but naturally have fewer counts).

The transverse momentum distributions look very similar for all different energies. This is due to the collisions being generated head-on, meaning a change in energy mainly changes the longitudinal momentum component in the Pythia generation. In more realistic collisions for the EIC there will be a non-zero crossing angle, and generation of such events are an important subject for future work. In these initial event simulations however, only head-on collisions are used. There is a clear difference between the distributions for all decay products and the pion-kaon pairs in transverse momentum, as can be seen by comparing Figures 6.18(b) and 6.18(d). The pion-kaon pairs have a higher transverse momentum, which again makes this a suitable decay channel for investigation as the detector efficiency increases with higher transverse momentum. This can also be seen in Section 6.5.3, where detector acceptance in relation to the generated physics events is investigated.

Certain heavy particles generated in a collision will decay after travelling a distance within the detector. Figure 6.19 shows an example event, displayed using a Python script showing position in the x-direction and z-direction. In the figure the primary (collision) and secondary (decay) vertices can be seen, and a D^0 meson and its decay are marked. Each line represent a particle, and each blue dot represents a vertex. The different colours represent different particle flavours, where the D^0 is marked by a purple line. The figure illustrates that the D^0 meson created immediately after the collision can have a significant displacement from the collision vertex before decaying.

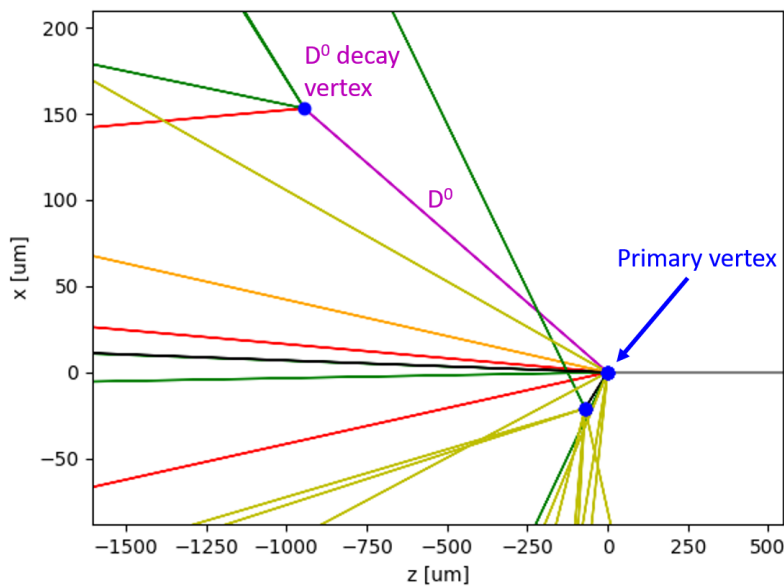


Figure 6.19: Example event display, showing vertex positions in the x-z plane. A D^0 meson is generated at the primary vertex, and decays after moving hundreds of micrometres in both the x and z directions.

The D^0 decay vertex displacement from the primary vertex is shown in Figure 6.20 for 18 GeV electrons colliding with 275 GeV protons (i.e. the highest investigated collision energy), in three dimensions and the transverse and longitudinal planes separately. The secondary vertex displacement in the transverse direction has a mean value of approximately $85 \mu\text{m}$, demonstrating the need of good transverse pointing resolution of the tracker to be able to separate primary and secondary vertices.

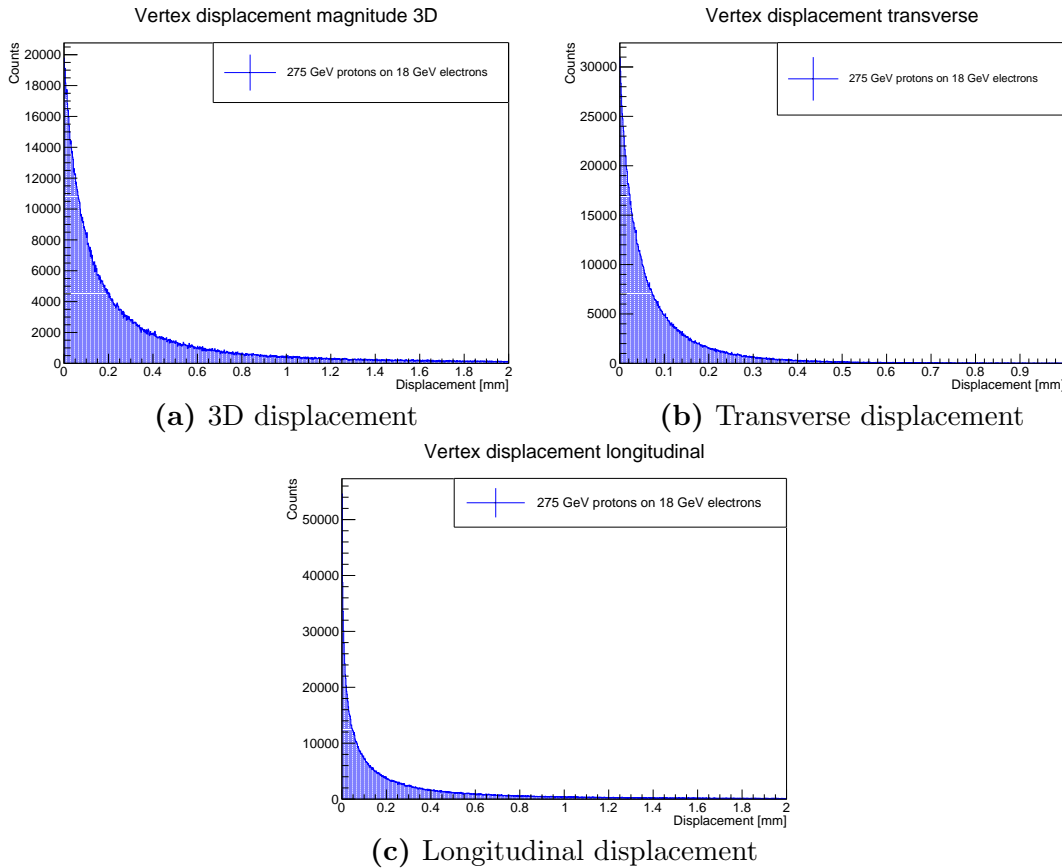


Figure 6.20: D^0 decay vertex displacement from collision vertex for collisions of 18 GeV electrons and 275 GeV protons.

Figure 6.21 shows the distributions for the different collision energies in terms of the proton momentum fraction x that is carried by the gluon in the photon-gluon fusion process. The left plot shows the range $0 \leq x \leq 0.3$, and the right plot is zoomed in on the lower- x region $0 \leq x \leq 0.05$. From these distributions, it is clear that a higher collision energy yields a lower minimum momentum fraction x . This is expected from theory, as the possible x values are inversely proportional to the collision centre-of-mass energy. The x value of the interaction will also affect the angle of the final-state hadron. This is investigated for the pions and kaons from D^0 decays, and shown in Figure 6.22, where x is plotted versus pseudorapidity for pion-kaon pairs from D^0 decays, for the four different energies.

This shows that a higher x makes the final state pions and kaons from a D^0 travel more in the negative pseudorapidity direction (i.e. the initial proton-going

direction). From these plots it can also be seen that most events are within a detector acceptance of $|\eta| \leq 3.25$, and that no particular x range is unreachable by the detector for this physics channel.

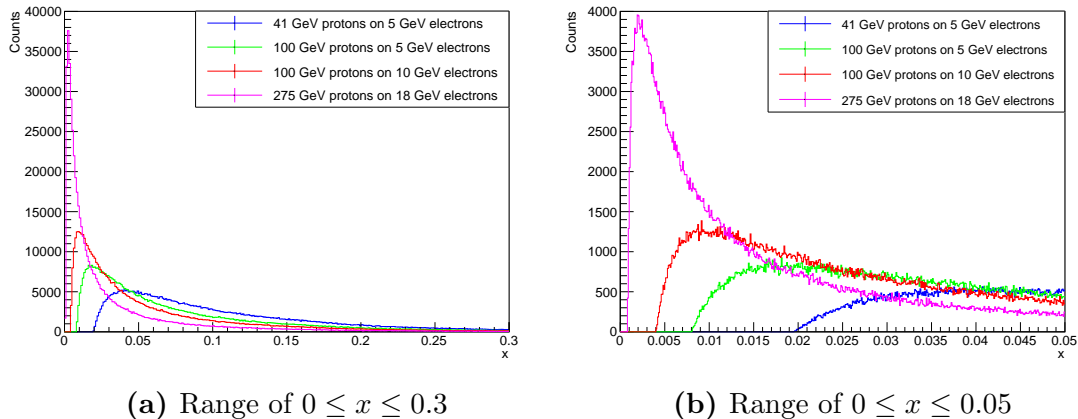


Figure 6.21: Distribution of the proton momentum fraction x carried by the gluon in the photon-gluon fusion process for the four investigated energy combinations. A total of 500 000 events are investigated for each energy combination.

6.5.3 Detector acceptance

Using the detector acceptance in pseudorapidity and transverse momentum derived from the results presented in Section 6.4, a study of the fraction of relevant generated particles that are outside of the acceptance can be made. This study is performed for the TPC baseline layout, but it will be similar for all tracker layouts as it is mainly affected by the inner radius of the disks and the layout of the innermost barrel layers. The detector acceptance in pseudorapidity is taken to be $-3.25 \leq \eta \leq 3.25$, as a reconstruction efficiency above 90% is never reached outside of this (due to most of the detector parts being missed; see Figure 6.13). The transverse momentum acceptance will depend on the magnetic field used, and for the purpose of this study the highest minimum detectable transverse momentum from Section 6.4 is taken as the limit. We thus get a limit of 140 MeV/c for a 1.5 T magnetic field, and 220 MeV/c for a 3.0 T magnetic field. These limits are applied to the generated distributions described in Section 6.5.2, and tables are made of the percentage of events outside the detector acceptance for both the case including all D^0 decay products, and only the pion-kaon pairs. Tables 6.9 and 6.10 show the resulting pseudorapidity acceptance values for all D^0 decay products and pion-kaon pairs from D^0 decays, respectively.

In these tables, “below” indicates events with $\eta < -3.25$, and “above” events with $\eta > 3.25$. The incoming electrons travel in the positive direction, and the protons in the negative direction. From the tables, it can be seen that the fraction of events outside the acceptance increases with the energy asymmetry of the collision; more particles are outside the acceptance in the initial proton-going direction the higher the relative energy of the proton is compared to the electron. It can also be seen

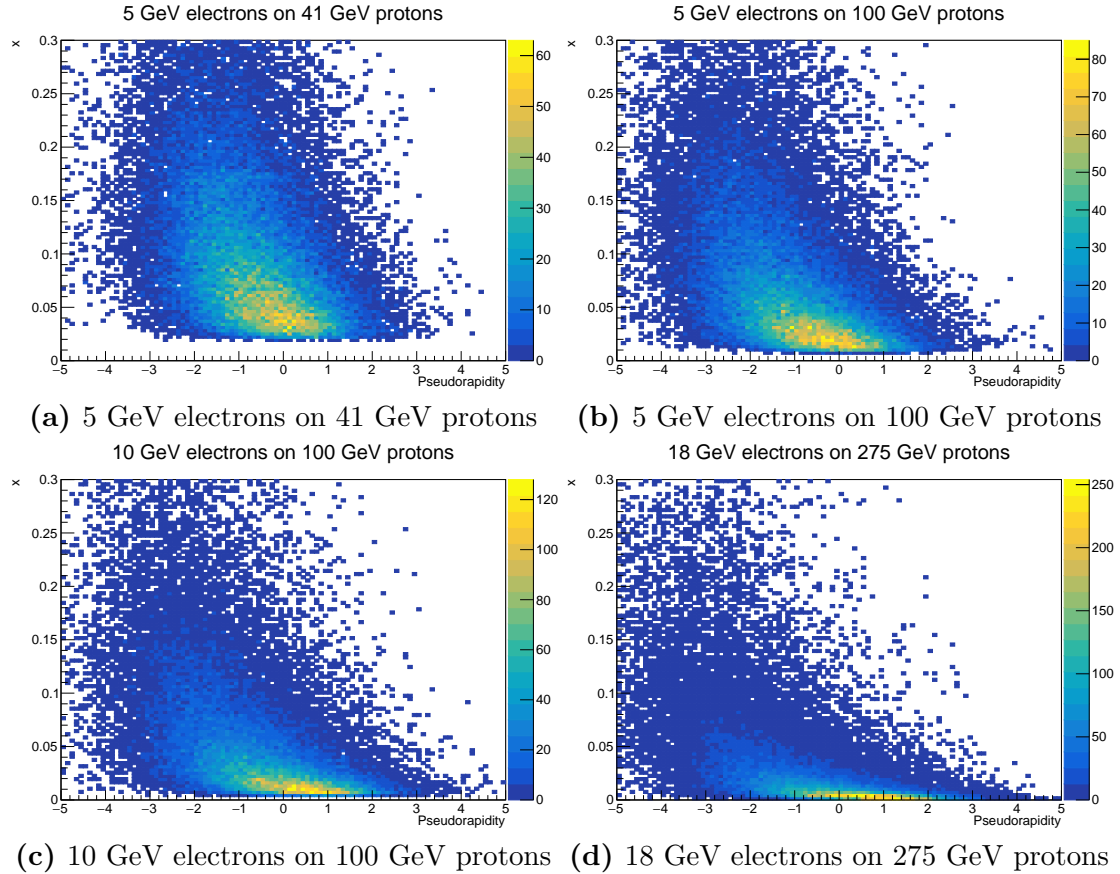


Figure 6.22: Pseudorapidity of pion-kaon pairs from D^0 decays, and proton momentum fraction x of the collision generating the D^0 , for the investigated four different energy combinations. The colour indicates the number of counts in a bin.

that for any of the tested energies, at least approximately 90% of the D^0 decay products are within the detector acceptance.

Table 6.11 shows the fraction of all D^0 decay products outside the transverse momentum acceptance of the detector for both a 1.5 T magnetic field and a 3.0 T magnetic field. For pion-kaon pairs from D^0 decays the results are shown in Table 6.12.

From the table with results from all D^0 decay products, it can be seen that a higher fraction of particles are outside the transverse momentum acceptance at low collision energies. The differences between different energies are small, however. Comparing the fraction below the momentum limits for 1.5 T and 3.0 T shows that a higher magnetic field strength is severely detrimental to the low-momentum acceptance; up to 20% of D^0 decay products are outside of the acceptance for a 3.0 T field. For the specific decay to pion-kaon pairs, the fraction outside of the acceptance is smaller (as is expected from the transverse momentum distributions presented in Section 6.5.2). Even with a 3.0 T magnetic field less than 4% of particles are outside the acceptance. This again leads to the conclusion that a tuneable magnetic field strength can be desirable, to be able to optimise the detector acceptance for different physics channels.

Beam energies	Fraction below	Fraction above	Fraction outside
5 × 41 GeV	2.86 ± 0.01 %	0.11 ± 0.01 %	2.96 ± 0.01 %
5 × 100 GeV	7.45 ± 0.02 %	0.07 ± 0.01 %	7.52 ± 0.02 %
10 × 100 GeV	5.35 ± 0.02 %	0.28 ± 0.01 %	5.63 ± 0.02 %
18 × 275 GeV	9.47 ± 0.02 %	0.60 ± 0.01 %	10.08 ± 0.03 %

Table 6.9: Fraction of all D^0 decay products outside a detector acceptance of $|\eta| \leq 3.25$. “Below” is the initial proton-going direction. The dataset is made up of 500 000 electron-proton collisions for each energy combination. The energies are given as electron × proton energy.

Beam energies	Fraction below	Fraction above	Fraction outside
5 × 41 GeV	1.98 ± 0.07 %	0.08 ± 0.01 %	2.05 ± 0.07 %
5 × 100 GeV	5.88 ± 0.12 %	0.07 ± 0.01 %	5.95 ± 0.12 %
10 × 100 GeV	4.17 ± 0.10 %	0.21 ± 0.02 %	4.39 ± 0.10 %
18 × 275 GeV	7.98 ± 0.14 %	0.41 ± 0.03 %	8.39 ± 0.14 %

Table 6.10: Fraction of pion-kaon pairs from D^0 decays outside a detector acceptance of $|\eta| \leq 3.25$. “Below” is the initial proton-going direction. The dataset is made up of 500 000 electron-proton collisions for each energy combination. The energies are given as electron × proton energy.

Beam energies	Fraction below 140 MeV/c (1.5 T limit)	Fraction below 220 MeV/c (3.0 T limit)
5 × 41 GeV	10.07 ± 0.03 %	20.58 ± 0.04 %
5 × 100 GeV	9.96 ± 0.03 %	20.43 ± 0.04 %
10 × 100 GeV	9.95 ± 0.03 %	20.24 ± 0.04 %
18 × 275 GeV	9.66 ± 0.03 %	19.77 ± 0.04 %

Table 6.11: Fraction of all D^0 primary decay products outside a detector acceptance in transverse momentum. The fraction of particles with $p_T \leq 140$ MeV/c (i.e. the 1.5 T highest low limit) and $p_T \leq 220$ MeV/c (i.e. the 3.0 T highest low limit) are shown.

Beam energies	Fraction below 140 MeV/c (1.5 T limit)	Fraction below 220 MeV/c (3.0 T limit)
5 × 41 GeV	1.45 ± 0.06 %	3.51 ± 0.09 %
5 × 100 GeV	1.39 ± 0.06 %	3.50 ± 0.09 %
10 × 100 GeV	1.48 ± 0.06 %	3.72 ± 0.09 %
18 × 275 GeV	1.45 ± 0.06 %	3.60 ± 0.09 %

Table 6.12: Fraction of all D^0 to pion-kaon pair decay products outside a detector acceptance in transverse momentum. The fraction of particles with $p_T \leq 140$ MeV/c (i.e. the 1.5 T highest low limit) and $p_T \leq 220$ MeV/c (i.e. the 3.0 T highest low limit) are shown.

6.6 Open charm event reconstruction

The generated physics events described in Section 6.5 are used as input in the Fun4All simulation framework, and propagated through different detector concepts in a full GEANT4 simulation. The reconstruction chain described in Section 6.1.2.1 is used to extract information for each particle in an event. This makes it possible to study the detector performance with respect to realistic physics observables, under realistic collision-induced background conditions. Using the reconstructed particle information, invariant mass spectra can be generated, and information about the invariant mass peaks of D mesons investigated and compared between different detector concepts.

The D^0 is the main particle under investigation, but studies are also made of the D^+ and the D^{*+} . All investigated particles decay to pions and kaons close to the primary interaction point. The studies are performed for the four different collision energies given in Table 6.8, using several of the detector layouts described in Section 6.1.3, and magnetic field strengths of 1.5 T and 3.0 T. For the all-silicon baseline for both magnetic field strengths, the TPC baseline at 1.5 T, and the 600 mm outer radius all-silicon layout at 1.5 T, 500 000 electron-proton collision events are propagated through the detector for each collision energy. For the other combinations of layouts and magnetic fields only 100 000 collisions are used, due to limitations of the available computing resources.

For physics studies it is important to know the production cross sections of particles and branching ratios of decay channels (as this helps constrain theoretical models), and this is commonly found by observing the reconstructed invariant mass peak. It is thus of importance to have a good mass peak resolution, and a good signal to background ratio of the peak. These figures of merit are used in this section to compare different detector layouts and magnetic field strengths. The mass peak resolution is taken as the standard deviation of a Gaussian fit to the peak, and the signal to background ratio is calculated by counting the number of hits for the signal and interpolated background in a region of $\pm 3\sigma$ from the Gaussian peak centre position.

To reconstruct the invariant mass peak in the studies presented here, the truth information about particle identity is initially used. This is extracted directly from the event generator files. The reconstructed information of all pions and kaons in an event are combined, which includes both the pions and kaons from a D meson decay and pions and kaons from other sources. Using the reconstructed momenta together with the particle masses (known from the particle identity), the invariant mass of a system of particles can be calculated. When the reconstructed invariant masses from all pion-kaon combinations in all events are put into a histogram, an invariant mass peak for the decayed D meson appears together with a combinatorial background. For the D^0 meson reconstruction, pairs of particles are combined to calculate the invariant mass. For the D^+ and D^{*+} , triplets of particles are combined.

6.6.1 D^0 reconstruction

For reconstruction of D^0 mesons, the decay channel $D^0 \rightarrow K^- + \pi^+$ and its charge conjugate are used, due to it having low multiplicity (and thus low combinatorial background), only charged particles in the final state, and also being a relatively common decay (branching ratio of 3.95%).

To find the D^0 mass peak, the invariant mass of pairs of pions and kaons is thus plotted, using their reconstructed momenta. The nominal D^0 mass is $1864.84 \pm 0.05 \text{ MeV}/c^2$ [31], and the invariant mass spectrum for the particle pairs is thus plotted between masses of $1700 \text{ MeV}/c^2$ and $2000 \text{ MeV}/c^2$. The particle identification is not ideal in a realistic detector, but extraction of particle ID and bespoke particle ID detectors are not implemented in the simulations used. A particle ID efficiency of 95% is thus assumed in these calculations. This is a conservative estimation of the projected particle ID efficiency of the EIC [133]. The uncertainty in particle ID is introduced by giving each particle a random chance of being misidentified. When combining particle pairs, a check is made of whether both particles are identified as a pion-kaon pair. If only a pion is identified the other particle is assumed to be a kaon, and vice versa. A cut is also applied making sure the two particles have opposite charge, and a cut on the reconstructed vertex positions for the two particles being within $500 \mu\text{m}$ of each other. These cuts were found to give a good value for the invariant mass peak significance and statistical errors. In this way, all pairs of particles are checked, and their invariant masses calculated and added to the histogram if they fulfil the criteria.

Figure 6.23 shows two examples of the invariant mass spectrum using the TPC baseline layout, and 100 000 collisions of 5 GeV electrons and 41 GeV protons for a 1.5 T magnetic field and a 3.0 T magnetic field. The figures show the invariant mass peak, and the combinatorial background coming from pions and kaons from other sources than the D^0 decay. The fit used is the sum of a Gaussian signal and a linear background. In these figures, there is a clear peak at the expected invariant mass of a D^0 meson. Comparing the two plots, it is also clear that the

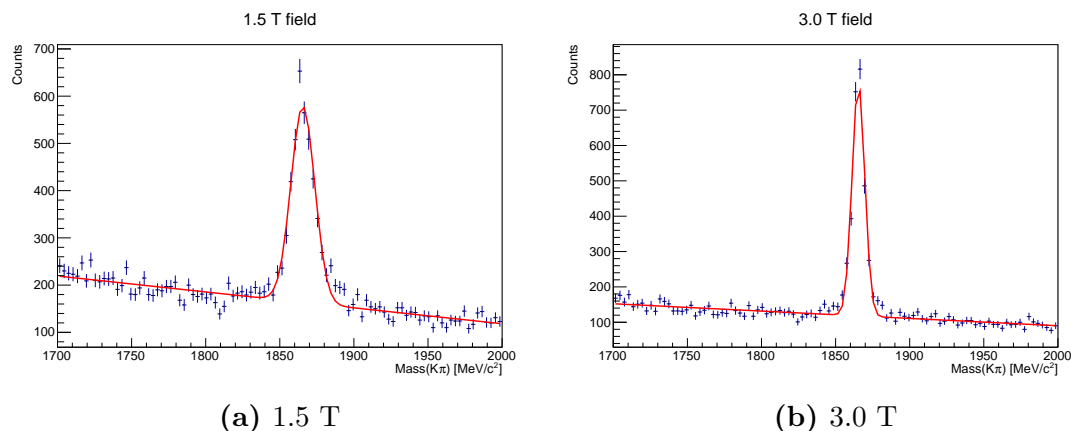


Figure 6.23: Pion-kaon pair invariant mass spectrum for two different magnetic field strengths, using the TPC baseline detector.

invariant mass peak resolution is better for a 3.0 T magnetic field than for a 1.5 T magnetic field (i.e. the mass peak is narrower). However, the 3.0 T spectrum has approximately 5000 events fewer in the interval, which amounts to a reduction of approximately 25%. This is in part due to events being lost from spiralling in the higher field.

A study is made of the mass peak width and signal to background ratio for four different detector concepts and four different collision energies. The TPC baseline layout is tested, along with the all-silicon baseline layout, the all-silicon concept with a 600 mm outer radius, and the all-silicon concept with a 775 mm outer radius. The resulting summary plots are shown in Figure 6.24. The different

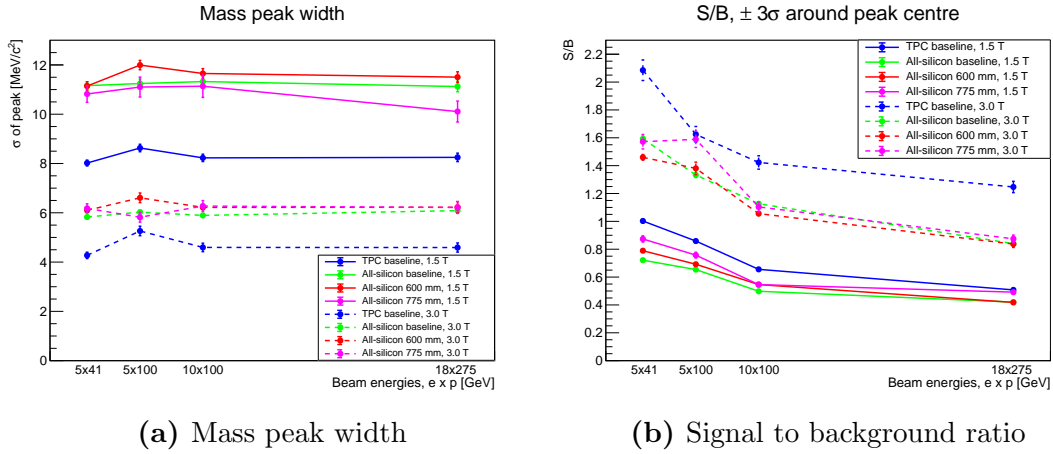


Figure 6.24: Mass peak width and signal to background ratio of the D^0 meson (in the decay channel $D^0 \rightarrow K^- + \pi^+$), for four different detector concepts and four different collision energies. Filled lines indicate a 1.5 T magnetic field, and dashed lines indicate a 3.0 T magnetic field.

colours in the figures represent different detector layouts. The filled lines are the results using a 1.5 T magnetic field, and the dashed lines using a 3.0 T magnetic field. From the mass peak width plot, it can be seen that there is not much difference for different collision energies. It is also clear that the D^0 mass peak is narrower when using a 3.0 T magnetic field, regardless of detector concept and energy. Comparing the different detector concepts, all three all-silicon layouts are very similar, and frequently within errors of each other. This is interesting as it shows that a compact all-silicon layout can perform as well as a larger-radius one. The TPC baseline layout (blue lines) always outperforms the all-silicon layouts, however. As the pions and kaons from D^0 decays have low transverse momentum (see Section 6.5.2), this matches previous results showing that the silicon plus TPC layout has better momentum resolution in this region (see Section 5.3.10 and Section 6.3).

The plot of signal to background ratio again shows that a 3.0 T field outperforms a 1.5 T field. There is also an energy dependence here; the signal to background ratio decreases as energy increases. This is due to more pions and kaons being created from other sources than D^0 decays at higher collision energies, increasing the

background. The signal remains approximately constant, as the same number of charm quarks are created in each initial collision and photon-gluon fusion process. From the plot of S/B , it can be seen that the TPC baseline outperforms the all-silicon layouts with this metric as well. There is again not much difference between different all-silicon layouts, except for a slight preference for larger radius at the two lower energy data points.

6.6.2 D^+ reconstruction

Using the same dataset, the invariant mass of D^+ mesons can be reconstructed via the decay channel $D^+ \rightarrow K^- + \pi^+ + \pi^+$ (and its charge conjugate). This decay channel has a branching ratio of 9.38% [31]. Ideal particle identification is used here, and the same cuts as for the D^0 reconstruction. Figure 6.25 shows the full reconstructed spectrum of kaon-pion-pion triplet invariant mass for 500 000 collisions between 5 GeV electrons and 41 GeV protons, using the silicon plus TPC baseline layout.

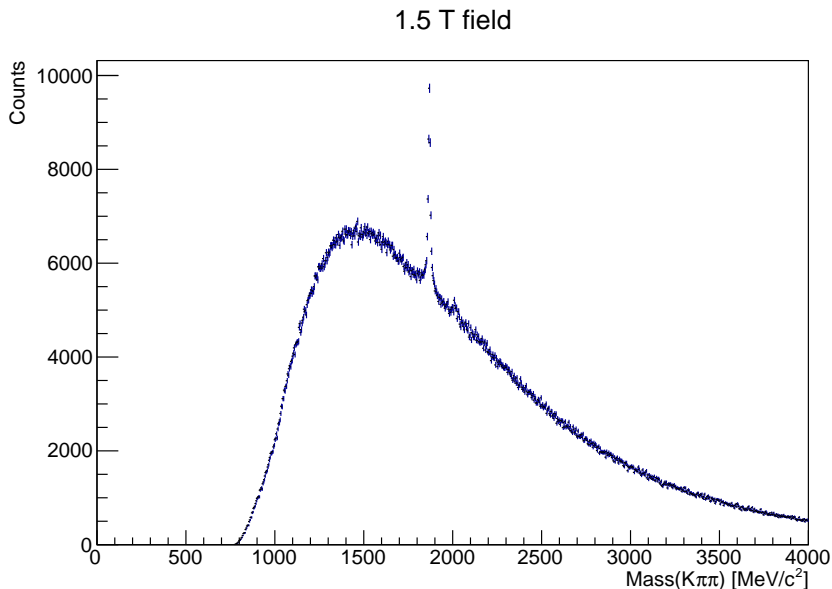


Figure 6.25: Full invariant mass spectrum of $K\pi\pi$ combinations from 500 000 collisions of 5 GeV electrons and 41 GeV protons, using the TPC baseline layout.

The mass of a D^+ meson is 1869.5 ± 0.4 MeV/ c^2 [31], and there is a distinct peak in the spectrum at this location, with fits to the reconstructed data giving the centroid position of the peak as 1869.7 ± 0.4 MeV/ c^2 . The fits to the peak are performed in a zoomed-in histogram of the range 1800 MeV/ c^2 to 2100 MeV/ c^2 , using a Gaussian with a linear background. The fit interval is set between 1800 MeV/ c^2 and 1950 MeV/ c^2 . The resulting mass peak widths and signal to background ratios are shown in Figure 6.26. From the plot of the mass peak widths, the same trends as were observed in the D^0 meson studies can be seen; a 3.0 T field gives better mass peak resolution than a 1.5 T field, the TPC baseline layout outperforms the all-silicon layouts with a 1.5 T field, and there is not much difference between

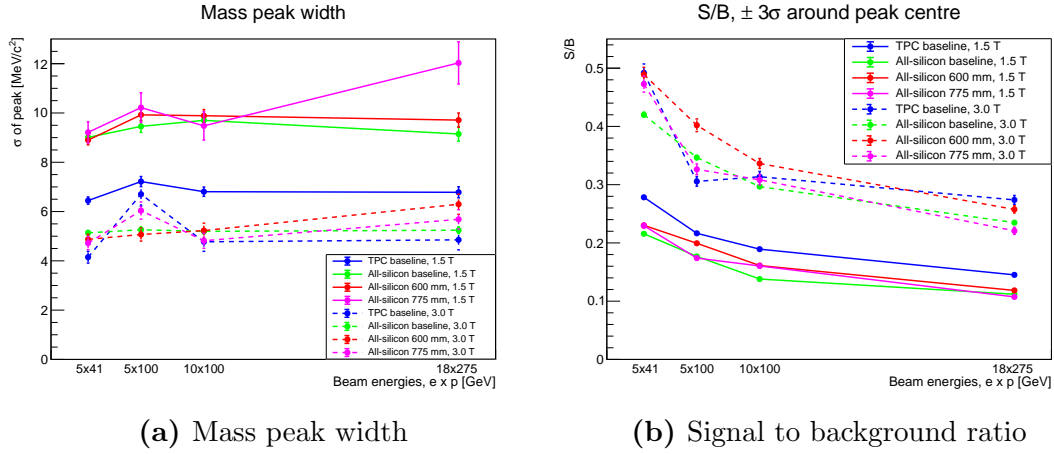


Figure 6.26: Mass peak width and signal to background ratio of the D^+ meson (in the decay channel $D^+ \rightarrow K^- + \pi^+ + \pi^+$), for four different detector concepts and four different collision energies. Filled lines indicate a 1.5 T magnetic field, and dashed lines indicate a 3.0 T magnetic field.

different all-silicon layouts. With a 3 T field however, the TPC baseline is worse than the compact all-silicon layouts at the collision of 5 GeV electrons and 100 GeV protons. This likely stems from the larger fraction of particles going in the negative direction at this energy (see Section 6.5.2), where the all-silicon layouts have better resolutions due to larger silicon disks. The all-silicon layout with a 775 mm outer radius (magenta line) jumps up at the highest energy for a 1.5 T magnetic field, but the error bars for it are large there, so it is likely a statistical fluctuation.

For a 1.5 T magnetic field, the plot of S/B also shows the same trends as for the D^0 meson study; the TPC baseline layout outperforms the all-silicon layouts. There is also a decrease in signal to background ratio as energy increases, due to more pions and kaons being created by other sources. It can also be seen that a 3.0 T field has a better S/B than a 1.5 T field, consistently. For a 3.0 T field however, the TPC baseline is not better than the all-silicon layouts, but rather within errors or worse than the 600 mm outer radius all-silicon layout, which is better than the other all-silicon layouts at all but the lowest collision energy.

6.6.3 D^{*+} reconstruction

With the simulated dataset, a reconstruction of the invariant mass of D^{*+} mesons can also be made. The decay channel $D^{*+} \rightarrow \pi^+ + D^0$ (and its charge conjugate) is frequently used to tag events that contain charm quarks [134, 135]. The mass of a D^{*+} meson is $2010.26 \pm 0.05 \text{ MeV}/c^2$ [31], which makes the mass difference $M(D^{*+}) - M(D^0)$ close to the pion mass, at approximately $145.4 \text{ MeV}/c^2$ (where the pion mass is $139.57 \text{ MeV}/c^2$). The pion from the D^{*+} decay will thus have a very small momentum in the restframe of the D^{*+} , and is commonly referred to as a “slow” pion and denoted π_s^+ . An event containing a D^{*+} can thus be effectively tagged by either detecting this low-momentum pion directly or by reconstructing the difference in invariant mass of a kaon-pion-pion triplet and a kaon-pion pair

close to the D^0 invariant mass [136]. Determining the charge of the slow pion also gives information of whether the event contains a D^0 or a \bar{D}^0 . Accurate tagging and separation of these two particles can for example be used in studies regarding matter-antimatter asymmetry [135].

The branching ratio for the decay $D^{*+} \rightarrow \pi^+ + D^0$ is 67.7%. To reconstruct the D^0 meson the subsequent decay $D^0 \rightarrow K^- + \pi^+$ is used however, giving a total branching ratio of the decay $D^{*+} \rightarrow \pi^+ + D^0(\rightarrow K^- + \pi^+)$ of 2.67%. Taking the difference between the invariant masses of the D^{*+} and the D^0 puts the peak in a region with very little combinatorial background, making it narrow and clear. Ideal particle identification is used for the tracks in this study, and the kaon-pion pair with an invariant mass closest to the D^0 mass is subtracted from the kaon-pion-pion invariant mass. Figure 6.27 shows an example spectrum of the invariant mass difference for 500 000 events of collisions of 5 GeV electrons with 41 GeV protons, and an example fit of the peak. The data come from reconstruction of the events using the TPC baseline layout in a 1.5 T magnetic field. The peak is located at the expected value of approximately 145.4 MeV/ c^2 , with fits giving the centroid location as 145.4 ± 0.02 MeV/ c^2 . The same fit as for the other D meson invariant mass peaks is used, as the background is locally approximately linear around the peak.

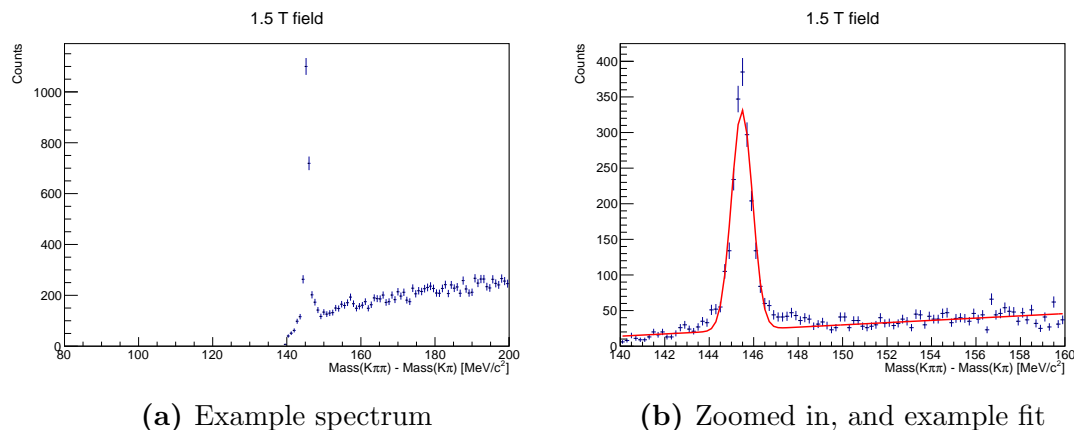


Figure 6.27: Invariant mass difference spectrum, $M(D^{*+}) - M(D^0) = M(K\pi\pi) - M(K\pi)$, for 500 000 collisions of 5 GeV electrons and 41 GeV protons using the TPC baseline layout in a 1.5 T magnetic field.

The mass peak widths and signal to background ratios for different detector layouts are shown in Figure 6.28.

It should be noted that the mass peak width in this case is much smaller, and the signal to background ratio much higher, compared to the D^0 and D^+ mass peaks. This again demonstrates that this method is a powerful way of tagging events containing a D^{*+} .

The difference between layouts is small here. For the mass peak width, it is again clear that a 3.0 T field improves the peak resolution. Comparing the different layouts, the all-silicon layouts are always within errors of each other. The TPC

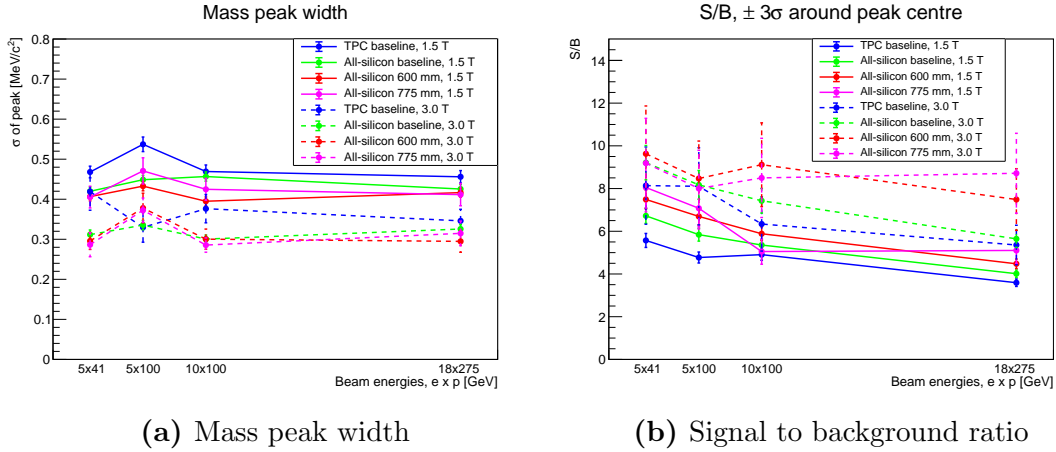


Figure 6.28: Mass peak width and signal to background ratio of the invariant mass difference $M(D^{*+}) - M(D^0) = M(K\pi\pi) - M(K\pi)$, for four different detector concepts and four different collision energies. Filled lines indicate a 1.5 T magnetic field, and dashed lines indicate a 3.0 T magnetic field.

baseline is slightly worse for the lowest energy for both magnetic fields, and the lowest two energies for a 1.5 T field. This likely stems from the reconstruction inefficiency of the TPC for low-momentum pions in the central region (see Section 6.4). At the other energies, it is within errors of the all-silicon layouts. For the signal to background ratio, a 3.0 T field is again better than a 1.5 T field. The error bars are large here, however. At the lowest two energies the TPC baseline layout is again worse than all of the all-silicon layouts.

6.6.4 All photoproduction processes activated

To have a more realistic background environment, events are generated in Pythia with more physics processes activated; photon-gluon fusion is now allowed to create any quark-antiquark pair, rather than just the previously used charm-anticharm. The lighter quarks will be favoured in the photon-gluon fusion process. The process of QCD Compton scattering is also allowed, where the incoming photon strikes a quark, resulting in a quark and a gluon as final products of the interaction. The quarks allowed in this process are all but the top quark. In total, 500 000 events are generated for each energy combination.

The events are propagated through the TPC baseline detector and the all-silicon baseline detector with a 1.5 T magnetic field, and all pions and kaons in an event are combined in pairs and the reconstructed invariant mass is extracted, using the same method and cuts as in the previous studies. The results for the D^0 mass peak width and signal to background ratio are shown in Figure 6.29. The figure also shows the corresponding results where only the photon-gluon fusion to $c\bar{c}$ process is active, for comparison.

The red and magenta lines have all the processes described above activated, while the blue and green lines result from events containing only the photon-gluon fusion

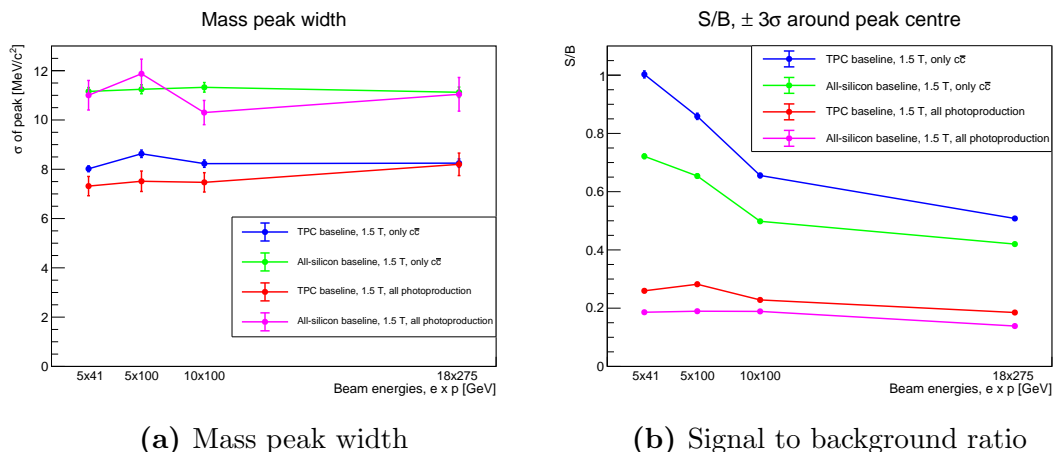


Figure 6.29: Mass peak width and signal to background ratio of the D^0 meson (in the decay channel $D^0 \rightarrow K^- + \pi^+$), for two different detector concepts in a 1.5 T magnetic field, with different physics processes activated.

to charm-anticharm process. The blue and red lines are results from using the TPC baseline layouts, and the green and magenta lines from using the all-silicon baseline layout.

It can be seen that the mass peak width difference is small for the different physics processes, other than an increase in errors when more processes are active. This makes sense as the fraction of events containing a D^0 decreases, and thus the statistical errors increase. The signal to background ratio is significantly lower for more active processes than for only the photon-gluon fusion to charm-anticharm. This again makes sense due to the decreased number of signal events and increased background (as having more up, down, and strange quarks will create more pions and kaons not from D^0 decays, increasing the combinatorial background).

This study gives a more realistic expectation of what would be seen in an experiment in the photoproduction region, as the studies with creation of only charm-anticharm pairs overestimates the number of correctly reconstructed D mesons compared to the background. The conclusion that can be drawn is that the mass peak width found in the previously presented D meson studies is realistic even when more processes are active, but the signal to background ratio will decrease compared to what has been found when using only charm-anticharm production. This agrees with the theory that the reconstructed mass peak width pertains more to the detector, and the signal to background ratio more to the underlying physics event (even if the effect of using different detector layouts also makes a difference).

6.6.5 Detector kinematic range

It is often of interest to find the differential production cross sections of particles, i.e. the cross section as a function of a kinematic variable. This can also give information about how well particles can be reconstructed in different parts of the

detector. In this section, plots of the mass peak width and signal to background ratio for D^0 mesons are made in bins of the proton momentum fraction x carried by the gluon in the photon-gluon fusion process, the transverse momentum of the D^0 meson, and the pseudorapidity of the D^0 meson. To make the plots, the invariant mass spectra are projected in bins of the kinematic variable under investigation, and a fit of the D^0 invariant mass peak is made in each bin. The fit results are then saved and plotted.

The studies are made with the same dataset as in Section 6.6.1, and using the same cuts and fit. For the plots in bins of x , all four energy combinations are combined, since they give access to different x ranges (see Figure 6.21). The lowest x region data thus come from collisions of 18 GeV electrons with 275 GeV protons, and the highest x region data from the collisions of 5 GeV electrons with 41 GeV protons. Figure 6.30 shows the mass peak width plotted versus the proton momentum fraction carried by the gluon, x , for three different detector concepts: the TPC baseline layout, the all-silicon baseline layout, and the all-silicon layout with a 600 mm outer radius. Each coloured line consists of four separate line segments, one from each collision energy. The filled lines shows results for a 1.5 T magnetic

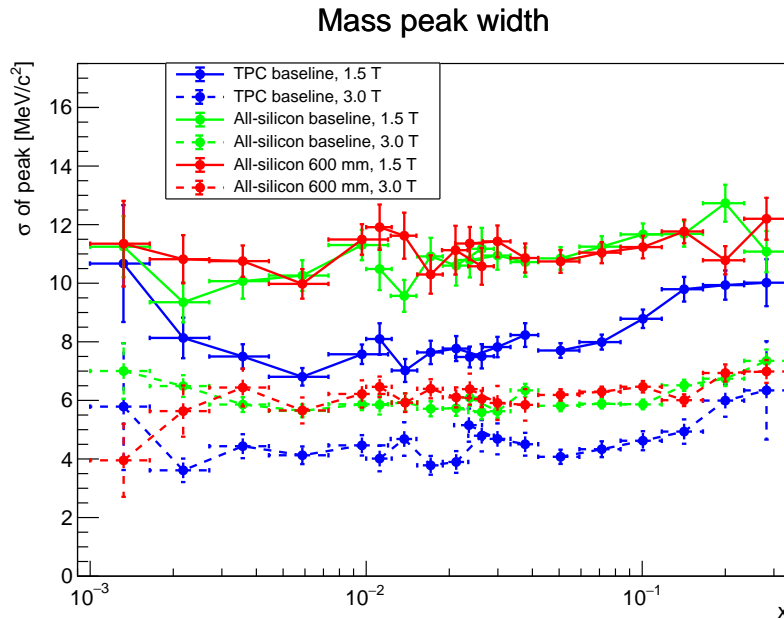


Figure 6.30: Mass peak width of a D^0 meson, in bins of the proton momentum fraction x carried by the gluon in the photon-gluon fusion process. Filled lines indicate a 1.5 T magnetic field strength, and dashed lines indicate a 3.0 T magnetic field strength.

field, and the dashed lines for a 3.0 T magnetic field. The x axis is logarithmic, as the available x distribution is narrower at smaller x values, so the bins can be narrower there without increasing the statistical error too much. The axis shows the range $0.001 \leq x \leq 0.33$.

From the plot, it is once again clear that a 3.0 T magnetic field outperforms a 1.5 T magnetic field; all the dashed lines have a better invariant mass peak resolution

than the filled lines. It can also be seen that for all but the lowest and highest values of x , the TPC baseline layout outperforms both all-silicon layouts. There is also very little difference between the performance of the two tested all-silicon layouts.

Figure 6.31 shows the results of the D^0 reconstructed invariant mass peak signal to background ratio versus x for the same detector concepts and magnetic fields. The x axis is again logarithmic.

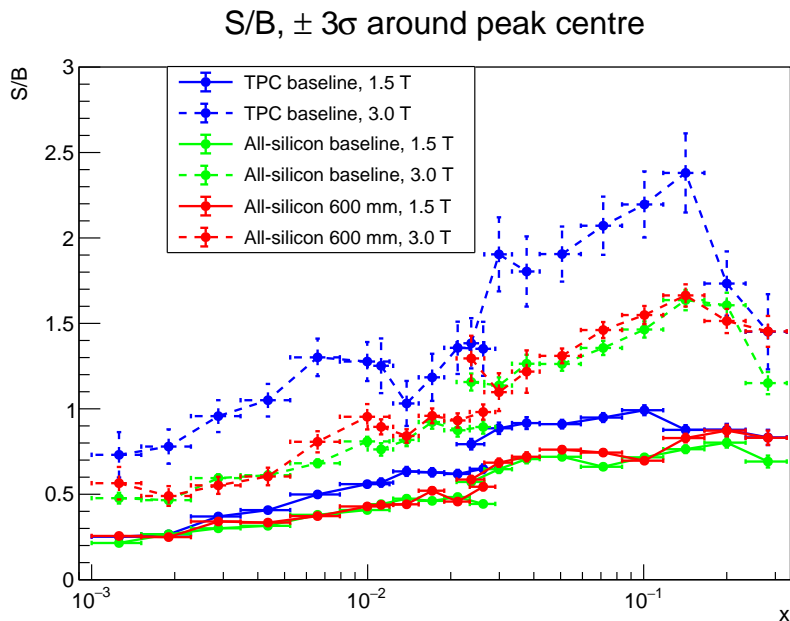


Figure 6.31: Signal to background ratio for the D^0 reconstructed invariant mass peak, in bins of x . Filled lines indicate a 1.5 T magnetic field strength, and dashed lines indicate a 3.0 T magnetic field strength.

It can once again immediately be seen that a 3.0 T magnetic field gives a better signal to background ratio than a 1.5 T field. There is also an increase in the ratio for increasing x , for all the tested layouts. Both the signal and the background decrease as x increases, but the background decreases more than the signal. The signal to background ratio is also higher for the lowest collision energy for all tested layouts (see Figure 6.24(b)), and lower collision energy corresponds to higher x .

For a 1.5 T magnetic field, the silicon plus TPC baseline layout has a better S/B than the all-silicon layouts in the range $0.004 \leq x \leq 0.1$. At higher and lower x , it matches the all-silicon layouts. For a 3.0 T magnetic field the TPC baseline also appears to perform better than the all-silicon layouts at most x . The error bars here are larger however, as the dataset for this layout and magnetic field only contains 100 000 collision events for each energy. For almost all but the highest x bin at 1.5 T, both all-silicon layouts are within errors of each other. At the x values where there is a difference, the 600 mm radius concept outperforms the baseline layout.

For the plots in bins of transverse momentum and pseudorapidity, all energies cover the full range investigated. The resulting plots follow the same trends between different detector layouts and magnetic fields for all four collision energies individually, so the middle collision energy (10 GeV electrons on 100 GeV protons) is shown here as a representative example. Figure 6.32 shows the results of the D^0 reconstructed invariant mass peak width and signal to background ratio versus transverse momentum, in the transverse momentum range $0 \leq p_T \leq 3.0$ GeV/c.

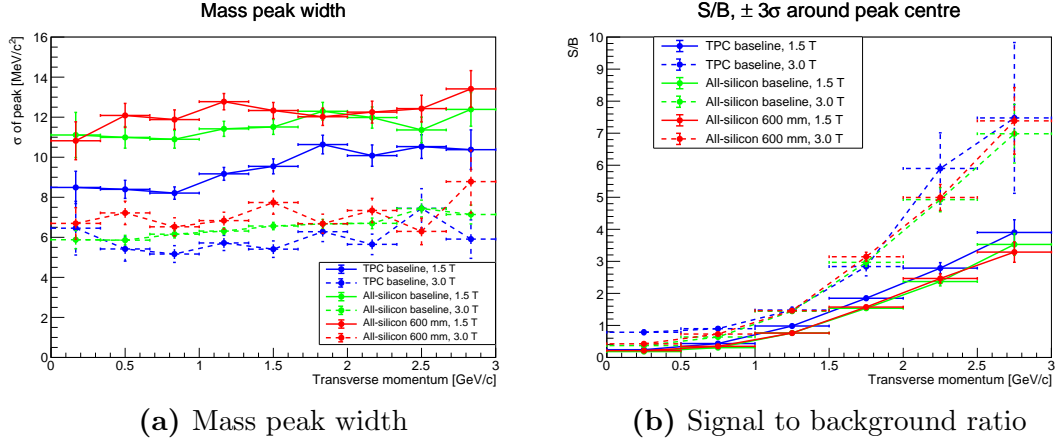


Figure 6.32: Mass peak width and signal to background ratio of the D^0 meson (in the decay channel $D^0 \rightarrow K^- + \pi^+$) in bins of the D^0 transverse momentum, for events from collisions of 10 GeV electrons and 100 GeV protons. Filled lines indicate a 1.5 T magnetic field strength, and dashed lines indicate a 3.0 T magnetic field strength.

The mass peak width is quite uniform across the p_T range investigated. For a 1.5 T magnetic field, the TPC baseline outperforms the two tested all-silicon layouts across the whole range. For the 3.0 T magnetic field, it is always as good as or better than both all-silicon layouts. The all-silicon layouts are again very similar to each other in performance. For all three tested layouts, a 3.0 T magnetic field gives better mass resolution than a 1.5 T field.

The signal to background ratio increases with increasing transverse momentum. This is both due to more D^0 events being properly reconstructed as p_T increases (as the detector reconstruction efficiency increases), and a decrease in background. The signal also decreases here however, but the background decreases more. The error bars grow at higher p_T , as the statistical errors grow due to fewer events in this region. For a 1.5 T magnetic field the TPC baseline layout outperforms the tested all-silicon layouts in a transverse momentum range of approximately $1 \leq p_T \leq 2.5$ GeV/c. For all other regions, and for all but the lowest transverse momentum for a 3.0 T magnetic field, all three concepts are within errors of each other. A 3.0 T field always has a better signal to background ratio than a 1.5 T field in this study.

In Figure 6.33, the results versus pseudorapidity are shown. The pseudorapidity range used is $-3.25 \leq \eta \leq 3.25$, as all tested detector concepts are inefficient outside of this region.

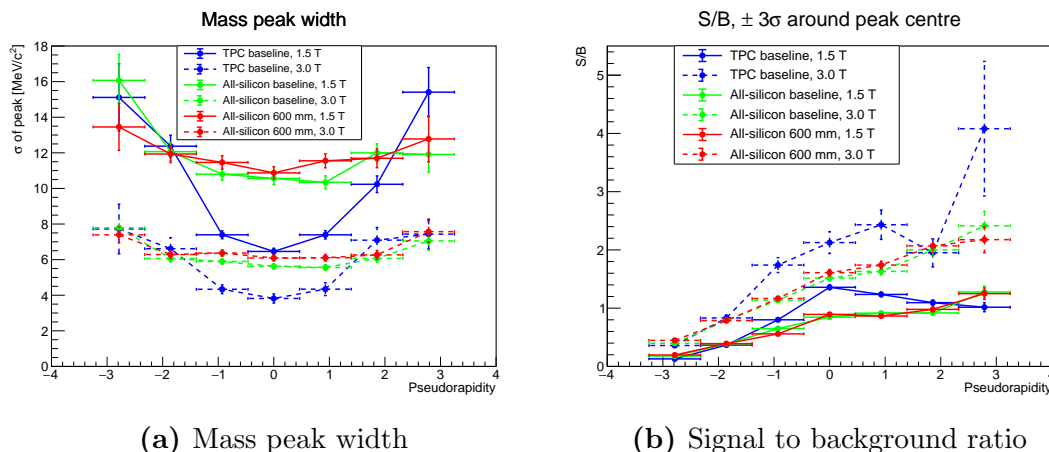


Figure 6.33: Mass peak width and signal to background ratio of the D^0 meson (in the decay channel $D^0 \rightarrow K^- + \pi^+$) in bins of the D^0 pseudorapidity, for events from collisions of 10 GeV electrons and 100 GeV protons. Filled lines indicate a 1.5 T magnetic field strength, and dashed lines indicate a 3.0 T magnetic field strength.

These plots have some interesting features. The upper corners of the TPC are located at $|\eta| = 1.11$, and the region where the full TPC is active shows up in both the mass peak width and the signal to background ratio. For the mass peak width, the curves for the TPC baseline are lowest in the middle (i.e. at $\eta = 0$), and then increase rapidly to the same level as the all-silicon layouts at $\eta \geq 1.11$. The all-silicon layouts are very similar and almost constant across the full pseudorapidity range. From this it can be deduced that the TPC aids mass peak resolution while the full TPC radius is being traversed by a track. As the D^0 decay products have relatively low transverse momentum (see Figure 6.18), this matches what has been seen before, in for example Sections 5.3.10 and 6.3; the silicon plus TPC layout has better momentum resolution than all-silicon concepts at low momenta in central regions.

The effect of the TPC can also be seen in the signal to background ratio plot; in the region $-1.11 \leq \eta \leq 1.11$, the S/B for the TPC baseline layout increases, and the layout has a higher ratio than the all-silicon layouts in this region. The two tested all-silicon layouts again have no significant difference between them. For all the tested detector layouts, the signal to background ratio has an overall increasing trend with increasing pseudorapidity (i.e. in the original electron-going direction). The decay products of a D^0 tend more to the negative pseudorapidity direction (see Figure 6.18). However, so do other particles from the collision, so there is an increase in both signal and background at negative pseudorapidities. As the pseudorapidity increases, the background decreases more than the signal. At the highest pseudorapidity however there is not much signal or background, making the error bars larger. This effect is especially clear for the datasets containing only 100 000 collisions. Comparing the dashed lines to the filled lines, it is clear that a 3.0 T magnetic field improves the S/B for all concepts and pseudorapidities compared to a 1.5 T magnetic field.

6.7 Conclusions and discussion

From the studies presented in this chapter, it can be concluded that it is essential to keep the material of the silicon detector low in order to maintain excellent pointing resolution with a large beampipe radius. A detector based on the ALICE ITS2 technology is insufficient for meeting the EIC physics requirements, so further developments such as the ITS3 technology are needed. It has also been seen in multiple studies that a 3.0 T magnetic field improves the performance of D meson reconstruction for both a silicon plus TPC detector concept and all-silicon detector concepts compared to a 1.5 T magnetic field. However, a large fraction of D^0 decay products cannot be reconstructed with such a high magnetic field. It is always beneficial to use a 3.0 T field for decays to pions and kaons from D mesons, but other decay channels and physics channels with lower final-state particle momenta will suffer. It has also been seen that not all physics requirements on relative momentum resolution can be met using a 1.5 T magnetic field however. It can thus be desirable to have a tuneable magnetic field, so that the detector can be optimised for a specific physics channel at runtime. A magnet with this feature is considered for the EIC [17,137]. The requirements on transverse pointing resolution can be met with any of the tested concepts, for either of the magnetic field strengths.

For D^0 meson decays, the presented detector concepts have a good acceptance. Around 90% of decay products are inside the detector acceptance in pseudorapidity, and in the pion-kaon pair decay channel over 96% of particles are within the transverse momentum acceptance. This will again vary for different physics channels however.

From the studies of D meson reconstruction, it can be seen that a compact all-silicon concept can perform as well as a large-radius all-silicon concept. This is encouraging for designs on building a more compact tracker. However, for the invariant mass reconstruction of D mesons, a concept with an inner silicon tracker and an outer TPC always matches or outperforms the tested all-silicon concepts. The results may be different for other physics channels, which can make a case for having two detectors with different trackers, optimised for different physics. With a compact all-silicon tracker the performance of particle ID detectors and calorimeters can potentially be improved. It is however also important to note that a TPC can give some particle ID information at low momenta. This is not accounted for in the performed simulations, as particle ID is either parameterised or ideal. The performance of a gas TPC can also improve in a higher magnetic field, which is also not taken into account in the simulations. Further studies of these effects and of different physics channels are required.

Chapter 7

Conclusions

7.1 Sensor studies

The studies of different sensors have indicated that the so-called “modified process” with a deep planar junction reaches a higher depletion than the “standard process”, resulting in a clearer signal and a faster charge collection. For smaller pixels the difference between the processes is found to be smaller, likely due to a larger fraction of the sensitive region already being depleted in the standard process for smaller pixels. The improvement in signal-to-background ratio of the modified process compared to the standard process is significant even at the smallest tested pixel size of $20 \times 20 \mu\text{m}^2$, however. As the potential difference between the p-well and the substrate increases, the charge collection performance in the modified process has been found to deteriorate. Through discussions with colleagues at CERN, it was concluded that the deterioration stems from an electric field minimum at pixel edges, trapping charges. The effect of this electric field minimum region increases with a higher bias voltage. It is less prominent at smaller pixel sizes however, as the distance between collection electrodes in neighbouring pixels decreases. Studies of further modified pixels with an extra deep p-well or a gap in the n-layer at the pixel edges have shown that the negative effects of the electric field minimum can be reduced with relatively small changes to the pixel geometry, even at high bias voltages and after irradiation of the sensors.

The investigated developments using the 180 nm CMOS imaging technology improve the charge collection properties compared to the ALPIDE sensor, and could be used in developing a sensor for a silicon vertex tracker for the EIC.

7.2 Simulations

From the general simulations, it has been found that the best silicon vertex tracker layout consists of two or three inner barrel layers, two outer barrel layers, and seven disks each in the forward and backward directions. The difference in performance between having seven disks and having five disks is small, but seven disks give

higher redundancy and detector coverage. The inner layers and innermost disks should be placed as close as possible to the interaction point, and the detector resolutions all benefit from having a small pixel size and a low material budget in all the detector layers. When using a gas TPC as an outer tracker, addition of a time-stamping layer in the barrel does not have a severe negative impact on the momentum resolution and pointing resolutions. In the disk region a time-stamping layer can have an increased material budget if it is located at the last disk position, but it is crucial to keep the pixel size low in order to retain the resolutions. If it is instead located at the penultimate disk position, the pixel size can increase as long as the material budget is kept low.

For particles with momenta above approximately 5 GeV/c it can be beneficial to replace the gas TPC with silicon layers, creating an all-silicon tracker. For low momenta a silicon plus TPC combination generally outperforms any all-silicon concept tested. If the outer radius of the tracker is decreased however, the best all-silicon concept outperforms the silicon plus TPC concept over a larger and larger momentum range the smaller the outer radius is. If a more compact tracker is desired, it is thus beneficial to use an all-silicon concept rather than a combination of silicon and a gas TPC.

The more focused detector simulations performed after site selection for the EIC show that it is essential to keep the sensor material thickness low in order to maintain the resolutions with a large-radius beampipe at low momenta, and thus that the projected ITS3-like sensors with a material budget of 0.05% X_0 for inner layers and 0.55% X_0 for outer layers are worth pursuing. It has also been found that all the tested designs (i.e. both the silicon plus TPC and various all-silicon concepts) exceed the physics requirements of the EIC in terms of pointing resolution, and the requirements on relative momentum resolution are met if a 3 T solenoid field is used. The pointing resolutions are exceeded by a level large enough that a pixel size larger than the tested $10 \times 10 \mu\text{m}^2$ may be viable, if available in a technology allowing a low material budget. The requirement on relative transverse momentum resolution cannot be met in the far-forward region by any of the tested detector concepts, however.

It has been found that a 3 T magnetic field improves the performance of D meson reconstruction in all the tested concepts, but also that such a high magnetic field makes it impossible to reconstruct a large number of particle tracks. A tuneable magnetic field strength may thus be desirable, to be able to trim the momentum acceptance of the detector to match the requirements for a main investigated physics channel at runtime. For D^0 meson decays in particular, the presented detector concepts have a good acceptance; around 90% of decay products are inside the detector acceptance in pseudorapidity, and in the pion-kaon pair decay channel over 96% of particles are within the transverse momentum acceptance even with a 3 T magnetic field.

From the studies of D meson reconstruction it can be seen that a compact all-silicon concept (with a radius of 432.5 mm) can perform as well as a large-radius all-silicon concept (with a radius of 775.0 mm). It can also be seen that a concept

combining layers of silicon with a TPC and silicon disks always matches or outperforms the tested all-silicon concepts. As the decay products of D mesons carry low momenta, this matches what has been seen in single-particle studies as well; the silicon plus TPC concept outperforms all-silicon concepts at momenta below approximately 5 GeV/c.

Chapter 8

Summary

Studies have been made of the design of a silicon vertex tracker for the electron-ion collider, both at the individual silicon sensor level using lab measurements, and at the full-size tracker level using simulations. The studied sensors have been prototype monolithic test chips, and the goal has been to investigate the performance of sensors created utilising a new method for achieving depletion of the full sensitive area while keeping the collection electrode small. This method is dubbed the “modified process” [55]. Four different sensors have been tested; two test structures called TowerJazz Investigator 1, in the “standard process” and the “modified process”, one sensor called TowerJazz Investigator 1B, and one called MiniMALTA. The standard process contains pixels similar to the ALPIDE sensor currently used in the ALICE experiment, and the modified process introduces a deep planar junction that depletion grows from, with the purpose of fully depleting the pixels in the sensor. The TowerJazz Investigator 1B has the same design as the TowerJazz Investigator 1, but allows separate biasing of the p-well and the substrate. This makes it possible to investigate the charge collection behaviour at different biasing configurations. The MiniMALTA sensor implements further process modifications for improved charge collection at the pixel edges.

The charge collection properties for different pixel sizes have been investigated and compared, using the TowerJazz Investigator 1 sensors in the modified process and the standard process that is ALPIDE-like. From this study, shown in Section 4.2.2, the modified process was found to improve the charge collection properties for all tested pixel sizes, due to the increased depletion. The TowerJazz Investigator 1B, produced using the modified process, allowed testing of different biasing voltages, and through the experiments presented in Section 4.2.3 it was unexpectedly found that a higher bias voltage reduces charge collection efficiency. Naïvely, a higher bias voltage should improve charge collection, as the electric field within the pixel grows stronger. Through discussions with colleagues at CERN however, the observed drop in efficiency was determined to come from an electric field minimum at pixel edges [113]. Charge making up the signal gets trapped in this minimum field region, and the effect of the minimum increases as the voltage difference between the substrate and the p-well increases (i.e. as the electric field lines under

the p-well become more vertical). To amend this, two different modifications at the pixel edges were proposed and implemented; an extra deep p-well was put in place, or a gap in the n-layer was introduced. Both modifications have the effect of funnelling the electric field more towards the collection electrode. The Mini-MALTA sensor contains pixels with these extra modifications intended to reduce the effect of the electric field minimum, and it was scanned with a fine beam of x-rays at the Diamond Light Source. Details of this study are shown in Section 4.3. Analysis of the data from this testbeam showed that the modifications are effective, significantly reducing the loss of charge collection efficiency when increasing the bias voltage. The developments with the added modifications thus have the potential to improve upon the currently existing sensors, and are considered a possible development path for an EIC-specific sensor. The developments allow more charge to be collected in a smaller pixel compared to current state-of-the-art MAPS sensors, which will help reach the resolution requirements set by the EIC physics programme. The timeline and requirements for the ALICE ITS3 upgrade align well with the EIC however, so the primary focus will be on partaking in the ITS3 developments and forking off an EIC sensor at a later date [51]. These developments are primarily intended to utilise the 65 nm CMOS imaging process, but use of this process in particle physics experiments is currently unproven. The current 180 nm developments presented in this thesis are thus kept as a fallback option for future EIC developments.

The simulations were carried out both with single particles and with realistic physics events, and studies were made both of all-silicon concepts and of combinations of silicon and gaseous detectors. Before site selection of the EIC in January 2020 the simulations were more general and explored and compared the performance of many different silicon vertex tracker layouts and parameters, such as pixel size, material budget, and silicon layer configuration. These studies are detailed in Chapter 5. The conclusions from the general simulation studies is that a small pixel size improves the pointing resolutions everywhere, and is crucial to have in the disks for the momentum resolution in the forward and backward regions. Two kinds of detector concepts were investigated; concepts with a TPC as an outer tracker, and all-silicon concepts. The favoured silicon vertex tracker design consists of two or three inner barrel layers close to the beampipe, two outer barrel layers close to the surrounding TPC (when present), and seven disks each in the forward and backward directions. A time-stamping layer with different parameters to the other silicon detector layers can be added without it being severely detrimental to the resolutions. Through the studies presented in Section 5.3.10.2 it was also found that if a more compact tracker is desired, it is more beneficial to use an all-silicon tracker with large disks than a combination of silicon and TPC.

After site selection in January 2020, the simulations could be more focused, taking constraints brought by the construction site into account. These focused simulations are presented in Chapter 6, building on from the simulations presented in Chapter 5. The main impact on the silicon vertex tracker design came from the beampipe envisioned for the selected Brookhaven location. The beampipe radius

was assumed to be 18 mm in the general simulations, but the radius after site selection is 31 mm. This forces the inner layers of the silicon vertex tracker further out than what was previously studied. At this time, the silicon sensor development for the EIC was also suggested to follow the ALICE ITS3 upgrade, and simulations were made using the projected performance of the ITS3-based sensors with the new beampipe. It was shown that a very low material thickness of the sensor layers is needed to meet the requirements from EIC physics channels, and the low power consumption of ITS3-based sensors can make this possible. Using ITS3-based sensors and results from the general simulations, different possible detector layouts were created. The “silicon plus TPC baseline” created in this work was adopted as one of the two tracker baselines in the EIC Yellow Report [17]. The detector resolutions for different layouts were parameterised, and compared to requirements provided by the EIC Yellow Report Physics Working Group. The parameterisations for the silicon plus TPC baseline layout were included in the EIC Yellow Report, and provided to the Physics Working Group to be included in “fast simulations”. It was found that the requirements on pointing resolution can be met in all regions by all investigated detector concepts, but the requirements on relative momentum resolution can only be met if a 3 T magnetic field is used. In the far-forward region, the relative transverse momentum resolution requirements cannot be met even with a 3 T field, so further developments are required there.

Simulations using physics events were also performed, both for a silicon plus TPC tracker design and several all-silicon designs. These studies are presented in Sections 6.5 and 6.6. The physics events were generated as electron-proton collisions of four different energy combinations using Pythia, with a focus on open charm production. The generated events were examined, compared to the detector acceptance, and propagated through a full GEANT4-based simulation of the tracking detector. The figures of merit used for the analysis were the reconstructed invariant mass peak width and signal to background ratio for the charmed D^0 , D^+ , and D^{*+} mesons, and the goal was to compare the performance of different tracking detector designs for different magnetic field strengths. It was found that a compact all-silicon concept can be designed to perform as well as a larger all-silicon concept for these figures of merit, that a 3 T magnetic field outperforms a 1.5 T magnetic field, and that a silicon plus TPC tracker outperforms all tested all-silicon concepts for these particular physics channels. It was also found that a 3 T magnetic field prevents many particle tracks from being reconstructed however, which is important to keep in mind for studies of other physics channels.

In conclusion, the work carried out has identified a detector technology possible for use in development of an EIC-specific sensor. A silicon vertex tracker design has also been developed, which meets the physics requirements for the EIC in a large part of the projected phase space. The best performing design varies depending on the particle momenta under investigation, which indicates that a tuneable magnetic field and two complementary tracking detector designs may be desirable, focusing on different physics channels.

Chapter 9

Future work

As previously mentioned, the timeline of the EIC aligns well with both the requirements and the timeline of the ALICE ITS3 upgrade, and the EIC is thus joining in the silicon sensor development effort for the ALICE ITS3 with the intention of forking off an EIC specific sensor at a later date. The first test structures in the 65 nm CMOS imaging technology will soon be available for testing, and the developments for the ITS3 should be actively participated in. The ITS3 developments may fall back on using the 180 nm technology, but the sensors developed for the ITS3 will still have new developments that will likely be useful to the EIC as well, reducing power consumption and pixel size compared to the currently existing state-of-the-art MAPS sensors. The results of the work presented in Chapter 4 give useful indications for development paths for such a sensor. Further studies of the charge collection properties of the newest design modifications using smaller pixel sizes would be of great interest, as initial results indicate that modifications are less important as pixels grow smaller. The modified process consistently provides a better signal-to-background ratio than the standard process, but further modifications at the pixel edges may not be necessary in small pixels.

It would also be of interest to investigate fast silicon sensors, for possible use in a time-stamping layer. Developments of the MALTA chip have been followed throughout the thesis work, and the time resolution of this chip appears to improve in newer sensor versions. The FASTPIX chip is also based on the same technology and modifications to improve charge collection, as discussed in Section 4.3.1 [138]. This chip is theorised to be able to reach sub-nanosecond time resolution, which is sufficient to time-stamp bunch crossings at the EIC. Other silicon technologies can also be interesting for this, such as single-photon avalanche diodes (SPADs).

A step that should be taken in the simulations is to use a different track reconstruction software that is more up to date and provides more accurate vertex information than GENFIT, such as ACTS [125]. The ACTS software has been developed by the ATLAS collaboration as a generic experiment-independent reconstruction package, and is a more modern and complete tool for event reconstruction than GENFIT. Using ACTS will also enable study of track finding, which can be an important factor in multi-track events. At the time of the simulations presented in

this thesis ACTS was not available in the Fun4All framework. It is however currently being implemented, and is used in sPHENIX simulations which also utilise the Fun4All framework.

Several things can be done to make the simulations more realistic. One of the main things is to implement realistic services in the simulated detector. Currently the implementation of services and support structures only extends to the individual detector staves, but in reality a relatively large amount of non-sensitive material required for holding the staves in place and providing powering and readout needs to be placed near the sensitive area, somewhere within the full detector acceptance [130]. This will negatively affect the detector resolutions in some direction, and it is thus important to implement it in simulations and try to optimise the positioning of the non-sensitive material. Implementation of realistic services outside the detector staves is thus one of the most important steps that needs to be taken to improve the validity of studies in the forward and backward regions. To fully realise and optimise the impact of services, the simulations will also require integration of other detector subsystems that may be impacted by the positioning of the non-sensitive material.

For studies outside of the central region, the solenoidal magnetic field map used may have a significant impact on the detector resolutions. The magnetic fields used in the simulations presented in this work have all been uniform and parallel to the beam axis, but in reality the magnetic field lines have to bend back at some point in the forward and backward directions. For the operation of a ring-imaging Cherenkov detector, which is planned to be situated just outside the last silicon disk, it is also desirable to have a magnetic field that is not parallel to the beam axis [139]. A realistic magnetic field used in the detector may thus differ significantly in the forward and backward disk regions from the uniform magnetic fields hitherto used in the simulations. As the EIC solenoid developments progress, more accurate magnetic field maps become available for use in the Fun4All framework, and it would be beneficial to run future simulations with an up-to-date field map for the results to be as realistic as possible.

In theory, the momentum resolution at high pseudorapidities could be vastly improved by adding a tracking layer far away from the interaction point, beyond the outermost silicon disk. This has been investigated both by colleagues at Berkeley and at the Los Alamos National Lab, but it may be worth investigating further while using a realistic implementation of services and a realistic magnetic field map. As demonstrated in Section 6.3 none of the detector concepts presented in this thesis match the EIC physics requirements for relative transverse momentum resolution in the high pseudorapidity region, so further developments are essential. There have been discussions of utilising a gaseous detector for this far away tracking layer, and an accurate implementation of such a detector should soon become available in Fun4All. Once it is, more complete silicon plus gas detector combinations can be investigated. The silicon plus MPGD layout presented in Section 6.1.3.1 can then for example be complemented with gaseous endcap detectors, and investigated further.

When the detector geometry is more fixed, it would also be of interest to simulate a more realistic detector response, both in silicon and gaseous detectors. Currently, an individual silicon detector resolution is taken to be the pixel size divided by $\sqrt{12}$, which represents the idealised case as shown in Section 2.2.1. In reality however the resolution can frequently be improved upon by using charge sharing algorithms. The resolution of a gas TPC alters with the magnetic field used, which is not taken into account in the simulations presented in this work. More detailed simulations of the TPC response than what is currently available are needed to be able to take it into account properly, but it can be an important parameter for the overall resolutions. It may thus be of interest to re-run the TPC simulations performed in this work with an approximated TPC resolution for a 3 T magnetic field already in the near future.

The TPC is also able to provide some particle identification information. For future physics simulations, it would in general be desirable to utilise other detector subsystems as well as the tracker, such as the bespoke particle identification detectors and calorimeters that will exist in a full detector. As a first step an accurate up-to-date parametrisation of the particle identification capabilities and the energy resolution can be used, but a long-term goal should be to integrate the different detector subsystems and perform simulations with a full detector concept. This will most likely become easier when detector collaborations form and work can be more focused on integration. The location and optimisation of services will again play an important role here.

All physics events used in the work carried out in this thesis were generated as head-on collisions. In reality the EIC interaction regions will have a beam crossing angle of up to 25 milliradians [17], and this may affect where the final products of a collision go, and their angles relative to the magnetic field. It would thus be interesting to study the effect of a non-zero crossing angle, and the impact it has on the reconstructions. All events studied so far have also been electron-proton collisions. A natural next step is to collide electrons with ions instead. It may also be of interest to introduce beam polarisation to the event generation.

The open charm event reconstructions presented in Section 6.6 could be expanded into a full physics impact study with further simulations. By using a number of events corresponding to a correct integrated luminosity for the EIC, and extracting the differential cross sections in terms of x and Q^2 for the D mesons, an estimation of the charm structure function $F_2^{c\bar{c}}(x, Q^2)$ can be made. This would however also require an accurate model of background events, something which is not present in the majority of the simulations carried out in the work presented here. A natural first step in the physics simulation work is to implement more accurate background, and extract the detector resolution versus Q^2 as well as x .

Appendices

Appendix A

Charged particle interactions

As charged particles move through matter they lose energy due to electromagnetic interactions with the atoms in the traversed material. For light charged particles (e.g. electrons and muons) the interactions can result in ionisation and excitation of the medium's atoms, emission of Cherenkov light, or emission of bremsstrahlung. For heavier charged particles, ionisation energy losses dominate over radiative energy losses. The mean energy loss per traversed length, dE/dx , for such a particle is approximated by

$$-\frac{dE}{dx} = \frac{4\pi N_A \cdot r_e^2 \cdot m_e c^2 \cdot \rho Z \cdot z^2}{A \cdot \beta^2} \cdot \left(\frac{1}{2} \ln \left(\frac{2m_e c^2 \beta^2 \gamma^2 W_{\max}}{I^2} \right) - \beta^2 - \frac{\delta(\beta\gamma)}{2} \right), \quad (\text{A.1})$$

which is known as the Bethe-Bloch formula [30, 31]. N_A denotes the Avogadro constant, r_e the classical electron radius ($2.82 \cdot 10^{-15}$ m), and m_e the electron mass. The density of the traversed material is denoted ρ , and its atomic number and atomic weight are denoted Z and A , respectively. The charge of the incident particle, in units of the elementary charge e , is denoted z . The velocity of the incident particle enters the equation via $\beta = v/c$ and $\gamma = 1/\sqrt{1-\beta^2}$. W_{\max} denotes the maximum possible energy transfer from a single collision between the incident particle and an electron in the traversed material. It is given by [31]

$$W_{\max} = \frac{2m_e c^2 \beta^2 \gamma^2}{1 + 2\gamma m_e/M + (m_e/M)^2}, \quad (\text{A.2})$$

where M is the mass of the incident particle. For $M \gg 2\gamma m_e$, the approximation $W_{\max} \simeq 2m_e c^2 \beta^2 \gamma^2$ can be applied.

The factor I in Equation A.1 is the mean excitation energy of the traversed material. It relates to the oscillator strengths of the material, and is difficult to determine analytically. Experimentally derived values for different materials are available in tables [31]. The final factor in the equation, $\delta(\beta\gamma)$, is the density effect correction term. As the incident charged particle traverses the material, its electric field polarises atoms along its path. This causes electrons to be shielded from the electric field of the moving particle, and thus energy loss is decreased. This effect is only important for highly relativistic particles.

Figure A.1 shows the mean energy loss of a positive muon traversing copper, as a function of $\beta\gamma$. Note that the unit on the y-axis is $\text{MeV cm}^2/\text{g}$. That is, dx is

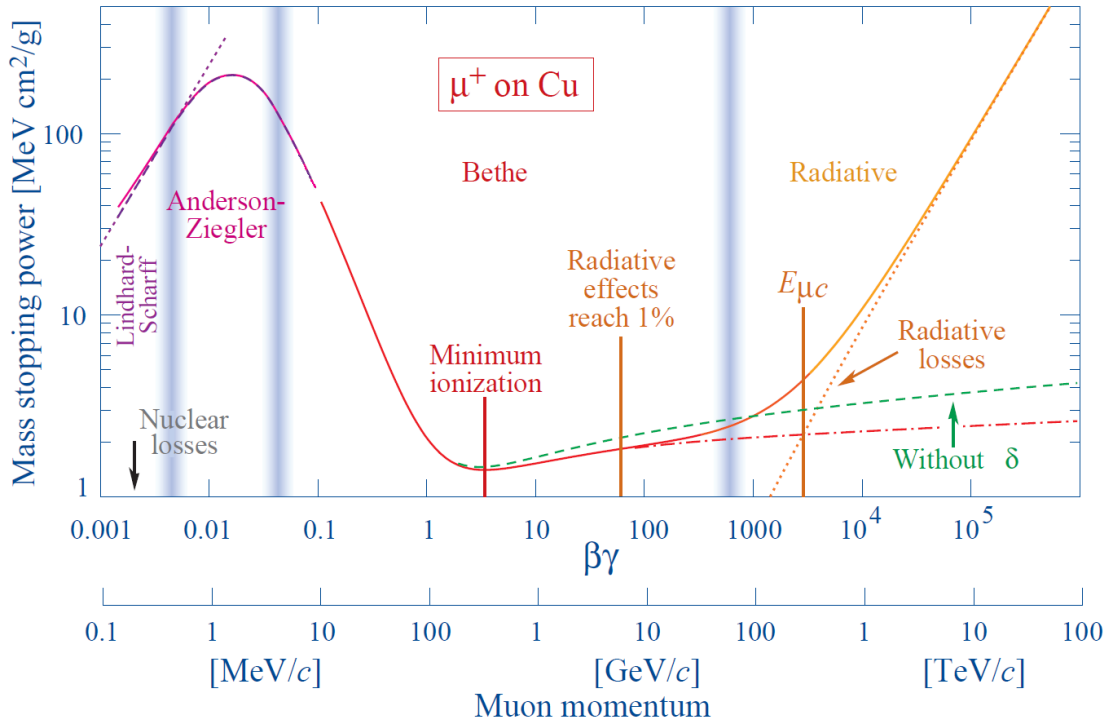


Figure A.1: Energy loss divided by material density (termed “mass stopping power”) for a positive muon traversing copper, as a function of $\beta\gamma$ [31]. The region marked “Bethe” is accurately described by Equation A.1. The dashed lines at $\beta\gamma > 3$ represent heavier charged particles, while the filled line for the muon also contains the bremsstrahlung losses that dominate the light charged particle energy loss at high energies. Figure from [32].

here defined as $\rho \cdot dx$ from Equation A.1. The Bethe-Bloch formula as it is defined in Equation A.1 is valid in the region marked “Bethe”, between $\beta\gamma \approx 0.05$ and $\beta\gamma \approx 1000$. Below $\beta\gamma \approx 0.05$, the velocity of the incident particle is comparable to the orbital velocity of the bound electrons, and the Bethe-Bloch formula breaks down. Radiative effects become more important at high energies, for light charged particles such as the muon shown in Figure A.1. The dashed lines in the figure show the energy loss for heavier particles, that are not as affected by radiative effects as the muon.

For the energy range described by the Bethe-Bloch formula, there is a minimum at around $\beta\gamma = 3$ (but the exact value varies with the atomic number Z of the traversed material). Between $\beta\gamma \approx 0.05$ and the minimum, the $1/\beta^2$ term in Equation A.1 is dominant. After the minimum, dE/dx is proportional to $\ln(\beta\gamma)$ (known as the relativistic rise), until it saturates at higher energies due to polarisation effects, which is where the $\delta(\beta\gamma)$ correction comes in. The effect of the $\delta(\beta\gamma)$ correction is also accentuated in Figure A.1, comparing the green dashed line with the red dashed line. At high energies, a small dependence on the mass

of the incident particle is also introduced, through the maximum possible energy transfer W_{\max} .

As $-dE/dx$ rises slowly with increasing energy, most particles (excluding the light charged particles at levels where they experience high radiative losses) have mean energy loss rates close to the minimum. Particles with $\beta\gamma \geq 3$ are thus called Minimum Ionising Particles (MIPs), and are often used as an approximation for particle energy loss calculations.

The dE/dx curve is particle dependent for values of $\beta\gamma$ below the minimum ionising energy. If the energy loss is plotted against the particle momentum, the curve will generally have the same shape, but be shifted slightly for different particle masses. This makes it possible to identify different particles in this energy range by measuring the energy loss.

The Bethe-Bloch formula gives the mean energy loss per traversed length of material for a charged particle. The fluctuation of energy loss around the mean value when traversing a material of finite length is described by a Landau distribution [33] or a Vavilov distribution [140], depending on the material thickness. For MIPs traversing thin materials, Landau's theory is the most accurate [30]. This theory requires some modification as well at the lowest thicknesses, such as for the silicon sensors this work pertains to [34]. The modification takes the form of a normal distribution convoluted with a Landau distribution. The result of this is a reduction of the average energy loss as the material grows thinner.

APPENDIX B. DIFFERENT SILICON LAYOUTS FOR COMPARISON WITH A TPC

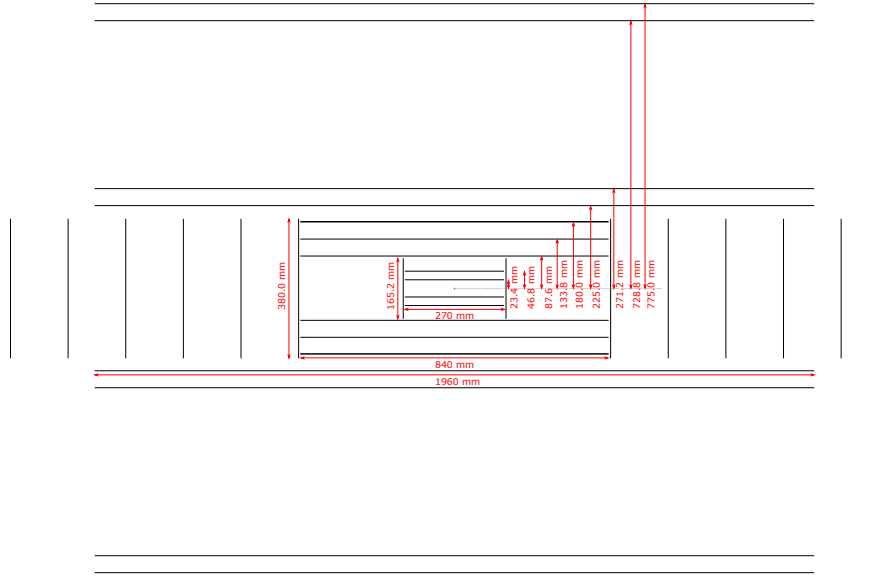


Figure B.2: Sketch of the simulated layout with standard disks, where the gas TPC is replaced by two inner and two outer long (1960 mm) silicon layers (*2+2 layers, long*).

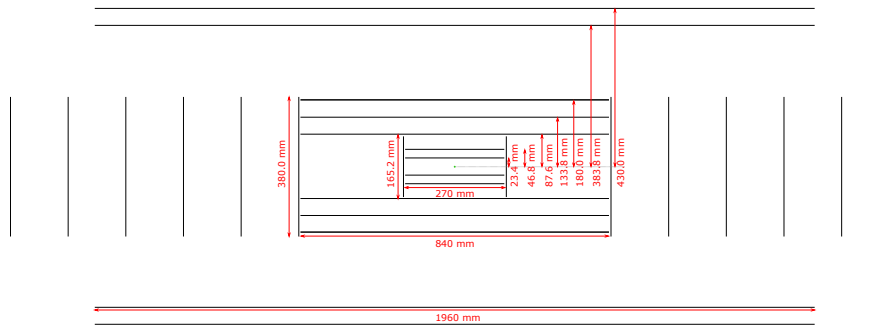


Figure B.3: Sketch of the simulated layout with standard disks, where the gas TPC is replaced by two long (1960 mm) silicon layers at a smaller outer radius (*2 layers, long, small radius*).

“2 layers, short, small radius; large disks” layout, Figure B.5 the “5 layers, short; large disks” layout, and finally Figure B.6 shows the “5 layers, short; optimised disks” layout. This layout has a combination of disks and rings (i.e. disks with a large inner radius), rather than only disks.

APPENDIX B. DIFFERENT SILICON LAYOUTS FOR COMPARISON WITH A TPC

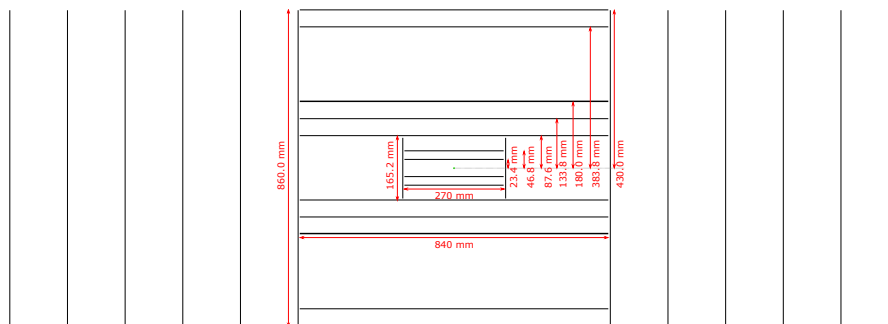


Figure B.4: Sketch of the simulated layout with large disks (860 mm diameter), where the gas TPC is replaced by two short (840 mm) silicon layers at a smaller outer radius (*2 layers, short, small radius; large disks*).

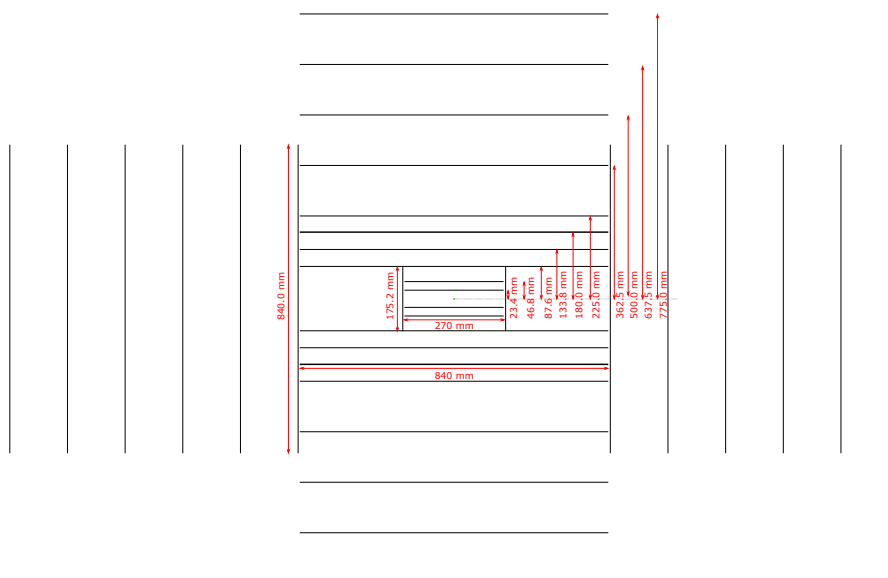


Figure B.5: Sketch of the simulated layout with large disks (840 mm diameter), where the gas TPC is replaced by five short (840 mm) radially equidistant silicon layers (*5 layers, short; large disks*).

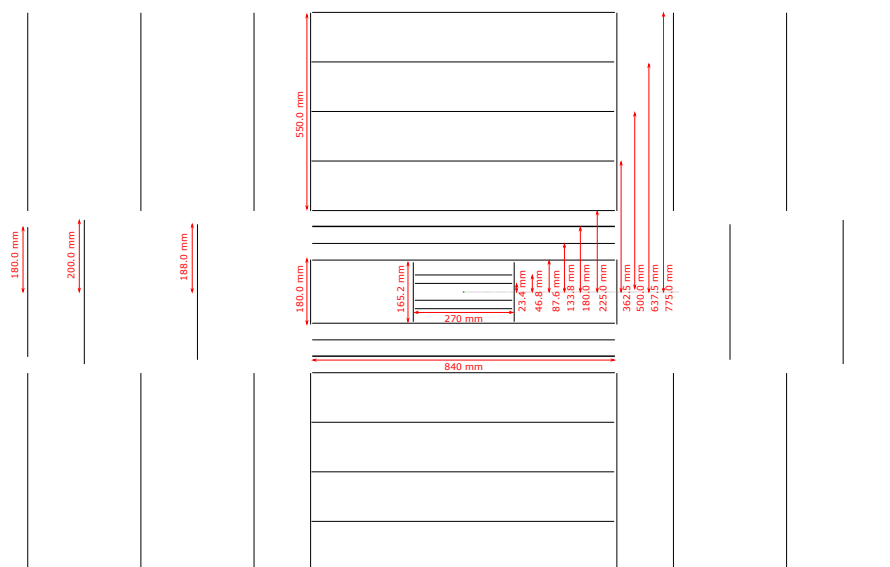


Figure B.6: Sketch of the simulated layout with optimised disks (*5 layers, short; optimised disks*), where the gas TPC is replaced by five equidistant short (840 mm) silicon layers, as well as disks and rings to give pseudorapidity coverage in the forward and backward regions.

Appendix C

Detector parametrisation fit results

This chapter contains the detailed fit results of the work described in Section 6.3, where a study is performed to parametrise the resolution of the four detector concepts described in Section 6.1.3, using the equations shown below;

$$\frac{\sigma_p}{p} = A \cdot p \oplus B = \sqrt{(A \cdot p)^2 + B^2} \quad (\text{C.1})$$

$$\frac{\sigma_{xy}}{p_T} = \frac{A}{p_T} \oplus B = \sqrt{\left(\frac{A}{p_T}\right)^2 + B^2}. \quad (\text{C.2})$$

For the fit of relative transverse momentum resolution, the momentum in Equation C.1 is replaced with the transverse momentum. Equation C.2 is also used to fit the longitudinal pointing resolution. For some layouts and pseudorapidity intervals, the relative momentum resolution fit does not describe the data well. In order to have the correct parametrisation to interface with the Physics Working Group, the fit is performed in two different momentum intervals.

The requirements presented by the EIC Yellow Report Physics Working Group relevant to the inner tracking system are summarised in the table below. There is no requirement on the longitudinal pointing resolution at the time of writing.

η interval	Relative momentum resolution [%]	Transverse pointing [μm]
$-3.5 \leq \eta \leq -2.5$	$A = 0.1, B = 0.5$	$A = 30, B = 40$
$-2.5 \leq \eta \leq -1.0$	$A = 0.05, B = 0.5$	$A = 30, B = 20$
$-1.0 \leq \eta \leq 1.0$	$A = 0.05, B = 0.5$	$A = 20, B = 5$
$1.0 \leq \eta \leq 2.5$	$A = 0.05, B = 1.0$	$A = 30, B = 20$
$2.5 \leq \eta \leq 3.5$	$A = 0.05, B = 2.0$	$A = 30, B = 40$

Tables C.1 through C.14 show the fit results for the four different detector concepts presented in Section 6.1.3. As the silicon plus MPGD layout is missing endcap detectors in the forward and backward regions, only the central region is studied for it.

APPENDIX C. DETECTOR PARAMETRISATION FIT RESULTS

Interval	p interval	Fit 1.5 T [%]		Fit 3.0 T [%]	
		A	B	A	B
$-3.5 \leq \eta \leq -2.5$	0 to 30 GeV/c	0.09 ± 0.01	3.71 ± 0.05	0.05 ± 0.01	1.90 ± 0.02
$-2.5 \leq \eta \leq -1.0$	0 to 8 GeV/c	0.24 ± 0.01	0.67 ± 0.01	0.11 ± 0.01	0.33 ± 0.01
	8 to 30 GeV/c	0.07 ± 0.01	1.81 ± 0.02	0.04 ± 0.01	0.88 ± 0.01
$-1.0 \leq \eta \leq 1.0$	0 to 5 GeV/c	0.21 ± 0.01	0.34 ± 0.01	0.11 ± 0.01	0.18 ± 0.01
	5 to 30 GeV/c	0.06 ± 0.01	1.09 ± 0.01	0.03 ± 0.01	0.54 ± 0.01
$1.0 \leq \eta \leq 2.5$	0 to 8 GeV/c	0.24 ± 0.01	0.67 ± 0.01	0.11 ± 0.01	0.33 ± 0.01
	8 to 30 GeV/c	0.07 ± 0.01	1.81 ± 0.02	0.04 ± 0.01	0.88 ± 0.01
$2.5 \leq \eta \leq 3.5$	0 to 30 GeV/c	0.09 ± 0.01	3.71 ± 0.05	0.05 ± 0.01	1.90 ± 0.02

Table C.1: Relative momentum resolution fit parameters using the fit presented in Equation C.1, for the silicon plus TPC layout.

Interval	p_T interval	Fit 1.5 T [%]		Fit 3.0 T [%]	
		A	B	A	B
$-3.5 \leq \eta \leq -2.5$	0 to 30 GeV/c	0.59 ± 0.01	4.23 ± 0.03	0.31 ± 0.01	2.11 ± 0.01
$-2.5 \leq \eta \leq -1.0$	0 to 4 GeV/c	0.50 ± 0.01	0.88 ± 0.01	0.23 ± 0.01	0.48 ± 0.01
	4 to 30 GeV/c	0.13 ± 0.01	2.20 ± 0.01	0.06 ± 0.01	1.11 ± 0.01
$-1.0 \leq \eta \leq 1.0$	0 to 4 GeV/c	0.25 ± 0.01	0.36 ± 0.01	0.12 ± 0.01	0.18 ± 0.01
	4 to 30 GeV/c	0.07 ± 0.01	1.10 ± 0.01	0.03 ± 0.01	0.55 ± 0.01
$1.0 \leq \eta \leq 2.5$	0 to 4 GeV/c	0.50 ± 0.01	0.88 ± 0.01	0.23 ± 0.01	0.48 ± 0.01
	4 to 30 GeV/c	0.13 ± 0.01	2.20 ± 0.01	0.06 ± 0.01	1.11 ± 0.01
$2.5 \leq \eta \leq 3.5$	0 to 30 GeV/c	0.59 ± 0.01	4.23 ± 0.03	0.31 ± 0.01	2.11 ± 0.01

Table C.2: Relative transverse momentum resolution fit parameters using the fit presented in Equation C.1, for the silicon plus TPC layout.

Interval	Fit 1.5 T [μm]		Fit 3.0 T [μm]	
	A	B	A	B
$-3.5 \leq \eta \leq -2.5$	49.28 ± 0.20	9.64 ± 0.02	48.51 ± 0.20	9.58 ± 0.02
$-2.5 \leq \eta \leq -1.0$	23.29 ± 0.08	3.32 ± 0.01	23.14 ± 0.08	3.31 ± 0.01
$-1.0 \leq \eta \leq 1.0$	14.07 ± 0.05	2.11 ± 0.01	13.66 ± 0.05	2.15 ± 0.01
$1.0 \leq \eta \leq 2.5$	23.29 ± 0.08	3.32 ± 0.01	23.14 ± 0.08	3.31 ± 0.01
$2.5 \leq \eta \leq 3.5$	49.28 ± 0.20	9.64 ± 0.02	48.51 ± 0.20	9.58 ± 0.02

Table C.3: Transverse pointing resolution fit parameters, using the fit presented in Equation C.2, for the silicon plus TPC layout.

APPENDIX C. DETECTOR PARAMETRISATION FIT RESULTS

Interval	Fit 1.5 T [μm]		Fit 3.0 T [μm]	
	A	B	A	B
$-3.5 \leq \eta \leq -2.5$	596.90 ± 1.51	41.05 ± 0.12	596.46 ± 1.50	40.79 ± 0.12
$-2.5 \leq \eta \leq -1.0$	78.30 ± 0.18	3.11 ± 0.02	78.12 ± 0.18	3.12 ± 0.02
$-1.0 \leq \eta \leq 1.0$	23.20 ± 0.06	2.64 ± 0.01	22.86 ± 0.06	2.64 ± 0.01
$1.0 \leq \eta \leq 2.5$	78.30 ± 0.18	3.11 ± 0.02	78.12 ± 0.18	3.12 ± 0.02
$2.5 \leq \eta \leq 3.5$	596.90 ± 1.51	41.05 ± 0.12	596.46 ± 1.50	40.79 ± 0.12

Table C.4: Longitudinal pointing resolution fit parameters, using the fit presented in Equation C.2, for the silicon plus TPC layout.

Interval	p interval	Fit 1.5 T [%]		Fit 3.0 T [%]	
		A	B	A	B
$-3.5 \leq \eta \leq -2.5$	0 to 30 GeV/c	0.09 ± 0.01	3.28 ± 0.04	0.04 ± 0.01	1.64 ± 0.02
$-2.5 \leq \eta \leq -1.0$	0 to 2.5 GeV/c	0.22 ± 0.02	0.85 ± 0.02	0.14 ± 0.01	0.38 ± 0.01
	2.5 to 30 GeV/c	0.03 ± 0.01	1.09 ± 0.01	0.01 ± 0.00	0.55 ± 0.01
$-1.0 \leq \eta \leq 1.0$	0 to 2.5 GeV/c	0.34 ± 0.01	0.66 ± 0.01	0.18 ± 0.01	0.31 ± 0.01
	2.5 to 30 GeV/c	0.04 ± 0.01	1.19 ± 0.01	0.02 ± 0.00	0.59 ± 0.01
$1.0 \leq \eta \leq 2.5$	0 to 2.5 GeV/c	0.22 ± 0.02	0.85 ± 0.02	0.14 ± 0.01	0.38 ± 0.01
	2.5 to 30 GeV/c	0.03 ± 0.01	1.09 ± 0.01	0.01 ± 0.00	0.55 ± 0.01
$2.5 \leq \eta \leq 3.5$	0 to 30 GeV/c	0.09 ± 0.01	3.28 ± 0.04	0.04 ± 0.01	1.64 ± 0.02

Table C.5: Relative momentum resolution fit parameters using the fit presented in Equation C.1, for the all-silicon baseline layout.

Interval	p_T interval	Fit 1.5 T [%]		Fit 3.0 T [%]	
		A	B	A	B
$-3.5 \leq \eta \leq -2.5$	0 to 30 GeV/c	0.62 ± 0.01	3.90 ± 0.02	0.31 ± 0.01	1.96 ± 0.01
$-2.5 \leq \eta \leq -1.0$	0 to 2.5 GeV/c	0.22 ± 0.02	1.03 ± 0.01	0.08 ± 0.01	0.54 ± 0.01
	2.5 to 30 GeV/c	0.06 ± 0.01	1.19 ± 0.01	0.03 ± 0.00	0.60 ± 0.01
$-1.0 \leq \eta \leq 1.0$	0 to 2.5 GeV/c	0.35 ± 0.01	0.70 ± 0.01	0.18 ± 0.01	0.35 ± 0.01
	2.5 to 30 GeV/c	0.04 ± 0.00	1.21 ± 0.01	0.02 ± 0.00	0.61 ± 0.01
$1.0 \leq \eta \leq 2.5$	0 to 2.5 GeV/c	0.22 ± 0.02	1.03 ± 0.01	0.08 ± 0.01	0.54 ± 0.01
	2.5 to 30 GeV/c	0.06 ± 0.01	1.19 ± 0.01	0.03 ± 0.00	0.60 ± 0.01
$2.5 \leq \eta \leq 3.5$	0 to 30 GeV/c	0.62 ± 0.01	3.90 ± 0.02	0.31 ± 0.01	1.96 ± 0.01

Table C.6: Relative transverse momentum resolution fit parameters using the fit presented in Equation C.1, for the all-silicon baseline layout.

Interval	Fit 1.5 T [μm]		Fit 3.0 T [μm]	
	A	B	A	B
$-3.5 \leq \eta \leq -2.5$	49.95 ± 0.19	10.70 ± 0.02	49.69 ± 0.19	10.74 ± 0.02
$-2.5 \leq \eta \leq -1.0$	23.52 ± 0.07	2.55 ± 0.01	23.60 ± 0.07	2.54 ± 0.01
$-1.0 \leq \eta \leq 1.0$	16.38 ± 0.05	2.04 ± 0.01	16.27 ± 0.05	2.02 ± 0.01
$1.0 \leq \eta \leq 2.5$	23.52 ± 0.07	2.55 ± 0.01	23.60 ± 0.07	2.54 ± 0.01
$2.5 \leq \eta \leq 3.5$	49.95 ± 0.19	10.70 ± 0.02	49.69 ± 0.19	10.74 ± 0.02

Table C.7: Transverse pointing resolution fit parameters using the fit presented in Equation C.2, for the all-silicon baseline layout.

Interval	Fit 1.5 T [μm]		Fit 3.0 T [μm]	
	A	B	A	B
$-3.5 \leq \eta \leq -2.5$	650.03 ± 1.58	48.84 ± 0.12	644.24 ± 1.59	49.11 ± 0.12
$-2.5 \leq \eta \leq -1.0$	82.58 ± 0.20	3.56 ± 0.02	83.93 ± 0.21	3.73 ± 0.02
$-1.0 \leq \eta \leq 1.0$	23.40 ± 0.06	2.35 ± 0.01	23.05 ± 0.06	2.36 ± 0.01
$1.0 \leq \eta \leq 2.5$	82.58 ± 0.20	3.56 ± 0.02	83.93 ± 0.21	3.73 ± 0.02
$2.5 \leq \eta \leq 3.5$	650.03 ± 1.58	48.84 ± 0.12	644.24 ± 1.59	49.11 ± 0.12

Table C.8: Longitudinal pointing resolution fit parameters, using the fit presented in Equation C.2, for the all-silicon baseline layout.

Interval	p_{T} interval	Fit 1.5 T [%]		Fit 3.0 T [%]	
		A	B	A	B
$-3.5 \leq \eta \leq -2.5$	0 to 30 GeV/c	0.71 ± 0.01	3.45 ± 0.03	0.37 ± 0.01	1.71 ± 0.01
$-2.5 \leq \eta \leq -1.0$	0 to 30 GeV/c	0.05 ± 0.01	1.06 ± 0.01	0.02 ± 0.01	0.53 ± 0.01
$-1.0 \leq \eta \leq 1.0$	0 to 2.5 GeV/c	0.28 ± 0.01	0.80 ± 0.01	0.13 ± 0.01	0.40 ± 0.01
	2.5 to 30 GeV/c	0.02 ± 0.01	1.03 ± 0.01	0.01 ± 0.01	0.51 ± 0.01
$1.0 \leq \eta \leq 2.5$	0 to 30 GeV/c	0.05 ± 0.01	1.06 ± 0.01	0.02 ± 0.01	0.53 ± 0.01
$2.5 \leq \eta \leq 3.5$	0 to 30 GeV/c	0.71 ± 0.01	3.45 ± 0.03	0.37 ± 0.01	1.71 ± 0.01

Table C.9: Relative transverse momentum resolution fit parameters using the fit presented in Equation C.1, for the 600 mm outer radius all-silicon layout.

Interval	Fit 1.5 T [μm]		Fit 3.0 T [μm]	
	A	B	A	B
$-3.5 \leq \eta \leq -2.5$	45.88 ± 0.21	9.99 ± 0.02	46.16 ± 0.21	9.93 ± 0.02
$-2.5 \leq \eta \leq -1.0$	22.48 ± 0.07	2.64 ± 0.01	22.36 ± 0.07	2.66 ± 0.01
$-1.0 \leq \eta \leq 1.0$	15.40 ± 0.05	1.97 ± 0.01	14.67 ± 0.05	1.99 ± 0.01
$1.0 \leq \eta \leq 2.5$	22.48 ± 0.07	2.64 ± 0.01	22.36 ± 0.07	2.66 ± 0.01
$2.5 \leq \eta \leq 3.5$	45.88 ± 0.21	9.99 ± 0.02	46.16 ± 0.21	9.93 ± 0.02

Table C.10: Transverse pointing resolution fit parameters using the fit presented in Equation C.2, for the 600 mm outer radius all-silicon layout.

Interval	Fit 1.5 T [μm]		Fit 3.0 T [μm]	
	A	B	A	B
$-3.5 \leq \eta \leq -2.5$	537.68 ± 1.59	40.85 ± 0.12	538.46 ± 1.59	40.99 ± 0.12
$-2.5 \leq \eta \leq -1.0$	80.25 ± 0.19	3.80 ± 0.02	78.87 ± 0.19	3.91 ± 0.02
$-1.0 \leq \eta \leq 1.0$	23.58 ± 0.06	2.57 ± 0.01	23.19 ± 0.06	2.58 ± 0.01
$1.0 \leq \eta \leq 2.5$	80.25 ± 0.19	3.80 ± 0.02	78.87 ± 0.19	3.91 ± 0.02
$2.5 \leq \eta \leq 3.5$	537.68 ± 1.59	40.85 ± 0.12	538.46 ± 1.59	40.99 ± 0.12

Table C.11: Longitudinal pointing resolution fit parameters using the fit presented in Equation C.2, for the 600 mm outer radius all-silicon layout.

Interval	p_{T} interval	Fit 1.5 T [%]		Fit 3.0 T [%]	
		A	B	A	B
$-1.0 \leq \eta \leq 1.0$	0 to 2.5 GeV/c	0.26 ± 0.01	0.70 ± 0.01	0.13 ± 0.01	0.35 ± 0.01
	2.5 to 30 GeV/c	0.11 ± 0.01	0.99 ± 0.01	0.05 ± 0.01	0.50 ± 0.01

Table C.12: Relative transverse momentum resolution fit parameters using the fit presented in Equation C.1, for the silicon plus MPGD layout.

Interval	Fit 1.5 T [μm]		Fit 3.0 T [μm]	
	A	B	A	B
$-1.0 \leq \eta \leq 1.0$	14.38 ± 0.05	2.27 ± 0.01	14.62 ± 0.05	2.21 ± 0.01

Table C.13: Transverse pointing resolution fit parameters using the fit presented in Equation C.2, for the silicon plus MPGD layout.

Interval	Fit 1.5 T [μm]		Fit 3.0 T [μm]	
	A	B	A	B
$-1.0 \leq \eta \leq 1.0$	23.23 ± 0.06	2.63 ± 0.01	23.48 ± 0.07	2.63 ± 0.01

Table C.14: Longitudinal pointing resolution fit parameters using the fit presented in Equation C.2, for the silicon plus MPGD layout.

References

- [1] Department of Energy. U.S. Department of Energy Selects Brookhaven National Laboratory to Host Major New Nuclear Physics Facility. <https://www.energy.gov/articles/us-department-energy-selects-brookhaven-national-laboratory-host-major-new-nuclear-physics>, January 2020. Accessed 29 October 2020. (Cited on p. 1.)
- [2] E. Rutherford. The scattering of α and β particles by matter and the structure of the atom. *The London, Edinburgh, and Dublin Philosophical Magazine and Journal of Science*, 21(125):669–688, 1911. doi:10.1080/14786440508637080. (Cited on p. 1.)
- [3] N. F. Mott. The scattering of fast electrons by atomic nuclei. *Proceedings of the Royal Society of London. Series A, Containing Papers of a Mathematical and Physical Character*, 124(794):425–442, 1929. doi:10.1098/rspa.1929.0127. (Cited on p. 1.)
- [4] M. N. Rosenbluth. High Energy Elastic Scattering of Electrons on Protons. *Phys. Rev.*, 79:615–619, August 1950. doi:10.1103/PhysRev.79.615. (Cited on p. 1.)
- [5] R. W. McAllister and R. Hofstadter. Elastic Scattering of 188-Mev Electrons from the Proton and the Alpha Particle. *Phys. Rev.*, 102:851–856, May 1956. doi:10.1103/PhysRev.102.851. (Cited on p. 1.)
- [6] M. Breidenbach, J. I. Friedman, H. W. Kendall, et al. Observed Behavior of Highly Inelastic Electron-Proton Scattering. *Phys. Rev. Lett.*, 23:935–939, October 1969. doi:10.1103/PhysRevLett.23.935. (Cited on p. 1.)
- [7] The European Muon Collaboration, J. Aubert, G. Bassompierre, et al. The ratio of the nucleon structure functions F_2^N for iron and deuterium. *Phys. Lett. B*, 123(3):275–278, 1983. ISSN 0370-2693. doi:10.1016/0370-2693(83)90437-9. (Cited on p. 2.)
- [8] The European Muon Collaboration, J. Aubert, G. Bassompierre, et al. A detailed study of the nucleon structure functions in deep inelastic muon scattering in iron. *Nucl. Phys. B*, 272(1):158–192, 1986. ISSN 0550-3213. doi:10.1016/0550-3213(86)90346-9. (Cited on p. 2.)

REFERENCES

- [9] M. Klein and R. Yoshida. Collider physics at HERA. *Prog. Part. Nucl. Phys.*, 61(2):343–393, 2008. ISSN 0146-6410. doi:10.1016/j.ppnp.2008.05.002. (Cited on p. 2.)
- [10] H1 Collaboration. *Technical proposal for the H1 detector*. DESY, Hamburg, 1986. (Cited on p. 2.)
- [11] ZEUS Collaboration. *The ZEUS detector: technical proposal*. DESY, Hamburg, 1986. (Cited on p. 2.)
- [12] COMPASS Collaboration. The COMPASS experiment at CERN. *Nucl. Instrum. Methods Phys. Res. A*, 577:455–518, 2007. doi:10.1016/j.nima.2007.03.026. (Cited on p. 2.)
- [13] B. Mecking, G. Adams, S. Ahmad, et al. The CEBAF large acceptance spectrometer (CLAS). *Nucl. Instrum. Methods Phys. Res. A*, 503(3):513–553, 2003. ISSN 0168-9002. doi:10.1016/S0168-9002(03)01001-5. (Cited on p. 2.)
- [14] J. Dudek et al. Physics Opportunities with the 12 GeV Upgrade at Jefferson Lab. *Eur. Phys. J. A*, 48:187, 2012. doi:10.1140/epja/i2012-12187-1. (Cited on p. 2.)
- [15] V. Burkert, L. Elouadrhiri, K. Adhikari, et al. The CLAS12 Spectrometer at Jefferson Laboratory. *Nucl. Instrum. Methods Phys. Res. A*, 959:163419, 2020. ISSN 0168-9002. doi:10.1016/j.nima.2020.163419. (Cited on p. 2.)
- [16] A. Accardi, J. Albacete, M. Anselmino, et al. Electron Ion Collider: The Next QCD Frontier—Understanding the glue that binds us all. *arXiv preprint arXiv:1212.1701*, 2012. (Cited on p. 2, 4, 37, 39, 76, 78, 100, and 106.)
- [17] R. Abdul Khalek, A. Accardi, J. Adam, et al. Science Requirements and Detector Concepts for the Electron-Ion Collider: EIC Yellow Report. *arXiv preprint arXiv:2103.05419*, 2021. (Cited on p. 3, 4, 5, 7, 37, 39, 113, 117, 158, 164, and 167.)
- [18] J. Yeck. Electron-Ion Collider Project Status, November 2020. 4th EIC Yellow Report Workshop at LBL, <https://indico.bnl.gov/event/9913/overview>. (Cited on p. 3.)
- [19] Thomas Ullrich. Generic Detector R&D for an Electron Ion Collider. https://wiki.bnl.gov/conferences/index.php/EIC_R%25D. Accessed 16 April 2021. (Cited on p. 3.)
- [20] A. C. Aguilar, Z. Ahmed, C. Aidala, et al. Pion and kaon structure at the electron-ion collider. *Eur. Phys. J. A*, 55(10):190, October 2019. ISSN 1434-601X. doi:10.1140/epja/i2019-12885-0. (Cited on p. 5.)
- [21] K. Meehan and STAR Collaboration. STAR Results from Au+Au Fixed-Target Collisions at $\sqrt{s_{NN}} = 4.5$ GeV. *Nucl. Phys. A*, 967:808–811, 2017. ISSN 0375-9474. doi:10.1016/j.nuclphysa.2017.06.007. The 26th Interna-

REFERENCES

- tional Conference on Ultra-relativistic Nucleus-Nucleus Collisions: Quark Matter 2017. (Cited on p. 5.)
- [22] C. Hadjidakis, D. Kikoła, J. Lansberg, et al. A fixed-target programme at the LHC: Physics case and projected performances for heavy-ion, hadron, spin and astroparticle studies. *Phys. Rep.*, 2021. ISSN 0370-1573. doi:10.1016/j.physrep.2021.01.002. (Cited on p. 5.)
- [23] H1 collaboration and ZEUS collaboration. Combination of measurements of inclusive deep inelastic $e^\pm p$ scattering cross sections and QCD analysis of HERA data. *Eur. Phys. J. C*, 75(12):580, 2015. doi:10.1140/epjc/s10052-015-3710-4. (Cited on p. 5 and 37.)
- [24] A. Kiselev. EIC Generic Detector R&D: tracking applications, July 2018. EIC Tracking Workshop. (Cited on p. 6 and 75.)
- [25] G. Wei, F. Lin, V. Morozov, et al. Integration of the full-acceptance detector into the JLEIC. In *8th Int. Particle Accelerator Conf.(IPAC'17), Copenhagen, Denmark, 14-19 May, 2017*, pages 3912–3914. JACOW, Geneva, Switzerland, 2017. (Cited on p. 6.)
- [26] PHENIX Collaboration, A. Adare, C. Aidala, et al. Concept for an Electron Ion Collider (EIC) detector built around the BaBar solenoid. *ArXiv e-prints arXiv:1402.1209*, February 2014. (Cited on p. 6 and 76.)
- [27] J. Repond. PID with fast silicon, July 2018. EIC User Group Meeting. (Cited on p. 6.)
- [28] T. Hemmick and P. Rossi. PID in the Yellow Report, November 2020. 4th EIC Yellow Report Workshop at LBL, <https://indico.bnl.gov/event/9913/overview>. (Cited on p. 7.)
- [29] B. Abelev, J. Adam, D. Adamová, et al. Technical Design Report for the Upgrade of the ALICE Inner Tracking System. Technical Report CERN-LHCC-2013-024. ALICE-TDR-017, November 2013. (Cited on p. 8, 26, 40, 75, 78, and 117.)
- [30] W. R. Leo. *Techniques for Nuclear and Particle Physics Experiments*. Springer-Verlag, 2nd edition, 1994. ISBN 0-387-17386-2. (Cited on p. 10, 11, 12, 13, 169, and 171.)
- [31] Particle Data Group, P. A. Zyla, R. M. Barnett, et al. Review of Particle Physics. *Prog. Theor. Exp. Phys*, 2020(8), August 2020. ISSN 2050-3911. doi:10.1093/ptep/ptaa104. 083C01. (Cited on p. 10, 11, 35, 36, 38, 40, 42, 44, 131, 147, 149, 150, 169, and 170.)
- [32] M. Tanabashi, K. Hagiwara, K. Hikasa, et al. Review of Particle Physics. *Phys. Rev. D*, 98:030001, August 2018. doi:10.1103/PhysRevD.98.030001. (Cited on p. 11 and 170.)
- [33] L. Landau. On the energy loss of fast particles by ionization. *J. Phys. (USSR)*, 8:201–205, 1944. (Cited on p. 11 and 171.)

REFERENCES

- [34] H. Bichsel. Straggling in thin silicon detectors. *Rev. Mod. Phys.*, 60:663–699, July 1988. doi:10.1103/RevModPhys.60.663. (Cited on p. 11 and 171.)
- [35] B. R. Martin. *Nuclear and Particle Physics*. John Wiley & Sons Ltd, 2nd edition, 2012. ISBN 978-0-470-74275-4. (Cited on p. 12 and 50.)
- [36] H. Kolanoski and N. Wermes. *Particle Detectors: Fundamentals and Applications*. Oxford University Press, 1st edition, 2020. ISBN 978-0-19-885836-2. (Cited on p. 12, 22, 24, 25, 26, 63, and 130.)
- [37] H. A. Bethe. Molière’s Theory of Multiple Scattering. *Phys. Rev.*, 89:1256–1266, March 1953. doi:10.1103/PhysRev.89.1256. (Cited on p. 13.)
- [38] V. L. Highland. Some practical remarks on multiple scattering. *Nucl. Instrum. Methods*, 129(2):497 – 499, 1975. ISSN 0029-554X. doi:10.1016/0029-554X(75)90743-0. (Cited on p. 13.)
- [39] G. R. Lynch and O. I. Dahl. Approximations to multiple Coulomb scattering. *Nucl. Instrum. Methods Phys. Res. B*, 58(1):6 – 10, 1991. ISSN 0168-583X. doi:10.1016/0168-583X(91)95671-Y. (Cited on p. 13.)
- [40] N. Wermes. Pixel vertex detectors. In *Proceedings, 34th SLAC Summer Institute on Particle Physics: The Next Frontier: Exploring with the LHC (SSI 2006): Menlo Park, California*. July 2006. (Cited on p. 15.)
- [41] R. Gluckstern. Uncertainties in track momentum and direction, due to multiple scattering and measurement errors. *Nucl. Instrum. Methods*, 24:381 – 389, 1963. ISSN 0029-554X. doi:10.1016/0029-554X(63)90347-1. (Cited on p. 17 and 18.)
- [42] F. Ragusa and L. Rolandi. Tracking at LHC. *New J. Phys.*, 9(9):336, 2007. (Cited on p. 18.)
- [43] M. Thomson. *Modern particle physics*. Cambridge University Press, 2013. ISBN 978-1-107-03426-6. (Cited on p. 20, 31, 32, 33, 34, 35, and 43.)
- [44] R. E. Kalman. A New Approach to Linear Filtering and Prediction Problems. *J. Basic Eng.*, 82(1):35–45, March 1960. ISSN 0021-9223. doi:10.1115/1.3662552. (Cited on p. 20.)
- [45] R. Frühwirth. Application of Kalman filtering to track and vertex fitting. *Nucl. Instrum. Methods Phys. Res. A*, 262(2):444 – 450, 1987. ISSN 0168-9002. doi:10.1016/0168-9002(87)90887-4. (Cited on p. 20 and 77.)
- [46] C. Höppner, S. Neubert, B. Ketzer, et al. A novel generic framework for track fitting in complex detector systems. *Nucl. Instrum. Methods Phys. Res. A*, 620(2):518 – 525, 2010. ISSN 0168-9002. doi:10.1016/j.nima.2010.03.136. (Cited on p. 22 and 115.)
- [47] C. Kittel. *Introduction to Solid State Physics*. John Wiley & Sons Ltd, 8th edition, 2004. ISBN 978-0-471-41526-8. (Cited on p. 22.)

REFERENCES

- [48] Z. He. Review of the Shockley–Ramo theorem and its application in semiconductor gamma-ray detectors. *Nucl. Instrum. Methods Phys. Res. A*, 463(1):250 – 267, 2001. ISSN 0168-9002. doi:10.1016/S0168-9002(01)00223-6. (Cited on p. 23.)
- [49] G. Fraser, A. Abbey, A. Holland, et al. The X-ray energy response of silicon Part A. Theory. *Nucl. Instrum. Methods Phys. Res. A*, 350(1):368–378, 1994. ISSN 0168-9002. doi:10.1016/0168-9002(94)91185-1. (Cited on p. 24 and 63.)
- [50] E. Simoen and C. Claeys. On the flicker noise in submicron silicon MOS-FETs. *Solid-State Electron.*, 43(5):865–882, 1999. ISSN 0038-1101. doi:https://doi.org/10.1016/S0038-1101(98)00322-0. (Cited on p. 24.)
- [51] L. Gonella. EIC Silicon Vertex and Tracking: Technology survey, March 2020. 1st EIC Yellow Report Workshop, <https://indico.bnl.gov/event/7449/overview>. (Cited on p. 25, 63, 74, and 163.)
- [52] L. Greiner, E. Anderssen, H. Matis, et al. A MAPS based vertex detector for the STAR experiment at RHIC. *Nucl. Instrum. Methods Phys. Res. A*, 650(1):68 – 72, 2011. ISSN 0168-9002. doi:10.1016/j.nima.2010.12.006. International Workshop on Semiconductor Pixel Detectors for Particles and Imaging 2010. (Cited on p. 26.)
- [53] I. Valin, C. Hu-Guo, J. Baudot, et al. A reticle size CMOS pixel sensor dedicated to the STAR HFT. *J. Instrum.*, 7(01):C01102–C01102, January 2012. doi:10.1088/1748-0221/7/01/c01102. (Cited on p. 26.)
- [54] G. Aglieri, C. Cavicchioli, P. L. Chalmet, et al. Monolithic active pixel sensor development for the upgrade of the ALICE inner tracking system. *J. Instrum.*, 8(12):C12041, 2013. (Cited on p. 26.)
- [55] W. Snoeys, G. A. Rinella, H. Hillemanns, et al. A process modification for CMOS monolithic active pixel sensors for enhanced depletion, timing performance and radiation tolerance. *Nucl. Instrum. Methods Phys. Res. A*, 871:90 – 96, 2017. ISSN 0168-9002. doi:10.1016/j.nima.2017.07.046. (Cited on p. 26, 46, 47, and 162.)
- [56] H. Augustin, N. Berger, S. Dittmeier, et al. The MuPix System-on-Chip for the Mu3e Experiment. *Nucl. Instrum. Methods Phys. Res. A*, 845:194–198, 2017. doi:10.1016/j.nima.2016.06.095. (Cited on p. 27.)
- [57] M. Mager. ALPIDE, the Monolithic Active Pixel Sensor for the ALICE ITS upgrade. *Nucl. Instrum. Methods Phys. Res. A*, 824:434 – 438, 2016. ISSN 0168-9002. doi:10.1016/j.nima.2015.09.057. Frontier Detectors for Frontier Physics: Proceedings of the 13th Pisa Meeting on Advanced Detectors. (Cited on p. 27.)
- [58] L. Musa. Silicon development in ALICE, January 2019. 11th FCC-ee workshop: Theory and Experiments. (Cited on p. 28.)
- [59] G. A. Rinella. The ALPIDE pixel sensor chip for the upgrade of the ALICE Inner Tracking System. *Nucl. Instrum. Methods Phys. Res. A*, 845:583 –

REFERENCES

- 587, 2017. ISSN 0168-9002. doi:10.1016/j.nima.2016.05.016. Proceedings of the Vienna Conference on Instrumentation 2016. (Cited on p. 28.)
- [60] E. Aschenauer, Y. Furletova, K. Gnanvo, et al. Electron-Ion Collider Detector Requirements and R&D Handbook, Version 1.1, January 2019. http://eicug.org/web/sites/default/files/EIC_HANDBOOK_v1.1.pdf. (Cited on p. 28.)
- [61] L. Musa. Letter of Intent for an ALICE ITS Upgrade in LS3. Technical Report CERN-LHCC-2019-018. LHCC-I-034, CERN, Geneva, December 2019. (Cited on p. 28.)
- [62] R. Turchetta, N. Guerrini, and I. Sedgwick. Large area CMOS image sensors. *J. Instrum.*, 6(01):C01099–C01099, January 2011. doi:10.1088/1748-0221/6/01/c01099. (Cited on p. 28.)
- [63] D. van den Ende, H. van de Wiel, R. Kusters, et al. Mechanical and electrical properties of ultra-thin chips and flexible electronics assemblies during bending. *Microelectron. Reliab.*, 54(12):2860 – 2870, 2014. ISSN 0026-2714. doi:10.1016/j.microrel.2014.07.125. (Cited on p. 29.)
- [64] M. Mager. Upgrade of the ALICE ITS in LS3. *PoS, Vertex2019:040*. 8 p, 2019. doi:10.22323/1.373.0040. (Cited on p. 29.)
- [65] Z. Ye, J. Arrington, R. J. Hill, et al. Proton and neutron electromagnetic form factors and uncertainties. *Phys. Lett. B*, 777:8 – 15, 2018. ISSN 0370-2693. doi:10.1016/j.physletb.2017.11.023. (Cited on p. 32.)
- [66] B. R. Martin and G. Shaw. *Particle Physics*. John Wiley & Sons Ltd, 3rd edition, 2009. ISBN 978-0-470-03294-7. (Cited on p. 32.)
- [67] G. Wolf. The Kinematics of Deep Inelastic Scattering in the Presence of Initial State Radiation. Technical Report hep-ex/9704006. DESY-97-047, DESY, Hamburg, April 1997. (Cited on p. 33.)
- [68] A. Blondel and F. Jacquet. In *Study of an ep Facility for Europe DESY, Hamburg*, page 393. Deutsches Electron Synchrotron / European Committee for Future Accelerators, Hamburg, Germany, April 1979. (Cited on p. 33.)
- [69] J. D. Bjorken. Asymptotic Sum Rules at Infinite Momentum. *Phys. Rev.*, 179:1547–1553, March 1969. doi:10.1103/PhysRev.179.1547. (Cited on p. 34.)
- [70] W. K. H. Panofsky. Low q electrostatics, elastic and inelastic electron (and muon) scattering. In *14th International Conference on High Energy Physics*. 1968. (Cited on p. 34.)
- [71] C. G. Callan and D. J. Gross. High-Energy Electroproduction and the Constitution of the Electric Current. *Phys. Rev. Lett.*, 22:156–159, January 1969. doi:10.1103/PhysRevLett.22.156. (Cited on p. 34.)

REFERENCES

- [72] F. Halzen and A. D. Martin. *Quarks & Leptons: An introductory course in modern particle physics*. John Wiley & Sons Ltd, 1st edition, 1984. ISBN 0-471-88741-2. (Cited on p. 34 and 43.)
- [73] L. Zheng, E. C. Aschenauer, J. H. Lee, et al. Accessing the gluon Sivers function at a future electron-ion collider. *Phys. Rev. D*, 98:034011, August 2018. doi:10.1103/PhysRevD.98.034011. (Cited on p. 37.)
- [74] A. Dumitru, O. Evdokimov, A. Metz, et al. Physics Working Group Requirements Overview, November 2020. 4th EIC Yellow Report Workshop at LBL, <https://indico.bnl.gov/event/9913/overview>. (Cited on p. 37, 39, and 126.)
- [75] M. Burkardt. Impact parameter space interpretation for generalized parton distributions. *Int. J. Mod. Phys. A*, 18(02):173–207, 2003. doi:10.1142/S0217751X03012370. (Cited on p. 37.)
- [76] M. Polyakov. Generalized parton distributions and strong forces inside nucleons and nuclei. *Phys. Lett. B*, 555(1):57–62, 2003. ISSN 0370-2693. doi:10.1016/S0370-2693(03)00036-4. (Cited on p. 37.)
- [77] F. Gelis, E. Iancu, J. Jalilian-Marian, et al. The Color Glass Condensate. *Annu. Rev. Nucl. Part. Sci.*, 60(1):463–489, 2010. doi:10.1146/annurev.nucl.010909.083629. (Cited on p. 37.)
- [78] E. Sichtermann. Gluon Saturation and EIC. *Nucl. Phys. A*, 956:233–239, 2016. ISSN 0375-9474. doi:10.1016/j.nuclphysa.2016.03.009. The XXV International Conference on Ultrarelativistic Nucleus-Nucleus Collisions: Quark Matter 2015. (Cited on p. 38.)
- [79] M. Arratia, Y. Furltova, T. J. Hobbs, et al. Charm jets as a probe for strangeness at the future Electron-Ion Collider, 2021. ArXiv:2006.12520. (Cited on p. 38.)
- [80] X. Ji. QCD Analysis of the Mass Structure of the Nucleon. *Phys. Rev. Lett.*, 74:1071–1074, February 1995. doi:10.1103/PhysRevLett.74.1071. (Cited on p. 38.)
- [81] D. Kharzeev, H. Satz, A. Syamtomov, et al. J/ψ -photoproduction and the gluon structure of the nucleon. *Eur. Phys. J. C*, 9(3):459–462, 1999. doi:10.1007/s100520050039. (Cited on p. 38.)
- [82] R. Jaffe and A. Manohar. The g_1 problem: Deep inelastic electron scattering and the spin of the proton. *Nucl. Phys. B*, 337(3):509–546, 1990. ISSN 0550-3213. doi:10.1016/0550-3213(90)90506-9. (Cited on p. 39.)
- [83] J. Ashman, B. Badelek, G. Baum, et al. A measurement of the spin asymmetry and determination of the structure function g_1 in deep inelastic muon-proton scattering. *Phys. Lett. B*, 206(2):364–370, 1988. ISSN 0370-2693. doi:10.1016/0370-2693(88)91523-7. (Cited on p. 39.)

REFERENCES

- [84] E.-C. Aschenauer, A. Bazilevsky, M. Diehl, et al. The RHIC SPIN Program: Achievements and Future Opportunities. 2015. ArXiv:1501.01220. (Cited on p. 39.)
- [85] C. Franco. $\Delta g/g$ results from the Open Charm production at COMPASS. In *5th International Workshop on Charm Physics*. August 2012. (Cited on p. 39.)
- [86] S. R. Klein and H. Mäntysaari. Imaging the nucleus with high-energy photons. *Nat. Rev. Phys.*, 1(11):662–674, November 2019. ISSN 2522-5820. doi:10.1038/s42254-019-0107-6. (Cited on p. 39.)
- [87] J.-J. Aubert, G. Bassompierre, K. H. Becks, et al. The ratio of the nucleon structure functions F_2^N for iron and deuterium. *Phys. Lett. B*, 123(CERN-EP-83-14):275–278. 10 p, January 1983. doi:10.1016/0370-2693(83)90437-9. (Cited on p. 39.)
- [88] A. W. Thomas. Reflections on the origin of the EMC effect. *Int. J. Mod. Phys. E*, 27(12):1840001, 2018. doi:10.1142/S0218301318400013. (Cited on p. 40.)
- [89] E. C. Aschenauer, S. Fazio, M. A. C. Lamont, et al. Nuclear structure functions at a future electron-ion collider. *Phys. Rev. D*, 96:114005, December 2017. doi:10.1103/PhysRevD.96.114005. (Cited on p. 40.)
- [90] Y. Chen, C. Colledani, W. Dulinski, et al. A heavy flavor tracker for STAR. Technical report, 2006. (Cited on p. 40.)
- [91] L. M. Jones and H. W. Wyld. Charmed-particle production by photon-gluon fusion. *Phys. Rev. D*, 17:759–764, February 1978. doi:10.1103/PhysRevD.17.759. (Cited on p. 41.)
- [92] H1 Collaboration. Inclusive D^0 and $D^{*\pm}$ production in deep inelastic ep scattering at HERA. *Z. Phys. C*, 72:593–605, 1996. doi:10.1007/s002880050281. (Cited on p. 41 and 42.)
- [93] H. Ralf Gerhards, ZEUS Collaboration. Charm and beauty production in electron proton scattering at HERA. *Nucl. Phys. B, Proc. Suppl.*, 115:126–130, 2003. ISSN 0920-5632. doi:10.1016/S0920-5632(02)01969-2. Hyperons, Charm and Beauty Hadrons. (Cited on p. 41.)
- [94] G. D’Agostini and D. Monaldi. Photon-gluon fusion at HERA: measurement of the fractional momentum of the gluon in low Q^2 events. *Z. Phys. C - Particles and Fields*, 48(3):467–470, September 1990. ISSN 1431-5858. doi:10.1007/BF01572028. (Cited on p. 42.)
- [95] J. J. Engelen, S. J. de Jong, M. Poletiek, et al. Photon gluon fusion cross sections at HERA energy. *Z. Phys. C - Particles and Fields*, 41(1):173–177, March 1988. ISSN 1431-5858. doi:10.1007/BF01412592. (Cited on p. 42.)

REFERENCES

- [96] F. D. Aaron et al. Measurement of the Charm and Beauty Structure Functions using the H1 Vertex Detector at HERA. *Eur. Phys. J.*, C65:89–109, 2010. doi:10.1140/epjc/s10052-009-1190-0. (Cited on p. 43.)
- [97] B. Andersson, G. Gustafson, G. Ingelman, et al. Parton fragmentation and string dynamics. *Phys. Rep.*, 97(2):31–145, 1983. ISSN 0370-1573. doi:10.1016/0370-1573(83)90080-7. (Cited on p. 43 and 116.)
- [98] S. Chekanov, T. Derrick, S. Magill, et al. Measurement of charm fragmentation ratios and fractions in photoproduction at HERA. *Eur. Phys. J. C - Particles and Fields*, 44, November 2005. doi:10.1140/epjc/s2005-02397-3. (Cited on p. 43.)
- [99] L. Gladilin. Charm hadron production fractions. December 1999. arXiv:hep-ex/9912064. (Cited on p. 43.)
- [100] E. Lohrmann. A Summary of Charm Hadron Production Fractions. December 2011. arXiv:1112.3757. (Cited on p. 43.)
- [101] G. Aglieri, C. Cavicchioli, P. L. Chalmet, et al. Monolithic active pixel sensor development for the upgrade of the ALICE inner tracking system. *J. Instrum.*, 8(12):C12041, 2013. (Cited on p. 45.)
- [102] CERN. *Investigator1 Chip Manual*. CERN, 2nd edition, 2014. (Cited on p. 45.)
- [103] J. Rieger. Development of a Standardised Readout System for Active Pixel Sensors in HV/HR-CMOS Technologies for ATLAS Inner Detector Upgrades. *J. Instrum.*, 11(02):C02075, 2016. (Cited on p. 47.)
- [104] C. Riegel, M. Backhaus, J. V. Hoorne, et al. Radiation hardness and timing studies of a monolithic TowerJazz pixel design for the new ATLAS Inner Tracker. *J. Instrum.*, 12(01):C01015, 2017. (Cited on p. 48 and 50.)
- [105] S. Ritt. *DRS4 Evaluation Board User's Manual*. Paul Scherrer Institute, 5.1 edition, 2017. <https://www.psi.ch/drs/documentation>. (Cited on p. 48 and 49.)
- [106] CIVIDEC Instrumentation GmbH. *Cividec product information sheet C1-HV*. CIVIDEC Instrumentation GmbH, 2017. <https://cividec.at/>. (Cited on p. 48.)
- [107] National Nuclear Data Center. Decay radiation results for ^{55}Fe . <https://www.nndc.bnl.gov/nudat2/decaysearchdirect.jsp?nuc=55FE&unc=nds>. Accessed 2 April 2021. (Cited on p. 49.)
- [108] R. Brun and F. Rademakers. ROOT — An object oriented data analysis framework. *Nucl. Instrum. Methods Phys. Res. A*, 389(1–2):81 – 86, 1997. ISSN 0168-9002. doi:http://dx.doi.org/10.1016/S0168-9002(97)00048-X. See also <http://root.cern.ch/>. (Cited on p. 50, 76, and 115.)
- [109] W. Snoeys and T. Kugathasan. Private communication, May 2019. (Cited on p. 52, 53, 54, and 56.)

REFERENCES

- [110] M. Munker. *Test beam and simulation studies on High Resistivity CMOS pixel sensors*. Ph.D. thesis, May 2018. doi:urn:nbn:de:hbz:5n-51913. (Cited on p. 52, 53, and 54.)
- [111] H. Pernegger, R. Bates, C. Buttar, et al. First tests of a novel radiation hard CMOS sensor process for Depleted Monolithic Active Pixel Sensors. *J. Instrum.*, 12(06):P06008, 2017. (Cited on p. 53.)
- [112] D. Maneuski. Private communication, November 2017. (Cited on p. 54.)
- [113] M. Munker, M. Benoit, D. Dannheim, et al. Simulations of CMOS pixel sensors with a small collection electrode, improved for a faster charge collection and increased radiation tolerance. *J. Instrum.*, 14(05):C05013–C05013, May 2019. doi:10.1088/1748-0221/14/05/c05013. (Cited on p. 59, 60, 62, 73, 74, and 162.)
- [114] R. Cardella, I. A. Tortajada, I. Berdalovic, et al. MALTA: an asynchronous readout CMOS monolithic pixel detector for the ATLAS High-Luminosity upgrade. *J. Instrum.*, 14(06):C06019–C06019, June 2019. doi:10.1088/1748-0221/14/06/c06019. (Cited on p. 60, 61, 67, 69, 71, and 73.)
- [115] M. Dyndal, V. Dao, P. Allport, et al. Mini-MALTA: radiation hard pixel designs for small-electrode monolithic CMOS sensors for the High Luminosity LHC. *J. Instrum.*, 15(02):P02005–P02005, February 2020. doi:10.1088/1748-0221/15/02/p02005. (Cited on p. 60 and 61.)
- [116] M. Mironova, P. Allport, I. Berdalovic, et al. Measurement of the relative response of small-electrode CMOS sensors at Diamond Light Source. *Nucl. Instrum. Methods Phys. Res. A*, 956:163381, March 2020. doi:10.1016/j.nima.2019.163381. (Cited on p. 62.)
- [117] A. Kiselev and eRHIC task force team. EIC detector simulations in FairRoot framework. In *APS Division of Nuclear Physics Meeting Abstracts*, page DG.004. October 2013. (Cited on p. 76.)
- [118] M. Al-Turany, D. Bertini, R. Karabowicz, et al. The FairRoot framework. *J. Phys. Conf. Ser.*, 396(2):022001, 2012. (Cited on p. 76.)
- [119] JLEIC Design Study Collaboration, T. Satogata, and Y. Zhang. JLEIC - A Polarized Electron-Ion Collider at Jefferson Lab. *ICFA Beam Dyn. Newslett.*, 74:92–182, 2018. (Cited on p. 76.)
- [120] eRD16 collaboration presentation. Forward/Backward Tracking at EIC using MAPS Detectors, July 2018. EIC Detector R&D Advisory Committee meeting. (Cited on p. 87.)
- [121] E.P. Sichtermann, N. Apadula, A. Collu, et al. eRD16: Forward/Backward Tracking at EIC using MAPS Detectors, July 2018. EIC Detector R&D Advisory Committee meeting. (Cited on p. 88.)

REFERENCES

- [122] L. Greiner. MAPS sensor/detector efforts at CERN with possible applications to EIC, December 2019. EIC User Group Yellow Report kick-off meeting, <https://indico.jlab.org/event/348/overview>. (Cited on p. 113.)
- [123] C. Hetzel. Detector vacuum chamber and SR studies, March 2020. 1st EIC Yellow Report Workshop, <https://indico.bnl.gov/event/7449/overview>. (Cited on p. 114.)
- [124] C. Pinkenburg et al. Fun4All, September 2015. EIC Software Meeting, <https://www.jlab.org/conferences/eicsw/>. (Cited on p. 115.)
- [125] C. Gumpert, A. Salzburger, M. Kiehn, et al. ACTS: from ATLAS software towards a common track reconstruction software. Technical Report ATL-SOFT-PROC-2017-030. 4, CERN, Geneva, January 2017. doi:10.1088/1742-6596/898/4/042011. (Cited on p. 115 and 165.)
- [126] S. Agostinelli, J. Allison, K. Amako, et al. Geant4—a simulation toolkit. *Nucl. Instrum. Methods Phys. Res. A*, 506(3):250–303, 2003. ISSN 0168-9002. doi:10.1016/S0168-9002(03)01368-8. (Cited on p. 116.)
- [127] T. Sjöstrand, S. Mrenna, and P. Z. Skands. A Brief Introduction to PYTHIA 8.1. *Comput. Phys. Commun.*, 178:852–867, 2008. doi:10.1016/j.cpc.2008.01.036. (Cited on p. 116.)
- [128] T. Sjöstrand, S. Mrenna, and P. Skands. PYTHIA 6.4 physics and manual. *J. High Energy Phys.*, 2006(05):026–026, may 2006. doi:10.1088/1126-6708/2006/05/026. (Cited on p. 116.)
- [129] M. Dobbs and J. B. Hansen. The HepMC C++ Monte Carlo Event Record for High Energy Physics. Technical Report ATL-SOFT-2000-001, CERN, Geneva, June 2000. Revised version number 1 submitted on 2001-02-27 09:54:32. (Cited on p. 116.)
- [130] L. Greiner. What to expect for radiation lengths for EIC Si structures, May 2020. 2nd EIC Yellow Report Workshop at Pavia University, <https://indico.bnl.gov/event/8231/overview>. (Cited on p. 117, 120, and 166.)
- [131] H. Klest. Overview and design of the sPHENIX TPC. *J. Phys. Conf. Ser.*, 1498:012025, April 2020. doi:10.1088/1742-6596/1498/1/012025. (Cited on p. 117.)
- [132] A. Dumitru, O. Evdokimov, A. Metz, et al. Physics Working Group: Overview and progress report, May 2020. 2nd EIC Yellow Report Workshop at Pavia University, <https://indico.bnl.gov/event/8231/overview>. (Cited on p. 139.)
- [133] S. Dalla Torre. Detector Matrix/Updates - Barrel PID, November 2020. 4th EIC Yellow Report Workshop at LBL, <https://indico.bnl.gov/event/9913/overview>. (Cited on p. 147.)

REFERENCES

- [134] G. Flucke. *Photoproduction of D^* Mesons and D^* Mesons Associated with Jets at HERA*. Ph.D. thesis, March 2005. doi:10.3204/DESY-THESIS-2005-006. (Cited on p. 150.)
- [135] The LHCb Collaboration. Measurement of mixing and CP violation parameters in two-body charm decays. *J. High Energy Phys.*, 04:129, 2012. doi:10.1007/JHEP04(2012)129. (Cited on p. 150 and 151.)
- [136] G. J. Feldman, I. Peruzzi, M. Piccolo, et al. Observation of the Decay $D^{*+} \rightarrow D^0 \pi^+$. *Phys. Rev. Lett.*, 38:1313–1315, June 1977. doi:10.1103/PhysRevLett.38.1313. (Cited on p. 151.)
- [137] E. C. Aschenauer, R. Rajput-Ghoshal, and R. Ent. Discussion on YR Content: Magnetic Field Strength, Magnet Bore, November 2020. 4th EIC Yellow Report Workshop at LBL, <https://indico.bnl.gov/event/9913/overview>. (Cited on p. 158.)
- [138] T. Kugathasan, T. Ando, D. Dannheim, et al. Monolithic CMOS sensors for sub-nanosecond timing. *Nucl. Instrum. Methods Phys. Res. A*, 979:164461, 2020. ISSN 0168-9002. doi:10.1016/j.nima.2020.164461. (Cited on p. 165.)
- [139] A. Kiselev. Boundary conditions on the EIC detector design, November 2020. 4th EIC Yellow Report Workshop at LBL, <https://indico.bnl.gov/event/9913/overview>. (Cited on p. 166.)
- [140] P. Vavilov. Ionization losses of high-energy heavy particles. *Sov. Phys. JETP*, 5:749–751, 1957. (Cited on p. 171.)